UNIVERSIDADE DA CORUÑA

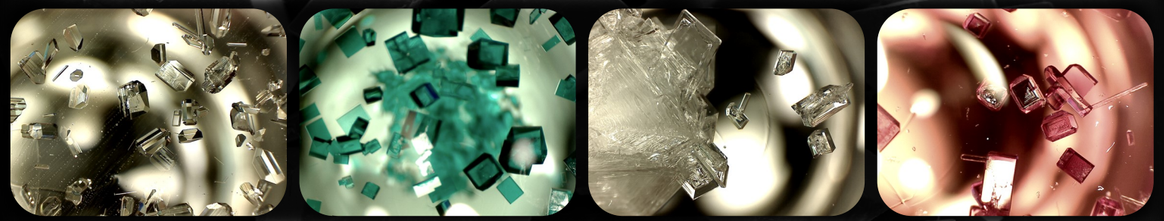

Classic molecular compounds and emergent organic-inorganic hybrid perovskites with (multi)functional properties and (multi)stimuli responsiveness

Juan M. Bermúdez García

2016

UNIVERSIDADE DA CORUÑA

DEPARTAMENTO QUÍMICA FUNDAMENTAL

1989 2014

UNIVERSIDADE DA CORUÑA

CICA

CENTRO DE INVESTIGACIÓNS CIENTÍFICAS AVANZADAS

Doctoral Thesis

Classic molecular compounds and emergent organic-inorganic hybrid perovskites with (multi)functional properties and (multi)stimuli responsiveness

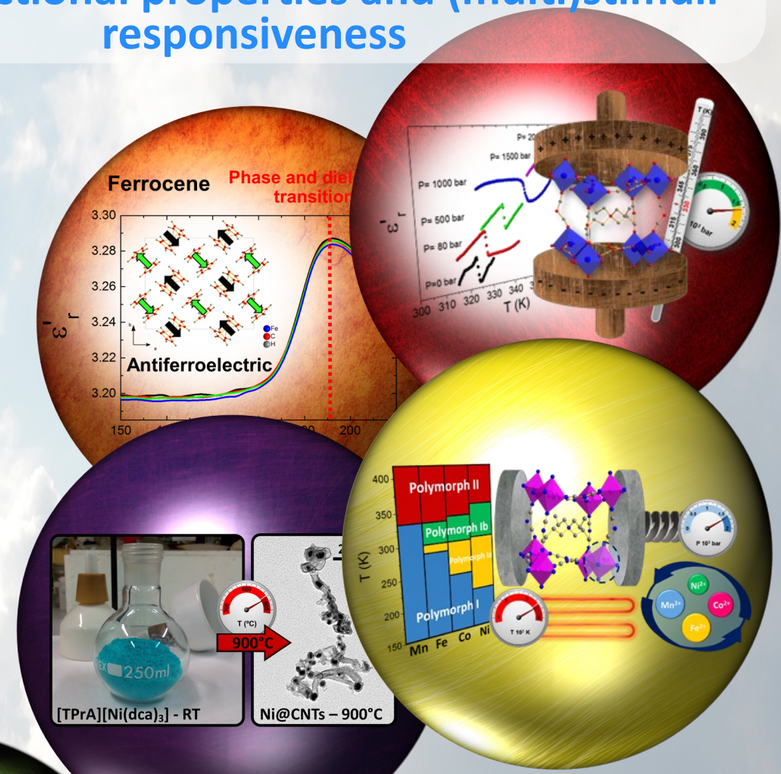

Juan Manuel Bermúdez García
A Coruña 2016

Classic molecular compounds and emergent organic-inorganic hybrid perovskites with (multi)functional properties and (multi)stimuli responsiveness

Juan Manuel Bermúdez García

Doctoral Thesis UDC 2016

Directores:

Dra. María Antonia Señarís Rodríguez

Dr. Manuel Sánchez Andújar

Departamento de Química Fundamental, Facultad de Ciencias
Centro de Investigacións Científicas Avanzadas (CICA)
Universidade da Coruña (UDC)

Programa regulado por el RD 99/2011: Química Ambiental y Fundamental

Memoria presentada en la Facultad de Ciencias de la Universidade da Coruña por **Juan Manuel Bermúdez García** para optar al Grado de Doctor en Química por la Universidade da Coruña.

A Coruña, Septiembre 2016

Doctorando

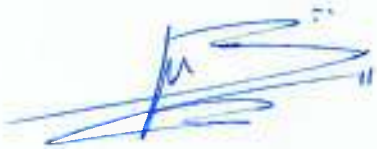

Juan Manuel
Bermúdez García

Directores

Dra. María Antonia
Señarís Rodríguez

Dr. Manuel Sánchez
Andújar

Departamento de Química Fundamental
UNIVERSIDADE DA CORUÑA

Dra. María Antonia Señarís Rodríguez, Catedrática de Universidad, y **Dr. Manuel Sánchez Andújar**, Profesor Titular de Universidad, pertenecientes al Área de Química Inorgánica de la Universidade da Coruña.

Hacen constar:

Que la presente memoria titulada "Classic molecular compounds and emergent organic-inorganic hybrid perovskites with (multi)functional properties and (multi)stimuli responsiveness" ha sido realizada bajo su dirección por el Licenciado en Química **Juan Manuel Bermúdez García** en el Área de Química Inorgánica dependiente del Departamento de Química Fundamental y, habiendo sido concluida, autorizan su presentación para optar al Grado de Doctor en Química con mención de Doctor Internacional.

A Coruña, Septiembre de 2016.

Dra. María Antonia Señarís Rodríguez

Dr. Manuel Sánchez Andújar

A mi familia
y a mis seres queridos,

Agradecimientos

El trabajo de investigación que aquí se presenta fue financiado por el **Ministerio de Economía y Competitividad (MINECO)** y por el **Fondo Europeo de Desarrollo Regional (FEDER)**, (proyectos MAT2010-21342-C02-01 y ENE2014-56237-C4-4-R) y la **Xunta de Galicia** (proyectos 10 PXIB 103 272 PR y GRC2014/042). Asimismo, durante la realización de este trabajo de investigación, he podido disfrutar de contratos asociados a los proyectos (10 PXIB 103 272 PR, MAT2010-21342-C02-01, ENE2014-56237-C4-4-R y GRC2014/042) y de una beca de la **Fundación Barrié** (Beca de Posgrado 2014) para realizar una estancia de investigación en la Universidad de Oxford.

La presente *Tesis Doctoral* ha sido desarrollada en un entorno de trabajo multidisciplinar, donde se ha contado con el apoyo y colaboración de investigadores pertenecientes a diversas universidades y centros de investigación, tanto nacionales como internacionales. Así pues, me gustaría dedicar las siguientes líneas a agradecerles el haberme permitido trabajar estrechamente junto a ellos.

En primer lugar, me gustaría agradecer especialmente a mis directores, la **Dra. María Antonia Señarís Rodríguez** y el **Dr. Manuel Sánchez Andújar**, así como a la **Dra. Socorro Castro García**, investigadores del grupo de *"Química Molecular y Materiales (QuiMolMat)"* perteneciente a la Universidade da Coruña (UDC) y al Centro de Investigacións Científicas Avanzadas (CICA). Desde el primer momento, me habéis facilitado todas las herramientas a vuestro alcance para formarme como investigador, y vuestra enorme dedicación ha supuesto para mí una fuente de motivación e inspiración continua, por lo que no tengo más que palabras de agradecimiento por haber tenido la fortuna de contar con vuestro apoyo en esta etapa de mi carrera.

También me gustaría agradecer a los siguientes investigadores con los que he tenido el placer de trabajar durante la realización de esta *Tesis Doctoral*:

I especially want to thank **Prof. Henry J. Snaith FRS**, **Dr. Amir A. Haghighirad**, **Dr. Jacob T. W. Wang** and all the ***"Snaithlings"***, for the opportunity of doing a research stay in their group of "Photovoltaic and Optoelectronic Devices" of the University of Oxford.

Al **Prof. Juan Bisquert**, director del grupo de investigación de "Dispositivos Fotovoltaicos y Optoelectrónicos" de la Universitat Jaume I de Castellón, y al **Dr. Emilio Juárez**, investigador del mismo grupo en el momento de mi estancia.

Al **Dr. Ángel Alegría** y a **Luis Botana**, del grupo "Polymers and Soft Matter" del Centro de Física de Materiales, Universidad del País Vasco - CSIC.

Al **Dr. Jorge Mira**, investigador del grupo de "Magnetismo y Nanotecnología" de la Universidad de Santiago de Compostela.

A la **Dra. Teresa A. Centeno**, investigadora en el Instituto Nacional del Carbon del CSIC, Oviedo.

Agradecimientos

A la **Dra. Sofía Calero**, al **Dr. Said Hamad** y a **José M. Vicent**, investigadores del grupo de "Materiales Nanoestructurados con Aplicaciones Tecnológicas" de la Universidad Pablo de Olavide, Sevilla.

Al **Dr. Ramón Artiaga**, al **Dr. Jorge López Beceiro** y a la **Dra. Sonia Zaragoza**, del grupo de investigación de "Propiedades Térmicas y Reológicas de Materiales" de la Universidade da Coruña.

Además, quisiera dar las gracias a los doctores con los que he compartido laboratorio en la Universidade da Coruña, **Martin Regueiro**, **Adrian Roca**, **Aurora Rodríguez**, **Marta Mato, Israel Carreira**, **Leticia Naya**, **Eva López**, y especialmente, **Susana Yáñez**, **Breogán Pato** y **Claudia Gómez**, quienes me enseñaron las primeras lecciones en esta etapa predoctoral.

No quisiera olvidar dar las gracias a mis compañeros doctorandos y maestrandos, **Lorena Alonso**, **Alberto García**, **Fernando Rodríguez**, **Ismael Marcos**, **Jorge Lado**, **Patricia Gaudino**, **Oscar Lenis**, **Rosa Pujales**, **Laura Caneda**, **Iago Neira**, **Tamara Rama**, **Olaya Domarco**, **Diana Martínez**, **Juan Carlos Fuentes**; jóvenes investigadores quienes, a pesar de las dificultades y las trabas encontradas, siguen luchando por mantener vivo el avance de la ciencia española.

En el ámbito de lo personal, quisiera permitirme la licencia de dedicarle unas líneas de agradecimiento a mi familia, en especial a mis padres, **Juan Bermúdez** y **Ángeles García**, y hermanos, **Gabriel Ángel** y **Nazaret Bermúdez García**, quienes me han enseñado los valores y principios, que a su vez aprendieron de mis abuelos, y que me han hecho ser quien soy. Espero haceros sentir orgullosos.

También me gustaría agradecer a mis amigos y familiares norteños, **Emiliano Caballero**, **Miguel Cuerva**, **Santiago Melo**, **Katia Caamaño**, **Sabela Baamonde**, **Adrián Andrade**, **Nerea Pérez**, **Ana Quiroga**, **Carola Heras**, **Fátima Lucio**, **Javier Rodríguez**, **Efrén Díaz**, **Ana Álvarez**, **Noelia Lago** y la pequeñita **Alicia Andrade**, sin olvidar a **Mar Marañón**, **Eva Alonso**, **Diego Alonso** y **Jesús Alonso.** Gracias a todos vosotros he encontrado un hogar en Galicia.

Por último, me gustaría agradecerte a ti, **Lorena Alonso**, el haberme enseñado que una caída inesperada puede ser el principio de un camino aún más inesperado, y por recordarme que la vida misma es *Química*.

Graciñas bolboreta

Abstract/Resumen/Resumo

Abstract:

This *Ph.D. Thesis* focus on the development of new (multi)functional and (multi)stimuli responsive materials, based on organic-inorganic hybrids and molecular compounds, where the application of different stimuli (temperature, external isostatic/uniaxial pressure and/or internal chemical pressure) is able to induce specific functionalities in the materials. Moreover, this work aims to find new hybrid precursors for nanostructured carbon materials. These are important areas of research in Solid State and Materials Science in view of their technological potential and environmental applications.

In this context, this *Ph.D. Thesis* has explored new functional properties on novel organic-inorganic hybrid materials with formula $[TPrA][M(dca)_3]$ (M = Mn^{2+}, Fe^{2+}, Co^{2+} and Ni^{2+}) perovskite-like structure, some of which are synthesized and/or described for the first time. Also two very well-known molecular compounds, namely ferrocene, $[Fe(C_5H_5)_2]$, and ammonia-borane, $(H_3N{\cdot}BH_3)$, are investigated in the search for ferroic order. In addition, these studies have revealed pressure-induced caloric effects in the $[TPrA][Mn(dca)_3]$, which shows a promising potential for solid state cooling applications. Finally, the $[TPrA][M(dca)_3]$ (M = Ni^{2+} and Co^{2+}) have been found to be very useful precursors in a simple, scalable and economical accessible synthetic method to obtain carbon nanotubes with magnetic nanoparticles embedded, M@CNTs (Ni^{2+} and Co^{2+}).

Resumen:

Esta *Tesis Doctoral* se centra en el desarrollo de nuevos materiales (multi)funcionales y (multi)sensitivos, basados en híbridos orgánico-inorgánicos y en compuestos moleculares, donde la aplicación de diferentes estímulos externos (temperatura, presión isostática/uniaxial externa y/o presión química interna) es capaz de inducir funcionalidades específicas en estos materiales. Además, este trabajo trata de buscar nuevos precursores híbridos de materiales nanoestructurados de carbono. Estas son importantes áreas de investigación en Ciencia de Materiales, debido al potencial tecnológico y las aplicaciones medioambientales de estos materiales.

En este contexto, en esta *Tesis Doctoral* se han explorado las propiedades funcionales en los nuevos compuestos híbridos orgánico-inorgánicos de fórmula molecular $[TPrA][M(dca)_3]$ (M = Mn^{2+}, Fe^{2+}, Co^{2+} y Ni^{2+}) y estructura tipo perovskita, algunos de los cuales se han sintetizado y/o descrito por primera vez. Además se han estudiado dos materiales moleculares muy conocidos, como son el ferroceno, $[Fe(C_5H_5)_2]$, y el amino-borano $(H_3N{\cdot}BH_3)$, en búsqueda de orden ferróico. Asimismo, estos estudios han revelado efectos calóricos inducidos por la presión en el compuesto $[TPrA][Mn(dca)_3]$, que muestra un gran potencial para aplicaciones de refrigeración en estado sólido. Finalmente, se ha encontrado que los compuestos $[TPrA][M(dca)_3]$ (M = Ni^{2+} y Co^{2+}) son precursores muy versátiles para obtener nanotubos de carbono con nanopartículas magnéticas embebidas su interior, M@CNTs (Ni^{2+} y Co^{2+}), mediante un método sencillo, escalable y económicamente accesible.

Resumo:

Esta *Tese de Doutoramento* céntrase no desenvolvemento de novos materiais (multi)funcionais e (multi)sensibles, baseados en híbridos orgánico-inorgánicos e compostos moleculares, onde a aplicación de diferentes estímulos externos (temperatura, presión isostática/uniaxial externa e/ou presión química interna) é capaz de inducir unha función específica nestes materiais. Ademais, este estudo trata de atopar novos precursores híbridos de materiais nanoestruturados de carbono. Estas son áreas importantes de investigación en Ciencia de Materiais por mor do potencial destes materiais para aplicacións tecnolóxicas e medioambientais, que están relacionadas coas súas propiedades funcionais como, por exemplo, piezoeletricidade, ferroeletricidade, ferromagnetismo, magnetorresistencia, supercondutividade, multiferroicidade, etc.

Neste contexto, esta *Tese de Doutoramento* explora as propiedades funcionais nos novos compostos híbridos orgánico-inorgánicos de fórmula molecular $[TPrA][M(dca)_3]$ (M = Mn^{2+}, Fe^{2+}, Co^{2+} e Ni^{2+}) e estrutura tipo perovskita; ademais de materiais moleculares coñecidos como o ferroceno, $[Fe(C_5H_5)_2]$, e o amino-borano ($H_3N{\cdot}BH_3$). Estes estudos tamén revelaron efectos calóricos inducidos pola presión sobre o composto $[TPrA][Mn(dca)_3]$, o que demostra gran potencial para aplicacións en refrixeración de estado sólido. Finalmente, verificouse que os compostos $[TPrA][M(dca)_3]$ (M = Ni^{2+} e Co^{2+}) son precursores versátiles para sintetizar nanotubos de carbono con nanopartículas magnéticas incorporadas, M@CNTs (M = Ni^{2+} e Co^{2+}), usando un método sinxelo, escalable e accesible.

Preface

Global warming, environment pollution, and massive energy and technology consumption are main signatures and drawbacks of our current society, see Figure P-1.

In this context, the scientific community faces very complex and urgent challenges, such as: having to develop sustainable energy sources and solutions, reducing their environmental footprint, avoiding the use of expensive and scarce materials (such as rare-earth magnetic alloys, lithium, indium, etc.) as well as of potentially global warming substances such as refrigeration greenhouse gases, etc. And, of course, having to improve the feasibility and efficiency of technological devices, which every time are desirable to become more and more lightweight, smaller and efficient.

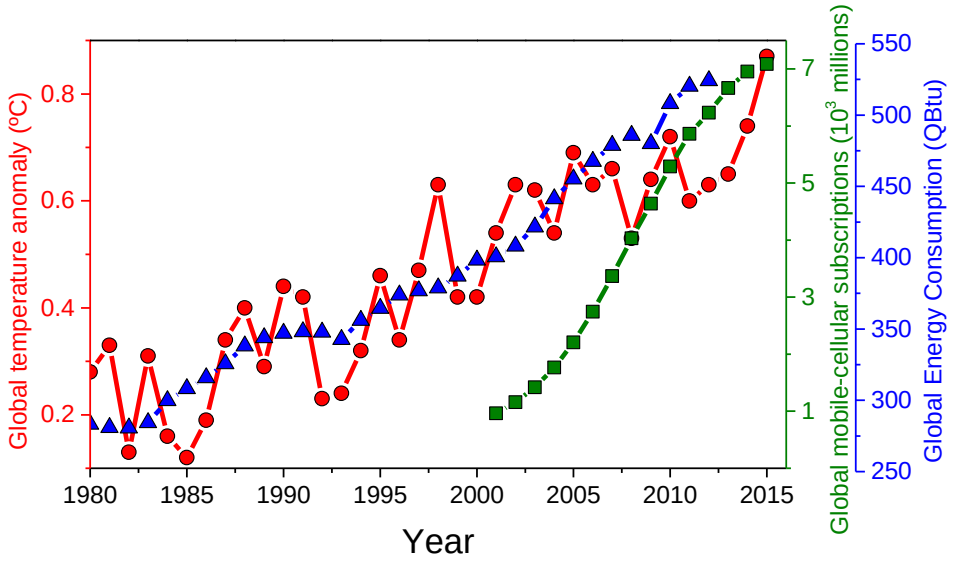

Figure P-1. Overlap of three statistical markers of global warming, energy crisis and technology consumption of the last 35 years. The red curve indicates temperature anomalies on global surface temperature compare with 1951-1980 average temperatures.[1] The blue curve show the total primary energy consumption in the world,[2] while the green curve represent the number of global mobile phone subscriptions.[3]

Looking for innovative solutions, and within the fields of Solid State and Materials Science, great efforts have been devoted in the last decades to the development of *"(multi)functional materials"*,[4] and "*(multi)stimuli responsive materials*",[5] where the application of external single or multiple stimuli is able to induce specific functionalities in the material, for instance a magnetic or an electric response, see Figure P-2.

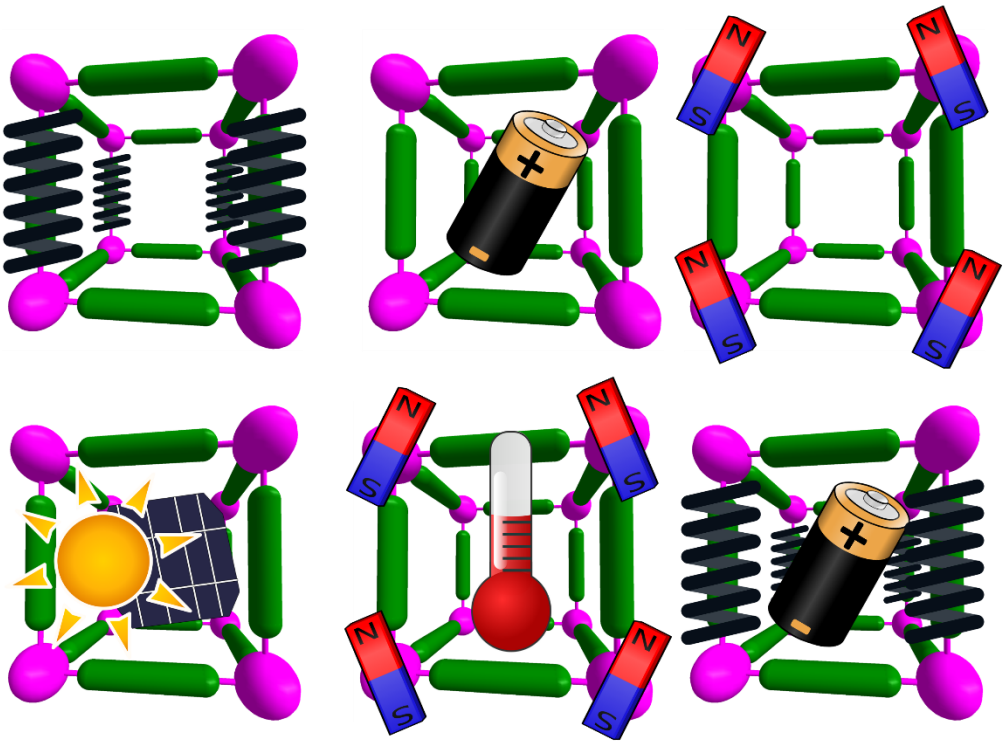

Figure P-2. Examples of (multi)functional and/or (multi)stimuli responsive materials whose structure and functional properties can be modulated by different external stimuli: pressure/strain, electric/magnetic field, light, temperature, etc.

Traditionally, most of these studies were focused on ceramic materials,[4] specially oxides and many of them perovskites. This latter compounds, with general formula ABX_3 (A: alkali, alkaline earth, or lanthanide cations, B: transition metal cation, X: O^{2-}) are crystalline solids whose structure can be defined as a tridimentional network of $[BX_6]$ octahedra sharing corners with the A-site cations located inside the resulting cubooctahedral cavities, see Figure P-3. These ABO_3 perovskites are known to show a large variety of functional properties, such as piezoelectricity, ferroelectricity, ferromagnetism, magnetoresistance, superconductivity, multiferroicity, etc.[6]

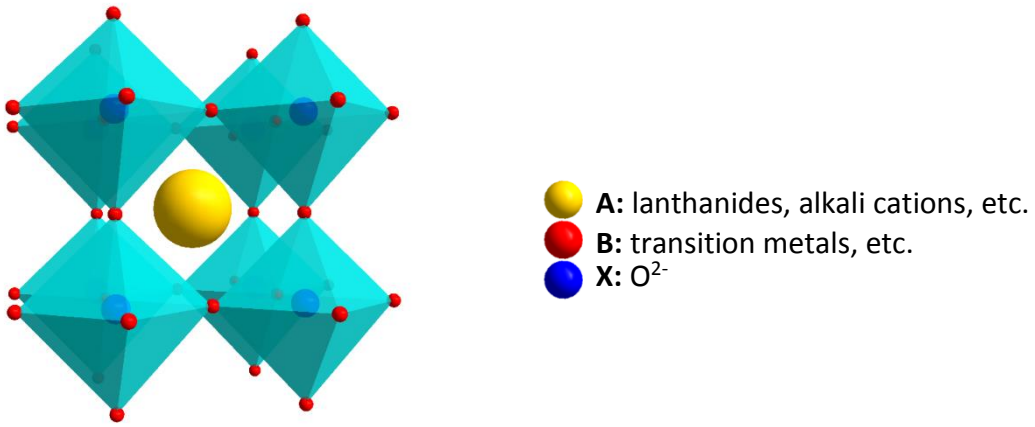

Figure P-3. Ideal ABX_3 perovskite structure.

More recently there is a growing interest in developing new (multi)functional and (multi)stimuli responsive materials based on organic-inorganic hybrid compounds, including metal organic frameworks (MOFs) and coordination polymers, which can exhibit a higher versatility, flexibility, structural richness, etc., due to the multiple possible combinations of different organic and inorganic units as building blocks in the structure.

In this modern field, significant efforts have been devoted in the very last few years to hybrid organic-inorganic materials with perovskite-like structure, the so-called hybrid perovskites,[7] where the A- and/or X-sites become organic building blocks see Figure P-4.

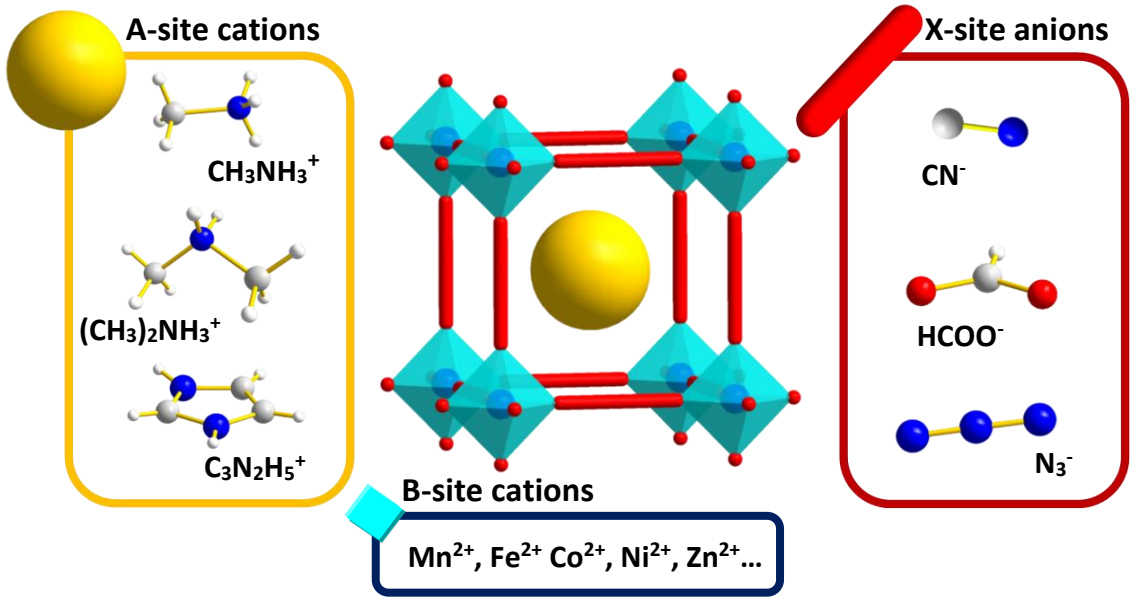

Figure P-4. Perovskite-like structure displayed by some organic-inorganic hybrids, where the A-site is normally occupied by midsize organic alkylammonium cations, X by organic or inorganic bidentate-bridging ligands ($HCOO^-$, CN^- or N_3^-) and the B-site by transition metal cations.

Some of these materials have already revealed remarkable functional properties such as the unprecedented photoconductivity in $[MA]PbI_3$ (MA = methylammonium cation, $CH_3NH_3^+$),[8] and the noteworthy cooperative magnetic, electric or elastic order in $[AmineH][M(X)_3]$ (AmineH = midsized protonated amines, M = divalent transition metal cations, X = polyatomic ligands such as $HCOO^-$, N_3^- or CN^-).[9] Even more, the metal-formates $[DMA][M(HCOO)_3]$ (DMA: dimethylammonium cation, $(CH_3)_2NH_2^+$) have been found to be type-I multiferroic materials,[10] and very recently, coupled magnetic and electric order has been demonstrated in $[MA][Co(HCOO)_3]$[11] opening the large, flexible, multifunctional and designable family of hybrid perovskites to magnetically induced multiferroic behaviour.

In addition, organic-inorganic hybrids, where the combination of different organic and inorganic parts allows to control the porosity and chemical composition of the resulting compounds,[12] have shown potential in a slightly different scenario: as strategically designed precursors of nanostructured carbon materials with interesting energy and environmentally important applications, such as energy storage, gas adsorption or pollutant removal, among others others.[13]

Preface

In view of this background, the main objectives of the present ***Ph.D. Thesis,*** which has been elaborated within the ***Environmental and Fundamental Chemistry Ph.D. Program*** of the ***University of A Coruna***, have been:

(i) the search for novel (multi)functional and (multi)stimuli materials.

(ii) the development of organic-inorganic hybrid as precursors of nanostructured carbon materials.

As for (i) even if such studies have been mainly carried out among "emergent" organic-inorganic hybrid frameworks, we have also used the alternative approach of revisiting two "old" compounds (namely the "classic" molecular compounds ferrocene and ammonia-borane) in the search for new functional properties

Moreover, along these studies we have discovered strong pressure-induced caloric effects in some of these compounds, which could be of interest for cooling applications, aspect that was further investigated in the last months of this *Ph.D. work*.

All these studies have comprised the synthesis of a number of compounds, their structural characterization and the study of their physico-chemical properties: ranging from the more traditional adsorption capacity, to the more recent functional dielectric, (multi)ferroic and refrigeration properties that can be easily modulated under the application of accessible external (multi)stimuli, mainly pressure and temperature.

To present the main contributions of this work this memory has been organised as follows:

Chapter 1 consist on an introductory section.

Chapters 2 to 6 contain self-contained studies presented as research papers which focus on different materials, their properties and applications.

In this context, **chapter 2 and 3** are devoted to a new family of organic-inorganic hybrids with perovskite-like structure, and formula [TPrA][M(dca)$_3$] with M = Mn^{2+} (**chapter 2**) and M = Fe^{2+}, Co^{2+} and Ni^{2+}(**chapter 3**), some of which are presented for the first time. As discussed there, these compounds display remarkable (multi)ferroic properties, multiple phase transitions and (multi)sensitive responsiveness. Even more, and as presented and discussed in **chapter 4**, these hybrid perovskites are found to display pressure-driven refrigeration properties, concept known as barocaloric effect. Very remarkably, and as far as we know, they would be the first hybrids showing this functionality.

In addition, the Ni and Co members of this [TPrA][M(dca)$_3$] family are found to be precursors of carbon nanotubes embedded with magnetic nanoparticles, materials of interest for pollutant removal and recovery under an applied magnetic field, aspect that is presented in **chapter 5**.

On the other hand, in **chapter 6**, two very well-known “classic” molecular compounds, specifically ferrocene, [Fe(C_5H_5)2], and ammonia-borane, ($H_3N.BH_3$), are revisited from a completely different point of view to the traditional one, revealing new functionalities that had not been described prior to this work.

Chapter 7 summarizes the main conclusions obtained out-of the results exposed along the previous chapters.

Annexe I contains tables with selected crystallographic data of the [TPrA][M(dca)$_3$] (M = Mn^{2+}, Fe^{2+}, Co^{2+} and Ni^{2+}) compounds.

A**nnexe II** contains a summary of the *Ph.D. Thesis* in Spanish language.

A**nnexe III** contains the publications in scientific journals and communications in specialized congresses of Juan Manuel Bermúdez García during this *Ph.D. work*.

References

1 NASA Goddard institute for space studies**,** *Global Climate Change*, 2016, http://climate.nasa.gov/vital-signs/global-temperature/

2 U.S. Energy Information Administration, *International Energy Statistics*, 2016, https://www.eia.gov/

3 International Telecommunication Union**,** 2016**,** http://www.itu.int/en/

4 Kang, Z. C.; Wang, L. Z. *Functional and smart materials*, Plenum Press, New York, 1998.

5 Coudert, X. *Chem. Mater.* 2015, **27**, 1905.

6 (a) Granger, P.; Parvulescu, V. I.; Kaliaguine, S.; Prellier, W. *Perovskites and Related Mixed Oxides: Concepts and Applications*, Wiley-VCH, Weinheim, Germany, 2015; (b) F. S. Galasso, *Structure, properties, and preparation of perovskite-type compounds*, Pergamon Press, New York, 1969; (c) Peña, M. A.; Fierro, J. L. G. *Chem. Rev.* 2001, **101**, 1981.

7 Kieslich, G.; Sun, S.; Cheetham, A. K. *Chem. Sci.* 2015, **6**, 3430.

8 Lee, M. M.; Teuscher, J.; Miyasaka, T.; Murakami, T. N.; Snaith, H. J. *Science* 2012, **338**, 643.

9 Xu, W.-J.; Du, Z.-Y.; Zhang, W.-X.; Chen, X.-M. *CrystEngComm* 2016, DOI: 10.1039/C6CE01485B.

10 Jain, P.; Ramachandran, V.; Clark, R. J.; Zhou, H. D.; Toby, B. H.; Dalal, N. S.; Kroto, H. W.; Cheetham, A. K. *J. Am. Chem. Soc.* 2009, **131**, 13625.

11 Gómez-Aguirre, L. C.; Pato-Doldán, B.; Mira, J.; Castro-García, S.; Señarís-Rodríguez, M. A.; Sánchez-Andújar, M.; Singleton, J.; Zapf, V. S. *J. Am. Chem. Soc.* 2016, **138**, 1122.

12 Cheetam, A. K.; Rao, C. N. R. *Science* 2007, **318**, 58.

13 Chaikittisilp, W.; Ariga, K.; Yamauchi, Y. *J. Mater. Chem. A* 2013, **1**, 14.

Index

Index

Index

Chapter 1:

Introduction

Introduction

1.1. Dielectric materials[1-3]

A dielectric material is an electrical insulator that can exhibit an electric dipole structure; that is, a separation of positive and negative electrically charged entities on an atomic or molecular level. In the presence of an electric field, these dipoles become aligned and oriented with the applied field, process known as polarization, which confer these materials a vast number of technological applications.

These materials are ubiquitous in quotidian systems, functioning as electric wire insulator coatings, printed circuit boards, frequency tuners, sensors and transductors of thermal, mechanic or even acoustic signals, etc. Some of the advanced technological applications range from non-volatile *Ferroelectric Random Access Memories* (*FeRAMs*) to microsensors or wireless microantennas incorporated in the so-called *wearable* devices (*smartglasses* or *activity tracker bands*), and even bio-acoustic sensors to control the next generation of *smartphones* projected directly on the skin (the so-called *Skinput* technology), see Figure 1-1.

Generally, the dielectric response of a material is studied in a parallel plate capacitor, which consists of two parallel plates containing the dielectric material in between, see Figure 1-2.

When a voltage is applied across the capacitor, the dielectric response can be measured in terms of *relative permittivity* (also known as *dielectric constant*), ε'_r, which represents the increase in charge storing capacity by insertion of the dielectric medium between the plates. This magnitude is equal to the rario $\varepsilon'_r = \varepsilon/\varepsilon_0$, where ε_0 and ε are the dielectric permittivity of the vacuum -a universal constant- and of the dielectric material, respectively.

The magnitude of ε'_r, depends on the degree of polarization that can occur in the material. In that context, the polarizability, α, of the dielectric is defined by $p = \alpha E$, where p is the dipole moment induced by the local electric field, E.

This polarizability has four possible components that can add up to each other, namely, electronic, ionic, orientation and space charge polarizability, which are described below:

Figure 1-1. Examples of devices and systems using dielectric materials.

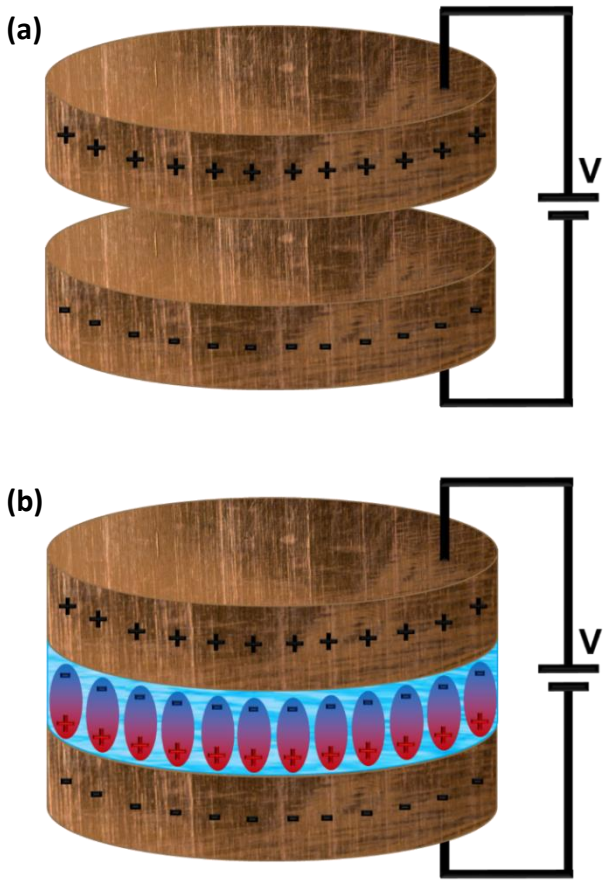

Figure 1-2. Parallel plate capacitor (a) when vacuum is present, and (b) when a dielectric material is present.

(i) The electronic polarizability (α_e) results from a slight displacement of the center of the negatively charged electron cloud of an atom relatively to the positively charged nucleus (see Figure 1.3a). This contribution is found in every dielectric material and only arises under the application of an external electric field.

(ii) The ionic polarizability (α_i) arises from a slight relative displacement or separation of anions and cations in a solid (see Figure 1.3b), and is the principal source of polarization in ionic crystals.

(iii) The orientation or dipolar polarizability (α_o), which is found only in compounds that possess permanent dipole moments, whose orientation can be modified by an external electric field (see Figure 1.3c).

(iv) The space charge polarizability, (α_s), which can occur in materials that are not perfect dielectrics but in which some long-range migration may take place.

The magnitude of α usually decreases in the order iv> iii> ii> i, although, of course, not all materials show all types of polarization.

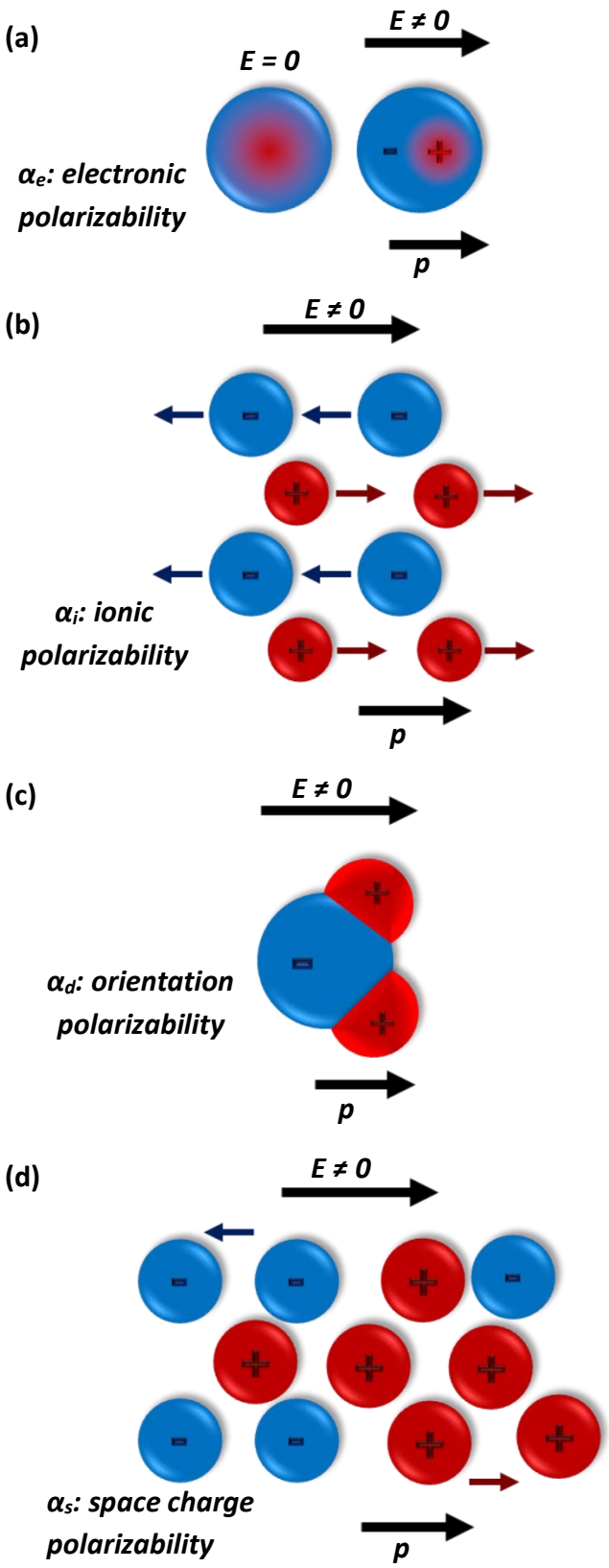

Figure 1-3. Different polarization mechanism, from top to bottom: electronic, ionic and dipolar polarization.

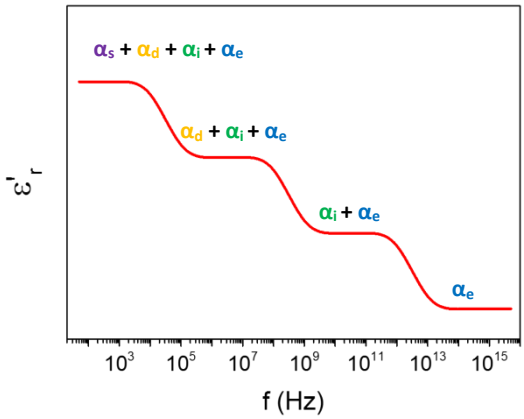

Figure 1-4. Variation of the dielectric constant with frequency of an AC field, with indication of the possible different contributions.

Experimentally the four contributions to α and ε'_r may be separated by making measurements over a wide range of AC frequencies.

As shown in Figure 1-4, at low frequencies (~10^3 Hz), all four (if present) may contribute to α. At higher frequencies ~10^6 Hz, space charge effects may not have time to build up and get effectively "relaxed out". At microwave frequencies (~10^9 Hz) dipoles do not usually have time to reorient themselves and get effectively relaxed out. The timescale of ionic polarizations is such that they do not occur at frequencies higher than infrarred (~10^{12} Hz), so that electronic polarization is the only one observable in the visible and UV region (f > 10^{14} Hz).

1.1.1. Relationship between the dielectric properties and the crystal symmetry[4-6]

The dielectric properties of crystalline solid state materials, which are one of the scopes of the present research studies, are closely related to their crystal structures, which can directly affect the charge distribution within the solid.

Attending to this charge distribution it is possible to classify the dielectric materials into three groups:

(i) *Nonpolar dielectrics*, which display a centrosymmetric charge distribution where the center of the positive and negative charges coincide.

(ii) *Neutral (polar) dielectrics*, which exhibit a non-centrosymmetric charge distribution where the charges centers (positive and negative) concur at the same point. In these materials it is possible to find polar directions, although they do not exhibit a net preferential polar direction.

(iii) *Polar dielectrics*, which also show a non-centrosymmetric charge distribution, but where the positive and negative charge centers do not concur at the same point. These materials, which show spontaneous polarization in absence of an external electric field, are defined as pyroelectric materials, and they exhibit polarization changes under application of uniform heating, inducing an electric charge on their surface.

Moreover, the dielectric materials with a non-centrosymmetric charge distribution, except those included in the 432 Laue class, are defined as piezoelectric materials. These singular compounds are able to generate electricity under mechanical stress, phenomenon known as piezoelectricity.

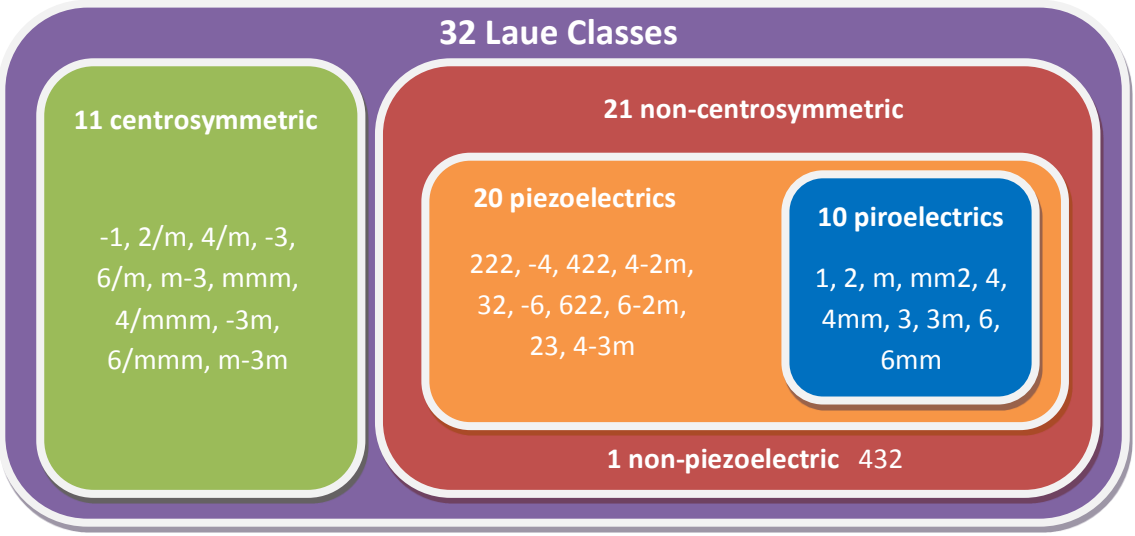

Figure 1-5. Relationship between the electric properties and the symmetry of crystalline materials.[7]

More details on the classification of the dielectric materials as a function of their crystalline symmetry can be found in the Figure 1-5. Here the 32 Laue crystalline classes are grouped as a function of the presence (or lack) of symmetry center, which determines the piezoelectric and pyroelectric properties. Within these materials, the highest relative permittivities are found in the group of the so-called ferroelectric materials, which display permanent dipoles aligned parallel along a defined polarization axis.

1.1.2. Ferroelectric and antiferroelectric materials[8-10]

A ferroelectric material is a pyroelectric where the spontaneous polarization, which is related to the presence of permanent dipoles, can be reversed by the application of an external electric field. Differently from the case of conventional dielectrics, in ferroelectric materials the relationship between the polarization, *P*, and the applied electric field, *E*, is not linear, and it displays a hysteresis cycle, see Figure 1-6a.

On the other hand, antiferroelectric materials, can be defined as those constituted by two spontaneously polarized sub-networks antiparallel aligned.

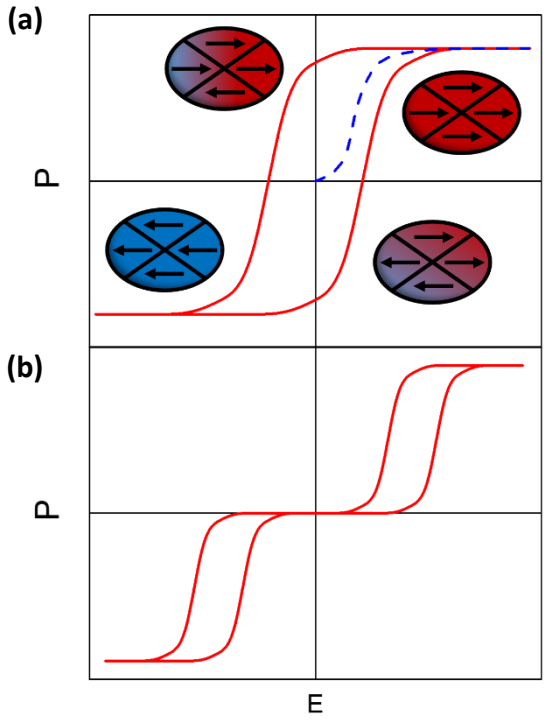

Figure 1-6. Hysteresis cycles for (a) ferroelectric and (b) antiferroelectric materials.

These materials, where a metastable ferroelectric phase can be induced by an electric field,[11] exhibit a double hysteresis cycle, see Figure 1-6b.

Most of the materials with ferroelectric and antiferroelectric properties, can undergo structural transitions at a critical temperature, T_t. Above this temperature the long-range dipole cooperative order is lost and a paraelectric phase, where the electric dipoles are randomly oriented, is obtained.

Ferroelectric properties can be essentially originated by two main processes related to structural phase transitions, namely:[12]

(i) *Ionic displacement processes*, where the macroscopic polarization is associated with a relative displacement of the positive and negative ions from their equilibrium positions. The most representative materials are those displaying perovskite and related structures, where the most typical example is the barium titanate ceramic, $BaTiO_3$.[13] Below T_t = 393 K (120 °C), $BaTiO_3$ shows a polar structure with tetragonal symmetry and *P4mm* space group, where the Ti^{4+} cations are in a distorted [TiO_6] octahedral environment.
This distortion originates a displacement of the positive charges, related to Ti^{4+} cations, respect to the negative charges, associated with the O^{2-} anions, see Figure 1-7.
As a result, below T_t, $BaTiO_3$ exhibits a ferroelectric structure.

Meanwhile, above the critical temperature T_t, it shows a nonpolar structure with cubic symmetry space group $Pm\bar{3}m$, where the Ti^{4+} cations are located in the center of regular [TiO_6] octahedra, giving rise to a *paralectric* phase.

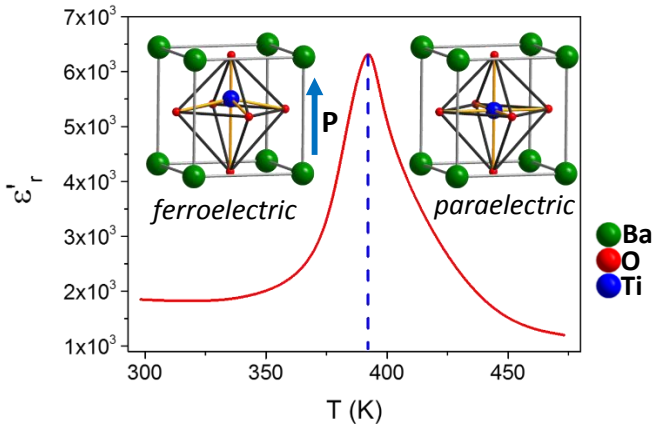

Figure 1-7. Ferroelectric-paraelectric transition associated with ionic displacement processes in $BaTiO_3$ (adapted from Ref. 13). Inset: Unit cell of BaTiO3 below and above the structural transition temperature, T_t = 393 K.

(ii) *Order-disorder processes*, where ions, molecules, or even hydrogen bonds can experience a transition from an ordered state to a disordered one, above a critical temperature T_t. Sodium nitrite, $NaNO_2$, and potassium hydrogen phosphate, KH_2PO_4, are very characteristic examples.

In the KH_2PO_4 compound, also known as KDP, the polarization is the result of the dynamic of the protons

within the hydrogen bonds, which induce a structural and dielectric transition,[12] see Figure 1-8a. Below T_t = 123 K (-150 °C) this material exhibits a tetragonal phase, space group $I\bar{4}2d$; meanwhile, above this temperature it displays an orthorhombic symmetry with a polar *Fdd2* space group. In both structures, the KDP exhibits PO_4^{3-} tetrahedra which alternate with K^+ cations along the *c*-axis, and where the phosphate units are linked by hydrogen bonds in the *ab*-plane forming a *3D* network.

Below T_t, the hydrogen atoms are ordered and locally bonded to a specific PO_4^{3-} oxygen atom, displaying a polar order (ferroelectric phase).

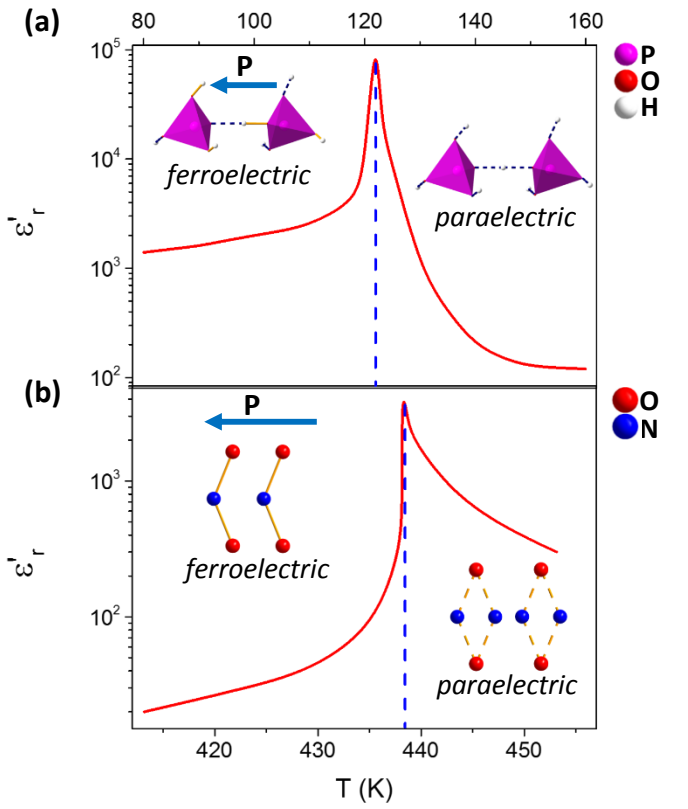

Figure 1-8. Dielectric transition associated to the order-disorder structural transition of (a) KH_2PO_4 (adapted from Ref. 14) and (b) $NaNO_2$ (adapted from Ref. 15).

Meanwhile above the critical temperature, the hydrogen atoms are randomly disordered between the oxygen atoms, although in average they are located in crystallographic positions at an equidistant distance between these oxygen atoms, giving rise to a paralectric phase.

On the other hand $NaNO_2$ displays a different order-disorder process. This compound undergoes a structural transition from a ferroelectric to a paraelectric phase at T_t = 438 K (165 °C).[15] In the ferroelectric phase this material exhibits a polar orthorhombic structure space group *Im*2*m*, where the NO_2^- are ordered and display electric dipoles which are parallel aligned along the *b*-axis of the crystal, see Figure 1-8b. Meanwhile, when increasing the temperature above T_t, the NO_2^- anions are crystallographically disordered and the polarization disappear.

It should be noted that the here presented classification of ferroelectrics as a function of these two main mechanisms is a simplification to facilitate their study; and that in most ferroelectric materials, both mechanisms often appear associated.[16]

1.2. Multiferroic materials

The so-called multiferroics are materials in which two or more ferroic properties coexist (ferroelectricity, ferromagnetism and/or ferroelasticity).

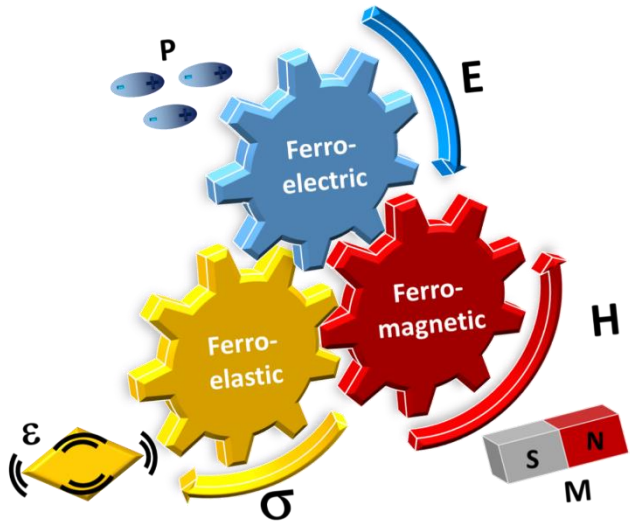

Figure 1-9. Scheme of coexistence and interactions of functional properties (polarization, *P*, magnetization, *M*, and deformation, ε) in multiferroic materials driven by different external stimuli: electric field (*E*), magnetic field (*H*) and stress (σ).

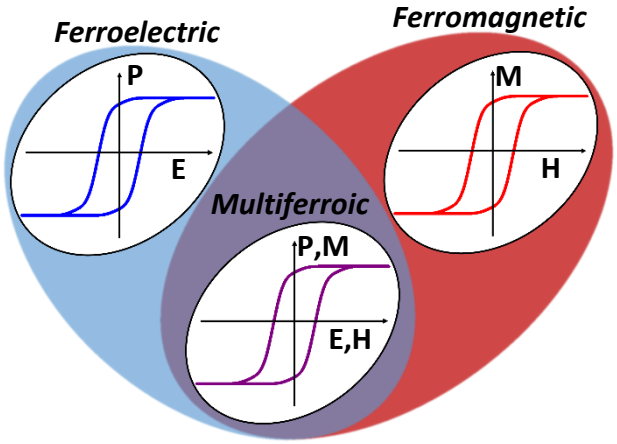

Figure 1-10. Properties coexisting in magnetoelectric-multiferroic materials (adapted from Ref. 17).

These compounds can exhibit spontaneous polarization (*P*), magnetization (*M*) and/or deformation (ε), which can be modulated by either an applied external electric field (*E*) or a magnetic field (*H*) and/or stress (σ), see Figure 1-9.

The growing trend of miniaturization of electronic devices, boosted by the society's demand, gives rise to an accelerated research on novel multifunctional materials which can supply the requirements of the technology industry. In this context, the multiferroic materials with magnetoelectric coupling, where magnetic and dielectric properties coexist and are coupled in a single phase material, have attracted great attention in view of the possibility of modifying the magnetization by an electric field or the polarization by the application of an external magnetic field,[18] see Figure 1-10.

Based on these properties, it would be possible to design a new generation of data storage devices where the information could be either electrically or magnetically written and/or read, giving rise to the so-called *multistate memories*.[19]

Advances on these multiferroic materials would broad the Materials Science frontiers and would set new horizons in technological applications, such as *spintronics* and *quantum computing*.

However, up-to-date, single phase multiferroics are rare as the conventional mechanisms for long-range electric order and cooperative magnetic order are mutually exclusive.[20] Most of the ferromagnetic materials display a centrosymmetric space group and require the presence and interactions of transition metal cations with unpaired electrons (mainly electrons at d or f orbitals). Meanwhile, ferroelectric materials usually involve off-centering of transition metal cations with d^0 configuration and they display non-centrosymmetric crystal structures.

Therefore, the search for new multiferroic compounds constitutes one of the big challenges in modern Solid State and Materials Science. The limited number of single phase magnetoelectric-multiferroic materials described so far are mainly oxides and can be classified into two subgroups as a function of the mechanisms responsible for their ferroelectricity:

(i) *Multiferroics type-I*, also known as proper multiferroics, where the ferroelectricity and the ferromagnetism show a different origin. Herein the magnetoelectric coupling is weak because the electric and magnetic order as they arise from two different sublattices of cations present within the same phase. A characteristic example is the ceramic $BiMO_3$ (M = Fe^{3+}, Mn^{3+}, Cr^{3+}, Co^{3+} and Ni^{3+}) with perovskite structure. In this case, the s^2 lone electron pair of the Bi^{3+} cations generate a structural distortion responsible for the ferroelectricity, while the magnetic order is related to the interaction of the d^n unpaired electrons of the M^{3+} cations through the O^{2-} anions.

(ii) *Multiferroics type-II*, also known as improper multiferroics, in which the ferroelectric order appears as a consequence of another type of order, such as a magnetic order or a charge reorientation. The hexagonal manganites are a clear example of improper multiferroics.[21] Above a critical temperature T_t, these compounds display a centrosymmetric crystalline structure, while when cooling below T_t, they undergo a complex magnetic transition that breaks the spatial inversion symmetry and induce a ferroelectric state.

1.3. Solid state cooling materials

Nowadays, refrigeration systems are ubiquitous in either industrial plants, service buildings or living spaces for maintaining the appropriate temperature of technological machines, electronics, foodstuffs, beverages, medicines, and a large list of daily utilities. Refrigeration represent more than 20 % of the total energy consumed in the world, and therefore is one of the main sinks of the global electricity consumption.[22,23] Even more, this energy demand is expected to grow dramatically in the coming decades.

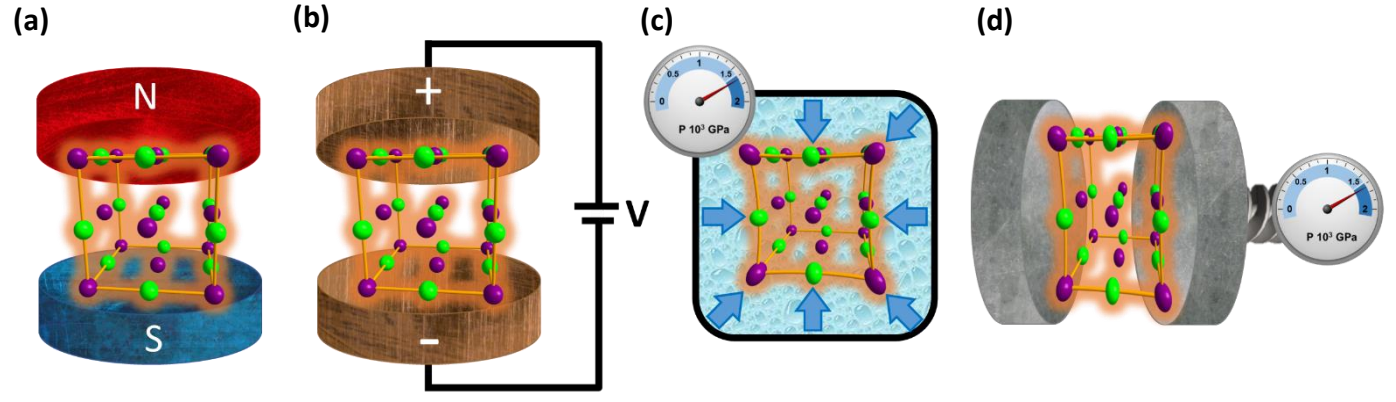

Figure 1-11. Stimuli-driven solid state cooling materials where the external stimuli can be a (a) magnetic field, (b) electric field, (c) isostatic pressure or (d) uniaxial strain.

Currently, the conventional cooling devices essentially relies on the vapour compression of hazardous gases, although, this mature and relatively low capital cost technology has a number of important drawbacks,[24] specially:

(i) The hazardous and pollutant gases involved in the compression processes, that include the use of hazardous chemicals (ammonia (NH_3)), ozone depleting chemicals (such as the already prohibited chlorofluorocarbons (CFCs)) , or greenhouse gases (hydrochlorofluorocarbons (HCFCs) and hydrofluorocarbons (HFCs), which in turn are going to be prohibited in Europe in 2020 by the EU Regulation No 517/2014).

(ii) Even the newest most efficient units operate well below the maximum theoretical efficiency, and few, if any, further improvements may be possible with the existing vapour-cycle technology.

In view of this background, refrigeration based on solid state materials with large caloric effects (that is, with large temperature changes when an external field is applied) is becoming a very attractive alternative to the vapour compression technology as it would offer a number of significant advances as compared with the gas compression technology,[22] specially:

(i) Considerable operating cost savings by eliminating the most inefficient part of the refrigerator, the compressor, resulting in cooling efficiencies which can be higher than the 45% in the best gas-compression refrigerators.

(ii) In addition to their energy savings potential, this technology is an environmental sound alternative to vapour-cycle refrigerators and air conditioners, as it does not use ozone-depleting or global-warming volatile fluid refrigerants, but only solid refrigerants and common heat transfer fluid (e.g.: water, alcohol, or air, between others).

(iii) It may be built more compactly because the main working material is a solid, and the smaller footprint for operation and the scalable mechanism open up further applications such as cooling of microsystems, very important, for example, for cooling electronic devices

(iv) These refrigerators generate much less noise.

Solid state materials with stimuli-driven caloric functional properties can be grouped into different categories depending on which external stimulus is needed to provoke the corresponding caloric effect, understood as an adiabatic change of the temperature and/or an isothermal change of the entropy induced by such stimuli.[22,25] In this context, and as sketched in Figure 1-11, there are four types of solid state caloric materials, namely: magnetocaloric materials (where the caloric effect is induced by an external magnetic field), electrocaloric materials (the effect is induced by an external electric field), elastocaloric materials (those whose effect is produced by an uniaxial strain) and barocaloric materials (where an isostatic pressure is responsible for the caloric effect) materials.

Normally, the entropy of a caloric material decreases when an external stimulus (magnetic, electric or mechanic field) is applied isothermally; meanwhile its temperature increases when this stimulus is applied adiabatically. This effect can be used in a cooling cycle, as shown in Figure 1-12. When an external field is applied, the material releases heat to a heat sink (e.g.: atmosphere, interchange fluid, etc.) and when the field is removed, the material cools down and absorb heat from the desired cold reservoir, device and/or space (fridge, *smartphone*, computer, etc.).

Figure 1-12 shows the main four stages of a cooling system based on solid state materials, the so-called refrigerating cycle. On the first step the stimulus is applied in adiabatic conditions, increasing the temperature of the material. Secondly, the material cools down under a constant value of the stimulus and transfers the heat to a heat sink. On the third stage, the stimulus is removed in adiabatic conditions and the material cools further.

Finally, the already cooled material absorbs heat from the cold reservoir (a fridge in this case) recovering the initial state.

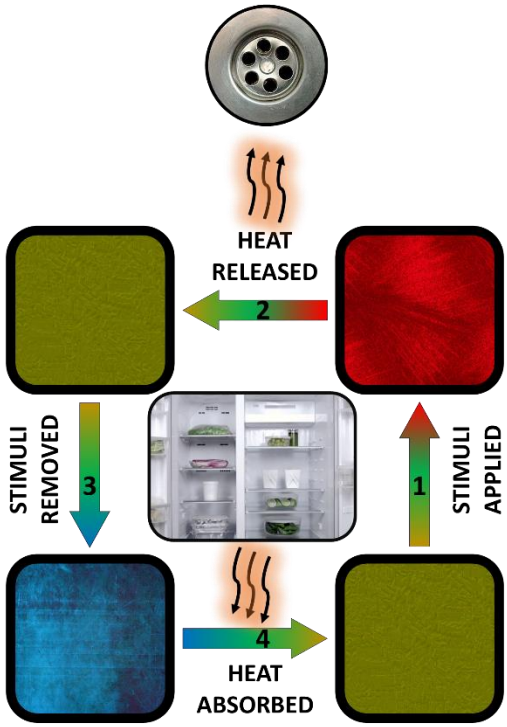

Figure 1-12. Refrigeration cycle for a solid state cooling material where the external stimulus can be either a magnetic or electric field, a uniaxial strain or a isostatic pressure.

Solid state cooling is a rather recent research area, where scientific publications remain scarce and where most of efforts have been focused on magnetocaloric and electrocaloric materials, the ones showing higher caloric effects,[22,23,25] see Figure 1-13. Notwithstanding, these materials often require complex synthesis methods, rather expensive materials (many of them containing rare-earths, such as Gd, $Gd_5Si_2Ge_2$ [Ref. 26] or $Fe_{49}Rh_{51}$ [Ref. 27]) and high magnetic or electric fields that are technologically limited and/or can produce breakdown of the materials.

Meanwhile, mechanical driven caloric effects (barocaloric and elastocaloric) would be in principle technological and economically more accessible. Nevertheless, less efforts have been devoted to their study, which have focused on expensive metal alloys and some inorganic salts.

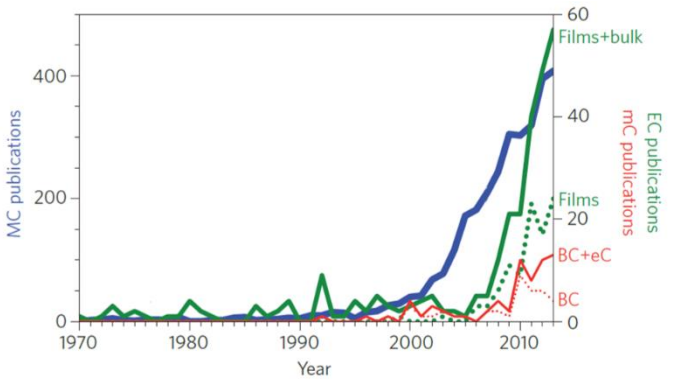

Figure 1-13. Publications on caloric materials along the last decades showing magnetocaloric (MC) publications (blue solid line), electrocaloric (EC) publications either in films (green dotted line) and bluk + films (green solid line), and mechanocaloric (mC) publications including barocaloric (BC) + elastocaloric (eC) materials (red solid line) or only barocaloric materials (red dotted line). Adapted from Ref. 28.

The reason for the limited exploration of mechanocaloric effects in solid state materials is that, up to now, such caloric effects have been observed to be negligible, due to their small entropy change associated with the phase transition and/or to the reduced pressure response.[23,28,29]

That is the case, for instance, of the inorganic perovskites $Pr_{1-x}La_xNiO_3$ [Ref. 30,31], $PbTiO_3$ [Ref. 32] and $BaTiO_3$ [Ref. 33], ($\Delta S \approx 3\text{-}4\ J\ K^{-1}\ kg^{-1}$). Nevertheless, recent studies have reported giant barocaloric effects associated with giant magnetocaloric response,[34,35] although they have only been described in a few and relative expensive magnetic materials.

Therefore, further exploration in novel compounds are indispensable to design more efficient and economically accessible stimuli-driven caloric materials in order to replace the conventional hazardous and pollutant refrigerant fluids.

1.4. Precedents of organic-inorganic hybrids with dielectric properties, multiferroicity and temperature and pressure responsiveness

Organic-inorganic hybrids can be defined as compounds which incorporate organic and inorganic units as building blocks in the same crystalline structure. Such building blocks consist of metal cations or metallic clusters linked by bidentate ligands, normally organic, which form frameworks with different dimensionalities (*1D*, *2D* or *3D*) that can allocate guest molecules inside their cavities, see Figure 1-14.[36,37]

The innumerable possibilities of different bidentate ligands, metallic clusters and/or guest molecules result into a great structural richness and functional versatility of these emergent materials, which can find applications in several scientific and technological fields. In addition, these materials can be classified as a function of their porosity into *porous* or *dense* hybrid materials.[38]

Those known as *porous* hybrids are composed by large and flexible ligands that form large opened cavities or channels which facilitate the diffusion, interchange and release of guest molecules, see Figure 1-15.

These materials have received a lot of attention since the 90s due to their potential applications in catalysis, molecular separation, gas storage or pollutant removal, between others.[39-41]

On the other hand, *dense* hybrids contain shorter ligands that form smaller cavities where the guest molecules are confined with a much more limited mobility, see Figure 1-16.

As a result, *dense* hybrids, with structures that remind of those of some classic inorganic solids, have been recently found to also present functional and multifunctional properties, such as optic, magnetic or electric properties.[42]

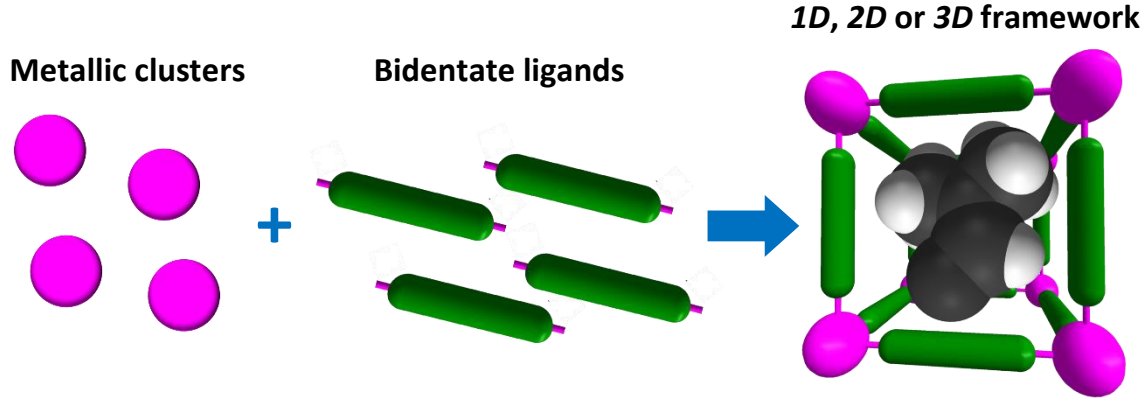

Figure 1-14. Coordination scheme of the building blocks that form an organic-inorganic hybrid material.

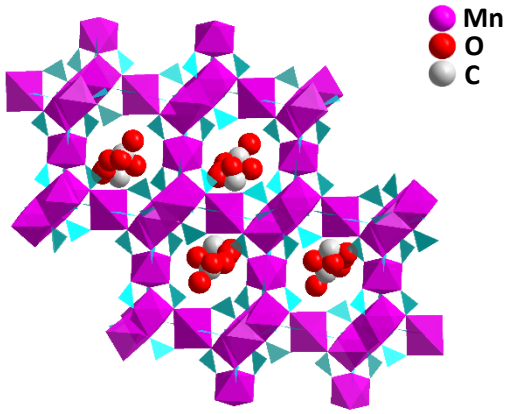

Figure 1-15. Crystalline structure of the porous MOF with molecular formula $[Mn_3(HCOO)_6]\cdot[G]$ (G = $H_2O\cdot CH_3OH$).

1.4.1. Dielectric and multiferroic hybrid materials with emphasis in hybrid perovskites

During the late 60s, K. Okada and H. Sugie[43] reported for the first time the dielectric response of an organic-inorganic hybrid material with molecular formula $Cu(HCOO)_2\cdot H_2O$, for which they described an antiferroelectric behaviour below 235 K. Nevertheless, it was not until 2005 when A. Kobayashi *et al.* observed a ferroelectric-paraelectric transition in *porous* hybrids of formula $[Mn_3(HCOO)_6]\cdot[G]$ (G = $H_2O\cdot CH_3OH$ and CH_3CH_2OH, respectively),[44,45] see Figure 1-15.

In the meantime, the first dielectric transitions found in *dense* hybrids was described by A. K. Cheetham *et al.* for the $[(CH_3)_2NH_2][M(HCOO)_3]$ (M = Zn^{2+}, Mn^{2+}, Co^{2+}, Ni^{2+} and Fe^{2+}) materials.[46,47] These materials display a perovskite-like structure, ABX_3 where A = dimethylammonium ($(CH_3)_2NH_2^+$), B = transition metal cations (M^{2+}) and X = formate anion ($HCOO^-$), see Figure 1-16.

These authors set the origin of this dielectric transition on an antiferroelectric-paraelectric phase transition driven by ordering of the hydrogen atoms between the dimethylammonium cations, $[(CH_3)_2NH_2^+]$, and the $M(HCOO)_3^-$ framework, in a mechanism similar to that exhibited by KH_2PO_4.

Nevertheless, a later study of our research group resolved the crystal structure of the $[(CH_3)_2NH_2][Mn(HCOO)_3]$ compound below the transition temperature, as non-centrosimetric space group *Cc*, and concluded that the compound shows a ferroelectric-paraelectric phase transition.[48] This study also reported the mechanism responsible for the dielectric transition associated with the structural one: an order-disorder phase transition, where at low temperature the dimethylammonium cations "freeze" inside the pseudo-cubooctahedral cavities in a cooperative ferro-arrangement.

Meanwhile above the transition temperature, these cations are rotating inside the cavities breaking the polar order, see Figure 1-17.

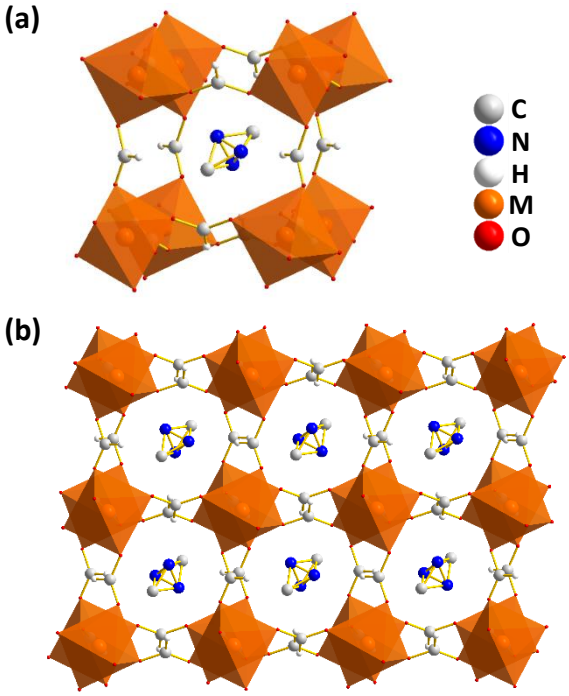

Figure 1-16. (a) Perovskite-like structure of the $[(CH_3)_2NH_2][M(HCOO)_3]$ compounds. (b) Detail of the order of the $[(CH_3)_2NH_2^+]$ cations located inside the cavities. The hydrogen of the $[(CH_3)_2NH_2^+]$ are omitted in both pictures for a better view.

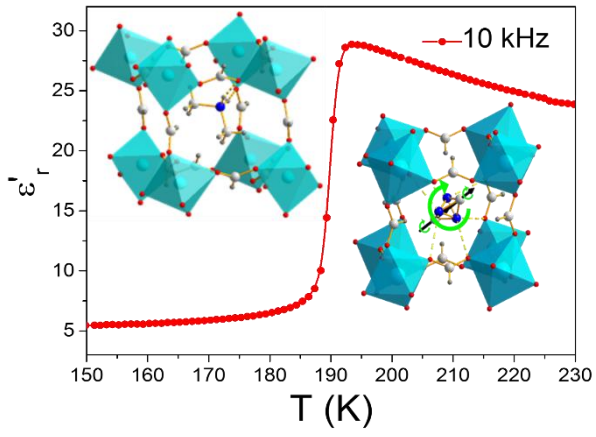

Figure 1-17. Real part of the dielectric permittivity as a function of temperature for the $[(CH_3)_2NH_2][Mn(HCOO)_3]$ compound. Inset: Order-disorder process associated with the $[(CH_3)_2NH_2]$ cations inside the perovskite caivities.

Similar dielectric properties are displayed by other members of the series $[(CH_3)_2NH_2][M(HCOO)_3]$ (M = Mg^{2+}, Mn^{2+}, Fe^{2+}, Co^{2+}, Ni^{2+}, Zn^{2+}, etc.) and also perovskite-like structure, with the Mg compound showing the highest T_t (~270 K).[49]

Very remarkably, in addition to dielectric properties, the $[(CH_3)_2NH_2][M(HCOO)_3]$ (M = Mn^{2+}, Fe^{2+}, Co^{2+} and Ni^{2+}) compounds also exhibit *weak ferromagnetism* (*wfm*), in a range of temperatures between 8.5-35.6 K,[50-52] meaning in turn that these materials are also multiferroic materials, see Figure 1-18.

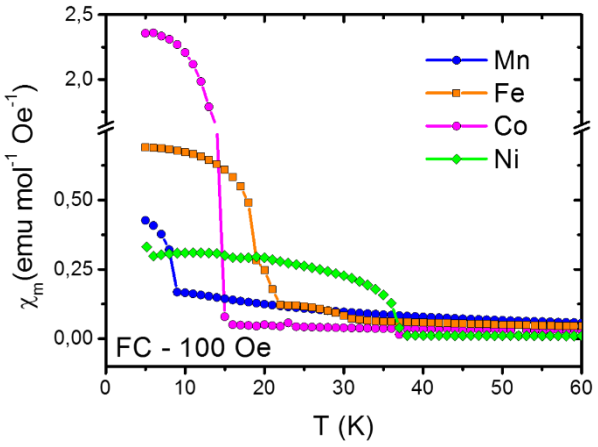

Figure 1-18. Magnetic transitions observed in the $[(CH_3)_2NH_2][M(HCOO)_3]$ hybrids (adapted from Ref. 53).

In view of these interesting functional and multifunctional properties of these hybrid perovskites, further studies were performed. One of the more recurrent strategies used in the recent years have consisted in maintaining the perovskite-like structure making carefully planned modifications, in order to find novel functional properties and establish structure-properties relationships. Beyond the substitution of the M^{2+} cations on the B-site, great efforts have been devoted to the introduction of different midsize alkylammonium cations in the A-site and even with different bidentate-bridge X-site anions. In this context, the A-site substitutions led to a large family of [AmineH][M(HCOO$_3$)] compounds, where the used alkylammonium cations can range from the linear ethylammonium ($CH_3CH_2NH_3^+$)[54] or hydrazinium ($NH_2NH_3^+$)[55] cations to the cyclic guanidinium ($C(NH_2)_3^+$)[56,57] or imidazolium ($C_3N_2H_5^+$)[58] cations. These hybrids perovskites also exhibit very interesting properties, for instance the $[C_3N_2H_5][Mn(HCOO)_3]$ displays a coexistence of magnetic order below 9 K and electric order below 220 K.[58]

The multiferroicity found in these [AmineH][M(HCOO)$_3$] (Amine = $CH_3NH_2^+$ or $C_3N_2H_5^+$) compounds, is described as multiferroicity type-I, where the magnetic properties arise from the interaction between the magnetic cations of the framework, and the dielectric properties are related to the dynamic of the alkylammonium cations inside cavities. On the other hand, recent discussion have opened up studies of multiferroicity type-II in this formate perovskites, where the electric polarization could be modulated by an external magnetic field and vice versa. This magnetoelectric coupling has been predicted by theoretical calculations in the $[C(NH_2)_3][Cu(HCOO)_3]$, $[C(NH_2)_3][Cr(HCOO)_3]$ and $[CH_3CH_2NH_3][Mn(HCOO)_3]$ compounds.[54,57,59,60] In addition, experimental data have revealed magnetoelectric coupling at temperatures above the magnetic transition in the case of the $[(CH_3)_2NH_2][Mn(HCOO)_3]$[61] and below the magnetic transition for the $[(CH_3)_2NH_2][Fe(HCOO)_3]$.[62] Very recently, our research group has reported the first example of magnetic ordering-induced multiferroic behaviour in a metal-organic framework magnet: the $[CH_3NH_3][Co(HCOO)_3]$ compound. In this material, the A-site cation strongly distorts the framework, allowing anisotropic magnetic and electric behaviour and coupling between them to occur, giving rise to a type-II multiferroic material.[63]

On the other hand, although most of the studies have been focused on formate-bridged perovskites, there are some examples of cyanide-bridged perovskite hybrids that also show thermally-induced structural transitions and dielectric responsiveness associated to order-disorder processes of the A-site cations. These cyanide-linked perovskites combine the alkali metal cation K^+ and different M^{3+} transition metal cations in the B-site, while diverse alkylammonium cations are located in the A-site, resulting in the so far described compounds $[Him]_2[KM(CN)_6]$ (Him = imidazolium cation, M = Fe^{3+} and Co^{3+}),[64,65] $[(CH_3)_2NH_2]_2[KCo(CN)_6]$,[66] and $[(CH_3)_nNH_{4-n}]_2[KFe(CN)_6]$ (n = 1-4).[67]

Aside from the wide structural and functional diversity found in [AmineH][M(HCOO)$_3$] and [AmineH]$_2$[KM(CN)$_6$] perovskite families, recent studies have also used azide (N_3^-) as X-site bidentate-bridged anions, finding new properties. For instance, a cation-dependent structural transition was described in the $[(CH_3)_nNH_{4-n}][Mn(N_3)_3]$ (*n* = 1–4) family, which also exhibits a magnetic bistability.[68] The analogous $[(CH_3)_2NH_2][Cd(N_3)_3]$ was found to exhibit ferroelasticity (cooperative deformation order) at room temperature.[69] Moreover, our research group has recently reported the coexistence of the three ferroic orders: ferroelectricity, ferromagnetism and ferro-elasticity in the $[(CH_3)_2NH_2][Mn(N_3)_3]$ compound.[70]

Another very promising, yet very less explored, family of perovskite-like materials is that which integrates the larger X-site bidentate-bridge dicyanamide anions ($N(CN)_2^-$).

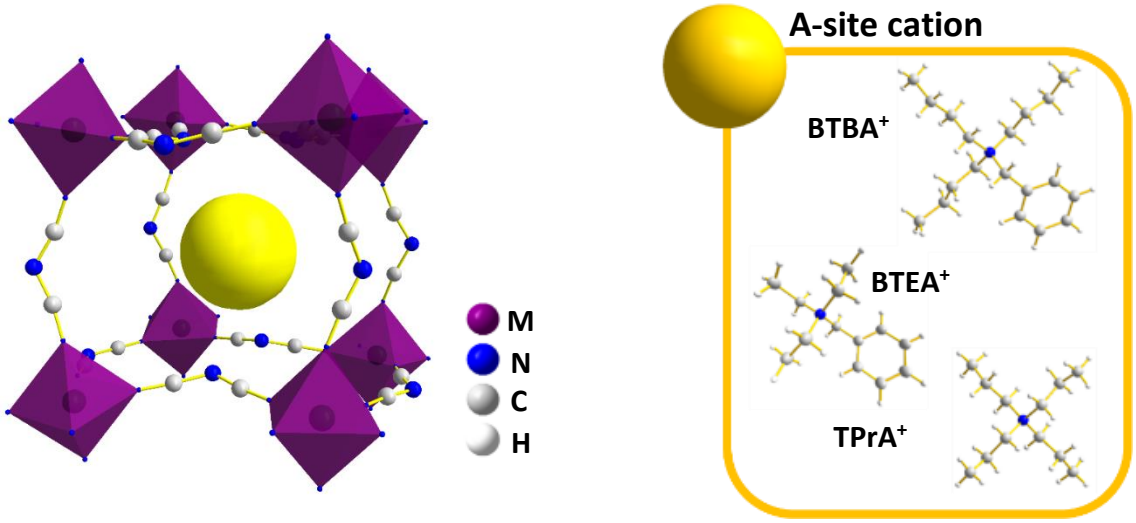

Figure 1-19. Perovskite-like structure of the [A][M(dca)$_3$] compounds.

In that regard, while the $HCOO^-$, N_3^- and CN^- ligands exhibit a similar length (447 pm, 447 pm, 395 pm, respectively),[71] $(N(CN)_2)^-$ is much longer (733 pm). Only very few relative voluminous A-site cations have been able to template a perovskite-like structure, so far benzyltributylammonium ($BTBA^+$), benzyltriethyl-ammonium ($BTEA^+$) and tetrapropylammonium ($TPrA^+$).[72,73] These resulting compounds are formed by [MN_6] octahedra linked by $\mu_{1\text{-}5}$-dicyanamide ligands (through both nitrile groups), where the A-cations are located in pseudo-cubooctahedral cavities, see Figure 1-19. It should be noted that attempts to use other A-site cations have led to other structures different from the perovskite, such as triple-rutile for A = tetrabutylammonium (TBA^+) or $LiSbO_3$-type structure for A = tetrapentylammonium (TPA^+).[73]

1.4.2. Temperature and pressure responsive hybrid materials

The high flexible nature of hybrid compounds together with the possibility of combining different functional building blocks, such as magnetic metal cations, polar molecules or chromophore groups, make these compounds a suitable target for (multi)stimuli responsive studies.

In principle, these materials can present very diverse responses as a function of external stimuli (magnetic or electric field, temperature, pressure, light, etc) which can be especially strong in the case of applying pressure and temperature due to their rather high flexible structures. In addition, these stimuli can be applied isolated or in combination, leading to multistimuli responsive materials that can give rise to multifunctional properties. In the present memory we are paying special attention to probably two of the more easily and economically accessible external stimuli: temperature and pressure.

Temperature is probably the most studied external stimulus towards which the hybrid materials are quite sensitive. The increase of temperature can produce either amorphization of the material, structural transitions and even anomalous effects, such as *negative thermal expansion* (NTE), that is, contraction when heated.[74] While NTE and thermal amorphization of hybrid materials are rare behaviours, the thermally-induced structural transitions are very common phenomena and attract great attention, especially, in *dense* hybrids where the phase transitions directly affect the functional properties, such as dielectric, magnetic and multiferroic properties, as it has been explained in the previous sections.

On the other hand, despite the fact that hybrids are expected to exhibit high sensitivity to applied external pressure, these kind of studies have remained scarce up-to-date. Nevertheless, the relative few data on hybrids exposed to external applied pressure have demonstrated a wide variety of mechanical behaviour towards this pressure,[75] namely, amorphization of the material (very common in zeolitic imidazolate frameworks, such as ZIF-4), phase transitions, bond rearrangement or proton transfer, see Figure 1-20.

Moreover within the elastic regime, it has been experimentally demonstrated (and/or theoretically predicted) that hybrids can display anomalous mechanical responses, such as *negative linear compressivity (NLC)* that occurs when under compression the material expands itself in a specific direction, although the overall volume gets reduced.[76]

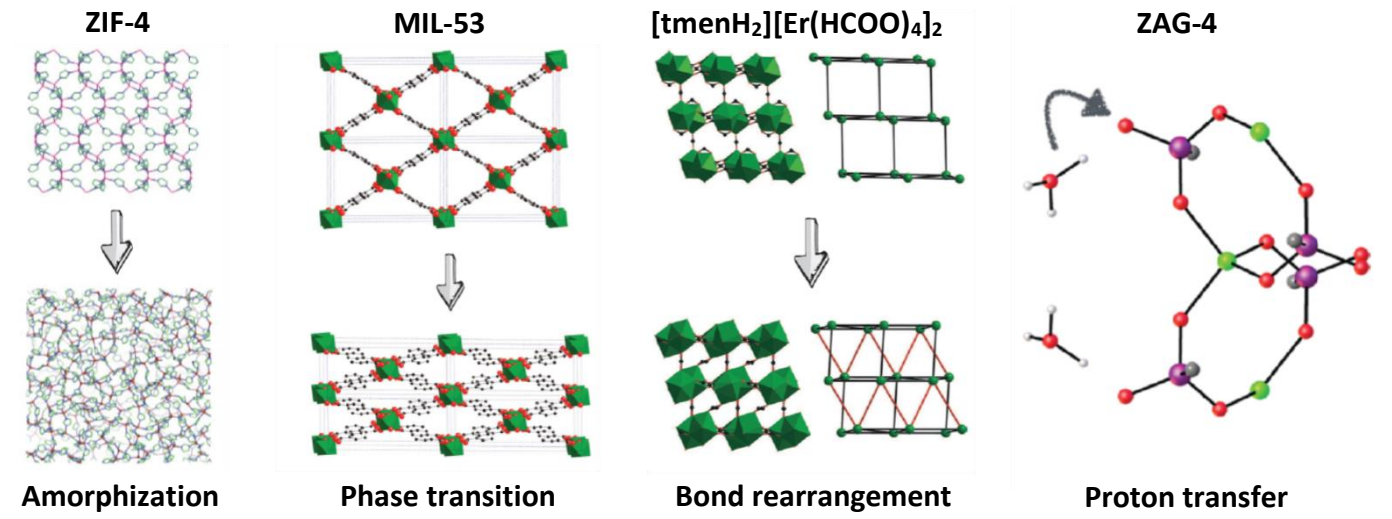

Figure 1-20. Representation of different responses of hybrid compounds to the application of external pressure (adapted from Ref. 75).

Besides the pressure-induced amorphization, which is more common within *porous* hybrids rather than in *dense* hybrids, some of these materials undergo phase transitions under high pressure application in the GPa scale. Earlier studies on *porous* hybrids dealt with phase transitions induced by internal pressure, triggered by the adsorption/desorption of guest molecules, known as "breathing" transitions. Meanwhile during the past few years, there has been an increasing interest in crystallographic studies under external applied pressure on diamond anvil equipped diffractometers, which have revealed that external pressure also drives structural transitions similarly to internal pressure. This is the case, for example, of the MIL-53 compound, which exhibits the same phase transition either by CO_2 adsorption or by isostatic external compression.[77]

An even more uncommon, but highly desirable, behaviour is that of pressure-induced chemical reactions. So far, there are only two described examples of hybrids which have experienced chemical reactions under applied pressure. The first case consist in a reversible pressure-induced bond rearrangement of the $[tmenH_2][Er(HCOO)_4]_2$ compound ($tmenH_2^{2+}$ = N, N, N', N'-tetramethylethylenediammonium).[78] The second example was found for a zinc alkyl gate compound (ZAG-4), where the external pressure provokes a reversible proton transfer between a water guest molecule and a phosphonate group of the framework.[79]

Although scarce, the pressure-response studies on organic-inorganic hybrids have revealed a high sensitivity towards this external stimulus that can induce even structural transitions with large entropy change associated. Nevertheless, as far as we know, there was not any study about the pressure-induced cooling properties of hybrid organic-inorganic materials. Therefore, this *Ph.D. Thesis* aims to be the first experimental study on the cooling properties of these flexible and large pressure-responsive organic-inorganic hybrid materials. As reported in chapter 4, these findings open new opportunities for solid state cooling materials, expanding the horizons of the emergent field of multifunctional and multistimuli organic-inorganic hybrid materials.

1.5. Precedents of organic-inorganic hybrid materials as precursor for functional carbon nanomaterials

Hybrid nanocomposites of carbon nanotubes embedded with magnetic nanoparticles (M@CNTs) are emerging materials with an enormous technological interest related to their multifunctional properties and applications in several fields, such as pollutant removal and magnetic recuperation, spintronic, enhanced optical properties, for very sensitive spectroscopic techniques, magnetic resonance imaging, drug delivery, cancer treatment through hyperthermia, between others. Nevertheless, nowadays most of synthetic procedures to obtain them involve several-step reactions, relatively complex operational conditions, high cost, low reproducibility or difficulties in terms of practical applications. Therefore, it is necessary to develop novel, simple, reproducible, scalable and low-cost methods to obtain well-defined M@CNTs.[80]

In this context, since organic-inorganic hybrid compounds combine organic subunits and metal ions/clusters and their composition and porosity can be easily controlled, these materials are very attractive as precursor for mesoporous and nanoporous carbon materials by simple direct calcination,[81] see Figure 1-21.

Recent studies have highlighted the potential of hybrid compounds, such as Al-PCPs,[82,83] MOF-5 and isoreticular compounds (IRMOF),[84,85] ZIF-8,[86] ZIF-67,[87] and related materials.

Nevertheless, results on obtaining carbon nanotubes embedded with magnetic nanoparticles remain very scarce up-to-date.[88,89]

Trying to elucidate novel and simple, as well as scalable and unexpensive, synthetic routes, the here presented *Thesis Dissertation* aims to explore the potential of new organic-inorganic hybrid materials as precursor for obtaining well-defined M@CNTs for environmental applications.

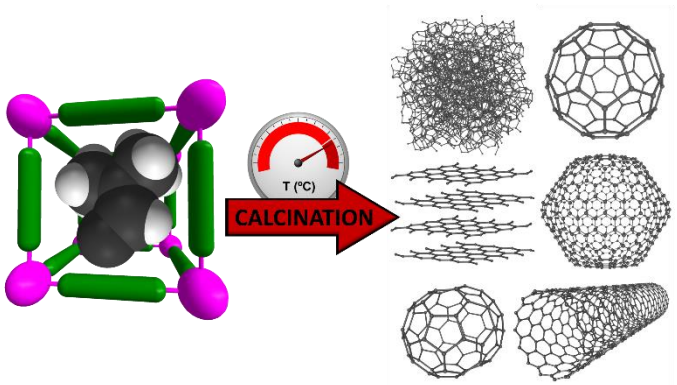

Figure 1-21. Scheme of carbon nanomaterials synthesis by direct calcination of organic-inorganic hybrids.

1.6. Main objectives of this work

As already mentioned in previous paragraphs, one of the main scopes of this *Ph.D. work* is to study and develop framework materials as candidates for displaying new (multi)functional properties that could be modulated by multiple external and internal stimuli and even tuning the properties by chemical doping. In addition, these studies also focus on the development of organic-inorganic hybrids as precursors of nanostructured carbon materials. Finally, the alternative approach of revisiting "old" compounds in the search for new functional properties has also been explored.

In this context, this dissertation revisits very well-known "classic" molecular materials and delve into the rather young, but very fast growing group of organic-inorganic hybrid compounds, especially those with perovskite-like structure.

Therefore, the main objectives of this work can be summarized as follow:

(i) Synthesis of "emergent" hybrid compounds with perovskite-like structure that could display structural phase transitions and functional properties, which could be modulated by different external stimuli. The selected "emergent" hybrid materials have been the dicyanamide-bridged $[TPrA][M(dca)_3]$ ($M = Mn^{2+}$, Fe^{2+}, Co^{2+} and Ni^{2+}) perovskites, that have being remained scarcely explored up-to-date.

(ii) Synthesis of nanostructured carbon materials by using hybrid organic-inorganic materials as precursors. The selected hybrid precursors have been the Ni and Co members of the dicyanamide-bridged $[TPrA][M(dca)_3]$ perovskite series.

(iii) Revisiting "classic" materials that are known to undergo thermally-induced phase transitions of order-disorder and displacive nature, and which could display functional properties. The selected candidates have been the very well-known ferrocene, $[Fe(C_5H_5)_2]$, and ammonia-borane, $(H_3N{\cdot}BH_3)$.

(iv) Compositional, structural and/or morphological characterization of the obtained samples by using elemental analysis, X-ray diffraction, IR and/or Raman spectroscopy, thermal analysis, electron microscopy, etc.

(v) Structural characterization of the obtained samples as a function of temperature by using single-crystal X-ray diffraction, powder X-ray diffraction and/or high-resolution synchrotron powder X-ray diffraction.

(vi) Calorimetric analysis of the obtained samples as a function of temperature, external hydrostatic/uniaxial pressure and internal chemical pressure.

(vii) Study of the dielectric properties as a function of different external stimuli: temperature, external hydrostatic/uniaxial pressure and internal chemical pressure.

(viii) Study of the adsorption capacity of the nanostructured carbon materials.

(ix) Establishing the relationships between crystal structure, (multi)functional properties and external stimuli, in the materials under study.

1.7. References

1 Callister, W. D.; Rethwisch, D. G. *Materials Science and Engineering: An Introduction*; John Wiley & sons, New York 2007.
2 West, A. R. *Solid State Chemistry and its Applications*; John Wiley & sons, New York, 1984.
3 Abella-Martín, J. M.; Martínez Duart, J. M. *Física de dieléctricos*; Boixareu: Barcelona, 1984.
4 Park, H. D. *Theory of Ferroelectric Pyroelectric Detectors*; Minnesota, U. of, Ed.; 1975.
5 Haertling, G. H. *J. Am. Ceram. Soc.* 1999, **82**, 797.
6 Samara, G. *Solid State Phys.* 2001, **56**, 239.
7 Zhang, W.; Xiong, R.-G. *Chem. Rev.* 2012, **112**, 1163.
8 Hippel, V. *Dielectrics and Waves*; John Wiley & sons, New York, 1954.
9 Schelkens, R. *Phys. Status Solidi* 1970, **37**, 739.
10 Horiuchi, S.; Tokura, Y. *Nat. Mater.* 2008, **7**, 357.
11 Martienssen, W.; Warlimont, H. *Ferroelectrics and antiferroelectrics in Handbook of condensed matter and materials data*; Mitsui, T., Ed.; Springer: Berlin Heidelberg, New York, 2005.

12 Lines, M. E.; Glass, A. M. *Principles applications of ferroelectric and related materials*, Oxford Unviersity Press, New York, 2001.
13 West, A. R.; Adams, T. B.; Morrison, F. D.; Sinclair, D. C. *J. Eur. Ceram. Soc.* 2004, **24**, 1439.
14 Young, K. F.; Frederikse, P. R. *J. Phys. Chem. Ref. Data* 1973, **2**, 313.
15 Ravindran, P.; Delin, A.; Johansson, B.; Eriksson, O.; Wills, J. M. *Phys. Rev. B* 1999, **59**, 1776.
16 Dalal, N. S., Bussmann-Holder, A. *Ferro- and antiferroelectricity: order/disorder versus displacive*; Springer: Berlin, Heidelberg, New York, 2007.
17 Khomskii, D. *Physics* 2009, **2**, 20.
18 Spaldin, N. A. *Science* 2005, **309**, 391.
19 Martin, L. W. *Engineering multiferroic materials and new functionalities in materials*; Spring, 2008.
20 Wang, K. F.; Liu, J.-M.; Ren, Z. F. *Adv. Phys.* 2009, **58**, 321.
21 Fiebig, M.; Lottermoser, T.; Fröhlich, D.; Goltsev, A. V; Pisarev, R. V. *Nature* 2002, **419**, 818.
22 Kitanovski, A.; Tusek, J.; Tomc, U.; Plaznik, U.; Ozbolt, M.; Poredos, A. *Magnetocaloric Energy Conversion From Theory to Applications*; Springer International Publishing, 2015.
23 Kitanovski, A, Plaznik, U.; Tomc, U.; Poredos, A. *Intern. J. Refrig.* 2015, **57**, 288.
24 Calm, J. M. *Int. J. Refrig.* 2008, **31**, 1123.
25 Fähler, S.; Rößler, U. K.; Kastner, O.; Eckert, J.; Eggeler, G.; Emmerich, H.; Entel, P.; Müller, S.; Quandt, E.; Albe, K. *Adv. Eng. Mater.* 2012, **14**, 10.
26 Pecharsky, V. K.; Gschneidner, Jr., K. A. *Phys. Rev. Lett.* 1997, **78**, 4494.
27 Nikitin, S. A.; Myalikgulyev, G.; Tishin, A. M.; Annaorazov, M. P.; Asatryan, K. A.; Tyurin, A. L. *Phys. Lett. A* 1990, **148**, 363.
28 Moya, X.; Kar-Narayan, S.; Mathur, N. D. *Nat. Mater.* 2014, **13**, 439.
29 Mañosa, Ll.; Planes, A.; Acet, M. *J. Mater. Chem. A*, 2013, **1**, 4925.
30 Alex Müller, K.; Fauth, F.; Fischer, S.; Koch, M.; Furrer, A.; Lacorre, P. *Appl. Phys. Lett.* 1998, **73**, 1056.
31 Strässle, T.; Furrer, A.; Hossain, Z.; Geibel, C. *Phys. Rev. B* 2003, **67**, 054407.
32 Mikhaleva, E. A.; Flerov, I. N.; Gorev, M. V.; Molokeev, M. S.; Cherepakhin, A. V.; Kartashev, A. V.; Mikhashenok, N. V.; Sablina, K. A. *Phys. Solid State* 2012, **54**, 1832.
33 Liu, Y.; Wei, J.; Janolin, P. E.; Infante, I. C.; Lou, X.; Dkhil, B. *Appl. Phys. Lett.* 2014, **104**, 162904.
34 Mañosa, L.; González-Alonso, D.; Planes, A.; Bonnot, E.; Barrio, M.; Tamarit, J.-L.; Aksoy, S.; Acet, M. *Nat. Mater.* 2010, **9**, 478.
35 Mañosa, L.; González-Alonso, D.; Planes, A.; Barrio, M.; Tamarit, J.-L.; Titov, I. S.; Acet, M.; Bhattacharyya, A.; Majumdar, S. *Nat. Commun.* 2011, **2**, 595.
36 Rao, C. N. R.; Cheetham, A. K.; Thirumurugan, A. *J. Phys. Condens. Matter* 2008, **20**, 083202.
37 Férey, G. *Chem. Soc. Rev.* 2008, **37**, 191.
38 Jain, P. *Ph.D. Thesis: Multiferroic metal organic frameworks with perovskite architecture*, The Florida State University, College of Arts and Sciences, 2010.
39 Li, H.; Eddaoudi, M.; Groy, T. L.; Yaghi, O. M. *J. Am. Chem. Soc.* 1998, **120**, 8571.
40 Yaghi, O. M.; O'Keeffe, M.; Ockwig, N. W.; Chae, H. K.; Eddaoudi, M.; Kim, J. *Nature* 2003, **423**, 705.
41 Fletcher, A. J.; Thomas, K. M.; Rosseinsky, M. J. *J. Solid State Chem.* 2005, **178**, 2491.
42 Cheetam, A. K.; Rao, C. N. R. Science, 2007, **318**, 58.
43 Okada, K.; Sugie, H. *J. Phys. Soc. Japan* 1968, **25**, 1128.
44 Cui, H.-B.; Takahashi, K.; Okano, Y.; Kobayashi, H.; Wang, Z.; Kobayashi, A. *Angew. Chem. Int. Ed. Engl.* 2005, **44**, 6508.
45 Cui, H.; Wang, Z.; Takahashi, K.; Okano, Y.; Kobayashi, H.; Kobayashi, A. *J. Am. Chem. Soc.* 2006, **128**, 15074.
46 Jain, P.; Dalal, N. S.; Toby, B. H.; Kroto, H. W.; Cheetham, A. K. *J. Am. Chem. Soc.* 2008, **130**, 10450.
47 Jain, P.; Ramachandran, V.; Clark, R. J.; Zhou, H. D.; Toby, B. H.; Dalal, N. S.; Kroto, H. W.; Cheetham, A. K. *J. Am. Chem. Soc.* 2009, **131**, 13625.
48 Sánchez-Andújar, M.; Presedo, S.; Yáñez-Vilar, S.; Castro-García, S.; Shamir, J.; Señarís-Rodríguez, M. A. *Inorg. Chem.* 2010, **49**, 1510.
49 Pato-Doldán, B.; Sánchez-Andújar, M.; Gómez-Aguirre, L. C.; Yáñez-Vilar, S.; López-Beceiro, J.; Gracia-Fernández, C.; Haghighirad, A. A.; Ritter, F.; Castro-García, S.; Señarís-Rodríguez, M. A. *Phys. Chem. Chem. Phys.* 2012, **14**, 8498.
50 Hagen, K. S.; Naik, S. G.; Huynh, B. H.; Masello, A.; Christou, G. *J. Am. Chem. Soc.* 2009, **131**, 7516.
51 Wang, X.-Y.; Gan, L.; Zhang, S.-W.; Gao, S. *Inorg. Chem.* 2004, **43**, 4615.
52 Wang, Z.; Zhang, B.; Otsuka, T.; Inoue, K.; Kobayashi, H.; Kurmoo, M. *Dalton Trans.* 2004, 2209.
53 Pato-Doldán, B. *Ph.D. Thesis: Búsqueda de nuevos materiales termoeléctricos, dieléctricos y multiferroicos basados en óxidos mixtos y en híbridos orgánico-inorgánicos*, University of A Coruña, Faculty of Sciences 2014.
54 Sante, D. Di; Stroppa, A.; Jain, P.; Picozzi, S. *J. Am. Chem. Soc.* 2013, **135**, 18126.
55 Chen, S.; Shang, R.; Hu, K.-L.; Wang, Z.-M.; Gao, S. *Inorg. Chem. Front.* 2014, **1**, 83.
56 Stroppa, A.; Jain, P.; Barone, P.; Marsman, M.; Perez-Mato, J. M.; Cheetham, A. K.; Kroto, H. W.; Picozzi, S. *Angew. Chem. Int. Ed.* 2011, **50**, 5847.
57 Hu, K. L.; Kurmoo, M.; Wang, Z.; Gao, S. *Chem. Eur. J.* 2009, **15**, 12050.
58 Pato-Doldán, B.; Gómez-Aguirre, L. C.; Bermúdez-García, J. M.; Sánchez-Andújar, M.; Fondado, A.; Mira, J.; Castro-García, S.; Señarís-Rodríguez, M. A. *RSC Adv.* 2013, 3, 22404.
59 Stroppa, A; Barone, P.; Jain, P.; Perez-Mato, J. M.; Picozzi, S. *Adv. Mater.* 2013, **25**, 2284.
60 Stroppa, A.; Jain, P.; Barone, P.; Marsman, M.; Perez-Mato, J. M.; Cheetham, A. K.; Kroto, H. W.; Picozzi, S. *Angew. Chem. Int. Ed. Engl.* 2011, **50**, 5847.
61 Wang, W.; Yan, L.-Q.; Cong, J.-Z.; Zhao, Y.-L.; Wang, F.; Shen, S.-P.; Zou, T.; Zhang, D.; Wang, S.-G.; Han, X.-F.; Sun, Y. *Sci. Rep.* 2013, **3**, 2024.
62 Tian, Y.; Stroppa, A.; Chai, Y.; Yan, L.; Wang, S.; Barone, P.; Picozzi, S.; Sun, Y. *Sci. Rep.* 2014, **4**, 6062.
63 Gómez-Aguirre, L. C.; Pato-Doldán, B.; Mira, J.; Castro-García, S.; Señarís-Rodríguez, M. A.; Sánchez-Andújar, M.; Singleton, J.; Zapf, V. S. *J. Am. Chem. Soc.* 2016, **138**, 1122.
64 Zhang, W.; Cai, Y.; Xiong, R. G.; Yoshikawa, H.; Awaga, K. *Angew. Chem. Int. Ed.* 2010, **49**, 6608.
65 Zhang, X.; Shao, X.-D.; Li, S.-C.; Cai, Y.; Yao, Y.-F.; Xiong, R.-G.; Zhang, W. *Chem. Commun.* 2015, **51**, 4568.
66 Zhang, W.; Ye, H. Y.; Graf, R.; Spiess, H. W.; Yao, Y. F.; Zhu, R. Q.; Xiong, R. G. *J. Am. Chem. Soc.* 2013, **135**, 5230.
67 Xu, W.-J.; Chen, S.-L.; Hu, Z.-T.; Lin, R.-B.; Su, Y.-J.; Zhang, W.-X.; Chen, X.-M. *Dalt. Trans.* 2015, 4224.
68 Zhao, X. H.; Huang, X. C.; Zhang, S. L.; Shao, D.; Wei, H. Y.; Wang, X. Y. *J. Am. Chem. Soc.* 2013, **135**, 16006.

69 Du, Z.-Y.; Zhao, Y.-P.; Zhang, W.-X.; Zhou, H.-L.; He, C.-T.; Xue, W.; Wang, B.-Y.; Chen, X.-M. *Chem. Commun.* 2014, **50**, 1989.
70 Gómez-Aguirre, L. C.; Pato-Doldán, B.; Stroppa, A.; Yang, L.-M.; Frauenheim, T.; Mira, J.; Yáñez-Vilar, S.; Artiaga, R.; Castro-García, S.; Sánchez-Andújar, M.; Señarís-Rodríguez, M. A. *Chem. Eur. J.* 2016, **22**, 7863.
71 Kieslich, G.; Sun, S.; Anthony, A. K. *Chem. Sci.* 2014, **5**, 4712.
72 Tong, M.-L.; Ru, J.; Wu, Y.-M.; Chen, X.-M.; Chang, H.-C.; Mochizuki, K.; Kitagawa, S. *New J. Chem.* 2003, **27**, 779.
73 Schlueter, J. A; Manson, J. L.; Geiser, U. *Inorg. Chem.* 2005, **44**, 3194.
74 Barrera, G. D.; Bruno, J. A. O., Barron, T. H. K., Allan, N. L. *J. Phys. Condens. Matter* 2005, **17**, R217.
75 Coudert, X. *Chem. Mater.* 2015, **27**, 1905.
76 Ogborn, J. M.; Collings, I. E.; Moggach, S. A.; Thomson, A. L.; Goodwin, A. L. *Chem. Sci.* 2012, **3**, 3011.
77 Neimark, A. V.; Coudert, F. X.; Triguero, C.; Boutin, A.; Fuchs, A. H.; Beurroies, I.; Denoyel, R. *Langmuir* 2011, **27**, 4734.
78 Li, M.; Liu, B.; Wang, B.; Wang, Z.; Gao, S.; Kurmoo, M. *Dalton Trans.* 2011, **40**, 6038.
79 Ortiz, A. U.; Boutin, A.; Gagnon, K. J.; Clearfield, A.; Coudert, F.-X. *J. Am. Chem. Soc.* 2014, **136**, 11540.
80 Soldano, C. *Prog. Mater. Sci.* 2015, **69**, 183.
81 Chaikittisilp, W., Ariga, K., Yamauchi, Y., *J. Mater. Chem. A* 2013, **1**, 14.
82 Hu, M.; Reboul, J.; Furukawa, S.; Radhakrishnan, L.; Zhang, Y.; Srinivasu, P.; Iwai, H.; Wang, H.; Nemoto, Y.; Suzuki, N.; Kitagawa, S.; Yamauchi, Y. *Chem. Commun.*, 2011, **47**, 8124.
83 Hu, M.; Reboul, J.; Furukawa, S.; Torad, N. L.; Ji, Q.; Srinivasu, P.; Ariga, K.; Kitagawa, S.; Yamauchi, Y. *J. Am. Chem. Soc.* 2012, **134**, 2864.
84 Hu, J.; Wang, H.; Gao, Q.; Guo, H. *Carbon* 2010, **48**, 3599.
85 Yang, S. J.; Kim, T.; Im, J. H.; S. Kim, Y.; Lee, K.; Jung, H.; Park, C. R. *Chem. Mater.*2012, **24**, 464.
86 Chaikittisilp, W.; Hu, M.; Wang, H.; Huang, H.-S.; Fujita, T.; Wu, K. C.-W.; Chen, L.-C.; Yamauchi, Y.; Ariga, K. *Chem. Commun*. 2012, **48**, 7259.
87 Torad, N. L.; Hu, M.; Ishihara, S.; Sukegawa, H.; Belik, A. A.; Imura, M.; Ariga, K.; Sakka, Y.; Yamauchi, Y. *Small* 2014, **10**, 2096.
88 Zhang, L.; Wang, X.; Wang, R.;Hong, M. *Chem. Mater.* 2015, **27**, 7610.
89 Chen, L.; Bai, J.; Wang, C.; Pan, Y.; Scheerc, M.; You, X. *Chem. Commun*. 2008, 1581.

Chapter 2:

Role of temperature and pressure on the multisensitive multiferroic dicyanamide framework [TPrA][Mn(dca)$_3$] with perovskite-like structure

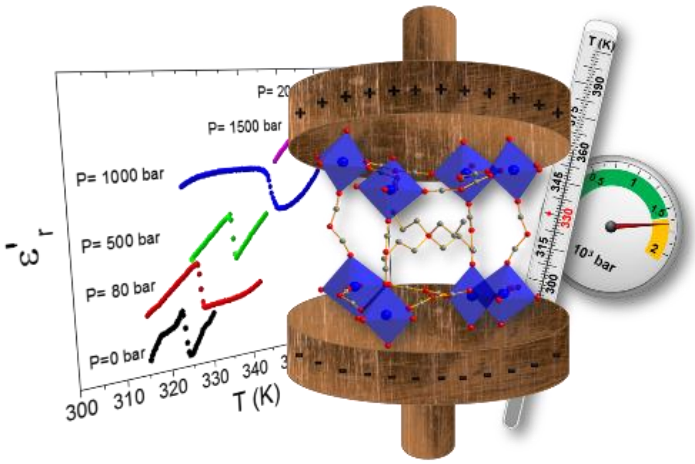

Role of temperature and pressure on the multisensitive multiferroic dicyanamide framework [TPrA][Mn(dca)$_3$] with perovskite-like structure

Abstract: This chapter focuses in the hybrid organic-inorganic perovskite-like [TPrA][Mn(dca)$_3$] compound, in which a multistimuli response to temperature and pressure is found related to a first-order structural phase transition near room temperature, $T_t \approx 330$ K. This phase transition involves a transformation from room temperature *polymorph I*, with the non-centrosymmetric space group $P\bar{4}2_1c$, to the high temperature *polymorph II*, with the centrosymmetric space group *I4/mcm*, and it implies ionic displacements, order-disorder phenomena, and a large and anisotropic thermal expansion (specially along the *c*-axis). As a consequence, [TPrA][Mn(dca)$_3$] exhibits a dielectric anomaly, associated with the change from a cooperative to a non-cooperative electric behaviour (antiferroelectric (AFE)-paraelectric (PE) transition). The former implies an AFE distribution of electric dipoles in *polymorph I*, related to the described off-shift of the apolar TPrA cations and the order-disorder of the polar dca ligands mechanisms, that are different from those reported, up to now, for others perovskite-like hybrid compounds. Such cooperative electric order, below $T_t \approx 330$ K, coexisting with long-range antiferromagnetic ordering below $T = 2.1$ K render the [TPrA][Mn(dca)$_3$] a new type-I multiferroic material. In addition, the obtained experimental results reveal that this compound is also a multistimuli responsive material, with a very large sensitivity toward temperature and applied external pressure, $\delta Tt/\delta P \approx 24$ K kbar^{-1}, even for small values of pressure (P < 2 kbar). Therefore, this material opens up a potential interest for future technological applications, such as temperature/pressure sensing.

2.1. Introduction and objectives

As already indicated in chapter 1, obtaining new single phase materials, where at least two ferroic orders coexist, is a focus area in multiferroic materials research.[1] The reason for this interest is related to their potential application in magnetic storage, novel circuits, sensors, microwave high-power applications, etc.[2,3] However, up-to-date, single phase multiferroics are rare as the conventional mechanism for long-range electric order (which usually involves off-centering of d^0 transition metal cations) and cooperative magnetic order (which requires the presence of d^n transition metal cations and their interactions through short ligands, such as O^{2-})[4] are mutually exclusive.[5]

Therefore, the search for new multiferroic compounds constitutes one of the big challenges in modern Materials Science. In this context, a major research current is devoted to the search for materials in which electric order is induced by alternative mechanisms to the one indicated above, among them, order-disorder processes,[6] frequently involving hydrogen bonds,[7,8] magnetically-induced ferroelectricity,[9] etc.

Beyond transition-metal oxides, that have been the most extensively investigated,[10] the family of hybrid organic-inorganic compounds and coordination polymers are attracting increased attention.[11-14] As demonstrated in the last years, in these versatile compounds the appropriate combination of building blocks (metal ions, ligands and species included in their frameworks) can not only give rise to new and interesting properties, but also afford possible coexistence and/or synergism of multiple functionalities and sensibilities within one material. Among them, the hybrid organic-inorganic formates with perovskite-like structure and formula [AmineH][M(HCOO)$_3$]$_n$ (where M = divalent transition metal cations, AmineH = midsized protonated amines) have been intensively studied as promising type-I multiferroic materials.[12,15-20] In these compounds, in which magnetic and electric ordering coexist, these properties arise from two different active "sublattices" in the perovskite-like structure: (a) the framework, that is based on [MO$_6$] octahedra connected through formate ligands, and that displays cooperative magnetism at low temperatures[21] and (b) the polar cations, that occupy the A-sites of the perovskite architecture, are linked to the framework via hydrogen bonds, and experience an order-disorder process that gives rise to dielectric transitions.[22]

Another related, yet very little explored, family of potentially interesting compounds is that of dicyanamide-bridged perovskite-like compounds of formula [TPrA][M(dca)$_3$] where dca represents the dicyanamide anion, $[N(CN)_2]^-$, TPrA corresponds to tetrapropylammonium cation, $[(CH_3CH_2CH_2)_4N]^+$ and, up to now, M = Mn^{2+} and Ni^{2+}.[23a] The dicyanamide ligands have been widely used to synthesized a vast family of

coordination polymers compounds, with very different and rich variety of crystal structures.[23] Nevertheless, the studies have been focused mainly on their interesting magnetic properties, thus the dielectric and multiferroic properties have remain unstudied.

In the perovskite-like [TPrA][M(dca)$_3$] compounds the dicyanamide ligands, with a dipolar moment related to their angular geometry, act as end-to-end mode ($\mu_{1,5}$-dca) bridging ligands between the transition metal cations, thus forming a 3D framework. Meanwhile, the TPrA cations, which are apolar and cannot form hydrogen-bonds to the framework, are located in the resulting pseudocubooctahedral cavities.[23a]

In the case of the Mn compound, [TPrA][Mn(dca)$_3$], it is known that at room temperature it crystallizes in the non-centrosymmetric tetragonal $P\bar{4}2_1c$ space group and its structure can be described as a 2 × 2 × 2 perovskite superstructure.[23a] According to the literature, it retains the same symmetry and space group down to 110 K and it exhibits long-range antiferromagnetic (AFM) order below 2.1 K.[23a]

Here, and for the first time, we explore the dielectric properties of this compound, its structural characteristics above room temperature and the influence of external hydrostatic pressure and temperature on its behaviour. Our interest is 2-fold: (a) we search for new multiferroic compounds as well as for new mechanisms allowing multiferroicity and (b) we are also interested in strong stimuli responsive materials that undergoes changes of large amplitude in response to external stimuli such as temperature, pressure, etc.;[24] these are of interest for different technological applications such as highly sensitive pressure detectors, shock absorbing materials, etc.

Along the next lines, we will present and discuss our results starting by those concerning the ambient pressure studies (phase transition, polymorphs, dielectric and magnetic transition) and followed by those obtained in the experiments carried out under external pressure (DSC studies, dilatometry and dielectric properties under pressure).

2.2. Experimental section

2.2.1 Synthesis

[TPrA][Mn(dca)$_3$] was prepared from commercially available Mn(NO$_3$)$_2$·xH$_2$O (97%, Aldrich), (TPrA)Br (98%, Aldrich), Na(dca) (96%, Aldrich), and absolute ethanol (Panreac), which were used as purchased without further purification. A reagent amount of deionized water was also used in the synthesis. The synthetic route used, which is an adaptation of the previously reported for the preparation of the [G][M(dca)$_3$]compounds,[23a] is template by alkylammonium cations and accomplished through a mild solution chemistry method at ambient temperature.

In a typical experiment, an aqueous solution of Mn(NO$_3$)$_2$·xH$_2$O (2 mmol) was placed at the bottom of a glass tube and it was layered by a mixture of (TPrA)Br (2 mmol) solution in 10 ml of ethanol and a solution of Na(dca) (6 mmol) in 10 ml of water. Cubic colorless crystals were obtained after 1 week and they were collected by filtration and washed several times with ethanol. The compound was obtained as a single phase material and its purity was confirmed by comparison of its experimental powder X-ray diffraction (PXRD) pattern at room temperature with the pattern simulated from the single-crystal X-ray diffraction (SCXRD), see Figure 2-1.

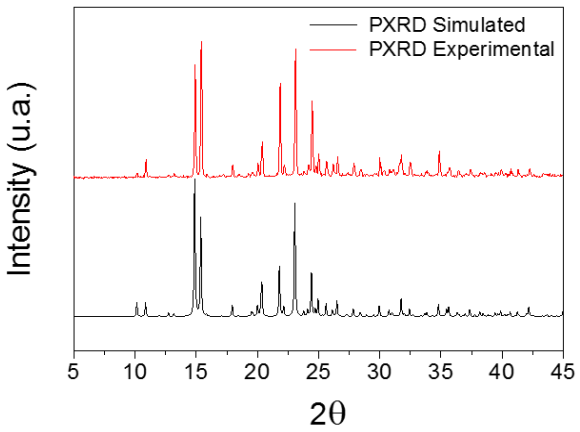

Figure 2-1. Room temperature PXRD patterns for the as-prepared [TPrA][Mn(dca)$_3$] compound and the simulated one based on its single-crystal structure at room temperature.

2.2.2. Single-crystal X-ray diffraction

Single-crystal data sets were collected at different temperatures (room temperature and 368 K) in a Bruker-Nonius x8 ApexII X-ray diffractometer equipped with a CCD detector and using monochromatic MoKα1 radiation (λ = 0.71073 Å). The data integration and reduction was performed using the Apex2 V.1.0-27 (Bruker-Nonius, 2005) suite software. The intensity collected was corrected for Lorentz and polarization effects, and for absorption by semiempirical methods on the basis of symmetry-equivalent data, using SADABS (2004) of the suite software. The structures were solved by the direct method using the SHELXS-97 program[25] and were refined by full-matrix least-squares method on SHELXL-97 program,[25] both programs are available within the WinGX package.[26] To solve the structures, anisotropic thermal factors were employed for the non-H atoms and non-disorder atoms. In the case of ordered TPrA cations, the hydrogen atoms of the propyl groups were added to the ideal positions and isotropic thermal factors were refined.

2.2.3. Powder X-ray diffraction

A Siemens D-5000 diffractometer, using CuKα radiation (λ = 1.5418 Å), was used to study this compound by powder X-ray diffraction (PXRD) at room temperature. The PXRD pattern was compared with the profile obtained from the single-crystal structure, which was generated by the Mercury 3.5.1 software.[27] In addition, high-resolution synchrotron powder X-ray diffraction was carried out as a function of temperature on heating (260 ≤ T (K) ≤ 400) in the ID22 beamline (λ = 0.3997 Å) at ESRF (Grenoble, France). For this purpose, the sample was loaded in a borosilicate capillary (ø = 0.7 mm) and rotated during data collection. We observed that the compound is sensitive to the high flux of the radiation. To prevent damages, we used two strategies: the collection of data was performed during 8 min for each temperature and the beam was focused on different regions of the capillary at each temperature. The obtained patterns had enough quality to allow their Le Bail analysis using the GSAS+EXPGUI software.[28,29]

2.2.4. Differential scanning calorimetry (DSC)

Differential scanning calorimetry (DSC) studies were carried out in a TA Instruments MDSC Q2000 equipped with a liquid nitrogen cooling system. The sample (with a mass around 5 mg) was heated and cooled with a rate of 20 K min^{-1}, from 130 up to 400 K, under nitrogen atmosphere.

Additionally, pressure differential scanning calorimetry (PDSC) tests were performed in a TA Instruments pressure cell mounted on a Q2000 modulated DSC. The cell was calibrated for temperature and heat with Indium at each of the pressures to be used in the measuring tests. The effect of pressure on the melting temperature and enthalpy of Indium was taken into account.[30] In a typical experiment, about 5 mg of sample were confined inside a pinhole aluminum capsule. The experiments were performed in N_2 atmosphere at a constant pressure (from 1 to 69 bar) while keeping a constant flow of 50 ml min^{-1} of N_2. The sample under a constant external pressure was heated and cooled at a rate of 2 K min^{-1} from room temperature to 343 K.

2.2.5 Pressure-Volume-Temperature (PVT) analysis.

To study the dilatometry of the material at different pressures, the PVT 100 SWO/ThermoHaake equipment was used. In a typical experiment, about 440 mg of powder material were loaded inside a cylinder between two pistons, which transmit an axial compressive force from 200 to 1600 bar to the sample. After applying the external pressure, the sample was heated at a rate of 5 K min^{-1} from 183 to 373 K and the axial thermal expansion of the sample was registered.

2.2.6. Dielectric measurements

The complex dielectric permittivity ($\varepsilon_r = \varepsilon'_r - i\,\varepsilon''_r$) of the cold-press pelletized sample was measured as a function of frequency and temperature with a parallel-plate capacitor coupled to a Solartron 1260A Impedance/Gain-Phase Analyzer, capable to measure in the frequency range from 10 μHz up to 32 MHz using an amplitude of 2 V. The capacitor was mounted in a Janis SVT200T cryostat refrigerated with liquid nitrogen, and with a Lakeshore 332 incorporated to control the temperature from 78 K up to 400 K. The data were collected on heating.

Pelletized samples, made out of cold-press nonoriented single crystals, with an area of approximately 133 mm^2 and a thickness of approximately 1.3 mm were prepared to fit into the capacitor, and gold was sputtered on their surfaces to ensure a good electrical contact with the electrodes.

All the dielectric measurements were carried out in a nitrogen atmosphere where several cycles of vacuum and nitrogen gas were performed to ensure that the sample environment was free of water.

Additionally, dielectric measurements were carried out in a pressure cell supplied by Novocontrol GmbH. The cell, basically a stainless steel cylinder with a hermetic seal, was filled with a silicone fluid which transmits an isostatic pressure from the piston to the sample. The dielectric response was measured for 10^3-10^6 Hz frequencies. The measurements were performed as a function of the temperature (310-380 K) for constant pressures (1, 80, 500, 1000, 1500, and 2000 bar).

2.3. Results and discussion

2.3.1. Studies at ambient pressure

2.3.1.1. Phase transition from DSC data. According to the DSC results, this material experiences a reversible phase transition above room temperature. As it can be seen in Figure 2-2 an acute endothermic peak is seen around 332 K when heating and the corresponding exothermic peaks is observed around 329 K on cooling.

The observed thermal hysteresis indicates the first-order character of such phase transition, that involves an enthalpy change of $\Delta H \approx 5581$ (heating) to 6077 (cooling) J mol^{-1} and an entropy change of $\Delta S \approx 16.8$ (heating) to 18.5 (cooling) J mol^{-1} K^{-1}, as determined from the area under the Cp/T curve and the peak temperature, T_{max}.

Taking into account that for an order-disorder transition $\Delta S = R\,ln(N)$, where R is the gas constant and N is the ratio of the number of configurations in the disordered and ordered system, a value of N ≈ 8 is calculated, thus pointing out toward a 8-fold order-disorder model for the [TPrA][Mn(dca)$_3$] compound. This value is higher, more than double, than those recently reported for the related hybrid perovskite [(CH$_3$)$_2$NH$_2$][M(HCOO)$_3$], with M^{2+} = Mn^{2+}, Fe^{2+}, Co^{2+}, Ni^{2+}, Zn^{2+}, and Mg^{2+}, where N ≈ 1.5-3, depending of the transition metal cation.[22b,31]

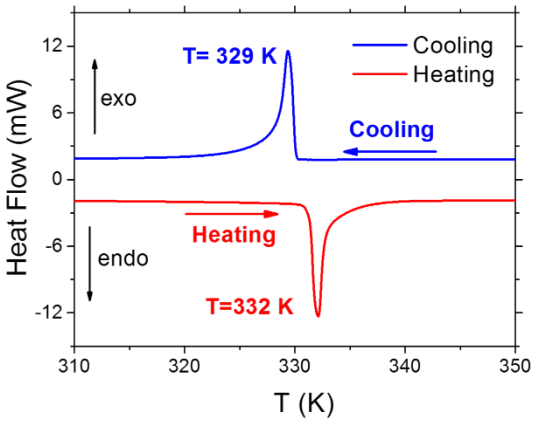

Figure 2-2. DSC results as a function of temperature obtained by heating and cooling the sample [TPrA][Mn(dca)$_3$] at a rate of 20 K min^{-1}.

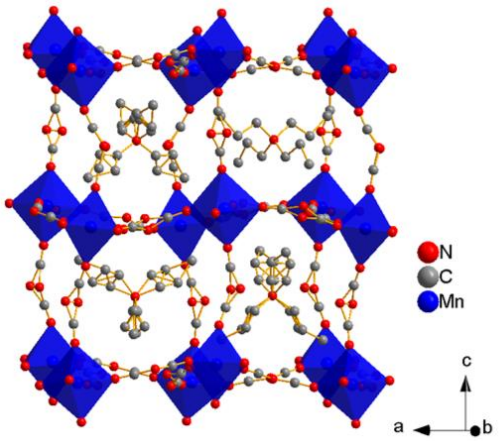

Figure 2-3. Conventional perovskite structure view of *polymorph I*. The dicyanamide ligands act as $\mu_{1,5}$-bridges between the Mn^{2+} cations. The N-amide and C atoms of the dicyanamide ligans along *c*-axis are modeled in four and three crystallographic positions, respectively. As for the TPrA cations, they are located inside the pseudocubooctahedral cavities, and two of the three present in the asymmetric unit display crystallographic disorder in the C atom positions. The H atoms of the TPrA cations have been removed to facilitate visualization of the structure.

2.3.1.2. Crystal structures. The single-crystal X-ray studies carried out above and below the DSC transition highlight that this compound presents two different crystal structures: At 300 K, the sample shows in the $P\bar{4}2_1c$ non-centrosymmetric spacegroup (*polymorph I*), while above room temperature it displays the *I4/mcm* centrosymmetric space group (*polymorph II*). The crystallographic data of these two polymorphs, which in both cases correspond to a perovskite-like structure, are compiled in Table AI-1 of Annexe I.

In the following paragraphs, we will comparatively describe both structures which are depicted in Figures 2-3, 2-4 and 2-5, focusing on aspects that are completely new (all those concerning *polymorph II*, which to the best of our knowledge is described for the first time in this study). We will also present important structural details of *polymorph I*, which were not given before[23a] and that are relevant to understand the properties.

It is also interesting noting that the transformation of p*olymorph I* into *polymorph II* is reversible and that the single crystal integrity is maintained during that process.

Polymorph I. As it has been previously reported the asymmetric unit of this compound, displays a tetragonal symmetry (S.G. = $P\bar{4}2_1c$), and it contains one independent metal cation, three dca anions and three TPrA cations. As a result, each Mn^{2+} cation is connected to its six nearest neighbors, through six $\mu_{1,5}$-dca bridges, in a distorted octahedral environment, with six different Mn-N distances, see Table AI-2 of Annexe I. The resulting [MnN$_6$] octahedra are cooperatively rotated along the main crystallographic axes (tilt systems $a^-b^+c^-$ at Glazer notation).[32]

On the other hand, the TPrA cations are located inside the cavities of the resulting framework.

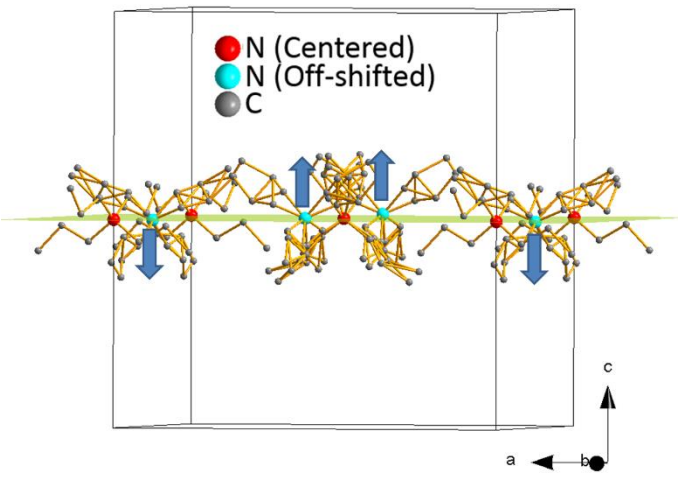

Figure 2-4. Representation of the TPrA cations of the *polymorph I* closer to the (002) plane. Half of them (those located on a 4-fold axis and represented by a red N-atom) are located in the plane. Meanwhile the other half (represented by blue N-atoms) are alternatively located above and below the plane, the off-shift of these cations being about 0.105 Å.

The here obtained structural data for this polymorph are summarized in Table AI-1 of Annexe I and Figure 2-3 and are in agreement with those previously reported in the literature.[23a]

As also already reported,[23a] the structure of this polymorph exhibits a certain disorder: in the N-amide

atoms and C atoms of the dca anions along the *c*-axis and in one of the dca anions within the *ab*-plane; as well as in the C atom positions of two of the three TPrA cations of the asymmetric unit, see Figure 2-3.

Furthermore, we remark a most interesting new structural feature: in this polymorph half of the TPrA cations (those located on a 2-fold axis) show a cooperatively off-center shift along the *c*-axis, following an antiferrodistortive up-down-up-down pattern, see Figure 2-4. It is worth noting that the value of such displacement, 0.105(3) Å, is of the same order than that reported in the case of the "classical" ferroelectric oxides, such as $BaTiO_3$ and related; even if in those oxides the B-site transition metal ion is the one that shifts.[8]

Polymorph II. At higher temperature (T = 368 K), this compound displays a different $\sim v2 \times \sim v2 \times 2$ perovskite superlattice with tetragonal symmetry. Analysis of the systematic absences present in the single-crystal X-ray diffraction data revealed three candidate space groups: *I4/mcm* (number 140, centrosymmetric) and its subgroups $I\bar{4}c2$ (number 120, non-centrosymmetric) and *I4cm* (number 108, non-centrosymmetric). Finally, the structural data (both from single-crystal X-ray diffraction and synchrotron powder X-ray diffraction) could be successfully refined in the centrosymmetric space group of highest symmetry, the *I4/mcm*, see Table AI-1 of Annexe I. In this case the asymmetric unit contains one independent Mn^{2+} cation, two dca anions and one TPrA cation. The Mn^{2+} cations are six coordinated by N atoms of the dicyanamide ligands in a distorted octahedral coordination environment, where the four equatorial Mn-N bonds within the *ab*-plane are shorter than the two Mn-N bonds along the *c*-axis, see Table AI-3 of Annexe I.

Differently from *polymorph I*, in *polymorph II* the [MnN_6] octahedra are rotated cooperatively within the *ab*-plane and display an anticlockwise arrangement along the *c*-axis (tilt systems $a^0a^0c^-$ at Glazer notation).

On the other hand, another very noticeable feature is the much larger disorder present in the structure of *polymorph II*, see Figure 2-5: (a) disorder in the dca ligands, particularly those located along the *c*-axis and (b) disorder in the TPrA cations located inside the pseudocubooctahedral cavities of the $[Mn(dca)_3]^-$ framework.

In connection with the former, the N and the C atoms of the dca ligands along the *c*-axis had to be modeled to occupy eight and four positions, respectively, with equal occupancy. These results suggest a dynamic disorder, which would in turn imply the rotation of the dca ligands around the *c*-axis, see Figure 2-5. Meanwhile the N and the C atoms of the dca ligands in the *ab*-plane, had to be modeled to occupy five and three positions, respectively.

As for the TPrA cations, they also present a much larger disorder than in polymorph I: disorder in all the C atoms of the propyl groups, which occupy four different positions, see Figure 2-5 inset.

Finally, and most importantly, in *polymorph II* the TPrA cations are located at the center of the cavities, in contrast to *polymorph I*, where as indicated above half of them are off-shifted.

2.3.1.3. Structural evolution as a function of temperature. Synchrotron powder X-ray diffraction experiments performed at different temperatures revealed a rather abrupt structural phase transition occurring at $T_t \approx 330$ K, and they allowed monitoring the thermal evolution of the lattice parameters.

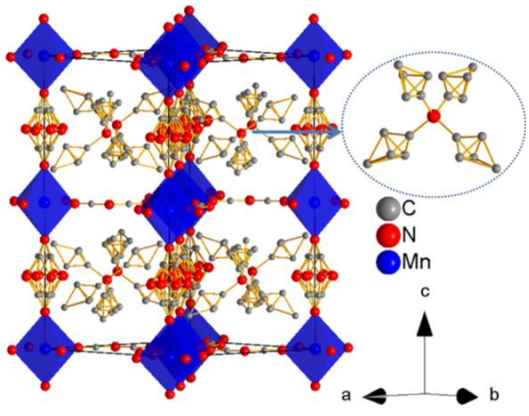

Figure 2-5. Crystal structure view of the more disordered *polymorph II*, where the N-amide atom of the dicyanamide ligands and the C atoms bonded to it are disordered. On the other hand, the TPrA cations present disorder in the C atoms of the propyl groups, as shown in the inset. The H atoms of the TPrA cations have been removed to facilitate visualization of the structure.

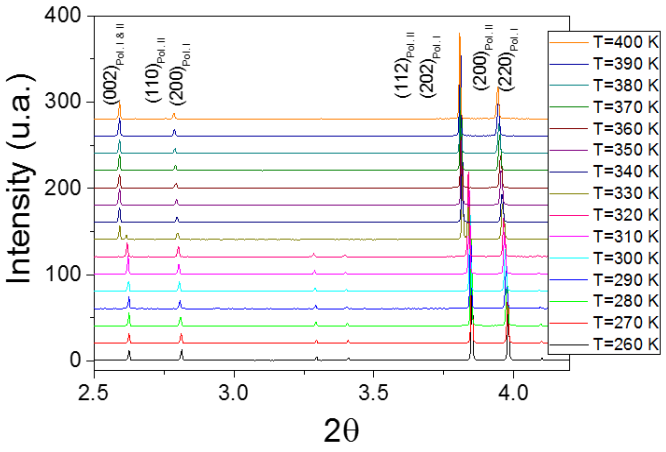

Figure 2-6. Detail of low-angle synchrotron powder X-ray diffraction patterns of the [TPrA][Mn(dca)$_3$] compound obtained at different temperatures between 260 K and 400 K in steps of 10 K.

As shown in Figure 2-6, for $T \leq 320$ K the only phase present is the one with $P\bar{4}2_1c$ symmetry (*polymorph I*). Otherwise, for $T > 330$ K, this phase has completely converted into *polymorph II*; and only in the experiment carried out at $T = 330$ K, both polymorphs coexist.

From Le Bail fit of the patterns obtained at different temperatures (see Figure 2-7), the cell parameters and volume of *polymorph I* and *II* were calculated.

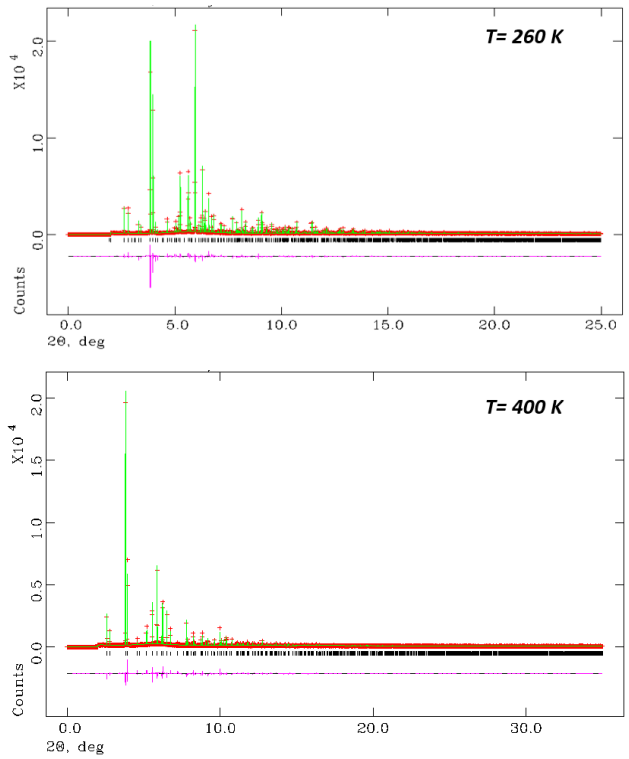

Figure 2-7. Le Bail refinement of synchrotron powder X-ray diffraction patterns for the [TPrA][Mn(dca)$_3$] compound at (a) T = 260 K (*polymorph I*) and (b) T = 400 K (*polymorph II*). Observed (red dots), calculated (green solid line) and difference (pink solid line at the bottom) profiles. The tick black marks indicate the positions of the allowed Bragg reflections.

The obtained results are presented and compared in Figure 2-8, taking into account that $a_{Pol.I} = \sqrt{2}\, a_{Pol.II}$ and $c_{Pol.I} = c_{Pol.II}$. Moreover, from the obtained data the linear thermal expansion (*TE*) coefficients $\alpha_a = (1/a)(\delta a/\delta T)_p$ and $\alpha_c = (1/c)(\delta c/\delta T)_p$, as well as the volumetric thermal expansion (*TE*) coefficient $\beta_V = (1/V)(\delta V/\delta T)_p$ were calculated (see Figure 2-9).

These results, reveal the following interesting features: (a) The phase transition is clearly first order. It implies a large and abrupt change in the volume and cell parameters, especially in *c*, which is very affected by the sudden change of the [MnN$_6$] octahedral tilting ($\Delta V/V \approx 1.25\%$, $\Delta c/c \approx 0.92\%$). (b) This compound shows a highly anisotropic thermal expansion, that is particularly large in *polymorph I* along the *c*-axis and for temperatures close to T_t. There it reaches a very seldomly found colossal value ($\alpha > 100 \times 10^{-6}$ K^{-1}).[33] Such anomalous thermal expansion along c is probably related to the presence of the antiferrodistortive pattern along this axis. Meanwhile, upon crossing T_t, the relative rate at which this material expands with temperature achieves an almost constant value. (c) The volumetric thermal expansion of both polymorphs is also colossal and more than 1 order of magnitude higher than the typically observed in other framework materials or dense inorganic compounds (with an habitual positive thermal expansion in the range of 10-40 $\times 10^{-6}$ K^{-1}),[34] being particularly noticeable in *polymorph I*.

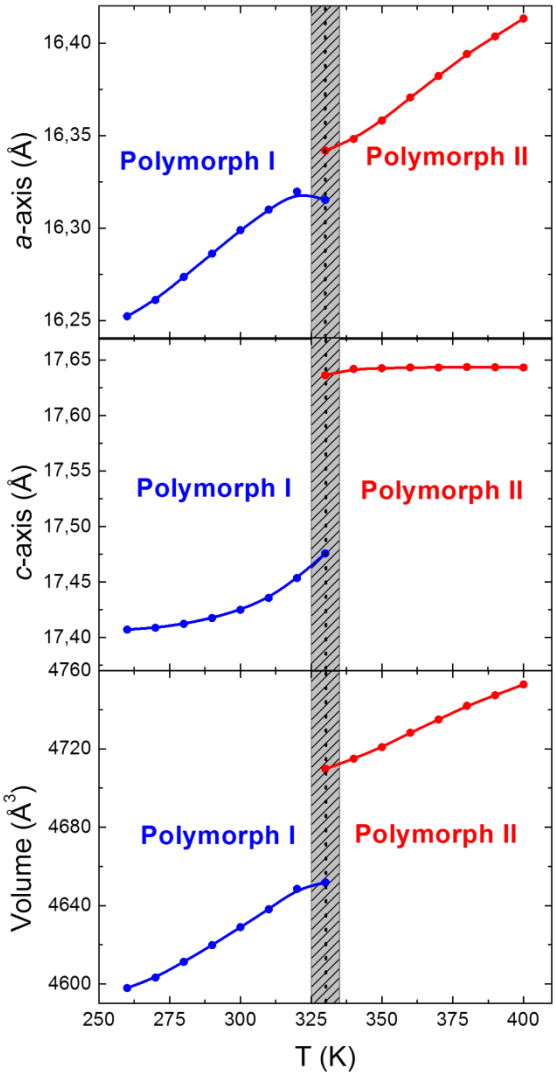

Figure 2-8. Temperature dependence of the cell parameters *a* and *c* and volume of *polymorph I* and *II*.

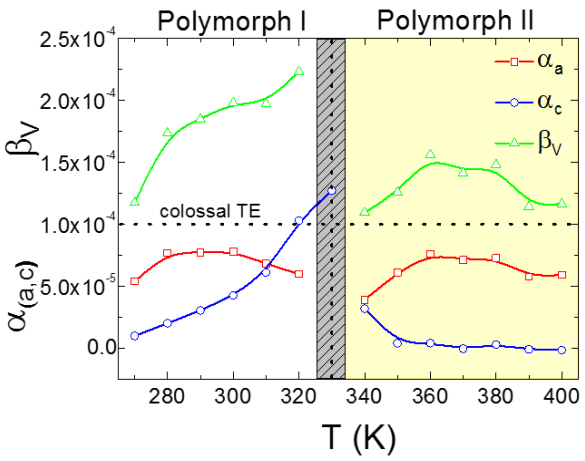

Figure 2-9. Linear thermal expansion coefficients (α_a, α_c) and volumetric thermal expansion coefficient (β_V) as a function of temperature as calculated for the two polymorphs of the [TPrA][Mn(dca)$_3$] compound.

Summarizing, the [TPrA][Mn(dca)$_3$] compound, which has demonstrated to be a strongly thermally responsive material, experiences a sharp first-order structural transition at $T_t \approx 330$ K from the room temperature *polymorph I* (non-centrosymmetric $P\bar{4}2_1c$) to the high temperature *polymorph II* (centrosymmetric *I4/mcm*).

The driving force for this structural phase transition is at least 3-fold: (a) the displacive transition of part of TPrA cations, from an off-centered position in *polymorph I* to centered positions in *polymorph II*; (b) the order-disorder of the dca ligands and the propyl groups of the TPrA cations; (c) the cooperative distortion of the framework due to the rotation of the [MnN$_6$] octahedra along the main axis, which is specially noticeable along the *c*-axis.

All these three processes are strongly correlated and take place simultaneously. This is probably due to rather strong steric interactions between the framework and the bulky TPrA cations, which make the former distort to accommodate the changing characteristics of the latter.

This behaviour reminds of that exhibited by other hybrid organic-inorganic perovskites, such as [(CH$_3$)$_2$NH$_2$][Mn(HCOO)$_3$], where the framework is rather flexible and distorts for a better adjust of the ordered and disordered versions of polar dimethylammonium cation.[31] Nevertheless, in that case, the interaction between the guest cations and the framework is relative larger as it also implies H-bonds, which cannot exist in the case of the here studied [TPrA][Mn(dca)$_3$] compound.

2.3.1.4. Dielectric properties. The temperature dependence of the real part of the complex dielectric permittivity, ε'_r, (the so-called dielectric constant) of this compound is shown in Figure 2-10. As it can be seen, the ε'_r vs *T* curves display a small peak around $T \approx 330$ K, very close to the temperature at which *polymorph I* transforms into *polymorph II*. It is also worth noting that while ε'_r is frequency independent for $T < 330$ K, it strongly depends on frequency for higher temperatures.

Taking into account that in *polymorph I* the cooperative off-center shift of the TPrA cations gives rise to electric dipoles in an antiferroelectric (AFE) arrangement, which are no longer present in *polymorph II*, such kink reflects the change from a cooperative AFE order to a non-cooperative behaviour at higher temperatures (above 330 K). In addition, the order-disorder transition experienced by the polar dca ligands at that temperature could also be contributing to the dielectric anomaly.

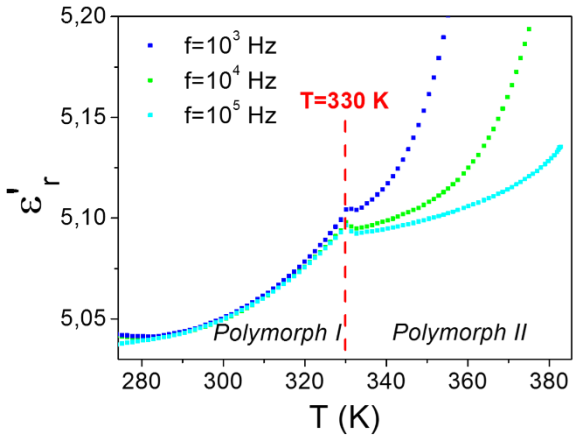

Figure 2-10. Temperature dependence of the dielectric constant (ε'_r) of [TPrA][Mn(dca)$_3$] measured at different frequencies (10^3-10^5 Hz).

As for the observed frequency dependence of ε'_r for $T > T_t$ is probably caused by the rotation of the dca ligands in *polymorph II*. These would be acting as polar rotators so that their hopping motion between different orientations could be responsible for the observed dielectric dispersion.

In view of these results, there are significant differences in the nature of the dielectric transition described in this work and those previously reported for another hybrid organic-inorganic compounds or coordination polymers with perovskite-like structures, such as the compounds with molecular formula [AmineH][M(HCOO)$_3$], (AmineH = midsized alkylammonium cations[12,14,16-20]), [(CH$_3$)$_2$NH$_2$]$_2$[KCo(CN)$_6$],[35] and [(CH$_3$)$_2$NH$_2$][Cd(N$_3$)$_3$].[36]

Hitherto, all described hybrid perovskites with dielectric properties contain polar cations inside the cubooctahedral cavities and/or H-bonds between the cations and the framework, and such dielectric transitions arise from order-disorder processes of the guest polar molecules.

Nevertheless, in the case of [TPrA][Mn(dca)$_3$] compound, where the guest TPrA cations are apolar and cannot form H-bonds, the dielectric transition has a completely different origin: it is related to a cooperative off-shift of the guest TPrA cations inside the cavities. Such mechanism reminds of that

shown by ceramic ferroelectrics with perovskite structure, such as $BaTiO_3$ even if in that materials the B-cation is the one experiencing the temperature dependent reversible displacement and gives rise to the electric order.

Therefore, and for the first time in a hybrid organic-inorganic compound with perovskite structure, we report a dielectric anomaly related to the appearance of long-range electric ordering induced by a displacive mechanism affecting the organic A-cations.

Even more, such dielectric transition involves a second outstanding process: the order-disorder of the polar dca ligands that connect the metal atoms in the framework. This is another very interesting finding because as these bridges are also involved in the magnetic interaction between the metal cations, they can provide a novel mechanism to couple the magnetic and dielectric properties.

2.3.2. Influence of external pressure on the structural and dielectric transition.

Since the transition found in [TPrA][Mn(dca)$_3$] is of first-order, its pressure dependence is represented by the Clausius-Clapeyron equation:

$$\frac{\partial T_t}{\partial P} = \frac{T_t(\Delta V/V)}{\Delta H_{molar}} V_{molar} \quad (2-1)$$

where T_t is the transition temperature, $\Delta V/V$ is the relative volume change at T_t, V_{molar} is the molar unit cell volume, and ΔH_{molar} represents the change in the molar enthalpy.

$\Delta V/V$ at the transition was taken from synchrotron powder X-ray diffraction results ($\Delta V/V \approx 1.25 \times 10^{-2}$) and ΔH_{molar} from the DSC data (6077 J mol^{-1}). V_{molar} (3.54 × 10^{-4} m^3 mol^{-1}) was calculated for *polymorph II* from the synchrotron powder X-ray data at 330 K ($V_{molar} = N_A V_{cell}/Z$, where N_A is the Avogadro number, V_{cell} is the unit cell volume, and Z is the number of structural units per unit cell).

From the obtained data the following pressure dependence of T_t was calculated: $\delta T_t/\delta P$ = (24.0 ± 0.1) K kbar^{-1}.

This strong pressure-response renders this compound an interesting pressure/temperature multisensitive material.

The obtained value is considerably large: it is 1 order of magnitude higher than that displayed by the perovskite-like formate $[(CH_3)_2NH_2][Mn(HCOO)_3]$[31] or 2 orders of magnitude higher than in the perovskite compounds $(NH_4)MF_3$ (M^{2+} = Mn^{2+}, Co^{2+}, Cd^{2+}, Mg^{2+} and Zn^{2+}),[37] which experience order-disorder phase transitions because of ordering of the guest cations below $T_t \approx 34$ K. Thus, these data reflect the more flexible nature of the dicyanamide perovskite as compared to formates or fluorides.

In what follows, we will focus on the experimental studies that we have carried out to check the sensitivity of its response under small external pressures ($P_{ext} \leq 2000$ bar).

Figure 2-11 shows the differential scanning calorimetry curves obtained when the sample was subjected to a small range of external pressure (from ambient pressure to 69 bar). As it can be seen, both the original endothermic and exothermic peaks experience a progressive and evident displacement toward higher temperatures under pressure, with an experimental mean increase value of $\delta T_t/\delta P$ = 25.7 K kbar^{-1}. Meanwhile, the enthalpy (ΔH) and entropy (ΔS) change remain constant in the whole studied pressure range.

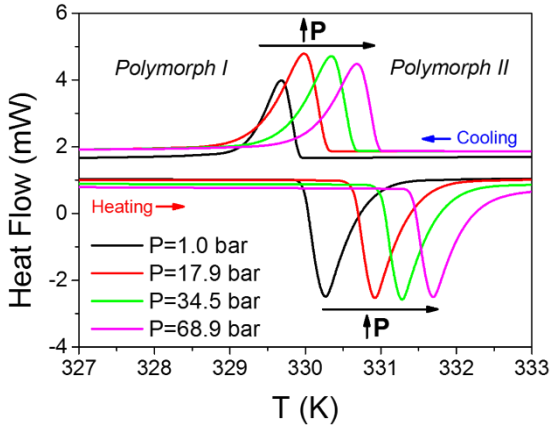

Figure 2-11. Pressure differential scanning calorimetry curves for [TPrA][Mn(dca)$_3$] obtained under different pressures (from 1 to 68.9 bar) with a flux of 20 ml min^{-1} of nitrogen gas, on heating (down curve) and cooling (up curve) the sample at a rate of 2 K min^{-1}.

We have also studied the behaviour of the axial dilatometry of this sample under applied external pressure, see Figure 2-12. Two interesting results come out from these experiments: (a) the phase transition from *polymorph I* to *II* can be easily monitored by this technique as the sharp increase in the length gives rise to a kink in the curves; (b) again, such phase transition is seen to shift to higher temperatures as pressure increases from 200 to 1600 bar. The estimated value for the pressure dependence of the transition temperature seen by this technique is $\delta T_t/\delta P$ = 24.2 K kbar^{-1}, again in good agreement with the value obtained by the Clausius-Clapeyron equation.

Finally, and for the first time in a hybrid organic-inorganic compound we have measured the dielectric permittivity of this compound as a function of temperature under applied external pressure (from 80 to 2000 bar).

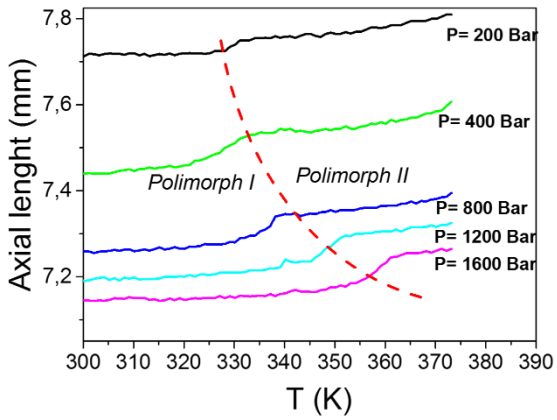

Figure 2-12. Pressure-volume-temperature curves obtained under different axial pressures (from 200 to 1600 bar) and showing a small kink around the structural transition temperature, which shifts to higher temperatures under increasing pressure (dash line).

As it can be seen in Figure 2-13, under increasing applied pressures, the dielectric anomaly observed at ambient pressure, measured at 10^5 Hz, remains present and it just gets displaced toward higher temperatures. We observed that the dielectric transition is reversible under heating and cooling cycle, see Figure 2-14. In addition, the calculated $\delta T_t/\delta P$ = 23.4 K kbar^{-1} value is very close to that obtained by the other techniques and very similar to the estimated by the Clausius-Clapeyron equation. This value is five times higher than in the case of the well-known AFE-paraelectric transition of $PbZrO_3$ perovskite ($\delta T_t/\delta P$ = 4.5 K kbar^{-1}).[38]

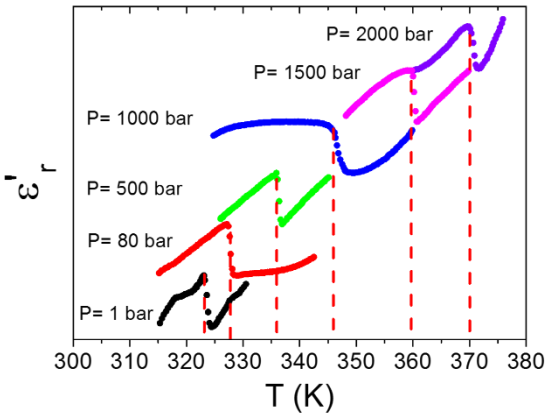

Figure 2-13. Temperature dependence of the dielectric constant (ε'_r) measured at 10^5 Hz under hydrostatic pressure conditions, from 1 to 2000 bar, where the curves have been normalized and conveniently displaced, for a better view.

These results prove that this compound displays a very large sensitivity toward applied external pressure, even for small pressure values, with the transition temperature (T_t) markedly increasing upon application of that external stimulus.

Such influence of pressure can be rationalized as follows: the application of pressure compresses the crystal structure cavities. This in turn constraints the degree of freedom of the ions (TPrA cations and dca ligands) and favors a more ordered structure. As a result, *polymorph I* (with smaller volume and more ordered) is stabilized up to higher temperatures at the expense of *polymorph II* (larger volume and more disordered) so that the temperature for the structural and associated dielectric transition achieves higher values.

Finally, the much larger pressure dependence of this hybrid organic-inorganic compound, as compared to oxides and even with another hybrid perovskites,[22] is reflecting the "softer" nature of this dicyanamide compound.

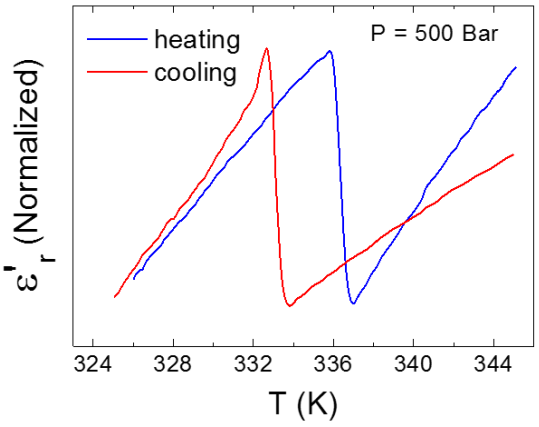

Figure 2-14. ε'_r vs T curves measured at 10^5 Hz on cooling and heating under an external pressure of 500 bar.

2.4. Conclusions

A multistimuli response is found in the hybrid organic-inorganic [TPrA][Mn(dca)$_3$] material, related to its singular structure. This compound displays a perovskite-like structure with $\mu_{1,5}$-dca bridges connecting the octahedrally coordinated metal centers and the TPrA cations located inside the cavities of the resulting framework. Above room temperature, a sharp first-order structural transition ($T_t \approx 330$ K) transforms the room temperature non-centrosymmetric *polymorph I* ($P\bar{4}2_1c$) into the novel high temperature centrosymmetric *polymorph II* (*I4/mcm*). The phase transition implies an off-center displacement of the nonpolar guest TPrA cations, order-disorder processes of the polar dca ligands and the TPrA cation propyl groups, and a change in the [MnN_6] octahedral tilting. As a consequence

[TPrA][Mn(dca)$_3$] exhibits a dielectric anomaly, associated with the change from a cooperative to a non-cooperative electric behaviour. The former implies an AFE distribution of electric dipoles in *polymorph I*, related to the described off-shift of the apolar TPrA cations and the order-disorder of the polar dca ligands mechanisms that are different from those reported, up to now, for others perovskite-like hybrid compounds. Meanwhile, the paraelectric phase (*polymorph II*) shows dielectric dispersion because of the disorder of the dca ligands, which would be acting as polar rotators.

Even more, as it is known that the dca ligands are also involved in the magnetic coupling between the metal cations, they could provide an additional novel mechanism for a direct magnetoelectric coupling at the much higher temperature of 330 K, converting this material into the singular case among hybrid organic-inorganic compounds, of a type-II multiferroic.

Additionally, the reported structural transition also leads to a large and anisotropic thermal expansion (remarkably along the *c*-axis). It is noteworthy that examples of colossal thermal expansion remain extremely rare, even among MOFs. Herein, this is an exceptional material, where the *polymorph I* exhibits a strong thermal response, specially along *c*, for temperatures close to T_t, where it displays colossal thermal expansion values, up to $\alpha > 100 \times 10^{-6}$ K^{-1}.

Finally, we have also studied the influence of external pressure in this strongly thermal responsive material. The obtained results indicate that the [TPrA][Mn(dca)$_3$] compound is very sensitive to this external stimuli, which induces a large shift of T_t toward higher temperatures, $\delta T_t/\delta P$ = 24.2 K kbar^{-1}, value that is much higher than in the well-known AFE perovskite material, $PbZrO_3$. This behaviour is associated with the larger flexibility of this hybrid-perovskite, where the application of even small pressures stabilizes the denser and more ordered *polymorph I* at the expense of *polymorph II*.

In summary, the here reported results show not only a promising multiferroic behaviour in the [TPrA][Mn(dca)$_3$] hybrid-perovskite, but also an unusual large response under pressure and temperature. These findings turn this compound into a very interesting multisensitive material, which could be of interest for technological applications, such as highly sensitive temperature and pressure sensors.

2.5. Notes

The work presented in this chapter has been published in the following article:

Bermúdez-García, J. M.; Sánchez-Andújar, M.; Yáñez-Vilar, S.; Castro-García, S.; Artiaga, R.; López-Beceiro, J.; Botana, L.; Alegría, A.; Señarís-Rodríguez, M. A. *Inorg. Chem.*, 2015, **54**, 11680-11687.

2.6. References

1 Fiebig, M. *J. Phys. D: Appl. Phys.* 2005, **38**, R123-152.
2 Scott, J. F. *Nat. Mater.* 2007, **6**, 256-275.
3 Chu, Y.-H.; Martin, L. W.; Holcomb, M. B.; Gajek, M.; Han, S.-J.; He, Q.; Balke, N.; Yang, C.-H.; Lee, D.; Hu, W.; Zhan, Q.; Yang, P.-L.; Fraile-Rodriguez, A.; Scholl, A.; Wang, S. X.; Ramesh, R. *Nat. Mater.* 2008, **7**, 478-482.
4 Goodenough, J. B. *Magnetism and the Chemical Bond*; Wiley and Sons: New York, 1963.
5 Hill, N. A. *J. Phys. Chem. B* 2000, **104**, 6694-6709.
6 Sawada, S.; Nomura, S.; Fujii, S.; Yoshida, I. *Phys. Rev. Lett.* 1958, **1**, 320.
7 Jain, P.; Dalal, N. S.; Toby, B. H.; Kroto, H. W.; Cheetham, A. K. *J. Am. Chem. Soc.* 2008, **130**, 10450-10451.
8 Lines, M. E.; Glass, A. M. *Principles & applications of Ferroelectric & Related Materials*; Oxford Unviersity Press: New York, 2001.
9 Khomskii, D. *Physics* 2009, **2**, 20-27.
10 Cheong, S.-W.; Mostovoy, M. *Nat. Mater.* 2007, **6**, 13-20.
11 (a) Cheetham, A. K.; Rao, C. N. R. *Science* 2007, **318**, 58-59. (b) Zhang, W.; Xiong, R. G. *Chem. Rev.* 2012, **112**, 1163-1195.
12 Jain, P.; Ramachandran, V.; Clark, R. J.; Zhou, H. D.; Toby, B. H.; Dalal, N. S.; Kroto, H. W.; Cheetham, A. K. *J. Am. Chem. Soc.* 2009, **131**, 13625-13627.
13 (a) Cui, H.; Wang, Z.; Takahashi, K.; Okano, Y.; Kobayashi, H.; Kobayashi, A. *J. Am. Chem. Soc.* 2006, **128**, 15074-15075. (b) Xu, G. C.; Zhang, W.; Ma, X. M.; Chen, Y. H.; Zhang, L.; Cai, H. L.; Wang, Z. M.; Xiong, R. X.; Gao, S. *J. Am. Chem. Soc.* 2011, **133**, 14948-14951. (c) Zhou, B.; Imai, Y.; Kobayashi, A.; Wang, Z.; Kobayashi, H. *Angew. Chem., Int. Ed.* 2011, **50**, 11441-11445.
14 Stroppa, A.; Jain, P.; Barone, P.; Marsman, M.; Perez-Mato, J. M.; Cheetham, A. K.; Kroto, H. W.; Picozzi, S. *Angew. Chem., Int. Ed.* 2011, **50**, 5847-5850.
15 Wang, Z.; Zhang, B.; Otsuka, T.; Inoue, K.; Kobayashi, H.; Kurmoo, M. *Dalt. Trans.* 2004, 2209-2216.
16 Chen, S.; Shang, R.; Hu, K.-L.; Wang, Z.-M.; Gao, S. *Inorg. Chem. Front.* 2014, **1**, 83-98.
17 Hu, K.-L.; Kurmoo, M.; Wang, Z.; Gao, S. *Chem. - Eur. J.* 2009, **15**, 12050-12064.
18 Mączka, M.; Ciupa, A.; Gągor, A.; Sieradzki, A.; Pikul, A.; Macalik, B.; Drozd, M. *Inorg. Chem.* 2014, **53**, 5260-5268.
19 Shang, R.; Xu, G.-C.; Wang, Z.-M.; Gao, S. *Chem. - Eur. J.* 2014, **20**, 1146-1158.
20 Pato-Doldán, B.; Gómez-Aguirre, L. C.; Bermúdez-García, J. M.; Sánchez-Andújar, M.; Fondado, A.; Mira, J.; Castro-García, S.; Señarís-Rodríguez, M. A. *RSC Adv.* 2013, **3**, 22404-22411.
21 Wang, X. Y.; Gan, L.; Zhang, S. W.; Gao, S. *Inorg. Chem.* 2004, **43**, 4615-4625.
22 (a) Sánchez-Andújar, M.; Presedo, S.; Yáñez-Vilar, S.; Castro-García, S.; Shamir, J.; Señarís-Rodríguez, M. A. *Inorg. Chem.* 2010, **49**, 1510-1516. (b) Pato-Doldán, B.; Sánchez-Andújar, M.; Gómez-Aguirre, L. C.; Yáñez-Vilar, S.; López-Beceiro, J.; Gracia-Fernández, C.; Haghighirad, A. A.; Ritter, F.; Castro-García, S.; Señarís-Rodríguez, M. A. *Phys. Chem. Chem. Phys.* 2012, **14**, 8498-8501.
23 (a) Schlueter, J. A.; Manson, J. L.; Geiser, U. *Inorg. Chem.* 2005, **44**, 3194-3202. (b) Manson, J. L. *Cooperative Magnetic Behavior in Metal-Dicyanamide Complexes*; Wiley-VCH Verlag GmbH & Co: Weinheim, Germany, 2005, 71-104. (c) Batten, S. R.; Murray, K. S. *Coord. Chem. Rev.* 2003, **246**, 103-130.

24 Coudert, F.-X. *Chem. Mater.* 2015, **27**, 1905-1916.
25 Sheldrick, G. M. *Acta Crystallogr., Sect. A: Found. Crystallogr.* 2008, **64**, 112-122.
26 Farrugia, L. J. *J. Appl. Crystallogr.* 2012, **45**, 849-854.
27 Mercury 3.5.1 (Build RC5) - Crystal Structure Visualisation (CCDC). http://www.ccdc.cam.ac.uk/mercury.
28 Larson, A. C.; Von Dreele, R. B. General Structure Analysis System (GSAS), Los Alamos National Laboratory Report LAUR 2000; Los Alamos National Laboratory, 2000; pp 86-748.
29 Toby, B. H. *J. Appl. Crystallogr.* 2001, **34**, 210-213.
30 (a) Dudley, J. D.; Hall, H. T. *Phys. Rev.* 1960, **118**, 1211-1216. (b) Höhne, G. W. H.; Dollhopf, W.; Blankenhorn, K.; Mayr, P. U. *Thermochim. Acta* 1996, **273**, 17-24.
31 Sánchez-Andújar, M.; Gómez-Aguirre, L. C.; Pato Doldán, B.; Yáñez-Vilar, S.; Artiaga, R.; Llamas-Saiz, A. L.; Manna, R. S.; Schnelle, F.; Lang, M.; Ritter, F.; Haghighirad, A. A.; Señarís-Rodríguez, M. A. *CrystEngComm* 2014, **16**, 3558.
32 Glazer, A. M. *Acta Crystallogr., Sect. B: Struct. Crystallogr. Cryst. Chem.* 1972, **28**, 3384-92.
33 Goodwin, A. L.; Calleja, M.; Conterio, M. J.; Dove, M. T.; Evans, J. S. O.; Keen, D. A.; Peters, L.; Tucker, M. G. *Science* 2008, **319**, 794-797.
34 Bouëssel du Bourg, L.; Ortiz, A. U.; Boutin, A.; Coudert, F.-X. *APL Mater.* 2014, **2**, 124110.
35 Zhang, W.; Cai, Y.; Xiong, R.-G.; Yoshikawa, H.; Awaga, K. *Angew. Chem., Int. Ed.* 2010, **49**, 6608-6610.
36 Du, Z.-Y.; Xu, T.-T.; Huang, B.; Su, Y.-J.; Xue, W.; He, C.-T.; Zhang, W.-X.; Chen, X.-M. *Angew. Chem.* 2015, **127**, 928-932.
37 Alexandrov, K. S.; Bartolome, J.; Gorev, M. V.; Flerov, I. N. *Phys. Status Solidi B* 2000, **217**, 785-791.
38 Samara, G. A. *Phys. Rev. B* 1970, **1**, 3777-3789.

Chapter 3:

Multiple phase and dielectric transitions on a novel multisensitive $[TPrA][M(dca)_3]$ ($M = Fe^{2+}$, Co^{2+} and Ni^{2+}) hybrid organic-inorganic perovskite family

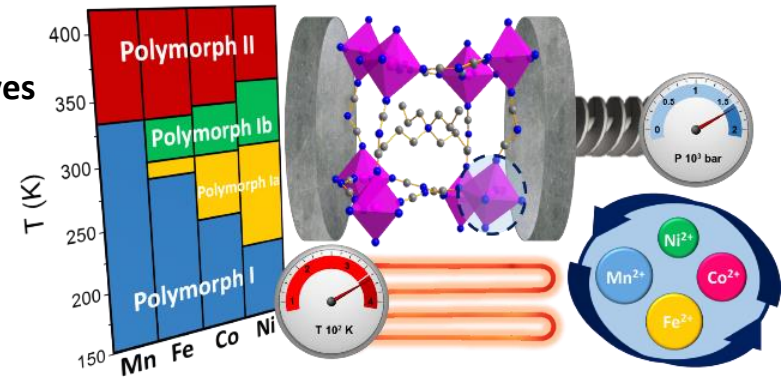

[TPrA][M(dca)$_3$] (M = Fe^{2+}, Co^{2+} and Ni^{2+})

Multiple phase and dielectric transitions on a novel multisensitive [TPrA][M(dca)$_3$] (M = Fe^{2+}, Co^{2+} and Ni^{2+}) hybrid organic-inorganic perovskite family

Abstract: This chapter is devoted to the hybrid organic-inorganic [TPrA][M(dca)$_3$] (M = Fe^{2+}, Co^{2+} and Ni^{2+}) compounds, where TPrA is the tetrapropylammonium cation and dca is the dicyanamide anion. As we will show, these compounds are unique multisensitive compounds, which display multiple phases and dielectric transitions. These materials exhibit up to three first-order structural transitions (between the *polymorphs I*, *Ia*, *Ib* and *II*) associated with the same number of dielectric transitions in the temperature range of 210-360 K. The mechanisms responsible for these dielectric responses are found to be novel within the hybrid perovskites, involving ionic displacements of the A-site cations (TPrA) and order-disorder processes of the X anions (dca). In addition, the phase transitions and dielectric transition temperatures can be tuned by applying external hydrostatic pressure or by inducing internal pressure by modifying the tolerance factor through ionic substitution in the B-sites. This multisensitive response towards temperature, external and internal pressure opens up promising technological applications for this family of materials, such as dielectric transductors or multistimuli sensors, whose response can be modulated in a wide range of temperatures and pressures.

3.1. Introduction and objectives

Perovskites and the phase transitions they can experience as a function of temperature, pressure, etc., have been at the center of a vast amount of research in Solid State and Materials Science over the last decades[1] in view of their huge scientific and technological interest. In that context, early studies on conventional inorganic perovskites, ABX_3 (A: lanthanides, alkaline-earth metals or similar cations, B: transition metal cations and X: oxide, sulphide or halide anions, etc.), specially mixed oxides, highlighted the exceptional functional and even multifunctional properties. This is the case, among others, of the very well-known and widely used ferroelectric $BaTiO_3$, the piezoelectric $Pb(Zr_{1-x}Ti_x)O_3$ (PZTs),[2] the high temperature superconductor $YBa_2Cu_3O_{7-\delta}$,[3] the colossal magnetoresistive $La_{1-x}Ca_xMnO_3$,[4] the mixed ionic-electronic conductors $La_{1-x}Sr_xCoO_{3-\delta}$,[1a] or more recently the multiferroic $BiFeO_3$.[5]

Interestingly, in the last few years, significant efforts have been devoted to the development of new members of the versatile family of the so-called perovskite-like hybrid organic-inorganic materials,[6] where the A- and/or X-site inorganic moieties of the conventional perovskites have been replaced by organic building blocks. Some of these materials, despite their recentness, have already revealed very remarkable functional properties. This is the case of the $(MA)PbI_3$ (MA = methylammonium cation),[7] which has revealed unprecedented photoconductivity; or the noteworthy [AmineH][M(X)$_3$] families (AmineH = midsized protonated amines in the A-site position of the perovskite, M = different divalent transition metal cations in the B-site, X = different bidentate-bridge ligands in the X-site position, such as N_3^-, CN^- or $HCOO^-$), which exhibit cooperative magnetic, electric or elastic order, even multiferroicity, associated in many cases to very interesting thermally-induced phase transitions.[8-17] Very remarkably magnetoelectric coupling has been recently reported experimentally in the paramagnetic state of $[(CH_3)_2NH_2][Fe(HCOO)_3]$,[16] and ferroelectricity induced by magnetic order has been demonstrated in $[CH_3NH_3][Co(HCOO)_3]$,[17] opening the large, flexible, multifunctional and designable family of hybrid perovskites to magnetically-induced multiferroic behaviour.

Another related, but so far much less explored, family of potentially interesting compounds is that of metal-dicyanamides with the formula [AmineH][M(dca)$_3$] and has perovskite-like structure. In these compounds, the dicyanamide anions, $[N(CN)_2]^-$ (dca), bridge the transition metal cations (up to now, M = Mn^{2+} (ref. 18 and 19) and Ni^{2+} (ref. 18)) in a $\mu_{1,5}$-dca end-to-end mode, forming a 3D framework. Meanwhile, the protonated amines (so far tetrapropylammonium, $[(CH_3CH_2CH_2)_4N]^+$ or TPrA) are located in the resulting pseudo-cubooctahedral cavities.[18]

In our previous work,[19] we have revisited the Mn compound [TPrA][M(dca)$_3$], finding a structural transition at 330 K, and studied the influence of external pressure on the structural and dielectric properties of this compound. Interestingly enough, we found that this material is a new type-I multiferroic, which is very sensitive to temperature and external pressure.

In the present work, we enlarge the family of [TPrA][M(dca)$_3$] perovskites with two new members (M = Fe^{2+} and Co^{2+}) that we describe for the first time; and we shed light on the unexplored structural features of the Ni compound, for which two structural transitions had been previously reported at 160 K and 210 K,[18] and we present two new additional polymorphs.

We also explore the dielectric properties of these materials, and present a systematic and careful study of the effect of external and internal pressure on the structural transitions and dielectric responses of these three [TPrA][M(dca)$_3$] (M = Fe^{2+}, Co^{2+} and Ni^{2+}) compounds.

Very interestingly, and as we will show below, we have found that these Fe, Co and Ni compounds display multiple phase transitions responsible for multiple dielectric transitions that are both very sensitive to temperature as well as to external and internal pressure.

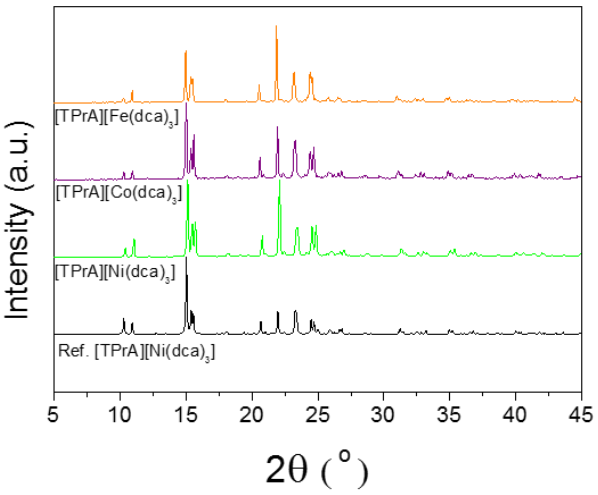

Figure 3-1. Room temperature PXRD patterns for the obtained [TPrA][M(dca)$_3$] (M = Fe^{2+}, Co^{2+} and Ni^{2+}) compounds and the simulated pattern based on the single-crystal structures at room temperature.

3.2. Experimental

3.2.1. Synthesis

[TPrA][M(dca)$_3$] (M = Fe^{2+}, Co^{2+} and Ni^{2+}) materials were prepared from commercially available $FeCl_2{\cdot}4H_2O$ (98%, Sigma-Aldrich), $Co(NO_3)_2{\cdot}6H_2O$ (98%, Sigma-Aldrich), $Ni(NO_3)_2{\cdot}6H_2O$ (≥98.5 %, Sigma-Aldrich), (TPrA)Br (98%, Aldrich), Na(dca) (96%, Aldrich) and absolute ethanol (Panreac), which were used as purchased without further purification. A reagent amount of deionised water was also used in the synthesis.

The synthetic route used here is an adaptation of the previously reported method for the preparation of the [TPrA][M(dca)$_3$] compounds (M = Mn^{2+} and Ni^{2+}),[18] where synthesis of the metal dicyanamide frameworks were templated by alkylammonium cations and accomplished through a mild solution chemistry method at room temperature.

In a typical experiment, 10 ml of an aqueous solution containing 2 mmol of $FeCl_2{\cdot}4H_2O$ or $M(NO_3)_2.6H_2O$ (M = Co^{2+} and Ni^{2+}), was placed at the bottom of a glass tube. This solution was layered by a mixture of a solution of (TPrA)Br (2 mmol) in 10 ml of ethanol and a solution of Na(dca) (6 mmol) in 10 ml of water.

Single crystals of the three compounds (cubic colourless for M = Fe^{2+}, cubic pink for M = Co^{2+}, and cubic green for M = Ni^{2+}) were obtained after one week and they were collected by filtration and washed several times with ethanol.

The compounds were obtained as single phase materials and their purity was confirmed by comparison of their experimental powder X-ray diffraction (PXRD) patterns at room temperature with those simulated from the single-crystal X-ray diffraction (SCXRD) data, see Figure 3-1.

3.2.2. Single-crystal X-ray diffraction

Single-crystal data sets were collected in a Bruker-Nonius x8 ApexII X-ray diffractometer equipped with a CCD detector and using monochromatic MoKα1 radiation (λ = 0.71073 Å) at different temperatures: 368 K, 323 K, 300 K (293 K in the case of the Fe compound), 200 K (180 K for the Ni compound) and 100 K. Suitable crystals of each sample were chosen and mounted on a glass fiber using instant glue. For the 100 K and 200 K (or 180 K) sets, the crystal temperature was maintained using a cold stream of nitrogen from a Kyroflex cryostream cooler. Data integration and reduction was performed using the Apex2 V.1.0 27 (Bruker-Nonius, 2005) suite software. The intensity collected was corrected for Lorentz and polarization effects, and for absorption by semi-empirical methods on the basis of symmetry-equivalent data, using SADABS (2004) from the suite software. The structures were solved by the direct method using the SHELXS-97 program[20] and were refined by the full-matrix least-squares method on the SHELXL-97 program,[20] both programs are available within the WinGX package.[21] To solve the structures, anisotropic thermal factors were employed for the non-H atoms and non-disordered atoms. In the case of ordered TPrA cations, the hydrogen atoms of the propyl groups were added to the ideal positions and isotropic thermal factors were refined.

3.2.3. Powder X-ray diffraction

A Siemens D-5000 diffractometer using CuKα radiation (λ = 1.5418 Å) was used to study these compounds by powder X-ray diffraction (PXRD) at room

temperature. The XRPD pattern was compared with the profile obtained from the single-crystal structure that was generated using Mercury 3.5.1 software.[22]

3.2.4. Differential scanning calorimetry (DSC)

Differential scanning calorimetry (DSC) studies were carried out in a TA Instruments MDSC Q2000 equipped with a liquid nitrogen cooling system. The samples (each with a mass around 5 mg) were heated and cooled with a rate of 20 K min^{-1} (2 K min^{-1} in the case of the Ni compound), from 135 to 375 K under a nitrogen atmosphere.

Additionally, pressure differential scanning calorimetry (PDSC) tests were performed in a TA Instruments pressure cell mounted on a Q2000 modulated DSC. The cell was calibrated for temperature and heat with indium at each of the pressures to be used in the measuring tests. The effect of pressure on the melting temperature and enthalpy of indium was taken into account.[23] In a typical experiment, about 5 mg of each sample was confined inside a pinhole aluminium capsule. The experiments were performed in N_2 atmosphere at a constant pressure (from 1 to 69 bar) while keeping a constant flow of 50 ml min^{-1} of N_2. The samples under a constant external pressure were heated and cooled at a rate of 2 K min^{-1} from room temperature to 343 K.

3.2.5. Pressure-Volume-Temperature (PVT) Analysis

To study the dilatometry of the materials at different pressures, PVT 100 SWO/ThermoHaake equipment was used. In a typical experiment, about 440 mg of powder material was loaded inside a cylinder between two pistons that transmit an axial compressive force from 200 to 1600 bar to the samples. After applying the external pressure, the samples were heated at a rate of 5 K min^{-1} from 183 K to 373 K and the axial thermal expansion of the samples was registered.

3.2.6. Dielectric measurements

The complex dielectric permittivity ($\varepsilon_r = \varepsilon'_r - i\,\varepsilon''_r$) of the cold-press pelletized samples were measured as a function of frequency and temperature with a parallel-plate capacitor coupled to a Solartron 1260A Impedance/Gain-Phase Analyzer, capable of measuring in the frequency range from 10 μHz up to 32 MHz using an amplitude of 2 V. The capacitor was mounted in a Janis SV*T*200T cryostat refrigerated with liquid nitrogen, and with a Lakeshore 332 incorporated to control the temperature from 78 to 400 K. Data were collected upon heating.

Pelletized samples, made from cold-press nonoriented single crystals with an area of approximately 133 mm^2 and a thickness of approximately 1.3 mm, were prepared to fit into the capacitor, and gold was sputtered on their surfaces to ensure a good electrical contact with the electrodes.

All the dielectric measurements were carried out in a nitrogen atmosphere where several cycles of vacuum and nitrogen gas were performed to ensure that the sample environment was free of water.

Additionally, dielectric measurements were carried out in a pressure cell supplied by Novocontrol GmbH. The cell, basically a stainless steel cylinder with a hermetic seal, was filled with a silicone fluid that transmits an isostatic pressure from the piston to the sample. The dielectric response was measured for 10^3-10^6 Hz frequencies. The measurements were performed as a function of temperature (310-380 K) for constant pressures up to 2000 bar.

3.3. Results and discussion

3.3.1. Studies at ambient pressure

3.3.1.1. DSC results. As shown in Figure 3-2, the DSC curves of the three compounds show three pairs of endothermic/exothermic peaks in the heating/cooling runs, revealing that each of them undergoes three reversible phase transitions in the temperature interval 135-375 K. The temperatures for such transitions are summarized in Table 3-1.

The observed thermal hysteresis indicates the first order character of such transitions, whose associated enthalpy and entropy changes are indicated in Table 3-2.

Taking into account that for an order-disorder transition $\Delta S = R\,ln(N)$, where R is the gas constant and N is the ratio of the number of configurations in the disordered and ordered system, a value of N ≈ 1.2 – 2.6 is

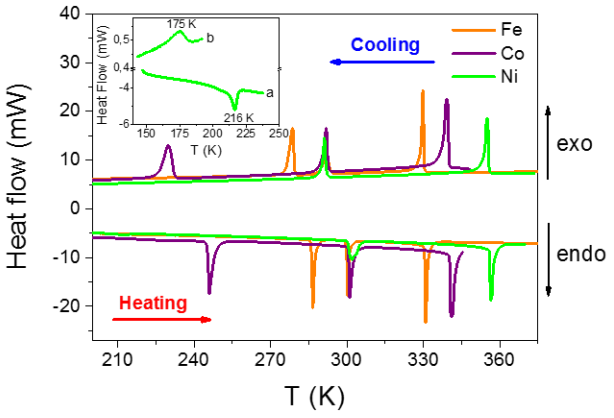

Figure 3-2. DSC results as a function of temperature obtained by heating and cooling the samples (TPrA)[M(dca)$_3$] (M = Fe^{2+}, Co^{2+} and Ni^{2+}) at a rate of 20 K min^{-1}. Inset: Detail of the DSC curve for the Ni compound around *T1* (a) on heating at a rate of 20 K min^{-1}, and (b) on cooling at a rate of 2 K min^{-1}.

Table 3-1. Summary of structural transition temperatures for Fe, Co and Ni compounds obtained by DSC analysis on heating and cooling.

	Heating			Cooling		
	T1	T2	T3	T1	T2	T3
Fe	286 K	300 K	331 K	279 K	292 K	330 K
Co	246 K	301 K	341 K	230 K	292 K	339 K
Ni	216 K	302 K	356 K	175 K	291 K	355 K

Table 3-2. Enthalpy and entropy obtained for the different structural transitions by DSC on heating and cooling for the Fe, Co and Ni compounds.

		ΔH (heating) J mol^{-1}	ΔH (cooling) J mol^{-1}	ΔS (heating) J K mol^{-1}	ΔS (cooling) J K mol^{-1}	N (average)
Fe	T1	2096	2307	7.3	8.3	2.6
	T2	1266	1253	4.2	4.3	1.7
	T3	2343	2673	7.1	8.1	2.5
Co	T1	1786	1940	7.3	8.4	2.6
	T2	1341	1356	4.5	4.6	1.7
	T3	2116	2580	6.2	7.6	2.3
Ni	T1	362	387	1.7	2.2	1.2
	T2	1182	1203	3.9	4.1	1.6
	T3	2005	2140	5.6	6.0	2.0

calculated for each transition, depending also on the given compound (see Table 3-2). Such values are much lower, than in the case of the analogue Mn compound, [TPrA][Mn(dca)$_3$], which exhibits a single phase transition with N ≈ 8.[19]

In the case of the Ni compound, we have to note that we identified by DSC the previously reported high temperature structural transition at ~210 K.[18] Nevertheless, we were not able to also find the reported lower temperature structural transition (~160 K), not even when measuring at the slow temperature rate of 2 K min^{-1}. As we will show below,[18] this result is in agreement with our single-crystal X-ray diffraction analysis, which also does not show the previously reported re-entrant structural transition at 160 K for this compound. We attribute this lack of transition to kinetic factors.

3.3.1.2. Crystal structures and structural transitions as a function of temperature. In order to understand the origin of these phase transitions, the crystal structures of the Fe, Co and Ni compounds were investigated at different temperatures.

According to SCXRD these compounds display four polymorphs (hereafter named as *I*, *Ia*, *Ib* and *II*) from 100 K to 368 K, all based on perovskite-like structures.

In the following paragraphs, we will comparatively describe the obtained structures, paying special attention to the novel polymorphs (the four, in the case of the Fe and Co compounds, two in the case of the Ni compound), and focussing on details that are relevant to understand the properties.

The crystallographic data for the four polymorphs of each of the three compounds are compiled in Tables AI-4 to AI-6 of Annexe I, and a summary of selected bond lengths and angles is provided in the Tables AI-7 to AI-10 of Annexe I.

Polymorph I. Below 286 K (M = Fe^{2+}), 246 K (M = Co^{2+}) and 216 K (M = Ni^{2+}) the structure of these compounds is tetragonal, space group $P\bar{4}2_1c$ (non-centrosymmetric), and it can be described as a $2a \times 2a \times 2a$ perovskite superstructure.

The asymmetric unit is defined by one independent metal cation, three dca anions and three TPrA cations. The metal cations are in a distorted [MN$_6$] octahedral environment with six different M-N distances, see Table AI-7 of Annexe I. The resulting [MN$_6$] octahedra are rotated cooperatively along the main crystallographic axes (tilt systems $a^-b^+c^-$ at Glazer notation).[24] The TPrA cations are located inside the cavities of the resulting framework.

As it also occurs in the other polymorphs, and as it could be expected, as the size of the M (perovskite B-site cation) decreases from Fe^{2+} to Ni^{2+}, the unit cell volume and the M-N bond lengths were observed to decrease. In addition, the octahedra tilting in the *ab*-plane decreases.

As seen in Figure 3-3, the structures exhibit a certain disorder in the dca anions (in the N-amide atoms along the *c*-axis) and in the C atoms of the TPrA cations, as it was previously described for the Ni and Mn compounds.[18,19] In addition, we remark a most interesting new feature: half of the TPrA cations inside the pseudo-cubooctahedral cavities (those located on a 2-fold axis) show a cooperatively off-center shift along the *c*-axis, following an antiferrodistortive up-down-up-down pattern, see Figure 3-4.

Such displacement, that increases as the size of the M (B-site cation) decreases, is 0.095(9) Å (M = Fe^{2+}), 0.069(0) Å (M = Co^{2+}) and 0.038(2) Å (M = Ni^{2+}).

The characteristics of this low temperature polymorph are similar to those recently reported for *polymorph I* of the Mn analogue[19] where the TPrA shift along the *c*-axis is even larger (0.105(3) Å). In the case of the Ni compound, for which this *polymorph I* has already been described before,[18] a re-entrant phase transition from *polymorph I* to *polymorph Ia* (described below) at 160 K is also reported.[18] Nevertheless, our SCXRD data (supported by our DSC analysis) do not reveal this structural transition. The *polymorph I* is maintained down-to 100 K. Therefore, we rationalize that the previously reported re-entrant structural transition could be related to kinetic factors that depend on the cooling rate and stabilization time.

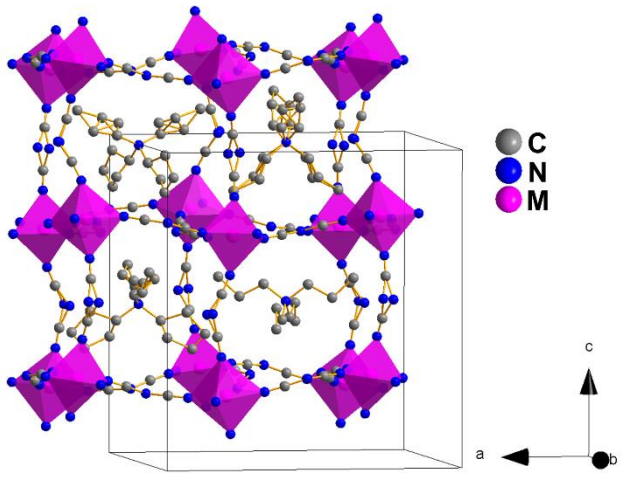

Figure 3-3. Conventional perovskite structure view and unit cell of *polymorph I*. The dca ligands act as $\mu_{1\text{-}5}$-bridges between the M cations. The N-amide atom of the dca ligans along the *c*-axis are modeled in two crystallographic positions. The TPrA cations are located inside the pseudo-cubooctahedral cavities, and two of the three present in the asymmetric unit display crystallographic disorder in the C atom positions. The H-atoms of the TPrA cations have been omitted to facilitate the visualization of the structure.

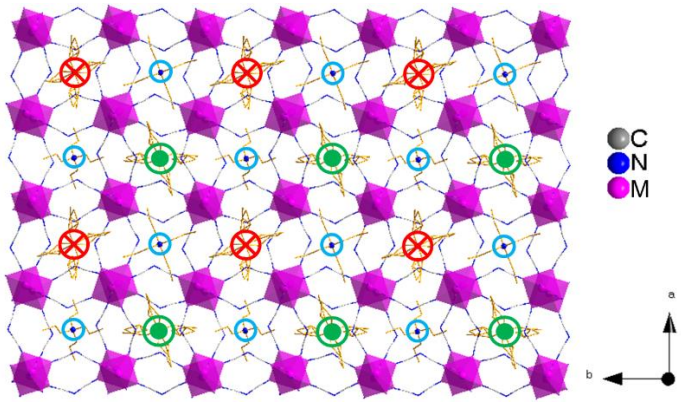

Figure 3-4. Cooperative displacement of the TPrA cations in the crystal structure of polymorph I. Half of the TPrA cations (represented by green circles and red crosses) show a cooperatively off-center shift along the *c*-axis, following an antiferrodistortive up-down-up-down pattern: The green circles indicates the off-center shift towards the up face of the pseudo-cubooctahedral cavity (out of the page) and the red crosses represent the off-center shift towards its down face (into the page). The blue small circles represent the half of the TPrA cations that remains centered in the middle of the pseudo-cubooctahedral cavities.

Polymorph Ia. At *T1* (see Table 3-1), the structure of *polymorph I* transforms into that of *polymorph Ia* of orthorhombic symmetry, space group *Pnna* (centrosymmetric) and a different $2a \times \sim 2\sqrt{2}a \times \sim 2\sqrt{2}a$ perovskite superlattice, , where $a_{pol.Ia} \approx c_{pol.I}$, and $b_{pol.Ia}$, $c_{pol.Ia} \approx \sqrt{2}a_{pol.\,I}$, see Tables AI-4 to AI-6 of Annexe I.

The asymmetric unit contains two independent metal cations, eight dca anions and four TPrA cations. As in *polymorph I*, each metal cation is in a distorted octahedral environment with six different M-N distances (see Table AI-8 of Annexe I) and the [MN_6] octahedra are cooperatively rotated following an $a^- b^+ c^-$ tilt system.

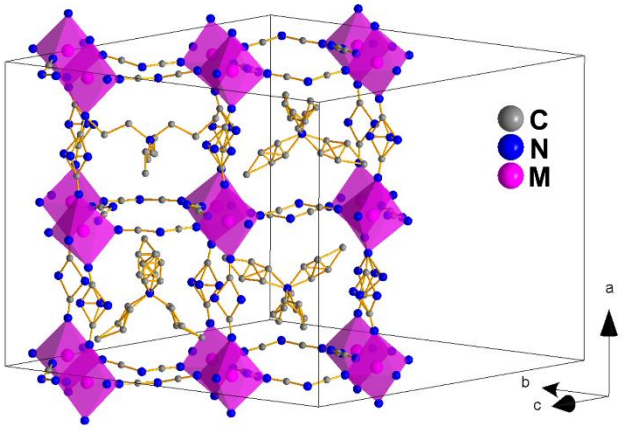

Figure 3-5. Perovskite structure view and unit cell of *polymorph Ia*. The N-amide atom of the dca ligans along the *c*-axis show more thermal disorder than in *polymorph I* and they are modeled in either two or three crystallographic positions. In addition, three of the four TPrA cations in the asymmetric unit show disorder in the C atoms. The H-atoms of the TPrA cations have been omitted to facilitate the visualization of the structure.

On the other hand, and as could be expected, this *polymorph Ia* shows a slightly larger disorder than *polymorph I* (Figure 3-5). The positions of the the N-amide of the dca ligands along the *a*-axis had to be modeled occupying two (or three positions depending on the dca ligand) with equal occupancies; also, three of the four TPrA cations in the asymmetric unit present disorder in the C atom positions of their propyl groups.

And most remarkably, all the TPrA cations are in off-center positions following a cooperative pattern different from that shown by *polymorph I*, see Figure 3-6: (a) half of them (those located on a 2-fold axis along the *a*-axis) show a cooperative off-center shift (about 0.23 Å, ~15 % larger than in *polymorph I* along such direction) along the *a*-axis towards one side of these cavities. These displaced TPrA cations are antiferrodistortively arranged along the *b*-axis, displaying an up-down-up-down pattern.

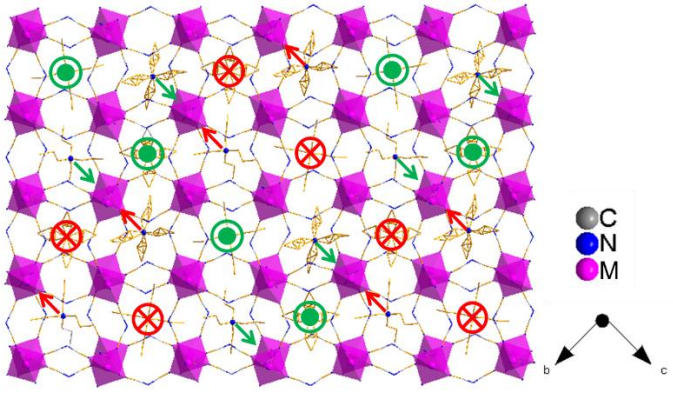

Figure 3-6. Cooperative displacement of the TPrA cations in the crystal structure of polymorph Ia. Half of the TPrA cations (represented by green circles and red crosses) show a cooperative off-center shift along the *a*-axis towards one side of these cavities. These displaced TPrA cations are antiferrodistortively arranged along the *b*-axis, displaying an up-down-up-down pattern: The green circles indicates the off-center shift towards the up face of the pseudo-cubooctahedral cavity (out of the page) and the red crosses represent the off-center shift towards its down face (into the page). The other half of the TPrA cations (represented by green and red arrows) show a cooperative off-center shift along the *c*-axis towards one edge of these cavities, following an antiferrodistortive pattern.

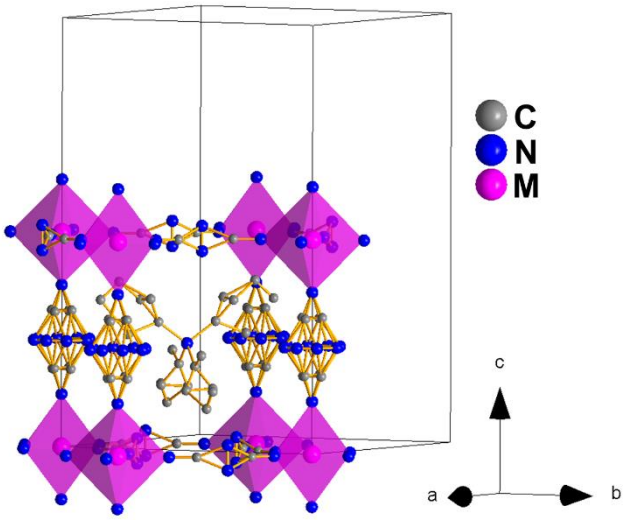

Figure 3-7. Crystal structure view and unit cell of *Polymorph Ib*. The N-amide and C atoms of the dca ligands along the *c*-axis are modeled in eight and four crystallographic positions, respectively. Moreover, the N-amide atom of the dca ligands in the *ab*-plane are modeled in two crystallographic positions. As for the TPrA cations, all of them display thermal disorder in the C atoms.

(b) The other half of the TPrA cations (those located on a 2-fold axis along the *c*-axis) show an even larger cooperative off-center shift (up to 0.62 Å) along the *c*-axis towards one edge of these cavities, following an antiferrodistortive pattern.

Polymorph Ib. At *T2*, the structure of these [TPrA][M(dca)$_3$], (M = Fe^{2+}, Co^{2+} and Ni^{2+}) compounds changes again: even if its symmetry remains orthorhombic, its space group changes to *Ibam* (centrosymmetric), and it has to be described on the basis of a different $\sim\sqrt{2}a \times \sim\sqrt{2}a \times 2a$ superlattice, see Tables AI-4 to AI-6 of Annexe I.

In this case, the asymmetric unit contains one independent metal cation, two dca anions and one TPrA cation. The transition metal cations are in a slightly distorted octahedral environment with three different M-N bond lengths, see Table AI-9 of Annexe I. And differently from *polymorph I* and *polymorph Ia*, here the [MN_6] octahedra are cooperatively rotated within the *ab*-plane and display an anticlockwise arrangement along the *c*-axis (tilt systems $a^0a^0c^-$ at Glazer notation).

Also, in this polymorph the dca ligands show a much larger disorder than in the case of *polymorph Ia*, especially along the *c*-axis, so that the N-amide atom and the C atom had to be modeled occupying 8 and 4 positions, respectively.

This increase suggests a dynamic disorder along such direction that would imply the rotation of the dca ligands around the *c*-axis, see Figure 3-7.

As for the TPrA cations, which are also more disordered than in *polymorph Ia*, the most important remark is that they are located at the center of the cavities (Figure 3-7). This is in contrast to the previous polymorphs. As indicated above, half (*polymorph I*) or all of them (*polymorph Ia*) are off-shifted.

Polymorph II. At *T3* (see Table 3-1) the structure of these compounds changes again and transforms into that of *polymorph II* with tetragonal symmetry and space group *I4/mcm* (centrosymmetric), even if the same perovskite superlattice as *polymorph Ib*, $\sim\sqrt{2}a \times \sim\sqrt{2}a \times 2a$. In fact, the space group of that lower temperature polymorph is a subgroup of *polymorph II*.

In that context, both *polymorphs Ib* and *II* are quite similar and their main differences rely on their symmetry and the even larger disorder of the dca ligands and TPrA cations in this higher temperature polymorph, see Figure 3-8. On the other hand, and as in *polymorph Ib*, the TPrA cations remain centered in the cavities.

Therefore, different from the previous transitions, this occurs only at *T3* and involves order-disorder phenomena with no ionic displacements.

This *polymorph II* of the Fe, Co and Ni compounds is similar to that recently reported for the Mn compound above 330 K.[19]

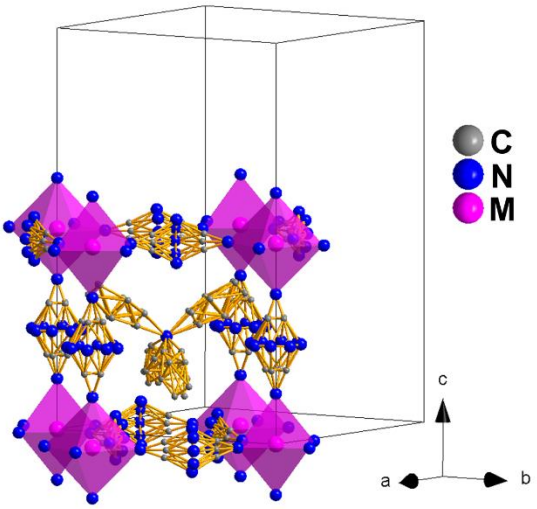

Figure 3-8. Conventional perovskite structure view and unit cell of *polymorph II*. Similar to *Polymorph Ib*, the N-amide and C atoms of the dca ligans along the *c*-axis are modeled in eight and four crystallographic positions, respectively. Meanwhile, the N-amide and C atoms of the dca ligands in the *ab*-plane are modeled in five and three crystallographic positions, respectively. In addition, all the TPrA cations display and even higher disorder in the C atoms.

3.3.1.3 Dielectric properties. The temperature dependence of the real part of the complex dielectric permittivity, ε'_r, (also known as the dielectric constant) of (TPrA)[M(dca)$_3$] (M = Fe^{2+}, Co^{2+} and Ni^{2+}) is shown in Figure 3-9. Very interestingly, as can be seen in Figure 3-9, in the three compounds three anomalies are detected in the vicinity of the structural phase transition, those occurring at *T1* and *T2* being sharper than that taking place at *T3*, specially the first one.

Taking into account the previous structural information, we ascribe such anomalies to the following processes: (a) At *T1* it is mainly related to the cooperative displacement of the TPrA cations between two different antiferrodistortive arrangements that involve off-centered positions, as the dca ligands remain disordered in both polymorphs. (b) At *T2*, we relate it to the displacement of the TPrA cations (which are off-center shifted in *polymorph Ia*) to center positions in *polymorph Ib*. In addition, the increase disorder experienced by the polar dca ligands could also be contributing to the observed dielectric anomaly. (c) Finally, at *T3*, we relate it to the additional order-disorder transition experienced by both the dca ligands and TPrA cations on passing from *polymorph Ib* to *polymorph II*.

This situation is reminiscent of that recently described for the Mn analogue, where a dielectric anomaly is observed above room temperature, $T_t \approx 330$ K, associated to the change from a cooperative to a non-cooperative electric behaviour (antiferroelectric (AFE) to paraelectric (PE) transition). The former implies an AFE distribution of electric dipoles in *polymorph I*, related to an off-shift of the apolar TPrA cations and the order-disorder of the polar dca ligands mechanisms.

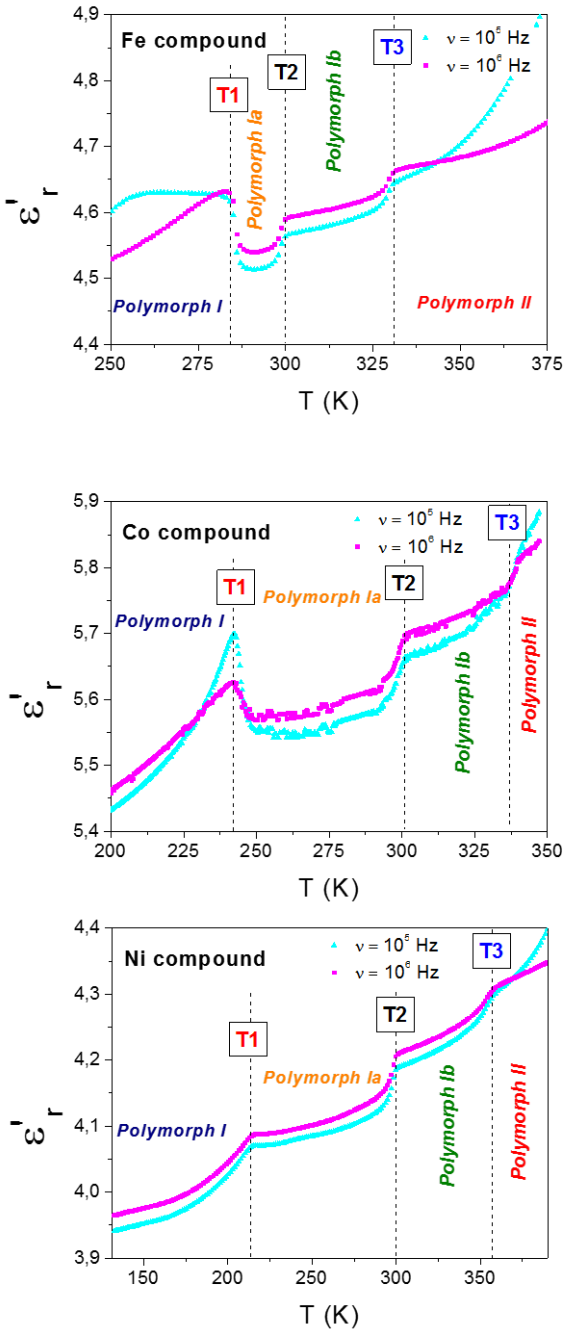

Figure 3-9. Temperature dependence of the dielectric constant (ε'_r) of the Fe, Co and Ni compounds measured at different frequencies (10^5-10^6 Hz).

Nevertheless, in the case of the here studied (TPrA)[M(dca)$_3$] (M = Fe^{2+}, Co^{2+} and Ni^{2+}), they not only show one but multiple dielectric anomalies that are related to the richer assortment of crystal structures displayed by these compounds.

Another aspect that should be emphasized is the significant difference in the origin of the dielectric transitions displayed by these (TPrA)[M(dca)$_3$] (M = Mn^{2+}, Fe^{2+}, Co^{2+} and Ni^{2+}) compounds, and those previously reported for other hybrid perovskites such as [AmineH][M(X)$_3$], (AmineH: midsized alkylammonium cations, X: N_3^-, CN^- or $HCOO^-$ ligands).[8-17] These latter contain polar cations inside the cubooctahedral cavities and/or H-bonds between the cations and the framework, and their dielectric transitions arise from order-disorder processes of the guest polar molecules.

Nevertheless, in the case of this novel dicyanamide family of [TPrA][M(dca)$_3$] (M = Mn^{2+}, Fe^{2+}, Co^{2+} and Ni^{2+}), the guest TPrA cations are nonpolar and cannot form H-bonds, so that the mechanisms associated with the dielectric response are completely different, namely: (a) this response is related to a contribution of a cooperative off-shift of the guest TPrA cations inside the cavities, that is reminiscent of the behaviour shown by ceramic ferroelectrics with perovskite structure, such as $BaTiO_3$ (where the B-site cation is the one experiencing the temperature dependent reversible displacement, giving rise to the electric order). (b) It is also related to order-disorder processes driven by the polar dca ligands. This interesting feature can provide a novel mechanism to couple the magnetic and dielectric response of these compounds since the dca bridges are also involved in the magnetic interaction between the metal cations.

3.3.2 Influence of external and internal pressure on the structural and dielectric transition

In what follows, we will show that these compounds are very sensitive to both applied external pressures, even small ones (P < 2 kbar), as well as to internal chemical pressure induced by modifying the size of the B-site cations.

3.3.2.1. Influence of external pressure. We have studied the behaviour of the axial dilatometry of these samples under applied external pressures in the range 200 ≤ P(bar) ≤ 1600. As it can be seen in Figure 3-10, the PVT analysis allows an easy monitoring of the transition temperatures as a function of pressure, as a kink-shaped anomaly is observed in the curves at *T1*, *T2* and *T3*.

Interestingly, the kinks at *T1* and *T3* are highly pressure dependent, while no significant pressure dependence is observed for that appearing at *T2*.

As for the kink observed at *T1*, that implies an increase in the axial length, it gets progressively displaced towards higher temperatures as pressure increases, that is, it exhibits positive pressure dependence, $\delta Tt/\delta P \approx +23$ K kbar^{-1}.

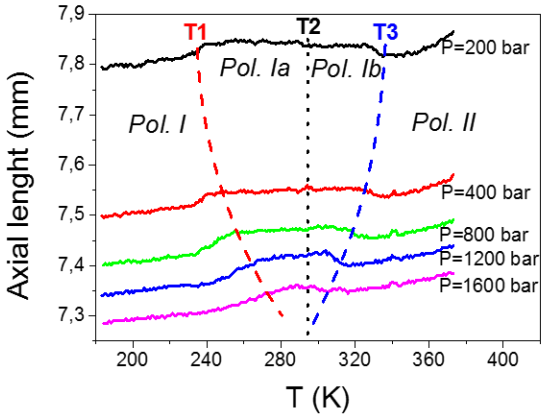

Figure 3-10. PVT graphic showing the length variation of the Co sample as a function of temperature measured at different axial pressures (from 200 bar to 1600 bar). Dash lines signal the temperature shift of *T1*, *T2* and *T3* as a function of pressure. Similar results are obtained for the other Fe and Ni compounds.

This value is of the same order than that previously reported for the Mn compound $\delta Tt/\delta P$ = + 24.2 K kbar^{-1}.[19] Meanwhile the anomaly observed at *T3*, which implies a sharp decrease in the axial length, it gets progressively displaced towards lower temperatures upon application of increasing pressures. This means that this transition displays a negative pressure dependence, $\delta Tt/\delta P$ < 0, whose absolute value is similar to that of the previous case, even if negative, $\delta Tt/\delta P \approx$ - 23 K kbar^{-1}.

To further deepen the peculiar pressure dependence of the transition occurring at *T3*, we have performed additional pressure differential scanning calorimetry (PDSC) studies applying smaller pressures (up to 69 bar).

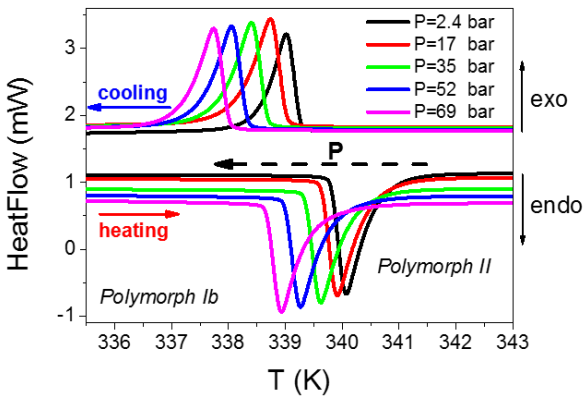

Figure 3-11. Pressure differential scanning calorimetry (PDSC) curves for the *T3* transition of the Co compound. Similar behaviour is found in the Fe and Ni compounds.

As can be seen in Figure 3-11, both the endothermic and exothermic peaks associated with this transition experience a progressive displacement towards lower temperatures as pressure is increased, with a value of $\delta T_{T3}/\delta P$ = -18.4 K kbar^{-1}, of the same order than that found in the PVT experiments. Meanwhile, we observed that the enthalpy (ΔH) and entropy (ΔS) changes involved in such transition remained constant under the applied external pressure.

We have also studied the effect of external pressures (up to $P \leq 2000$ bar) in the temperature dependence of the dielectric permittivity of these compounds. As an example of such behaviour, we show in Figure 3-12 the effect of external pressure on the dielectric response of the Co compound in the temperature range where the anomaly at *T3* is detected.

As can be seen, for $P < 1500$ bar, the kink observed at *T3* in the ε'_r vs T curve experiences a progressive displacement towards lower temperatures as pressure increases, in agreement with the previous experiments.

Meanwhile, and very interestingly, when pressures that are higher than those previously used are applied, $P \geq 1500$ bar, the shape of the kink changes and a new transition (T_N) is found, which gets shifted to higher temperatures as pressure is further increased.

Taking into account that the shape and pressure dependence of such peak is similar to that experienced by the Mn compound,[19] we ascribe it to a new pressure-induced structural transition transforming directly *polymorph I* to *polymorph II* in these Fe, Co, and Ni compounds.

This in turn means that *polymorphs Ia* and *Ib* become thermodynamically unstable under applied pressure, and that both will disappear for $P > 1600$ bar.

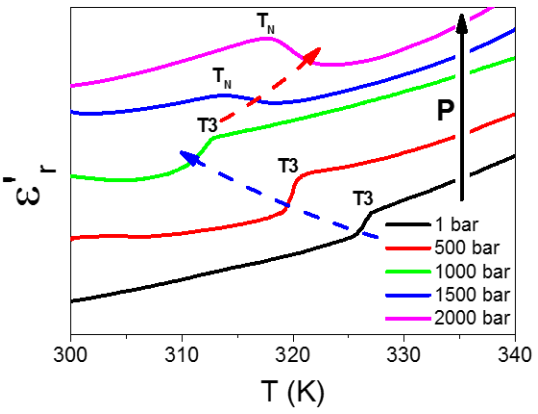

Figure 3-12. Temperature dependence of the dielectric constant (ε'_r) of the Co compound, measured at 10^5 Hz under hydrostatic pressure conditions, from 1 to 2000 bar. The curves have been normalized and displaced for a better view. The Fe and Ni compounds exhibit a similar behaviour.

In fact, for higher pressures, a single structural transition between *polymorph I* and *II* is expected, similar to the case of the Mn analogue.[19]

3.3.2.2. Influence of internal chemical pressure. Chemical pressure is a well-established physical variable that can greatly affect the properties of perovskites, as widely recognized in the field of perovskite oxides ABO_3.[3,4, 25-27]

As it is well-known in those compounds, the origin of the internal chemical pressure is in the size mismatch that occurs when the A-site ions are too small to fill the space in the three-dimensional network of [MO_6] octahedral. This mismatch can be estimated as $\eta = 1 - \alpha$, which is the deviation of the tolerance factor (α) of the structure from the ideal value.[25-27]

Extending this idea to the here studied [TPrA][M(dca)$_3$] (M = Mn^{2+}, Fe^{2+}, Co^{2+} and Ni^{2+}) perovskite compounds, where the ionic radius of the B-site cations follows the sequence r_B: $Mn^{2+} > Fe^{2+} > Co^{2+} > Ni^{2+}$, it can be expected that the tolerance factor will increase along the series while the internal pressure will decrease.

Moreover, we have calculated the value of such tolerance factors (α) following the approach recently introduced by Kieslich et al.[28] to extend the concept of Goldschmidt's tolerance factor to hybrid organic-inorganic perovskites.

For that purpose, and using the modified Goldschmidt's equation, $\alpha = (r_{A(eff)} + r_{X(eff)}) / \sqrt{2}\,(r_B + 0.5\, h_{X(eff)})$,[28] we have calculated the value of α from experimental room temperature crystallographic data of A-site (TPrA) and X-site (dca) ions, and using the Shannon ionic radii tables[29] for the B-site (transition metal) cations.

Table 3-3. The ionic radii for the B-site transition metal cations were obtained from the Shannon ionic radii tables.[29]

Calculated cationic radii and anionic cylinder parameters					Tolerance Factor α	
TPrA	$r_{A(mass)}$ (pm)	$r_{A(ion)}$ (pm)	$r_{A(eff)}$ (pm)		Mn	1.02(6)
	388	15	403		Fe	1.03(8)
dca	$r_{X(mass)}$ (pm)	$r_{X(ion)}$ (pm)	$r_{X(eff)}$ (pm)	$h_{X(eff)}$ (pm)	Co	1.04(6)
	103	146	249	732	Ni	1.05(9)

The effective radii for the TPrA cations ($r_{A(eff)} = r_{A(mass)} + r_{A(ion)}$) and the cylinder parameters of the dca anions ($h_{X(eff)}$ *and* $r_{X(eff)} = r_{X(mass)} + r_{X(ion)}$) were calculated by using experimental room temperature crystallographic data. Differences between the TPrA and dca ligands were observed as a function of the crystallographic structure due to their large flexibility. Thus, an average value was calculated with and estimated error of 3%.

From the obtained values, which are summarized in Table 3-3. and range between 1.02(6) (M = Mn^{2+}) and 1.05(9) (M = Ni^{2+}), it is worth highlighting two aspects: (a) they reflect the expected increase in the tolerance factor as the size of B decreases, even if the large values of X (and A) prevent them from a larger variation. (b) Taking into account the large and complex A and X ions involved, and the simplicity of the model assumed to calculate their effective ionic sizes, the values obtained for the tolerance factor are extremely good. They fit very nicely within the TF region for which perovskite structures are expected to form (between 0.8-1.0 ± 6%)[28] even if in this particular [TPrA][M(dca)$_3$] system the upper limit is going to be slightly larger. These results also indicate that, in this dicyanamide series, the formation of hexagonal polytypes will require at least $\alpha > 1.05(9)$.

Another very interesting point that comes out from these results is the parallelism between the effect on internal pressure and external pressure on the structure of these dicyanamide compounds: both increasing external pressure or increasing the size of B reduces the temperature range in which the intermediate *polymorphs Ia* and *Ib* exist, until they finally disappear, as observed for the case of the Mn compound and for external pressures above 1500 bar, see Figure 3-13.

A final aspect that is worth referring to, is the origin of the different pressure dependence displayed by the three consecutive thermally-induced phase transitions, and whose trend is again similar in the case of external and internal pressure. In that context, and as mentioned before, while the transition occurring at *T1* shows the more commonly observed $\delta Tt/\delta P > 0$, that at *T3* shows a more scarcely seen pressure dependence of the negative sign $\delta Tt/\delta P < 0$, and that at *T2* is almost pressure independent.

To understand this behaviour, it is interesting to revisit previous studies carried out on oxidic and halidic perovskites, which have established that the sign of $\delta Tt/\delta P$ can depend on two factors: (a) the mechanism of the phase transition, whether it is displacive or an order-disorder type, and (b) the value of the tolerance factor that determines the change of stability of its cubic phase under *P*.[30]

As for (a), order-disorder transitions can be responsible for $\delta Tt/\delta P < 0$, while displacive transitions give $\delta Tt/\delta P > 0$.[30] In the case of (b), when α is below the ideal value 1, the pressure reduces the stability of the cubic phase and favours those of lower symmetry, resulting in $\delta Tt/\delta P > 0$. Meanwhile in systems with $\alpha > 1$ and hexagonal stacking, pressure stabilizes the cubic stacking at the expense of the former, resulting in $\delta Tt/\delta P < 0$.[25]

In the case of the here studied [TPrA][M(dca)$_3$] series, where the four compounds exhibit perovskite-like distorted structures and none of them the hexagonal stacking expected for $\alpha > 1$, we relate the different pressure dependence displayed by the three consecutive thermally-induced phase transitions to the prevailing mechanism of each of them: this would be the displacive one in the transition occurring at *T1* and the order-disorder one in the case of *T3*. Meanwhile the close competition between these two mechanisms in the case of *T2* will result in almost no pressure dependence.

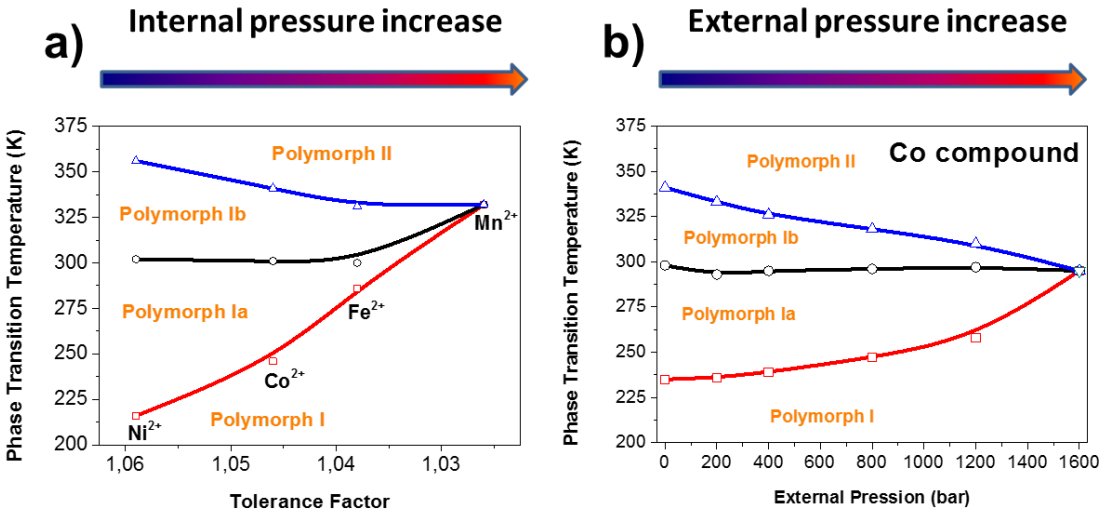

Figure 3-13. (a) Tolerance factor and internal pressure effect on the phase transition temperature for different transition metal substitution in [TPrA][M(dca)$_3$] (M = Mn^{2+}, Fe^{2+}, Co^{2+}, Ni^{2+}). (b) External pressure effect on the phase transition temperature for the different polymorphs of [TPrA][Co(dca)$_3$]. Similar results are obtained for the other Fe and Ni compounds.

These external/internal pressure-responses reveal an easy tuning of the structural transition temperature for these hybrid perovskites. Since these structural transitions are in turn related to the dielectric properties, they can be used to modulate different dielectric responses in a wide range of temperatures near room temperature (from 210 to 360 K) either by applying small external pressures (P < 2 kbar) or simply by making appropriate ionic substitutions.

Therefore, this family of [TPrA][M(dca)$_3$] dicyanamides provides promising technological applications as dielectric transductors, sensitive towards small changes of temperature and pressure values, that can even be easily modulated by appropriate ionic substitutions.

3.4. Conclusions

The hybrid organic-inorganic [TPrA][M(dca)$_3$] (M = Fe^{2+}, Co^{2+} and Ni^{2+}) compounds are singular materials with perovskite-like structure. In these materials, [MN_6] octahedral are linked by $\mu_{1,5}$-dca bridges forming pseudo-cubooctahedral cavities that hold TPrA cations inside.

Remarkably, they exhibit multiple phase transitions that display up to three first-order structural transition between four different polymorphs (*I*, *Ia*, *Ib* and *II*) in a range of temperatures near room temperature (210-360 K). This finding is in contrast with the analogous Mn compound that only displays one first-order transition at $T_t \sim 330$ K.

Interestingly, these compounds also show multiple dielectric anomalies that are related to their richer assortment of crystal structures. Another aspect that should be emphasized is the significant difference in the origin of the dielectric transitions displayed by these (TPrA)[M(dca)$_3$] (M = Fe^{2+}, Co^{2+} and Ni^{2+}) compounds, and those previously reported for other hybrid perovskites. In the case of these novel dicyanamide perovskite-like compounds, the guest TPrA cations are nonpolar and cannot form H-bonds, so that the mechanisms associated with the dielectric response are related to: (a) the contribution of a cooperative off-shift of the guest TPrA cations inside the cavities; and (b) order-disorder processes driven by the polar dca ligands.

In addition, we have studied the parallelism between the effect of the external hydrostatic pressure (P < 2 kbar) and the internal chemical pressure (by modifying the ionic radii and thereby the tolerance factor) on the phase and dielectric transitions. It is important to highlight that we can modulate the structural and dielectric transition temperature as a function of external/internal pressure: by increasing the external pressure or increasing the M (perovskite B-site cations) ionic radii (decreasing the tolerance factor), we can reduce the thermal stability of the intermediate *polymorphs Ia* and *Ib*, and even suppress them.

Therefore, the hybrid perovskites [TPrA][M(dca)$_3$] (M = Fe^{2+}, Co^{2+} and Ni^{2+}) are unique multisensitive materials, where their multiple phase and dielectric transitions can be easily tuned as a function of external pressures as well as by internal chemical pressure. To our knowledge, these are the first examples of hybrid organic-inorganic perovskite-like materials with multiple dielectric transitions that offer easy temperature, pressure and chemical modulation. In that event, these singular materials offer potential interest for future technological applications, such as temperature and pressure sensing.

3.5. Notes

The work presented in this chapter has been published in the following article:

Bermúdez-García, J. M.; Sánchez-Andújar, M.; Yáñez-Vilar, S.; Castro-García, S.; Artiaga, R.; López-Beceiro, J.; Botana, L.; Alegría, A.; Señarís-Rodríguez, M. A. *J. Mater. Chem. C*, 2016, **4**, 4889-4898.

3.6. References

1 (a) Granger, P.; Parvulescu, V. I.; Kaliaguine, S.; Prellier, W. *Perovskites and Related Mixed Oxides: Concepts and Applications*, Wiley-VCH, Weinheim, Germany, 2015; (b) Galasso, F. S. *Structure, properties, and preparation of perovskite-type compounds*, Pergamon Press, New York, 1969. (c) Peña, M. A.; Fierro, J. L. G. *Chem. Rev.*, 2001, **101**, 1981-2018.

2 (a) Lines, M. E.; Glass, A. M. *Principles applications of ferroelectric and related materials*, Oxford Unviersity Press, New York, 2001; (b) Jona, F.; Shirane, G. *Ferroelectric Crystals*, Pergamon Press, Oxford, 1962.

3 Tarascon, J. M.; Bagley, B. G. *Chemistry of superconducting materials*, (Ed: T. A. Vanderah), Noyes Publications, 1992.

4 Rao, C. N. R.; Raveau, B. *Colossal magnetoresistance, charge ordering and related properties of Manganese oxides*, World Scientific Publications, Hackensack, NJ, USA 2004.

5 Spaldin, N. A.; Fiebig, M. *Science*, 2005, **309**, 391-392.

6 Mitzi, D. *Progress in Inorganic Chemistry*, Vol. 48 (Ed: K. D. Karlin), John Wiley & Sons, New York, USA 1999, Ch.1.

7 (a) Lee, M. M.; Teuscher, J.; Miyasaka, T.; Murakami, T. N.; Snaith, H. J. *Science*, 2012, **338**, 643-647. (b) Burschka, J.; Pellet, N.; Moon, S. J.; Humphry-Baker, R.; Gao, P.; Nazeeruddin, M. K.; Grätzel, M. *Nature*, 2013, **499**, 316-319. (c) Jeon, N. J.; Noh, J. H.; Yang, W. S.; Kim, Y. C.; Ryu, S.; Seo, J.; Seok, S. I. *Nature*, *2015*, **517**, 476-480. (d) Sessolo, M.; Bolink, H. J. *Science*, *2016*, **350**, 917-917.

8 (a) Zhao, X.-H.; Huang, X.-C.; Zhang, S.-L.; Shao, D.; Wei, H.-Y.; Wang, X.-Y. *J. Am. Chem. Soc.* 2013, **135**, 16006-16009.(b) Du, Z.-Y.; Zhao, Y.-P.; Zhang, W.-X.; Zhou, H.-L.; He, C.-T.; Xue, W.; Wang, B.-Y.; Chen, X.-M. *Chem. Commun.*, 2014, **50**, 1989-1991. (c) Du, Z.-Y.; Zhao, Y.-P.; He, C.-T.; Wang, B.-Y.; Xue, W.; Zhou, H.-L.; Bai, J.; Huang, B.; Zhang, W.-X.; Chen, X.-M. *Cryst. Growth Des.* 2014, **14**, 3903-3909. (d) Du, Z.-Y.; Sun, Y.-Z.; Chen, S.-L.; Huang, B.; Su, Y.-J.; Xu, T.-T.; Zhang, W.-X.; Chen, X.-M. *Chem. Commun.,* 2015, **51**, 15641-15644. (e) Du, Z.-Y.; Xu, T.-T.; Huang, B.; Su, Y.-J.; Xue, W.; He, C.-T.; Zhang, W.-X.; Chen, X.-M. *Angew. Chem.*, 2015, **127**, 928-932. (f) Gómez-Aguirre, L. C.; Pato-Doldán, B.; Stroppa, A.; Yang, L.-M.; Frauenheim, T.; Mira, J.; Yáñez-Vilar, S.; Artiaga, R.; Castro-

García, S.; Sánchez-Andújar, M.; Señarís-Rodríguez, M. A. *Chem. Eur. J.*, 2016, **22**, 7863-7870.
9 (a) Zhang, W.; Cai, Y.; Xiong, R.-G.; Yoshikawa, H.; Awaga, K. *Angew. Chem. Int. Ed.*, 2010, **122**, 6758-6760. (b) Zhang, W.; Ye, H.-Y.; Graf, R.; Spiess, H. W.; Yao, Y.-F.; Zhu, R.-Q.; Xiong, R.-G. *J. Am. Chem. Soc.* 2013, **135**, 5230-5233. (c) Zhang, X.; Shao, X.-D.; Li, S.-C.; Cai, Y.; Yao, Y.-F.; Xiong, R.-G.; Zhang, W. *Chem. Commun.*, 2015, **51**, 4568-4571. (d) Xu, W.-J.; Chen, S.-L.; Hu, Z.-T.; Lin, R.-B.; Su, Y.-J.; Zhang, W.-X.; Chen, X.-M. *Dalton Trans.*, 2016, **45**, 4224-4229.
10 (a) Jain, P. ; Dalal, N. S.; Toby, B. H.; Kroto, H. W.; Cheetham, A. K. *J. Am. Chem. Soc.*, 2008, **130**, 10450-10451; (b) Jain, P.; Ramachandran, V.; Clark, R. J.; Zhou, H. D.; Toby, B. H.; Dalal, N. S.; Kroto, H. W.; Cheetham, A. K. *J. Am. Chem. Soc.*, 2009, **131**, 13625-13627. (c) Zhang, Z.; Li, W.; Carpenter, M. A.; Howard, C. J.; Cheetham, A. K. *CrystEngComm.*, 2015, **17**, 370-374. (d) Kieslich, G.; Forse, A. C.; Sun, S.; Butler, K. T.; Kumagai, S.; Wu, Y.; Warren, M. R.; Walsh, A.; Grey, C. P.; Cheetham, A. K. *Chem. Mater.*, 2016, **28**, 312-317. (e) Kieslich, G.; Kumagai, S.; Butler, K. T.; Okamura, T.; Hendon, C. H.;. Sun, S; Yamashita, M.; Walsh, A.; Cheetham, A. K. *Chem. Commun.*, 2015, **51**, 15538-15541.
11 (a) Shang, R.; Xu, G.-C.; Wang, Z.-M.; Gao, S. *Chem. Eur. J.*, 2014, **20**, 1146-1158. (b) Chen, S.; Shang, R.; Hu, K.-L.; Wang, Z.-M.; Gao, S. *Inorg. Chem. Front.*, 2014, **1**, 83-98. (c) Chen, S.; Shang, R.; Wang, B.-W.; Wang, Z.-M.; Gao, S. *Angew. Chem.*, 2015, **127**, 11245-11248. (d) Shang, R.; Chen, S.; Wang, B.-W.; Wang, Z.-M.; Gao, S.; *Angew. Chem.* 2016, **128**, 2137-2140.
12 (a) Sánchez-Andújar, M.; Presedo, S.; Yáñez-Vilar, S.; Castro-García, S.; Shamir, J.; Señarís-Rodríguez, M. A. *Inorg. Chem.*, 2010, **49**, 1510-1516. (b) Pato-Doldán, B.; Sánchez-Andújar, M.; Gómez-Aguirre, L. C.; Yáñez-Vilar, S.; López-Beceiro, J.; Gracia-Fernández, C.; Haghighirad, A. A.; Ritter, F.; Castro-García, S.; Señarís-Rodríguez, M. A. *Phys. Chem. Chem. Phys.*, 2012, **14**, 8498-8501. (c) López-Beceiro, J.; Gracia-Fernández, C.; Gómez-Barreiro, S.; Castro-García, S.; Sánchez-Andújar, M.; Artiaga, R. *J. Phys. Chem. C* 2012, **116**, 1219-1224 (d) Pato-Doldán, B.; Gómez-Aguirre, L. C.; Bermúdez-García, J. M.; Sánchez-Andújar, M.; Fondado, A.; Mira, J.; Castro-García, S.; Señarís-Rodríguez, M. A. *RSC Adv.*, 2013, **3**, 22404-22411. (e) Sánchez-Andújar, M.; Gómez-Aguirre, L. C.; Pato-Doldán, B.; Yáñez-Vilar, S.; Artiaga, R.; Llamas-Saiz, A. L.; Manna, R. S.; Schnelle, F.; Lang, M.; Ritter, F.; Haghighirad, A. A.; Señarís-Rodríguez, M. A. *CrystEngComm.*, 2014, **16**, 3558-3566. (f) Gómez-Aguirre, L. C.; Pato-Doldán, B.; Stroppa, A.; Yáñez-Vilar, S.; Bayarjargal, L.; Winkler, B.; Castro-García, S.; Mira, J.; Sánchez-Andújar, M.; Señarís-Rodríguez, M. A. *Inorg. Chem.*, 2015, **54**, 2109-2116.
13 (a) Zhou, B.; Imai, Y.; Kobayashi, A.; Wang, Z.-M.; Kobayashi, H. *Angew. Chem. Int. Ed. Engl.*, 2011, **50**, 11441-11445. (b) Imai, Y.; Zhou, B.; Ito, Y.; Fijimori, H.; Kobayashi, A.; Wang, Z. M.; Kobayashi, H. *Chem. Asian J.*, 2012, **7**, 2786-2790.
14 (a) Stroppa, A.; Barone, P.; Jain, P.; Perez-Mato, J. M.; Picozzi, S. *Adv. Mater.*, 2013, **25**, 2284-2290. (b) Tian, Y.; Stroppa, A.; Chai, Y.-S.; Barone, P.; Perez-Mato, M.; Picozzi, S.; Sun, Y. *Phys. Status Solidi (RRL)*, 2015, **9**, 62-67 (c) Ptak, M.; Mączka, M.; Gągor, A.; Sieradzki, A.; Stroppa, A.; Di Sante, D.; Perez-Mato, J. M.; Macalik, L. *Dalton Trans.*, 2016, **45**, 2574-2583.
15 (a) Mączka, M.; Ciupa, A.; Gągor, A.; Sieradzki, A.; Pikul, A.; Macalik, B.; Drozd, M. *Inorg. Chem.* 2014, **53**, 5260-5268. (b) Mączka, M.; Pietraszko, A.; Macalik, B.; Hermanowicz, K. *Inorg. Chem.*, 2014, **53**, 787-794. (c) Mączka, M.; Gągor, A.; Macalik, B.; Pikul, A.; Ptak, M.; Hanuza, J. *Inorg. Chem.*, 2014, **53**, 457-467. (d) Mączka, M.; Gągor, A.; Hermanowicz, K.; Sieradzki, A.; Macalik, L.; Pikul, A. *J. Solid State Chem.*, 2016, **237**, 150-158.
16 (a) Tian, Y.; Stroppa, A.; Chai, Y.; Yan, L.; Wang, S.; Barone, P.; Picozzi, S.; Sun, Y. *Scientific Reports*, 2014, **4**, 6062. (b) Tian, Y.; Shen, S.; Cong, J.; Yan, L.; Wang, S.; Sun, Y. *J. Am. Chem. Soc.*, 2016, **138**, 782-785.
17 Gómez-Aguirre, L. C.; Pato-Doldán, B.; Mira, J.; Castro-García, S.; Señarís-Rodríguez, M. A.; Sánchez-Andújar, M.; Singleton, J.; Zapf, V. S. *J. Am. Chem. Soc.*, 2016, **138**, 1122-1125.
18 Schlueter, J. A.; Manson, J. L.; Geiser, U. *Inorg. Chem.*, 2005, **44**, 3194-3202.
19 Bermúdez-García, J. M.; Sánchez-Andújar, M.; Yáñez-Vilar, S.; Castro-García, S.; Artiaga, R.; López-Beceiro, J.; Botana, L.; Alegría, A.; Señarís-Rodríguez, M. A. *Inorg. Chem.*, 2015, **54**, 11680-11687.
20 Sheldrick, G. M. *Acta Cryst. A*, 2008, **64**, 112-122.
21 Farrugia, L. J. *J. Appl. Cryst.*, 2012, **45**, 849-854.
22 Mercury 3.5.1 (Build RC5) – Crystal Structure Visualisation (CCDC) http://www.ccdc.cam.ac.uk/mercury.
23 (a) Dudley, J. D.; Hall, H. T. *Phys. Rev.* 1960, **118**, 1211-1216; (b) Höhne, G. W. H.; Dollhopf, W.; Blankenhorn, K.; Mayr, P.U. *Thermochim. Acta*, 1996, **273**, 17-24.
24 Glazer, A. M. *Acta Crystallogr. B*, 1972, **28**, 3384-3392.
25 Goodenough, J. B.; Kafalas, J. A.; Longo, J. M. *Preparative methods in Solid State Chemistry*, (Ed: P. Hagenmüller), Academic press, New York, USA 1972, Ch. 1.
26 Kugel, K. I.; Rakhmanov, A. L.; Sboychakov, A. O.; Poccia, N.; Bianconi, A. *Phys. Rev. B*, 2008, **78**, 165124-1 - 165124-7.
27 Hwang, H. Y.; Palstra, T. T.; Cheong; S.-W.; Batlogg, B. *Phys. Rev. B*, 1995, **52**, 15046-15049.
28 (a) Kieslich, G.; Sun, S.; Cheetham, A. K. *Chem. Sci.*, 2014, **5**, 4712-4715; (b) Kieslich, G.; Sun, S.; Cheetham, A. K. *Chem. Sci.*, 2015, **6**, 3430-3433.
29 Shannon, R. D. *Acta Cryst. A*, 1976, **32**, 751.
30 Aleksandrov, K. S.; Bartolome, J.; Gorev, M. V.; Flerov, I. N. *Phys. Stat. Sol. (B)*, 2000, **217**, 785-791.

Chapter 4:

Giant barocaloric effect in the ferroic organic-inorganic hybrid [TPrA][Mn(dca)$_3$] perovskite under easily accessible pressures

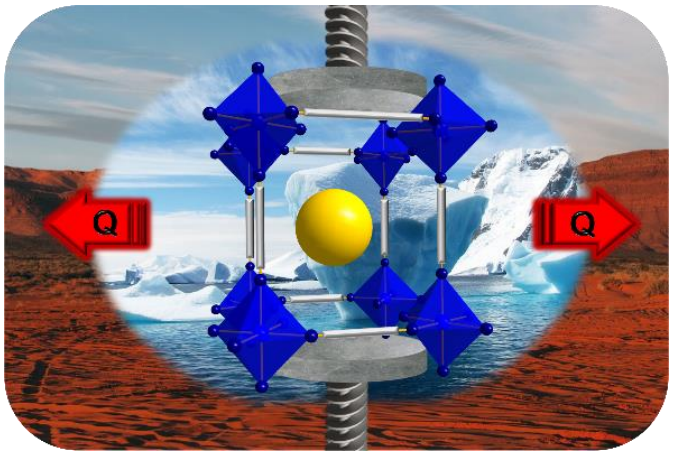

Giant barocaloric effect in the ferroic organic-inorganic hybrid [TPrA][Mn(dca)$_3$] perovskite under easily accessible pressures

Abstract: In this chapter, we will show that organic-inorganic hybrid compounds can also have great potential in another up to now unexplored field such as that of solid state cooling. In this context we will present the first example of giant barocaloric effects near room temperature under easily accessible pressures (P < 70 bar) in the hybrid perovskite [TPrA][Mn(dca)$_3$] (TPrA: tetrapropylammonium, dca: dicyanamide). Moreover, we will propose that this will not be an isolated example for such an extraordinary behaviour as many other organic-inorganic hybrids (MOFs and coordination polymers), exhibit the basic ingredients to display large caloric effects which can be very sensitive to pressure and other external stimuli.

4.1. Introduction and objectives

Refrigeration and air conditioning already represents more than 20% of the world´s energy consumption and demand on these fields is expected to grow dramatically in the coming decades. Nevertheless, the conventional cooling technology that is used nowadays suffers from a relatively low efficiency and relies on the vapour compression of gases that have been proof to be hazardous and/or pollutants, such as the greenhouse gases (hydrochlorofluorocarbons (HCFCs) and hydrofluorocarbons (HFCs)), which in turn are going to be prohibited in Europe in 2020 (EU Regulation No 517/2014).

Therefore, finding environmentally friendly and more efficient cooling alternatives constitutes a major issue and concern, and one of the present big scientific and technological challenges.

In that context, a promising approach is based on solid state materials that experience caloric effects,[1-3] and in which the refrigeration capacity is associated with an isothermal entropy change or with an adiabatic temperature change induced by different external stimuli, [1-6] such as mechanical stress -namely, uniaxial strain (the so-called elastocaloric effect)[7] or hydrostatic pressure (barocaloric effect)[8]-, electric field (electrocaloric effect),[9,10] or magnetic field (magnetocaloric effect).[11-13]

Up to now, the most promising materials are those exhibiting giant magnetocaloric effect.[1,2] However, they require the applications of rather large magnetic fields (H > 2 T) and are rather expensive magnetic materials, many of them containing rare-earths, drawbacks for the wide industrial and commercial application of the resulting so-called magnetic refrigeration.

On the other hand, and even if in principle solid state caloric effects driven by applied pressure/stress could be technological and economically more accessible, less efforts have been devoted to their study because they were expected to be minimal due to the small entropy changes and/or reduced pressure sensibility of solids.[4] For example, in the case of the ceramic (inorganic) perovskite $Pr_{1-x}La_xNiO_3$ the application of hydrostatic pressures up to 5 kbar (0.5 GPa) is known to induce a small effective cooling, in competition with the elastic heating;[14,15] and in the related $PbTiO_3$ and $BaTiO_3$ perovskites those values have been predicted to be relatively small.[16,17] Nevertheless, quite recently, giant barocaloric effects have been found near room temperature associated with the giant magnetocaloric response of a few magnetic alloys,[18,19] in some perovskite-like fluorides and oxyfluorides,[20] and in ferrielectric ammonium sulphate,[8] even if under the application of pressures P > 0.1 GPa.

What we report in this work is the finding of giant barocaloric effects near room temperature induced by considerable smaller pressures in a solid of formula [TPrA][Mn(dca)$_3$] (TPrA: tetrapropylammonium cation, $[CH_3CH_2CH_2]_4N^+$; dca: dicyanamide anion, $N(CN)_2^-$) with perovskite-like structure. This compound belongs to the rather young, but very fast growing group of compounds widely known as organic-inorganic hybrids, which include the large family of metal-organic frameworks (MOFs),[21] and coordination polymers.[22]

These hybrids, where the multiple possible combinations of inorganic and organic moieties allow for an enormous structural and chemical diversity,[23] are arising great interest in many diverse fields such as gas adsorption or catalysis (in the case of hybrids with open porous structures); and more recently, in connection with remarkable functional and multifunctional

properties displayed by members with denser structures, many of them belonging to the group of the so-called hybrid perovskites with general formula ABX_3. This is the case of the $(MA)PbI_3$ (MA = methylammonium),[24,25] which has revealed unprecedented photoconductivity, or the outstanding $[AmineH][M(X)_3]$ families (AmineH = midsized protonated amines in the A-site position of the perovskite, M = different divalent transition metal cations in the B-site, X = different bidentate-bridge ligands in the X-site position, such as N_3^-, CN^- or $HCOO^-$), which exhibit cooperative magnetic, electric or elastic order, and even magnetically induced multiferroicity.[26-36]

Nevertheless, an aspect that had not yet been explored in these hybrid materials, and that we report for the first time in this work, is their potentiality as solid state caloric materials, in view of the stimuli-driven caloric effects they can display.

For this purpose, we focus in the hybrid perovskite $[TPrA][Mn(dca)_3]$ (TPrA: $[CH_3CH_2CH_2]_4N^+$, dca: $N(CN)_2^-$),[35] where our recent studies have revealed a first-order phase transition at $T_t \approx 330$ K, which involves an order-disorder process with N ≈ 8 and that shows a large response towards pressure and temperature.[35] According to our previous characterization, both above and below the transition the Mn^{2+} ions, which are in an octahedral $[MnN_6]$ coordination, are bridged by dca-ligands forming a 3D framework, while the TPrA cations are located in the resulting pseudo-cubooctahedral cavities. Nevertheless, *polymorph I* ($T < T_t$) shows a more ordered crystal structure and a cooperative antiferrodistortive displacement of the A-cations; meanwhile *polymorph II* ($T > T_t$) shows a much larger thermal disorder in the C atoms of the TPrA cations and in the N and C atoms of the dca ligands and a centred distribution of the A-cations.

4.2. Experimental section

4.2.1 Synthesis

Single phase powder $[TPrA][Mn(dca)_3]$ was prepared from aqueous solution at ambient temperature as reported.[35] All reagents were commercially available and were used as purchased without further purification: $Mn(NO_3)_2 \bullet xH_2O$ (97%, Aldrich), (TPrA)Br (98%, Aldrich), Na(dca) (96%, Aldrich), and absolute ethanol (Panreac). Also, a reagent amount of deionized water was used in the synthesis. A mixture of (TPrA)Br (2 mmol) solution in 10 ml of ethanol and a solution of Na(dca) (6 mmol) in 10 ml of water was layered on top of an aqueous solution of $Mn(NO_3)_2 \bullet xH_2O$ (2 mmol). Colourless polycrystalline powder was obtained and collected by filtration and washed several times with ethanol.

4.2.2 Powder X-ray diffraction

A Siemens D-5000 diffractometer, using CuKα radiation (λ=1.5418 Å), was used to study this compound by powder X-ray powder diffraction (PXRD) at room temperature. The PXRD pattern was compared with that reported in the literature.[35] The single phase of the as-synthesized compound was confirmed by Le Bail refinement of PXRD patterns. PXRD analysis were also performed after sample compression/decompression cycles, results which showed that the material is still fully crystalline and *polymorph I* is the phase present at room conditions, see Figure 4-1.

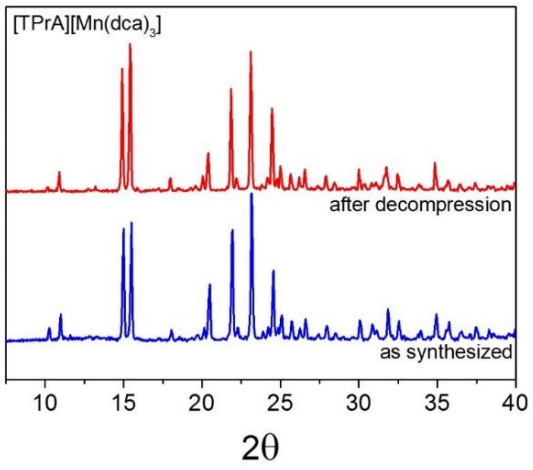

Figure 4-1. Powder XRD patterns of the $[TPrA][Mn(dca)_3]$ sample as synthesized (bottom blue curve) and after decompression of 68.9 bar in the PDSC analysis (red top curve).

4.2.3 Differential scanning calorimetry (DSC and PDSC)

Standard and pressure differential scanning calorimetry (DSC and PDSC) analysis were performed in a TA Instruments (standard or pressure) cell mounted on a Q2000 modulated DSC. The cell was calibrated for temperature and heat with indium at each of the pressures to be used in the measuring tests. The effect of pressure on the melting temperature and enthalpy of indium was taken into account.[37,38] In a typical experiment, about 5 mg of the sample were confined inside a pinhole aluminium capsule. The experiments were performed in N_2 atmosphere at a constant pressure (from 1 to 68.9 bar) while keeping a constant flow of 50 ml min^{-1} of N_2. Heating and cooling ramps at 2 K min^{-1} were programmed from room temperature to 343 K. However, as a consequence of the intrinsic features of pressure DSC cells, temperature control during the cooling ramp is worse than on heating and some deviations were observed. Therefore, only heating

data were used for subsequent calculations of the barocaloric effect. Three cycles of pressure application/release were performed in the sample at each pressure value, confirming the reversible behaviour of the process and its reproducibility. Moreover, the same behaviour was observed in different batches.

4.2.3 Elastic heating calculation.

The elastic heating ($\sim\beta$ x v x ΔP) was calculated from the volumetric thermal expansion coefficient and the specific volume, both obtained from synchrotron powder X-ray diffraction (S-PXRD),[35] with a value of $\beta \approx 2.25 \times 10^{-4}$ K^{-1} and $v \approx 7.97 \times 10^{-4}$ m^3 kg^{-1}, respectively; and the maximum pressure increase of $\Delta P = 68.9 \times 10^5$ N m^2 (68.9 bar).

4.3. Results and discussion

4.3.1. Differential scanning calorimetry under applied pressure

To study the barocaloric effect induced by small external hydrostatic pressures (P < 0.007 GPa) in this compound, we have performed additional differential scanning calorimetry (DSC) studies as a function of pressure, from 1 bar to 68.9 bar (1×10^{-4} GPa - 6.8×10^{-3} GPa), and of temperature (from room temperature to 340 K), see Experimental section.

The obtained results fully corroborate, in first place, the first-order nature of the phase transition, which displays a small hysteresis of 2 K and a large value of associated entropy change per mass unit of $\Delta S_{phase} \approx 45$ J kg^{-1} K^{-1}, see Figure 4-2.

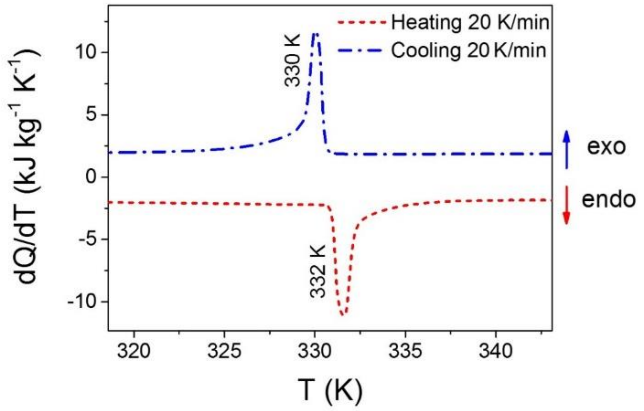

Figure 4-2. Heat Flow δQ/δT (kJ kg^{-1} K^{-1}) versus temperature, T(K), curves measured by DSC on heating (red dash line) and cooling (blue dash-dot line) of the sample [TPrA][Mn(dca)$_3$] at a rate of 20 K min^{-1}.

They also indicate that the phase transition, which gets progressively displaced towards higher temperatures when increasing the pressure ($\delta T_t/\delta P$ = 25.6 K $kbar^{-1}$ on heating), is fully reversible with recovery of the initial situation after decompression, even when performing several cycles, see Figure 4-3. The reversibility of this process is also corroborated by the powder X-ray diffraction data, which show that after decompression the material is still fully crystalline and *polymorph I* is the phase present at ambient conditions, see Figure 4-1.

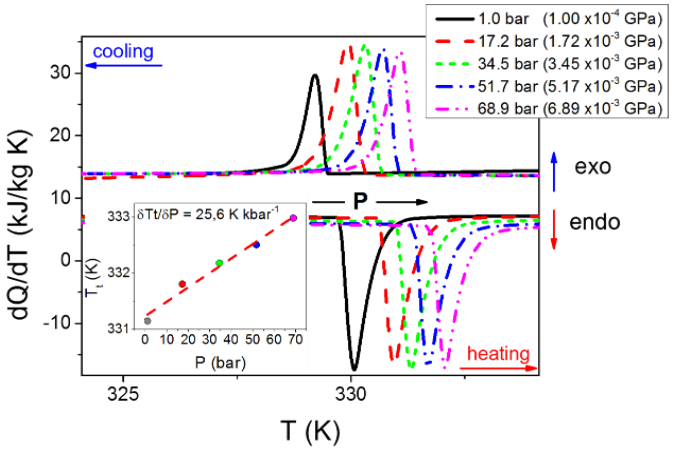

Figure 4-3. Heat Flow δQ/δT (kJ kg^{-1} K^{-1}) versus temperature, T(K), DSC curves measured at different pressures (1 - 68.9 bar), on heating (bottom curves) and cooling (top curves), for the sample [TPrA][Mn(dca)$_3$] at a programmed rate of 2 K min^{-1}. It should be noted that in this plot the cooling exothermal peak at ambient pressure appears smaller than the other peaks due to the fact that the programmed cooling rate was not achieved, (it was only around 0.95 K/min). In any case, its integration along time results in an area similar to that of the other peaks and the entropy change associated to the phase transition (ΔS_{phase}) on the well-controlled heating curves remains constant in the whole pressure range under study. Inset: linear fit for the pressure dependence of the transition temperature, $\delta T_t/\delta P$, on heating.

4.3.2. Isobaric and isothermal entropy change

From the calorimetric data obtained on heating (see Experimental section), we have calculated the isobaric entropy change, ΔS_{ib}, of this compound as a function of temperature at each pressure, using equation (4-1),[3,39] where Q(P) is the experimental heat flux measured at different pressures, T' is the heating rate and T is the temperature:

$$\Delta S_{ib} = S(T,P) - S(T_0,P) = \int_{T_0}^{T} \frac{1}{T} \frac{Q(P)}{T'} dT \quad (4\text{-}1)$$

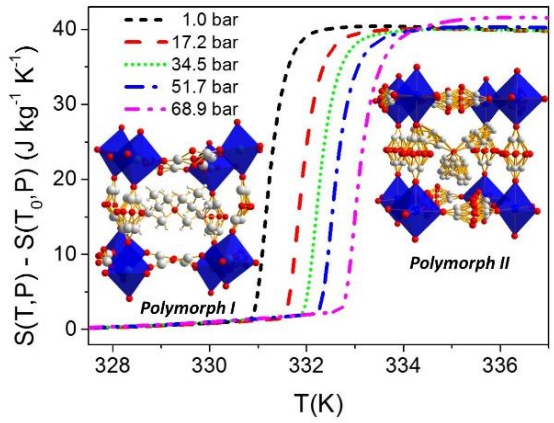

Figure 4-4. Isobaric entropy change as a function of temperature at different pressures (1-68.9 bar), related to the transition from *polymorph I* to *II*.

The obtained data, shown in Figure 4-4, reveal that the entropy increases up to a plateau of ~40 J kg^{-1} K^{-1} when the material undergoes the phase transition from *polymorph I* to *polymorph II*. This sets the maximum value of entropy attainable in the caloric effect related to such phase transition. Also, they show a systematic shift of the entropy curves towards higher temperatures, as the hydrostatic pressure stabilizes the more ordered *polymorph I* at the expense of the more disordered *polymorph II*.

The associated barocaloric effect for this material, which can be defined as the isothermal entropy change induced by hydrostatic pressure and calculated as the difference between the data at different pressures, $\Delta S_{it} = \Delta S_{ib}(P\neq1) - \Delta S_{ib}(P=1)$, is shown in Figure 4-5a. As it can be seen, the isothermal application of pressure results in a decrease in entropy up to a value of ΔS_{it} = 37.8 J kg^{-1} K^{-1} at T = 332.5 K and P = 68.9 bar. Interestingly enough, despite the relative small pressure applied (P < 0.007 GPa), the peak values are very close to the maximum obtainable caloric effect, ΔS_{ib} ≈ 40 J kg^{-1} K^{-1}, and appear slightly above room temperature. In addition, we find that in this compound the elastic heating, which in principle could compete with the barocaloric effect, and that can be calculated as $\sim\beta \times v \times \Delta P$ (see "Methods" section), is almost negligible: at 68.9 bar it shows a value of 1.23 J kg^{-1} K^{-1}, which is ~30 times lower than the value of the corresponding barocaloric effect of ΔS_{it} = 37.8 J kg^{-1} K^{-1}.

4.3.3. Clausius-Clapeyron method

Since this material undergoes a first-order phase transition, the entropy change associated to the barocaloric effect can be also calculated using the indirect Clausius-Clapeyron method and equation (4-2): [4]

$$(\delta T_t/\delta P) = \Delta v/\Delta S_{C.C.} \quad (4\text{-}2)$$

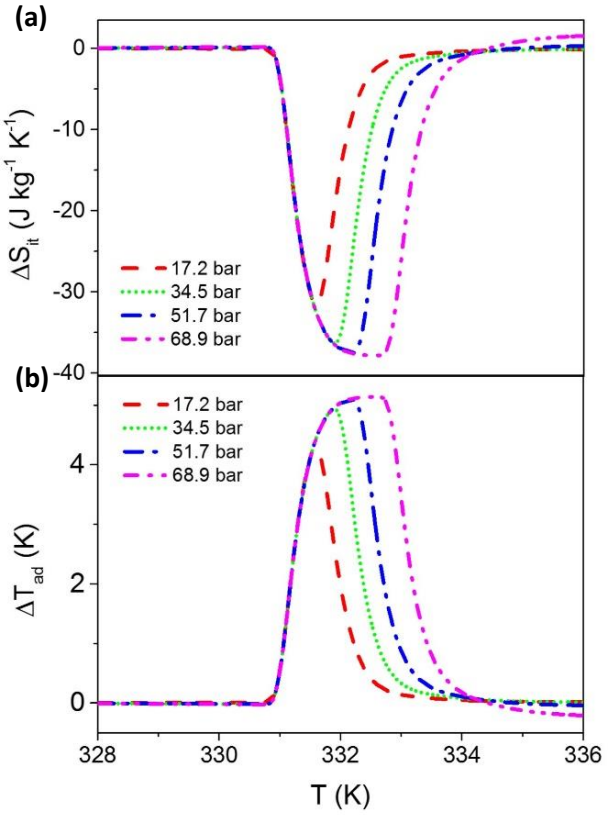

Figure 4-5. Barocaloric effect as a function of temperature at different applied hydrostatic pressures (from 1 bar to 68.9 bar), defined as (a) isothermal entropy change, ΔS_{it}, and (b) adiabatic temperature change, ΔT_{ad}.

where δTt/δP is the transition temperature dependence with the applied pressure, also known as the barocaloric coefficient (δTt/δP = 25.6 K $kbar^{-1}$); Δv is the change in the specific volume of the material, which we have obtained by synchrotron powder X-ray diffraction (Δv ≈ 1 x 10^{-5} m^3 kg^{-1}); and $\Delta S_{C.C.}$ is the isothermal entropy change calculated by means of this Clausius-Clapeyron method. The obtained result, $\Delta S_{C.C.}$ = 39.06 J kg^{-1} K^{-1}, is in fully agreement with that obtained by direct DSC calorimetric measurements, ΔS_{it} = 37.8 J kg^{-1} K^{-1}.

4.3.4. Adiabatic temperature change

On the other hand, and as it is usually done in the literature for first-order transitions, we have also calculated the barocaloric effect of this material expressed in terms of the pressure-induced adiabatic temperature change, ΔT_{ad}, which is directly related to the isothermal entropy change, ΔS_{it}, through equation (4-3):[20]

$$\Delta T_{ad} = -T/C_p \times \Delta S_{it} \quad (4\text{-}3)$$

where, C_P is the constant specific heat capacity independent of pressure and of the phase transition,[4,8] estimated in this case to be 2450 J K^{-1} kg^{-1}; and T is the temperature at which the barocaloric effect occurs (here T ≈ 333 K).

The results, shown in Figure 4-5b, give a ΔT_{ad} ≈ 5.1 K, value which is very large taking into account the relative low pressures used (P = 68.9 bar). This value is very competitive with those previously reported for barocaloric materials exhibited at much higher pressures, see Table 4-1.

Even more, in view of the warning recently raised by some authors,[40] claiming that the "ideal" values obtained using this method can be far from the "real" ones measured in prototypes due, among other reasons, to underestimation of the irreversible entropy changes driven by the external stimulus (in this case pressure, but magnetic field or electric field in the case of the more studied magnetocaloric or electrocaloric materials), we have also estimated ΔT_{ad} taking into account both thermal and pressure hysteresis. When doing so, we obtain the corrected value $\Delta T_{ad(corr)}$ ≈ 3.2 K, which even if smaller than the value obtained directly from equation (4-3) is still relatively quite a large number for this pressure (P=68.9 bar).

4.3.3. Relative cooling power

To compare the refrigeration capacity of this hybrid with that displayed by other caloric materials, we make use of the figure of merit called relative cooling power (RCP), that has been defined as indicated in equation (4-4):[20,41]

$$RCP = -\Delta S_{it}^{max} \times \partial T_{FWHM} \quad (4\text{-}4)$$

where δT_{FWHM} is the full width at half maximum for the maximum isothermal entropy change, ΔS_{it}^{max}. It should be indicated that for the same magnitude of applied-stimulus (pressure, magnetic or electric field), a larger RCP indicates a better caloric material. The RCP of [TPrA][Mn(dca)$_3$] at 68.9 bar (a relatively low pressure) turns to be as high as ~67 J kg^{-1}, as indicated in Table 4-1, where selected caloric parameters for the up to now best baro-, magneto- and electrocaloric materials are summarized and compared. In addition to the isothermal entropy change (ΔS_{it}) and adiabatic temperature change (ΔT_{ad}) for each material, this Table 4-1 also includes the value of the external stimulus applied to the caloric material (namely, value of pressure -|ΔP|-, magnetic field -|ΔH|- or electric field -|ΔE|-), the maximum RCP achieved under those conditions, and the RCP normalized per magnitude of the applied stimulus (RCP/|ΔP|, RCP/|ΔH|, RCP/|ΔE|). Interestingly enough, and as it can be seen there, the RCP of [TPrA][Mn(dca)$_3$] per pressure unit is very competitive with the best barocaloric materials,[8,18-20,42-44] and widely overpass the RCP per magnetic or electric field unit of the best performing magneto- and electrocaloric materials.[9,20,45]

Table 4-1. *Selected caloric parameters of some of the best baro-, magneto- and electrocaloric materials described up-to-date.*

Giant BC Material	T_t (K)	$\lvert\Delta S_{it}\rvert$ (J kg^{-1} K^{-1})	$\lvert\Delta T_{ad}\rvert$ (K)	|ΔP| (GPa)	RCP (J kg^{-1})	RCP/|ΔP| (J kg^{-1} GPa^{-1})	Ref.
$Ni_{49.26}Mn_{36.08}In_{14.66}$	293	24	4.5	0.26	120	462	8, 18
$LaFe_{11.33}Co_{0.47}Si_{1.2}$	237	8.7	2.2	0.20	81	405	8, 19
$Gd_5Si_2Ge_2$	270	11	1.1	0.20	180	900	8, 42
$Fe_{49}Rh_{51}$	308	12.5	8.1	0.11	105	955	8, 43
Mn_3GaN	285	21.6	4.8	0.09	125	1389	8, 44
$(NH_4)_3MoO_3F_3$	297	55	15	0.5	5200	10400	20
$(NH_4)_2SO_4$	219	60	8	0.1	276	2760	8
[TPrA][Mn(dca)$_3$]	330	37.8	5.1	0.00689	67	9724	Herein
Giant MC Material	**T_t (K)**	**$\lvert\Delta S\rvert_{it}$ (J kg^{-1} K^{-1})**	**$\lvert\Delta T\rvert_{ad}$ (K)**	**|ΔH| (T)**	**RCP (J kg^{-1})**	**RCP/|ΔH| (J kg^{-1} T^{-1})**	**Ref.**
Gd	296	11	11	5	780	156	20
$Fe_{1-x}Rh_x$	313	55	33	5	900	180	20
$Pr_{0.63}Sr_{0.37}MnO_3$	300	8.52	5.7	5	511	102	45
$Gd_5Si_2Ge_2$	276	18.4	15	5	535	107	45
Giant EC Material	**T_t (K)**	**$\lvert\Delta S\rvert_{it}$ (J kg^{-1} K^{-1})**	**$\lvert\Delta T\rvert_{ad}$ (K)**	**|ΔE| (kV cm^{-1})**	**RCP (J kg^{-1})**	**RCP/|ΔE| (J cm kg^{-1} kV^{-1})**	**Ref.**
$PbZr_{0.95}Ti_{0.05}O_3$	500	8	12	480	1080	2.25	9, 20

BC, barocaloric; MC, magnetocaloric; EC, electrocaloric; T_t, transition temperature; $\lvert\Delta S_{it}\rvert$, isothermal entropy change; $\lvert\Delta T_{ad}\rvert$, adiabatic temperature change; |ΔP|, pressure change; |ΔH|, magnetic field change; |ΔE|, electric field change. RCP, relative cooling power; RCP/|ΔP|, relative cooling power normalized per pressure unit; RCP/|ΔH|, relative cooling power normalized per magnetic field unit; RCP/|ΔE|, relative cooling power normalized per electric field unit.

4.4. Conclusions

In this work, we report an outstanding and unprecedented giant barocaloric effect in the hybrid [TPrA][Mn(dca)$_3$] perovskite material near room temperature. Moreover, in this rather flexible material, this giant response is obtained under very small pressures comparable to the working pressure of the current commercial refrigerant gases, P < 70 bar.

Even more, we anticipate that this hybrid will not be an isolated example for such an extraordinary behaviour. In fact, many other organic-inorganic hybrids, including MOFs and coordination polymers, exhibit the basic ingredients to also display large caloric effects, namely: large and reversible entropy changes commonly related to first-order phase transitions of order-disorder nature[46] (often associated, in turn, with ferroic transitions), as well as remarkable external multistimuli responses (towards magnetic and/or electric field, pressure, temperature, etc.), which can be especially strong in the case of applying pressure due to the rather high flexible structures of these hybrid materials.

Therefore, these findings not only set up a new horizon for the scientific community working on organic-inorganic hybrid materials, and Materials Science in general, but also open up new opportunities for developing the next generation of refrigerant systems based on environmentally friendly and economically more accessible solid state materials.

4.5. Notes

The work presented in this chapter has been submitted for publication as communication in a scientific journal.

4.6. References

1 Kitanovski, A.; Tusek, J.; Tomc, U.; Plaznik, U.; Ozbolt, M.; Poredos, A. *Magnetocaloric Energy Conversion From Theory to Applications*; Springer International Publishing, 2015.
2 Kitanovski, A, Plaznik, U.; Tomc, U.; Poredos, A. *Intern. J. Refrig.* 2015, **57**, 288-298.
3 Mañosa, Ll.; Planes, A.; Acet, M. *J. Mater. Chem. A* 2013, **1**, 4925-4936.
4 Moya, X.; Kar-Narayan, S.; Mathur, N. D. *Nat. Mater.* 2014, **13**, 439-450.
5 Moya, X.; Defay, E.; Heine, V.; Mathur, N. D. *Nat. Phys.* 2015, **11**, 202-205.
6 Fähler, S.; Rößler, U. K.; Kastner, O.; Eckert, J.; Eggeler, G.; Emmerich, H.; Entel, P.; Müller, S.; Quandt, E.; Albe, K. *Adv. Eng. Mater.* 2012, **14**, 10-19.
7 Bonnot, E.; Romero, R.; Mañosa, Ll.; Vives, E.; Planes A. *Phys. Rev. Lett.* 2008, **100**, 125901.
8 Lloveras, P.; Stern-Taulats, E.; Barrio, M.; Tamarit, J-Ll.; Crossley, S.; Li, W.; Pomjakushin, V.; Planes, A.; Mañosa, Ll.; Mathur, N. D.; Moya, X. *Nat. Commun.* 2015, **6**, 8801 (2015).
9 Mischenko, A. S.; Zhang, Q.; Scott, J. F.; Whatmore, R. W.; Mathur, N. D. *Science* 2006, **311**, 1270-1271.
10 Neese, B.; Chu, B.; Lu, S. G.; Wang, Y.; Furman, E.; Zhang, Q. M. *Science* 2008, **321**, 821-823.
11 Pecharsky, V. K.; Gschneidner Jr.; K. *Phys. Rev. Lett.* 1997, **78**, 4494.
12 Tegus, O.; Brück, E.; J. Buschow, K. H.; de Boer, F. R. *Nature* 2002, **415**, 150-152.
13 Krenke, T.; Duman, E.; Acet, M.; Wassermann, E. F.; Moya, X.; Mañosa, Ll.; Planes, A. *Nature Mater.* 2005, **4**, 450-454.
14 Müller, K. A.; Fauth, F.; Fischer, S.; Koch, M.; Furrer, A.; Lacorre, P. *Appl. Phys. Lett.* 1998, **73**, 1056.
15 Strässle, Th.; Furrer, A.; Hossain, Z.; Geibel, Ch. *Phys. Rev. B* 2003, **67**, 054407.
16 Mikhaleva, E. A.; Flerov, I. N.; Gorev, M. V.; Molokeev, M. S.; Cherepakhin, A. V.; Kartashev, A. V.; Mikhashenok, N. V.; Sablina, K. A. *Phys. Solid State* 2012, **54**, 1832-1840.
17 Liu, Y.; Wei, J.; Janolin, P. E.; Infante, I. C.; Lou, X.; Dkhil, B. *Appl. Phys. Lett.* 2014, **104**, 162904.
18 Mañosa, Ll.; González-Alonso, D.; Planes, A.; Bonnot, E.; Barrio, M.; Tamarit, J.-Ll.; Aksoy, S.; Acet, M. *Nature Mater.* 2010, **9**, 478-481.
19 Mañosa, Ll.; González-Alonso, D.; Planes, A.; Barrio, M.; Tamarit, J.-Ll.; Titov, I. S.; Acet, M.; Bhattacharyya, A.; Majumdar, S. *Nat. Commun.* 2011, **2**, 595.
20 Flerov, I. N.; Gorev, M. V.; Tressaud, A.; Laptash, N. M. *Crystallogr. Rep.* 2011, **56**, 9-17.
21 Yaghi, O. M.; O'Keeffe, M.; Ockwig, N. W.; Chae, H. K.; Eddaoudi, M.; Kim, J. *Nature* 2003, **423**, 705-714.
22 Janiak, C. *Dalton Trans.* 2003, **14**, 2781-2804.
23 Cheetham, A. K.; Rao, C. N. R. *Science* 2007, **318**, 58-59.
24 Burschka, J.; Pellet, N.; Moon, S.-J.; Humphry-Baker, R.; Gao, P.; Nazeeruddin, M. K.; Grätzel, M. *Nature* 2013, **499**, 316-319.
25 Lee, M. M.; Teuscher, J.; Miyasaka, T.; Murakami, T. N.; Snaith, H. J. *Science* 2012, **338**, 643-647.
26 Zhang, W.; Ye, H.-Y.; Graf, R.; Spiess, H. W.; Yao, Y.-F.; Zhu, R.-Q.; Xiong, R.-G. *J. Am. Chem. Soc.* 2013, **135**, 5230-5233.
27 Du, Z.-Y.; Zhao, Y.-P.; He, C.-T.; Wang, B.-Y.; Xue, W.; Zhou, H.-L.; Bai, J.; Huang, B.; Zhang, W.-X.; Chen, X.-M. *Cryst. Growth Des.* 2014, **14**, 3903-3909.
28 Jain, P.; Ramachandran, V.; Clark, R. J.; Zhou, H. D.; Toby, B. H.; Dalal, N. S.; Kroto, H. W.; Cheetham, A. K. *J. Am. Chem. Soc.* 2009, **131**, 13625-13627.
29 Sánchez-Andújar, M.; Presedo, S.; Yáñez-Vilar, S.; Castro-García, S.; Shamir, J.; Señarís-Rodríguez, M. A. *Inorg. Chem.* 2010, **49**, 1510-1516.
30 Ptak, M.; Maczka, M.; Gagor, A.; Sieradzki, A.; Stroppa, A.; Di Sante, D.; Perez-Mato, M. J.; Macalik, L. *Dalton Trans.* 2016, **45**, 2574-2583.
31 Chen, S.; Shang, R.; Hu, K.-L.; Wang, Z.-M.; Gao, S. *Inorg. Chem. Front.* 2014, **1**, 83-98.
32 Zhou, B.; Imai, Y.; Kobayashi, A.; Wang, Z.-M.; Kobayashi, H. *Angew. Chem. Int. Ed. Engl.* 2011, **50**, 11441-11445.
33 Gómez-Aguirre, L. C.; Pato-Doldán, B.; Mira, J.; Castro-García, S.; Señarís-Rodríguez, M. A.; Sánchez-Andújar, M.; Singleton, J.; Zapf, V. S. *J. Am. Chem. Soc.* 2016, **138**, 1122-1125.
34 Pato-Doldán, B.; Gómez-Aguirre, L. C.; Bermúdez-García, J. M.; Sánchez-Andújar, M.; Fondado, A.; Mira, J.; Castro-García, S.; Señarís-Rodríguez, M. A. *RSC Adv.* 2013, **3**, 22404-22411.
35 Bermúdez-García, J. M.; Sánchez-Andújar, M.; Yáñez-Vilar, S.; Castro-García, S.; Artiaga, R.; López-Beceiro, J.;

Botana, L.; Alegría, A.; Señarís-Rodríguez, M. A. *Inorg. Chem.* 2015, **54**, 11680-11687.
36 Bermúdez-García, J. M.; Sánchez-Andújar, M.; Yáñez-Vilar, S.; Castro-García, S.; Artiaga, R.; López-Beceiro, J.; Botana, L.; Alegría, A.; Señarís-Rodríguez, M. A. *J. Mater. Chem. C*, 2016, **4**, 4889-4898.
37 Dudley, J. D.; Hall, H. T. *Phys. Rev.* 1960, **118**, 1211-1216.
38 Höhne, G. W. H.; Dollhopf, W. Blankenhorn, K. Mayr, P.U. *Thermochim. Acta,* 1996, **273**, 17-24.
39 Planes, A.; Mañosa, Ll. *Solid State Phys.* 2001, **55**, 159-267.
40 Gutfleisch, O.; Gottschall, T.; Fries, M.; Benke, D.; Radulov, I.; Skokov, K. P.; Wende, H.; Gruner, M.; Acet, M.; Entel, P.; Farle, M. *Phil. Trans. R. Soc. A* 2016, **374**, 20150308.
41 Gschneidner Jr.; K. A.; Pecharsky, V.K. *Annu. Rev. Mater. Sci.* 2000, **30**, 387-429.
42 Yuce, S.; Barrio, M.; Emre, B.; Stern-Taulats, E.; Planes, A.; Tamarit, J.-Ll.; Mudryk, Y.; Gschneidner Jr.; K. A.; Pecharsky, V. K.; Mañosa, Ll. *Appl. Phys. Lett.* 2012, **101**, 071906.
43 Stern-Taulats, E.; Planes, A.; Lloveras, P.; Barrio, M.; Tamarit, J.-Ll.; Pramanick, S.; Majumdar, S.; Frontera, C.; Mañosa, Ll. *Phys. Rev. B* 2014, **89**, 214105.
44 Matsunami, D.; Fujita, A.; Takenaka, K.; Kano, M. *Nature Mater.* 2015, **14**, 73-78.
45 Phan, M. H.; Yu, S. C. *J. Magn. Magn. Mater.* 2007, **308**, 325-340.
46 Cairns, A. B.; Goodwin, A. L. *Chem. Soc. Rev.;* 2013, **42**, 4881-4893.

Chapter 5:

A simple method to synthesize carbon nanotubes embedded with magnetic nanoparticles by using the organic-inorganic hybrid perovskite $[TPrA][M(dca)_3]$ (M = Ni^{2+} and Co^{2+}) as precursor

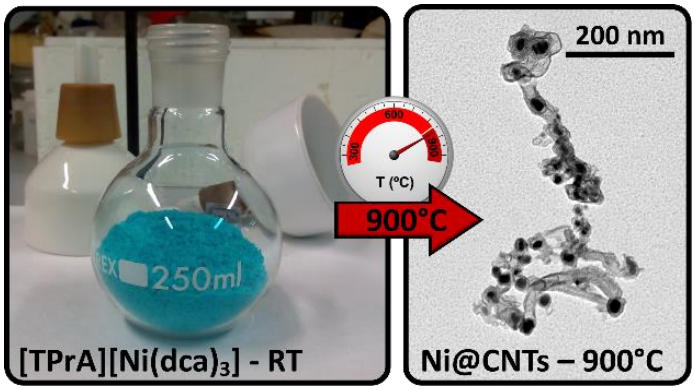

A simple method to synthesize carbon nanotubes embedded with magnetic nanoparticles by using the organic-inorganic hybrid perovskite [TPrA][$M(dca)_3$] (M = Ni^{2+} and Co^{2+}) as precursor

Abstract: This chapter shows another potentiality of these compounds which can be used as precursors of nanostructured carbon mayerials- In this context, we show that the incorporation of dicyanamide building blocks in organic-inorganic hybrid compounds can be a promising strategy for the synthesis of multiwall carbon nanotubes embedded with magnetic nanoparticles (M@CNTs). As we will show, following a novel one-step, scalable and fast synthetic route, M@CNTs can be obtained by simple calcination of the organic-inorganic hybrid perovskite [TPrA][$M(dca)_3$] (TPrA = tetrapropylammonium, M = Ni^{2+} and Co^{2+}, dca = dicyanamide). The resulting M@CNTs (M = Ni^{2+} and Co^{2+}) display a regular morphology, and an essentially mesoporous network of ~250 m^2 g^{-1}. Whereas the Co@CNT composite displays a broad pore size distribution up to 6 nm, Ni@CNTs show a strictly controlled unimodal PSD, centered at around 5 nm. The monitoring of their thermal decomposition by X-ray diffraction, electron microscopy, thermogravimetric and spectroscopic analysis allows proposing a synthesis mechanism and establish the conditions to obtain optimum materials. Moreover, magnetization studies reveal a ferromagnetic behaviour of the obtained M@CNTs, with small coercive fields due to the size of the magnetic nanoparticles. All these physicochemical properties, allows us to propose these composites as potential materials for nitrogen-rich CNT common applications.

5.1. Introduction and objectives

Hybrid nanocomposites of carbon nanotubes with encapsulated magnetic nanoparticles (M@CNTs) are emerging materials with an enormous technological interest related to their multifunctional properties.[1,2] Since their discovering in the early 90s,[3] carbon nanotubes (CNTs) have shown to exhibit unique mechanical, thermal and chemical stabilities together with a tunable electric conductivity, among other functional properties.[4] Thus, these materials find applications in a wide range of fields such as micro- and nanoelectronic (flat panel displays,[5] sub-22 nm node technologies,[6] flash memories,[7] spintronics,[8] etc.), energy storage systems (supercapacitors,[9] batteries,[10] etc.), and even biomedical and pharmacological applications[11,12] due to their chemical inertness and biocompatibility.

Moreover, combining CNTs with magnetic nanoparticles (NPs) can lead to novel and enhanced multifunctional properties, as demonstrated in several areas. For instance, the porous surface of CNTs in combination with the magnetic behaviour of the NPs allow removing pollutants from water and recovering of the material by an external magnet.[13] In another context, magnetic nanoparticles embedded in carbon nanotubes can induce magneto-conductance for spintronic applications.[14] The electromagnetic behaviour of these materials can also enhance optical properties, which are interesting to develop very sensitive spectroscopic techniques, such surface-enhanced Raman scattering.[15] Moreover, such composite materials can be used as probes in characterization ferromagnetic resonance imaging[16] and even contrast agents for medical magnetic resonance imaging (MRI).[17] In addition, the chemical inertness, biocompatibility and water solubility of these materials, render these electromagnetic compounds great candidates for bio- and nanomedical applications, such as nanocarriers for targeted drug delivery,[18] "nano-syringes" for metal transport[19] or hyperthermia for cancer treatment.[20]

Generally speaking, it is preferable to use nanoparticle-filled nanotubes, instead of CNTs decorated with external nanoparticles. For instance, in the filled systems the external surface of the CNTs is more accessible to the adsorption or to an additional functionalization. Moreover, when using metals as magnetic nanoparticles, the encapsulation protects the metals against their oxidation.

In the case of the nanoparticle-filled CNTs, it is further desirable to control the nanoparticle filling. Thus, for example, a partial filling allows a channel-like structure for accessible adsorption and transporting sites. In this context, the synthesis of hybrid carbon nanotubes heterostructures with encapsulated magnetic nanoparticles can developed by two main strategies: *in-situ* and *ex-situ* methods.[1] *In-situ* processes involves the

filling of the tube during the synthetic route and include mainly CVD and arch discharge methods, where a metal catalyst controls the kinetic growing. Conversely, the *ex-situ* techniques consist of filling the carbon nanotubes after their synthesis by means of wet chemistry, electrochemistry and gas or evaporation techniques.

Since most of these procedures involve several-step reactions, relatively complex operational conditions, high cost, low reproducibility or difficulties in terms of practical applications, it is desirable to find simple, reproducible, scalable and low-cost methods to synthesize M@CNTs, with a good control in terms of type, diameter, length, morphology and orientation of the nanoparticles and the CNTs.

Recent studies have highlighted the potential of some relatively new families of compounds such as organic-inorganic hybrid materials as precursors and templates for the preparation of nanoporous carbon structures, by means of direct carbonization.[21] This is the case of metal-organic frameworks (MOFs) and porous coordination polymers (PCPs) such as Al-PCPs,[22,23] MOF-5 and isoreticular compounds (IRMOF),[24-25] ZIF-8,[26] ZIF-67,[27] and related materials. Notwithstanding, there are few results on obtaining carbon nanotubes by direct calcination of organic-inorganic hybrid materials.[28,29]

To fill this gap we have carried out the present study. The starting research hypothesis lies in the idea that the inclusion of dicyanamide anions and magnetic metal cations within organic-inorganic hybrid structures could be a promising strategy to obtain nitrogen-enriched carbon nanotubes with embedded magnetic nanoparticles by simple calcination.

Dicyanamide ligands (dca) are known to be useful precursors for obtaining N-rich carbons. Thus, it has been reported that molecular dicyanamide salts trimerize heated above 300 °C, forming triazine units[30-33] that can be used as precursors for nitrogen-rich graphite sheets.[34] More recently, dicyanamide-containing ionic liquids[35-37] and molecular salts[38-42] have been used to obtain N-graphite materials. Nevertheless, there are very scarce studies about carbon nanotubes and "nanoworms" with embedded magnetic nanoparticles derived from direct calcination of dicyanamide related-salts or ionic liquids.[35,43]

In this work, we use the new multisensitive organic-inorganic hybrids of formula $[TPrA][M(dca)_3]$ (TPrA: tetrapropylammonium, $(CH_3CH_2CH_2)_4N^+$; dca: dicyanamide, $(N(CN)_2)^-$; M = Ni^{2+} and Co^{2+}) and perovskite-like structure[44-46] as precursors, as they can provide both nitrogen-rich carbon sources and metal catalysts for the formation of CNTs during their calcination.

In order to get reliable insights into the calcination mechanism, the thermal evolution of the samples has been monitored by means of thermogravimetric analysis (TGA), elemental analysis, fourier transform infrared (FT-IR) and Raman spectroscopies, powder X-ray diffraction (PXRD), transmission electron microscopy (TEM), nitrogen adsorption and magnetisation studies. The combination of these diverse techniques has led to a complete characterization of the resulting materials.

As shown below, this has led us to one of the first successful synthesis of carbon nanotubes with embedded Ni and Co nanoparticles, M@CNTs, achieved by direct calcination of an organic-inorganic hybrid compound with perovskite-like structure.

Additionally, preliminary studies reveal promising oil adsorption capacity of the obtained samples.

5.2. Experimental section

5.2.1. Synthesis of the $[TPrA][M(dca)_3]$ hybrid precursors

The $[TPrA][M(dca)_3]$ (M = Ni^{2+} and Co^{2+}) compounds were prepared from commercially available reagents without further purification, namely $Co(NO_3)_2.6H_2O$ (98%, Sigma-Aldrich), $Ni(NO_3)_2.6H_2O$ (≥98.5%,Sigma-Aldrich), [TPrA]Br (98%, Aldrich), Na(dca) (96%, Aldrich) and absolute ethanol (Panreac). A reagent amount of deionised water was also used in the synthesis.

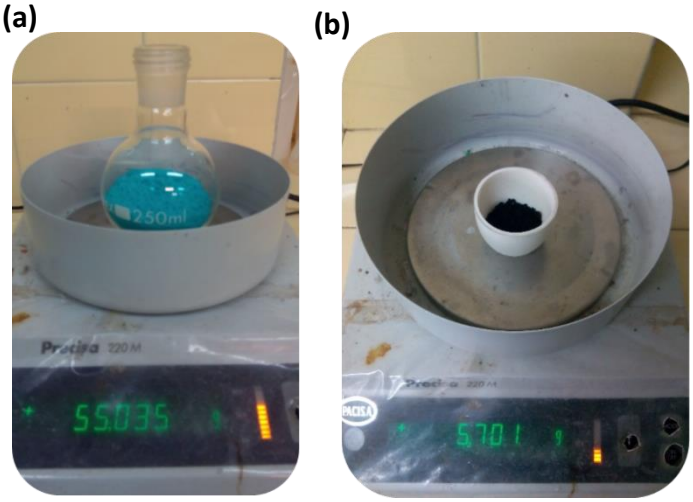

Figure 5-1. (a) $[TPrA][Ni(dca)_3]$ powder obtained by the here presented method with a yield of ~95%. (b) Ni@CNT powder obtained by direct calcination of 35g of $[TPrA][Ni(dca)_3]$ precursor at 900 °C.

The synthetic method used is a variation of that previously reported for obtaining $[TPrA][M(dca)_3]$ (M = Mn^{2+}, Fe^{2+}, Co^{2+} and Ni^{2+}) hybrids.[46] The procedure was as follows: a mixture of a solution of [TPrA]Br in ethanol and a solution of Na(dca) in water was mixed with another solution of $M(NO_3)_2.6H_2O$ in water, where M = Ni^{2+} and Co^{2+}. After stirring at 30 °C, the solvent was evaporated in a rotary evaporator and a polycrystalline powder was obtained (green for the Ni compound and pink for the

Co compound) with a yield of ~95% in both cases. The precipitate was collected by filtration and washed with ethanol. This variation of the synthesis considerably shortens the previously reported 1-week method[46] and highly enlarge the amount of organic-inorganic hybrid compounds that can be obtained, see Figure 5-1a.

5.2.2. Synthesis of the M@CNTs

M@CNTs (M = Ni^{2+} and Co^{2+}) were synthesized in a relative large scale (see Figure 5-1b) by thermolysis of the precursor inside a conventional tubular furnace, equipped with a quartz tube and under a nitrogen flux of 350 ml min^{-1}. The thermal program used was heating at 5 °C min^{-1} from room temperature to 900 °C and cooling back to room temperature during 10 hours.

5.2.3. Powder X-ray diffraction

The formation of the precursor compounds, of the final M@CNTs and the evolution of the intermediate samples (annealed at ~300 °C, ~500 °C, ~600 °C, ~900 °C and ~1300 °C) were followed by powder X-ray diffraction (PXRD) using a Siemens D-5000 diffractometer , with CuKα radiation (λ=1.5418 Å) working at room temperature. The PXRD patterns of the $[TPrA][M(dca)_3]$ M = Ni^{2+} and Co^{2+} hybrids were compared with the profiles obtained from their single-crystal structure, which were generated by the Mercury 3.5.1 software.[47] The obtained patterns had enough quality to allow their Le Bail analysis using the GSAS+EXPGUI software.[48,49] The PXRD patterns of the samples annealed at different temperatures were compared with those PXRD patterns of the $M(dca)_2$ (Ref. 50), Ni (JCPDS No. 00-004-0850), NiO (JCPDS No. 00-073-1523), Co (JCPDS No. 00-015-0806), CoO (JCPDS No. 00-065-2902) and C-graphite (JCPDS No. 00-001-0640) phases, respectively.

5.2.4. Elemental analysis

Elemental analyses for C, N, and H content in the precursors $[TPrA][M(dca)_3]$ (M = Ni^{2+} and Co^{2+}) and in the final M@CNTs were carried out using a FLASHEA1112 (Thermo-Finnigan) Analyzer.

5.2.5. Thermal characterization

Thermogravimetric analysis (TGA) were carried out in a TGA-DTA Thermal Analysis SDT2960 equipment. For these experiments, approximately 25 mg of sample were heated at a rate of 5 °C min^{-1} from 25 °C to 1300 °C using corundum crucibles under a flow of dry nitrogen.

5.2.6. Infrared and Raman spectroscopies

Infrared spectra of the solid products, and of the gases released during the TGA analysis, were analyzed on a Bruker vector FT-IR spectrometer TGA, in the range of 400 to 4000 cm^{-1}. The Raman spectra of the products were recorded using a T64000 Jobin-Ybon spectrometer, with a charge coupled device (CCD) camera (40-4000 cm^{-1}) and a photocounting device (10-200 cm^{-1}). The 514.5 nm linear polarized line of Ar^+ laser was chosen for excitation. The effect on the laser power on the Raman spectra was previously studied in order to prevent the self-heating of the sample.

5.2.7. Transmission electron microscopy

The morphology of the samples obtained after calcination was studied by transmission electron microscopy (TEM) on a JEOL 1010 microscope operating at 100 kV. For that purpose the samples were suspended in isopropanol, and deposited onto copper grids.

5.2.8. Assessment of the porous structure

Textural characterization was carried out by N_2 physisorption at 77 K on a Micromeritics ASAP 2010 volumetric adsorption system. The total pore volume was calculated from the amount adsorbed at a relative pressure of 0.99 whereas the specific surface area was estimated by using the Brunauer-Emmett-Teller (BET) equation. The pore size distributions were obtained by applying the Quenched Solid State Functional Theory (QSDFT) method assuming pores of cylindrical shape.[51]

5.2.9. Magnetic studies

The magnetization of the M@CNTs (M = Ni^{2+} and Co^{2+}) samples as a function of the applied magnetic field, *M(H),* was studied at room temperature using a vibrant sample magnetometer (VSM), model DMS-1660. For that purpose a magnetic field was applied from -10kOe to +10 kOe and the data were registered in steps of 200 Oe in the range of 0 to 2500 Oe, and in steps of 1500Oe in the range of 2500to 10000 Oe.

5.2.10. Oil adsorption-desorption essays

A commercial motor lubricant based on ester, 100% synthetic (ρ = 0.862 g cm^{-3}at 20 °C and μ = 46.4 mm^2 s^{-1} at 40 °C) was used for the adsorption tests. For each test, an aliquot of 50 mg of M@CNTs was spilled on top of the oil-water mixture up to saturation of the materials (2 minutes). The desorption of oil from the M@CNT materials was induced by heating from room temperature to 600 °C with a ramp of 5 °C min^{-1} in a TGA-DTA Thermal Analysis SDT2960 instrument equipped with a Bruker vector FT-IR spectrometer to monitoring the released gases.

5.3. Results and discussion

5.3.1. Characterization of the $[TPrA][M(dca)_3]$ precursors

The Le Bail refinement of the PXRD patterns confirm the formation of the $[TPrA][M(dca)_3]$ (M = Ni^{2+} and Co^{2+}) as both obtained samples exhibit the orthorrombic *Pnna* crystalline structure described in the literature for these compounds at room temperature,[46] see Figure 5-2.

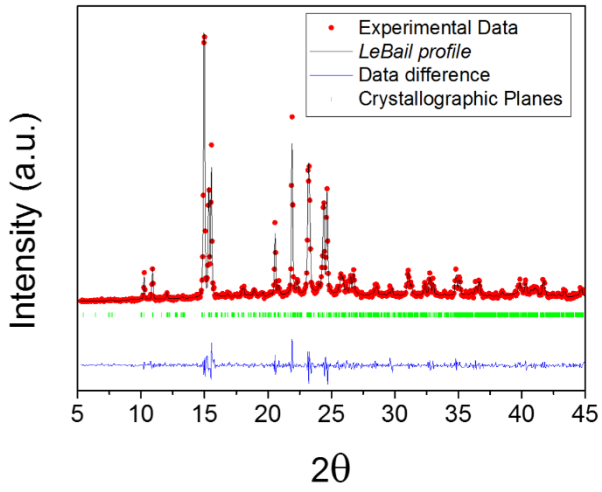

Figure 5-2. Le Bail refinement of PXRD patterns for the [TPrA][Co(dca)$_3$] compound at room temperature. Observed (red dots), calculated (black solid line) and difference (blue solid line at the bottom) profiles. The tick green marks indicate the positions of the allowed Bragg reflections.

Moreover, these samples are single-phase materials without associated secondary phases. The elemental analysis data, summarized in Table 5-1, are also in agreement with those reported for these compounds.[44]

The results of the FT-IR spectra for both compound (shown in Figure 5-3 and Table 5-2) are also in fully agreement with the literature data.[33,44]

Table 5-1. Results of elemental analysis for the (TPrA)[M(dca)$_3$] samples (Obs.) compared with the theoretical values (Calc.) and with reported data (Ref. 44).

		C (%)	H (%)	N (%)
[TPrA][Ni(dca)$_3$]	Ref. 44	48.62	6.41	31.41
	Calc.	48.78	6.37	31.61
	Obs.	49.24	6.22	31.08
[TPrA][Co(dca)$_3$]	Calc.	48.76	6.36	31.59
	Obs.	49.01	6.18	31.10

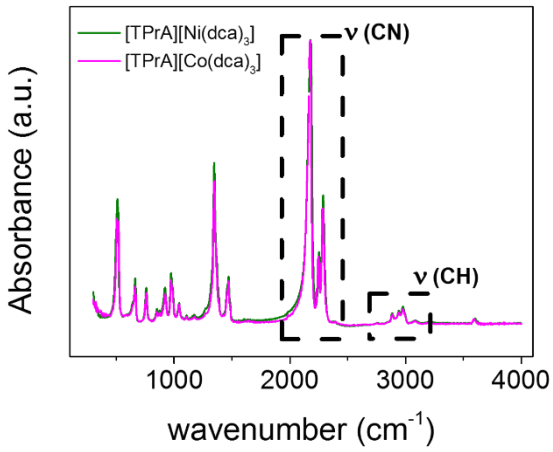

Figure 5-3. FT-IR spectra of [TPrA][M(dca)$_3$] where M = Ni^{2+} (green) and Co^{2+}(pink). The IR bands between 2000 cm^{-1} and 2360 cm^{-1} are related to the dicyanamide ligand ν(CN) bands: 2286 cm^{-1} νs (C≡N), 2230 cm^{-1} νas(C–N) + νs(C–N), 2175 cm^{-1} νas (C≡N), and the region between 2800 cm^{-1} and 3200 cm^{-1} correspond to C-H stretching bands of the tetrapropylammonium cations.

Table 5-2. IR stretching bands of the [TPrA][M(dca)$_3$] (M = Ni^{2+} and Co^{2+}) compounds.

[TPrA][M(dca)$_3$] IR bands	wavenumber (cm^{-1})
νs(C≡N)	2286
νas(C–N) νs(C–N)	2230
νas(C≡N)	2175
(C-H)	2800 – 3200

5.3.2. Thermal decomposition of the [TPrA][M(dca)$_3$] (M = Ni^{2+} and Co^{2+}) precursors

The thermal decomposition of the [TPrA][M(dca)$_3$] (M = Ni^{2+} and Co^{2+}) compounds was monitored by TGA. As it can be seen in Figure 5-4. both the Ni and Co precursors exhibit a quite similar thermal evolution, with four weight losses as a function of temperature: (i) a first abrupt weight loss in the interval [250-300] °C, (ii) a second weight loss at [300-500] °C, (iii) a third progressive weight loss at [500-650] °C, (iv) a last and smaller weight loss that continues up to 1300 °C.

The FT-IR spectra of the gases released during the TGA help understanding the decomposition mechanism see Figure 5-4 and 5-5.

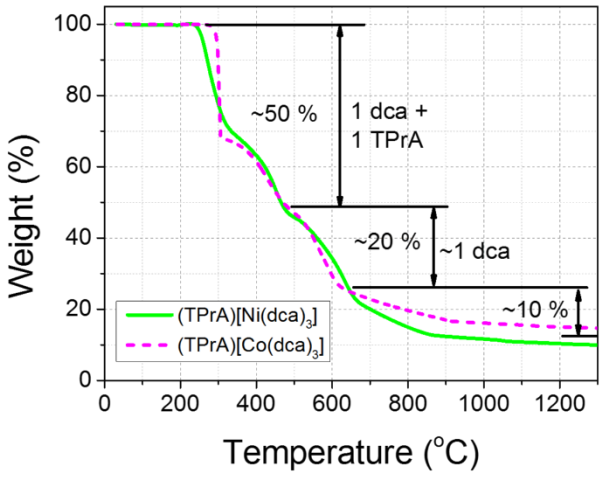

Figure 5-4. TGA decomposition curve for the precursor (TPrA)[M(dca)$_3$] materials, where M = Ni^{2+} (green) and Co^{2+} (pink).

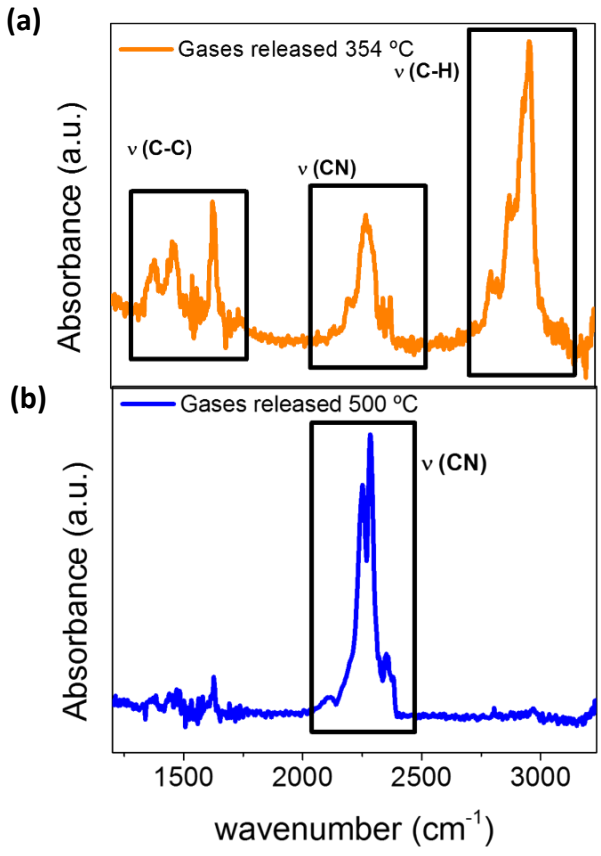

Figure 5-5. FT-IR spectra of the gases released during the thermal decomposition of the precursor [TPrA][Ni(dca)$_3$]: (a) at 354 °C, (b) at 500 °C. ν(CN) represent both ν(C N) and ν(C≡N). Graphic (a) is representative of the behaviour during the two first weight losses: we observe the IR bands related to dca ligands (ν(CN) = ν(C-N) + ν(C≡N)) and TPrA cations (ν(C-C) and ν(C-H)). Graphic (b) is representative of the third and fourth weight losses: only the dca ligand bands remain, and their intensity decreases when increasing the temperature.

In that context, during the first and second weight losses IR bands around [1000-1500] cm^{-1} and [2800-3200] cm^{-1} are observed , which can be assigned to ν(C-C) and ν(C-H), and attributed to the TPrA cations, as well as bands around [2000-2360] cm^{-1} can be assigned to ν(C-N) and ν(C≡N) vibrations of the dca ligands. Meanwhile, during the third weight loss the former are no longer detected while those of the the dca ligands are still present .and can also be observed up to 1300 °C, even if its intensity decreases as temperature increases.

On the basis of these TGA and FT-IR results we have estimated the nature and amount (per formula unit) of the species released during the thermal treatment as follows (see Figure 5-4): (a) the two first weight losses (~50 %) correspond to ~1 dca anions and ~1 TPrA cations; (b) the third weight loss (~20 %) is equivalent to ~1.5 dca anions and (c) the fourth weight loss (~10 %) is assigned to ~0.4 dca anions.

In addition, this thermal decomposition has also been followed by analysing the PXRD patterns of the [TPrA][M(dca)$_3$] samples annealed at 305 °C, 440 °C, 470 °C, 600 °C, 900 °C and 1300 °C. In that context, it should be indicated that both the Ni and Co compounds exhibit the same behaviour illustrated in Figure 5-6 for the Ni-one. The room temperature [TPrA][M(dca)$_3$] (M = Ni^{2+} and Co^{2+}) structure has transformed into M(dca)$_2$ [Ref. 50] in the interval [305-440] °C, with coexistence of amorphous material, evidenced by the hump-shape of de PXRD pattern (Figure 5-7).

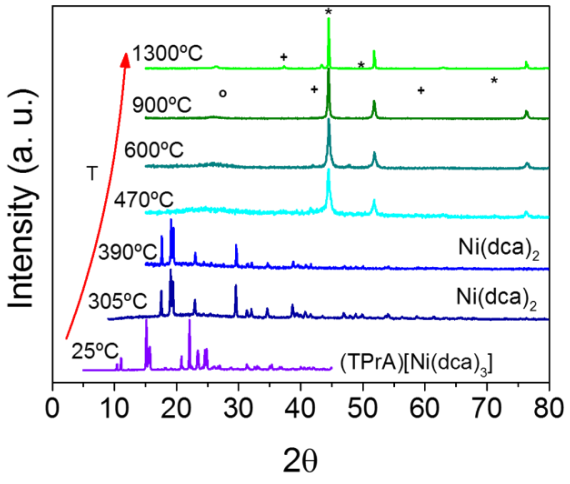

Figure 5-6. Structure evolution as a function of temperature for the precursor Ni compound. These XRD patterns have been obtained by stopping the thermal decomposition of this precursor at the showed temperatures. The XRD pattern have been normalized and displaced along the *Intensity*-axe for a better view. (**o** = graphite; ***** = Ni; **+** = NiO).

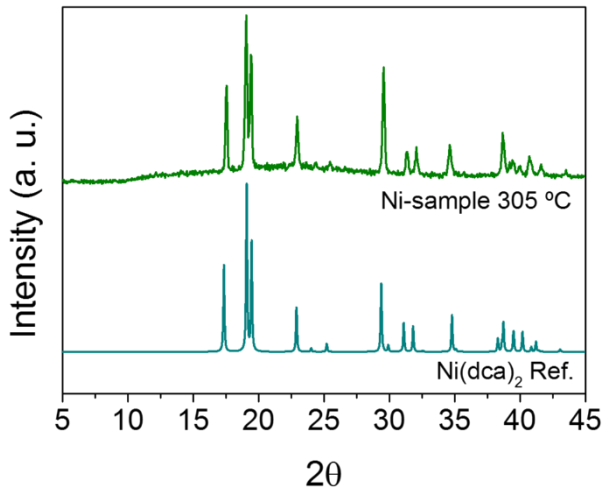

Figure 5-7. PXRD pattern of the [TPrA][Ni(dca)$_3$] precursor material annealed at 305ºC compared with the Ni(dca)$_2$ reported.[44]

After the second weight loss, and from 470 °C to 1300 °C, peaks at around 44.5 (44.2), 51.9 (51.6) and 76.4 (75.8) °2θ are observed in the patterns and assigned to metallic M = Ni^0 and Co^0, respectively, with cubic symmetry (space group *Fm-3m*), and a weak peak around 26.3 °2θ attributed to the characteristic (002) graphite crystallographic plane (Figure 5-8a). At 1300 °C peaks 37.3 (36.5), 43.3 (42.4), and 63.0 (61.6) °2θ are also identified, corresponding to a metal oxide impurity (NiO and CoO, repectively, cubic, S.G.: *Fm-3m*), negligible for lower temperatures.

It is worth noting that in the temperature range [470-900] °C we only observed the coexistence of graphite and metallic Ni^0 and Co^0, respectively, meanwhile at higher temperatures (1300 °C), part of the metals oxidize to the corresponding NiO and CoO. As temperature increases, the peak at 26.3 °2θ becomes narrower and the signal to noise ratio increases (Figure 5-8a), indicating the improvement of the graphite crystallinity. Moreover, the diffraction peaks corresponding to metallic Ni^0 and Co^0 also become narrower (Figure 5-8b), pointing to an increase of the crystal size of the metallic particles with temperature.

Summarizing, during thermal heating the precursor compounds [TPrA][M(dca)$_3$] (M = Ni^{2+} and Co^{2+}), transform into M(dca)$_2$ and an amorphous material in the temperature interval ~[250-450] °C, releasing up to ~1 dca ligand and ~1 TPrA cation per formula unit. Subsequently, in the interval ~[450-900] °C the as-obtained M(dca)$_2$ compound continues releasing dca ligands, and the M^{2+} cations (M = Ni^{2+} and Co^{2+}) get reduced to M^0 metals. In addition, the remaining dca ligands seem to transform into a graphite-like material. Finally, when continuing heating at increasingly higher temperatures, the metallic M^0 particles increase their size while the carbon material improves its crystallinity. Nevertheless, at 1300 °C part of these M^0 particles re-oxidize to M^{2+} forming metal oxides (MO).

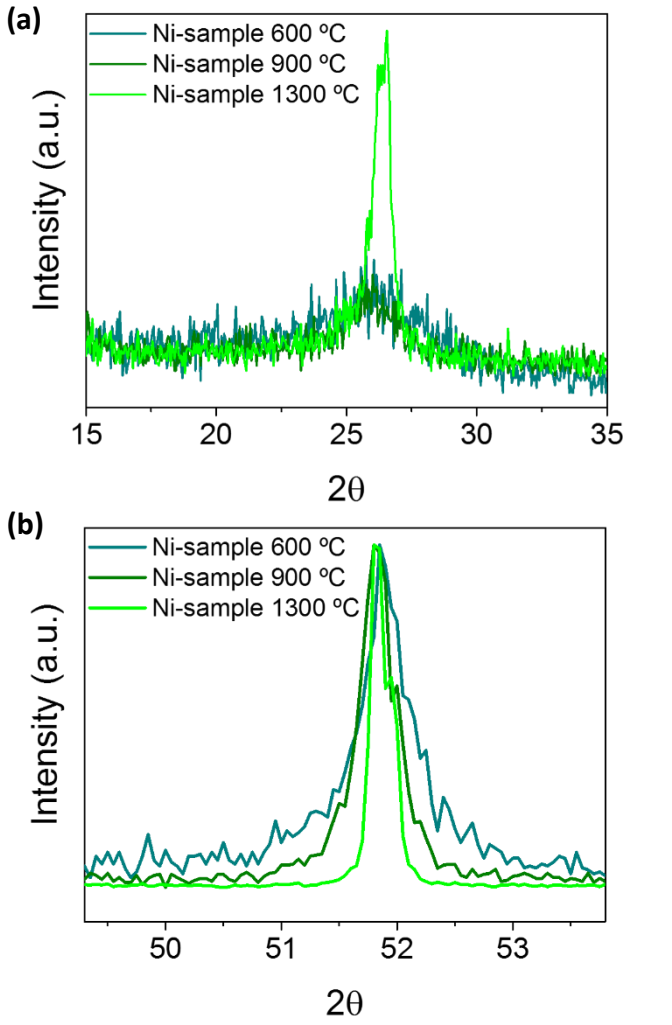

Figure 5-8. (a) Comparison of the graphite peak (26.3 °2θ) for the Ni sample annealed at different temperatures (600 °C, 900 °C and 1300 °C), with absolute intensities. (b) Comparison of the metallic Ni peak (51.9 °2θ) for the Ni sample annealed at different temperatures (600 °C, 900 °C and 1300 °C), with normalized intensities for a better comparison of the peak shape.

5.3.3. Morphology, crystallinity and composition of the M@CNTs

The morphology of the Ni and Co samples at different annealing temperatures (600, 900 and 1300 °C) was studied by transmission electron microscopy (TEM) and is shown in Figure 5-9. As it can be seen there, in the samples annealed at 600 °C metallic nanoparticles covered by amorphous carbon shells are observed together with a few multiwall carbon nanotubes, also embedded with metallic nanoparticles.

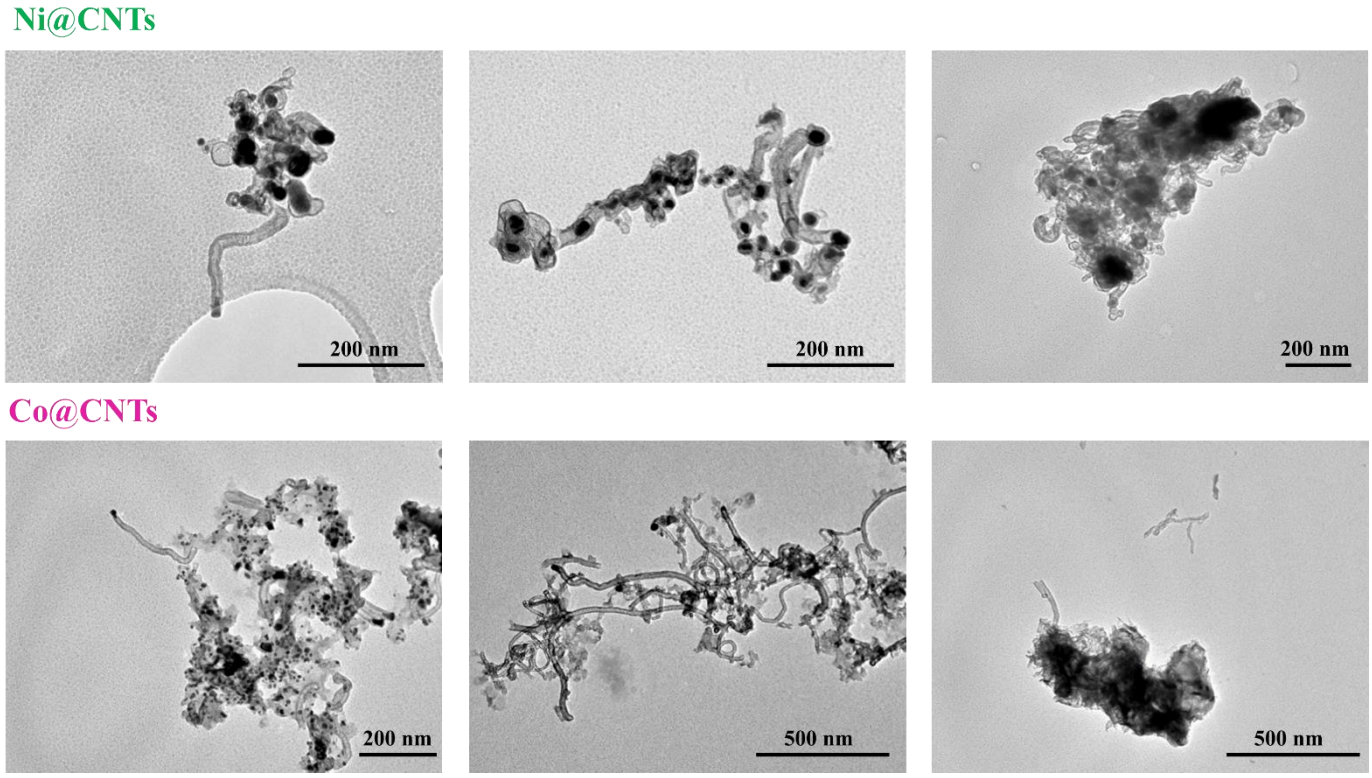

Figure 5-9. TEM micrographs of the samples obtained after annealing at different temperatures: 600 °C, 900 °C and 1300 °C.

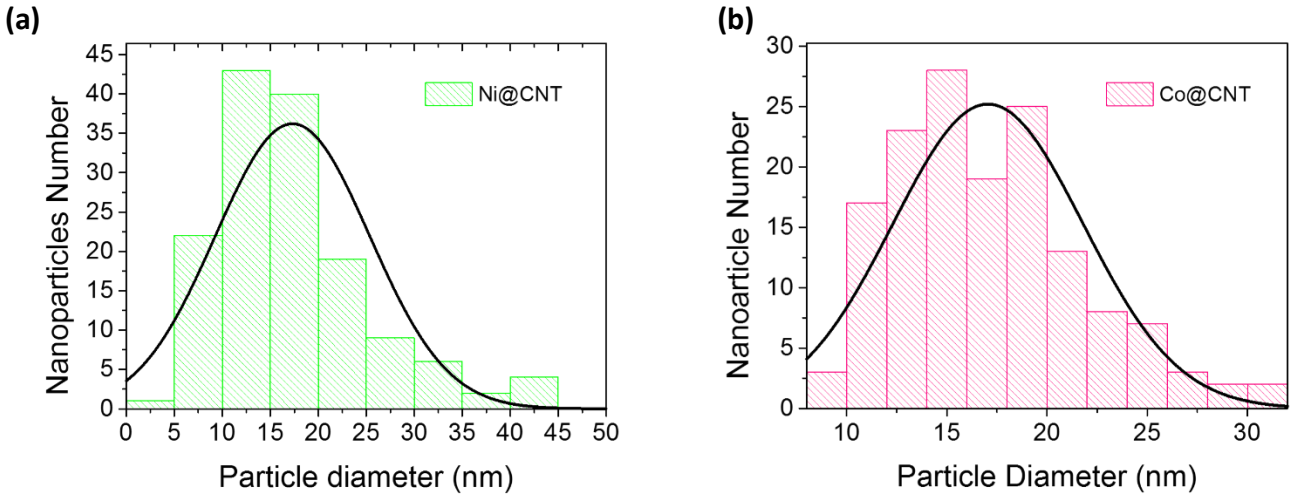

Figure 5-10. Size distribution of the M nanoparticles in the M@CNTs obtained at 900 °C, estimated by measuring the diameter of 100 nanoparticles from TEM micrographs: (a) Ni; (b) Co.

More interestingly, in the samples annealed at 900 °C only well-formed multiwall carbon nanotubes covering the metallic nanoparticles are observed. Such CNTs have a diameter of 24±6 nm and 20±10 nm in the case of the Ni@CNTs and the Co@CNTs, respectively.

Meanwhile, the length of the CNTs is higher for the Co sample, up to 1 µm, compared with 300 nm for the Ni@CNTs. Another interesting remark is that the metal nanoparticle size is of 17±8 nm for Ni and 17±5 nm for Co (Figure 5-10), similar to carbon-coated nanoparticles obtained by other high precision techniques, such as pressure chemical vapour deposition (~20 nm).[52]

Nevertheless, in the case of the 1300 °C-annealed samples bigger agglomerate metallic particles surrounded by a non-so well defined carbon material are identified, indicating the destruction of the CNTs as

observed in the literature.53 This observation suggests that the partial loss of the protection-carbon coat at temperatures as high as 1300 °C allows the partial oxidation of the M^0 to MO, as detected by PXRD patterns.

The crystallinity of the M@CNTs obtained at 900 °C was also checked by Raman spectroscopy. A typical Raman spectra, as that shown in Figure 5-11, consists of a strong band at ~1580 cm^{-1} (G band), assigned to the E_{2g} first-order mode of the graphite plane, other strong band at ~1350 cm^{-1}, assigned to the D band that is related to the presence of defects and impurities in the carbon nanotubes, and a weaker band at ~2570 cm^{-1} (2D band or the second-order harmonic of the D band) in full agreement with the literature for highly graphitized nanostructures.[28,29,54] Nevertheless, the calculated values for the intensity ratio I_D/I_G of 0.95 and 0.70 for Ni@CNTs and Co@CNTs, respectively, reveal the presence of defects in our samples (in higher number in the Ni than in Co sample) due to disruptions of the perfect graphitic lattice of the sp^2-hybridized carbon.[54]

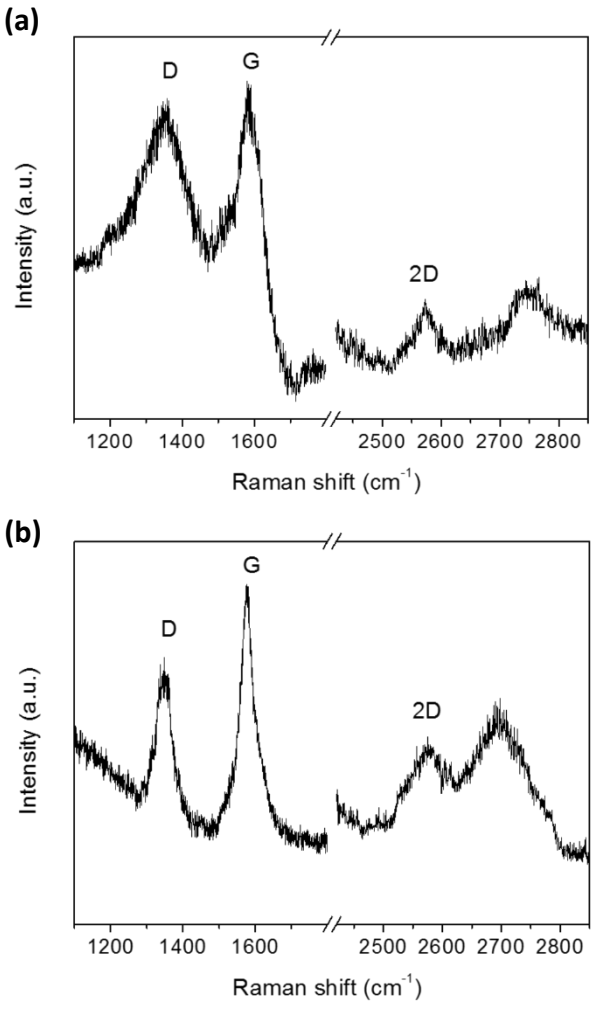

Figure 5-11. Raman spectra of the samples (a) Ni@CNTs and (b) Co@CNTs.

Those defects can be probably caused by the nitrogen incorporation,[43] supporting that the samples obtained contain nitrogen-rich CNTs. Moreover, the chemical composition of the well-formed M@CNTs at 900 °C was estimated by elemental analysis of C, N and H. Table 5-3. summarizes and compares the chemical composition of the $[TPrA][M(dca)_3]$ precursors –calculated from the nominal formula– with the chemical composition of the M@CNTs –found by elemental analysis and deduced from TGA (% relative to the precursor initial mass and % normalized per final M@CNT mass)–.

Table 5-3. Comparison of the elemental composition of the precursors $[TPrA][M(dca)_3]$ (calculated from the nominal formula) and the compounds after annealing at 900 °C from TGA data (% relative and normalized) and from elemental analysis (E.A.) of C, N and H.

		Hybrid Precursor	Annealed at 900 °C (Relative)	Annelaed at 900 °C (Norm.)	E.A.
Ni Comp.	Ni(%)	13.24 %	13.24 %	79.90 %	
	C (%)	48.78 %			19.83 %
	N (%)	31.61 %	3.33 %	20.10 %	1.09 %
	H (%)	6.37 %			< 0.1 %
Co Comp.	Co(%)	13.29 %	13.29 %	55.08 %	
	C (%)	48.76 %			38.93 %
	N (%)	31.59 %	10.84 %	44.92 %	1.26 %
	H (%)	6.36 %			< 0.1 %

As it can be seen there, the elemental analysis of Ni@CNTs leads to C(19.83%), N(1.09%) and H(<0.1%); thus, the rest (~78.98%) can only be reasonably attributable to Ni. This result is in full agreement with the estimations from TGA: around 20.10% of the weight corresponds to the carbon part and the rest (around 79.90%) corresponds to Ni.

In the case of Co@CNTs, the elemental analysis evidences C(38.93%), N(1.26%), H(<0.1%), being 59.71% attributable to Co; meanwhile from TGA we estimate around 55.08% of Co. It is noteworthy that this higher proportion of M in Ni@CNTs (79.90%) compared to Co@CNTs (55.08%) agrees with the results observed by TEM

Another very interesting result is the content of N found in both Ni@CNT (1.09%) and Co@CNT (1.26%) samples, resulting in N/C ratios of 5.5:100 and 3.2:100, respectively comparable to those previously reported in nitrogen-rich carbon nanotubes (i. e. 5.2:100).[43]

5.3.4. Comparison of [TPrA][M(dca)$_3$] with M(dca)$_2$ as precursors of M@CNTs

As thermal monitoring could suggest the M(dca)$_2$ species as starting materials to obtain M@CNTs, we have synthesized the Ni(dca)$_2$ as reported[50] (from now on Ni(dca)$_2$-pure), and we have annealed the sample under similar conditions to those used for [TPrA][Ni(dca)$_3$]. Nevertheless, after the annealing at 900 °C significant different morphology are observed for both samples by TEM (Figure 5-12): the sample from Ni(dca)$_2$-pure results to be much less ordered, with higher size and shape dispersion of the NPs and CNTs. Significantly, the colours of the samples before this annealing at 900 °C were already quite different (as shown in Figure 5-12): Ni(dca)$_2$-pure was green, while the sample derived from [TPrA][Ni(dca)$_3$] annealing was brown (light-brown at 305 °C and dark brown at 440 °C), even if PXRD shows the same Ni(dca)$_2$ crystalline structure for the three samples, but with a hump-shape for the [TPrA][Ni(dca)$_3$]-derived due to the co-existence of some amorphous material (Figure 5-7), as previously commented.

Also the FT-IR spectra are different (Figure 5-13): the annealed [TPrA][Ni(dca)$_3$] exhibit a broader band in the ~[830-1750] cm^{-1} region, which is attributed to the overlapping of the bands associated with new C-C, C=C and C-N bonds formed during the thermal treatment and related to the amorphization. Moreover, the elemental analysis of the [TPrA][Ni(dca)$_3$] annealed at 305 °C exhibit a higher percentage of organic material (% CNH) than the Ni(dca)$_2$-pure (Table 5-4).

Based on these findings, we conclude that the organic TPrA building blocks of the [TPrA][M(dca)$_3$] precursors contribute to the formation of amorphous material which, in turn, play a key role in the morphology of the final M@CNTs.

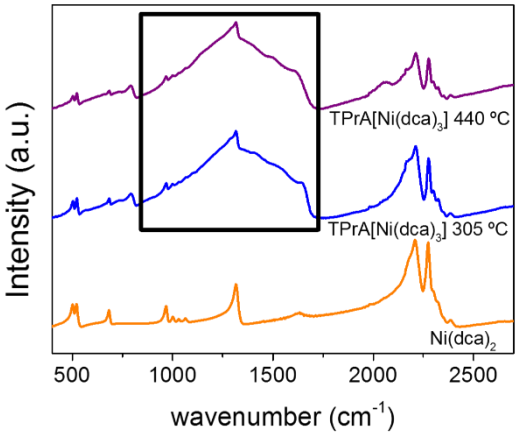

Figure 5-13. FT-IR spectra of the Ni(dca)$_2$-pure (synthesized according to the literature[50]) and the product obtained from the annealing of [TPrA][Ni(dca)$_3$] at 305 °C and 440 °C.

Table 5-4. Elemental analysis of the Ni(dca)$_2$-pure (synthesized accordingly to the literature[50]) and the product obtained from the annealing of [TPrA][Ni(dca)$_3$] at 305 °C and 440 °C.

	% N	% C	% H	% Total (CNH)
Ni(dca)$_2$-pure RT	40,99	23,66	0,54	65,18
[TPrA][Ni(dca)$_3$] 305 °C	38,22	33,75	2,42	74,38
[TPrA][Ni(dca)$_3$] 440 °C	34,88	26,40	1,77	63,05

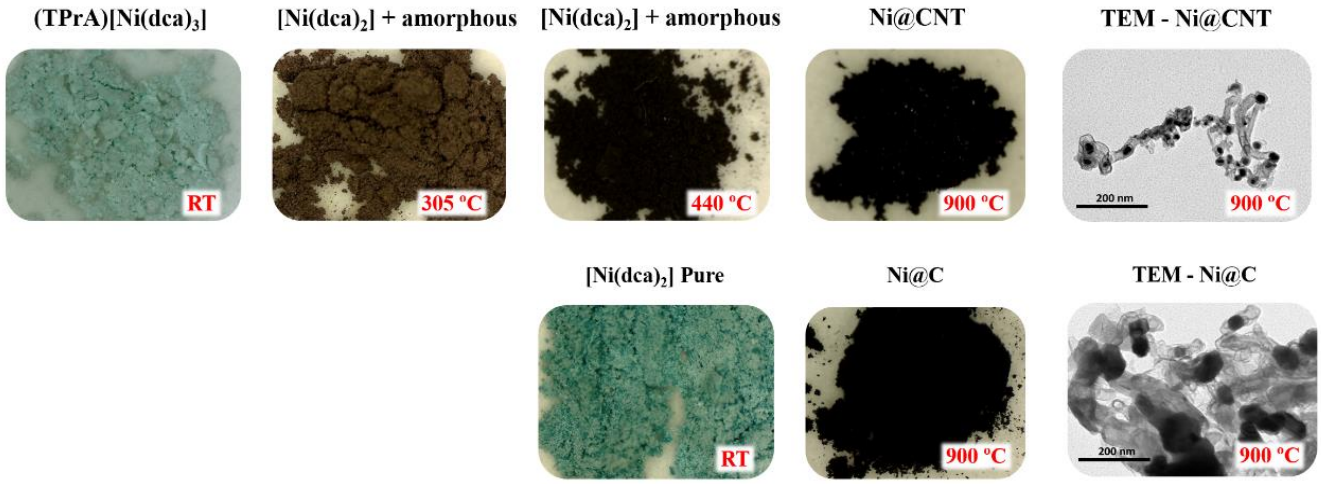

Figure 5-12. Aspect of the Ni(dca)$_2$-pure and [TPrA][Ni(dca)$_3$] samples, at RT and after annealing at different temperatures, as seen by optical microscopy (on the left of the blue line) and transmission electronic microscopy (on the right of the blue line).

5.3.5. Porous structure of M@CNTs

The N_2 adsorption-desorption isotherms and the pore size distributions illustrate the highly mesoporous character of the obtained M@CNTs (Figure 5-14). Ni@CNTs achieve a total pore volume of 0.29 $cm^3\ g^{-1}$ and an equivalent BET-surface area of 235 $m^2\ g^{-1}$, whereas Co@CNTs reach values of 0.19 $cm^3\ g^{-1}$ and 277 $m^2\ g^{-1}$. The more significant difference in the porous structure is the strictly controlled unimodal pore size distribution, centered at around 5 nm, for Ni@CNTs, compared with a broad PSD for Co@CNTs up to 6 nm. (Figure 5-15). The isotherm analysis for both materials by the D-R equation reports characteristic energy E_o of 16-17 kJ mol^{-1}, which indicates somewhat supermicropores of about 1.8-2 nm.[55]

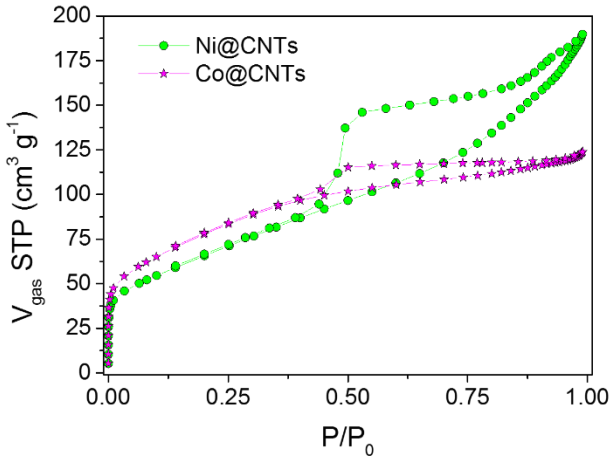

Figure 5-14. N_2 adsorption/desorption isotherms of the M@CNT samples (M = Ni^{2+} and Co^{2+}).

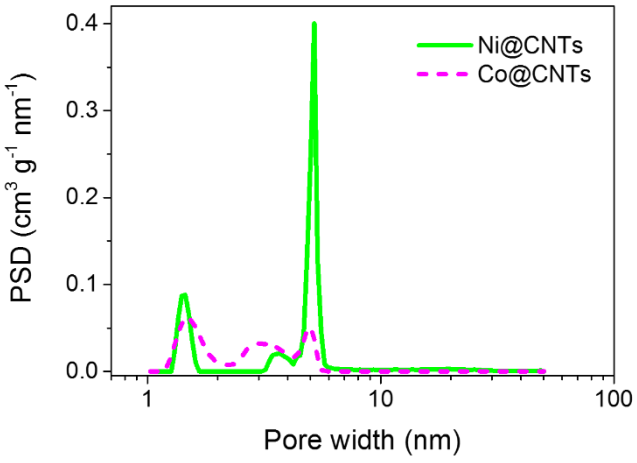

Figure 5-15. Pore size distribution (PSD) versus pore-width for the M@CNTs (M = Ni^{2+} and Co^{2+})

5.3.6. Magnetic characterization of M@CNTs

The room temperature magnetisation versus magnetic field curves of the M@CNTs annealed at 900 °C are shown in Figure 5-16. As it can be seen there, both samples exhibit ferromagnetic behaviour at room temperature as indicated by the open hysteresis loops with remnant magnetisation M_R of 1.79 emu g^{-1} (Ni@CNTs) and 2.01 emu g^{-1} (Co@CNTs), saturation magnetisation M_s reached at rather small magnetic fields (10000 Oe or 1 T), and finite coercive fields H_c (67 Oe and 282 Oe, for Ni@CNT and Co@CNT samples, respectively).

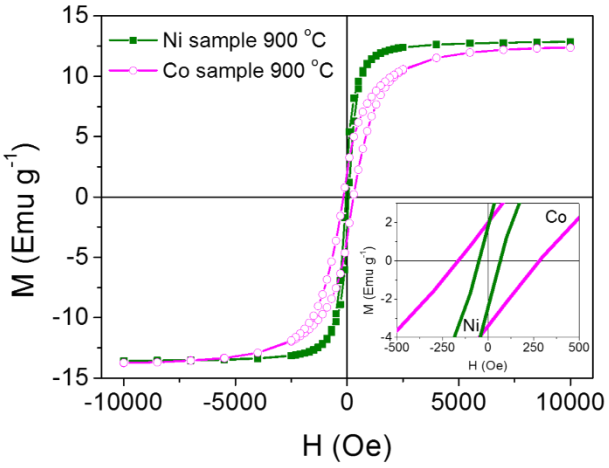

Figure 5-16. Magnetization (emu g^{-1}) versus Magnetic Field (Oe) of M@CNTs obtained at 900 °C, (M = Ni^{2+} and Co^{2+}). Inset: enlarged view of the low field region.

The low values of the M_s (around 12.85 emu g^{-1} for Ni@CNTs and 12.38 emu g^{-1} for Co@CNTs) in comparison to the bulk materials (~54 emu g^{-1} for Ni bulk and ~160 emu g^{-1} for Co bulk)[56] are due to the mass ratio of the magnetic material and the carbon in the M@CNTs.

The particularly small hysteresis and low critical fields H_c for Ni@CNTs is related with the small diameter of the Ni nanoparticles. For Ni and Co this critical diameter (the magnetic single domain size) is calculated to be 55 nm and 15 nm, respectively.[57]

Therefore, in these Ni@CNTs the Ni-particle size is below the critical diameter, while that of the Co-particle size is near the critical diameter value. Consequently, the here proposed synthetic method is a good approximation to obtain ferromagnetic M@CNTs with magnetic NPs near the size region of magnetic single domain.

5.3.7. Oil absorption and desorption

We have also performed preliminary essays of the capability of the obtained M@CNT samples for selective oil adsorption in an oil-water mixture. As showed in Figure 5-17a, the M@CNT sample floated on the oil film,

which shranks toward the sample until saturation of the M@CNTs. After 2 minutes, the oil-saturated M@CNT material could be easily collected using a magnet (see Figure 5-17b).

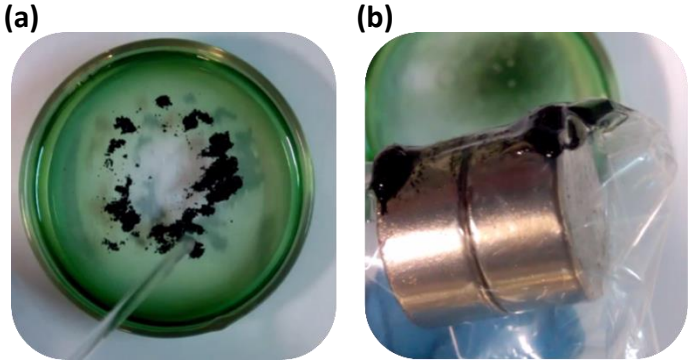

Figure 5-17. (a) M@CNT materials spilled on top of oil-water sample and (b) recovery of M@CNTs with oil adsorbed, using a magnet

After the oil adsorption, the M@CNTs was heated in the TGA equipment from room temperature to 600 °C, with a ramp of 5 °C min^{-1}, in order to thermally desorb the oil pollutant. In these conditions, the oil desorption started at ~70 °C and it was completed at ~450 °C (Figure 5-18a), in the temperature range in which the M@CNTs are thermally stable. As evinced in Figure 5-18b, FT-IR spectra of the gas released indicated only oil desorption in the whole temperature range, therefore confirming selective adsorption of the oil in the M@CNTs while water was not adsorbed. From weight measurements and TGA analysis we found a selectively oil adsorption capacity ($m_{(Oil+M@CNTs)} - m_{(M@CNTs)}/m_{M@CNTs}$) of 2.2 g g^{-1}, for both Ni@CNT and Co@CNT samples.

This oil adsorption capacity, which is comparable to values described in the literature for other carbon-coated magnetic nanoparticles,[58] reveal a promising potential for spilled oil recovery using this easily-synthesized material.

5.4. Conclusions

This work shows that the incorporation of dicyanamide building blocks in organic-inorganic hybrid compounds is a promising strategy to use such materials as precursors for the synthesis of multiwall carbon nanotubes with embedded magnetic nanoparticles (M@CNTs). Herein, it is described a novel one-step, scalable and fast synthetic route that, at difference with other complex CVD or arc-discharge methods, just by direct calcination of the organic-inorganic hybrid perovskite $[TPrA][M(dca)_3]$ (M = Ni^{2+} and Co^{2+}), allows to obtain M@CNTs (M = Ni^0 and Co^0) with regular morphology and essentially mesoporous sturcture. Their specific surface-area is around 250 m^2 g^{-1} but whereas Co@CNTs display a broad pore size distribution up to 6 nm, Ni@CNTs show a strictly controlled unimodal PSD, centered at around 5 nm.

The monitoring techniques for the calcination evolution (TGA, FT-IR and Raman spectroscopies, elemental analysis and PXRD) suggest that the precursors $[TPrA][M(dca)_3]$ (M = Ni^{2+} and Co^{2+}) evolve towards a coexistence of crystalline $M(dca)_2$ (M = Ni^{2+} and Co^{2+}) with amorphous material, which under further heating transform into M@CNTs (M = Ni^0 and Co^0). The calcination temperature is critical to obtain homogeneous well-defined M@CNTs, being ~900 °C the optimal temperature. Meanwhile, at 600 °C the formation of CNTs is not completed and at 1300 °C these CNTs are unstable and the magnetic NPs become less homogeneous and more agglomerated.

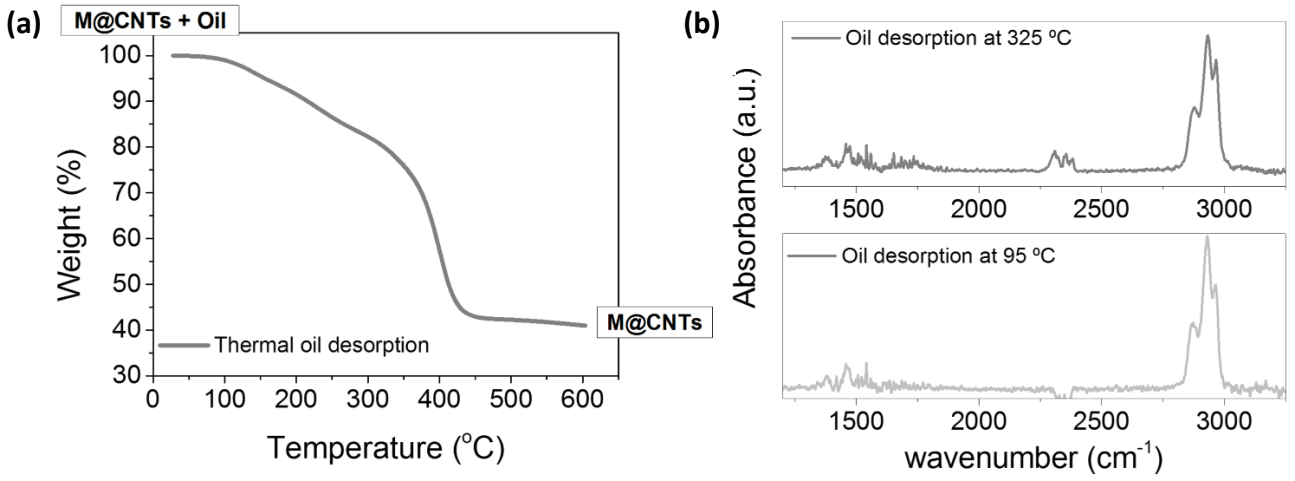

Figure 5-18. (a) TGA graph for the thermal oil desorption from the M@CNT materials, measured from room temperature to 600 °C, with a ramp of 5 °C min^{-1}; and (b) FT-IR spectra of the gas released at 95 °C and 325 °C.

Magnetisation analysis as a function of magnetic field reveals a ferromagnetic behaviour of the obtained M@CNTs, with the magnetic NPs exhibiting particle sizes in the region of magnetic single domain.

Additionally, these M@CNTs can selectively adsorb oil from an oil-water mixture with a capacity of 2.2 g g^{-1}, which was thermally desorbed at temperatures between 70 °C and 450 °C; temperature interval where these M@CNTs remains stable.

In addition, in view of all these physicochemical properties, including the large N/C ratio found in these compounds (up to 5.5:100), render these materials as good candidates for other nitrogen-rich CNT common applications.

This work can, therefore, encourage further research on the applications and development of M@CNTs by this route with improved properties.

5.5. Notes

The work presented in this chapter has been submitted for publication as full paper in a scientific journal.

5.6. References

1 Soldano, C. *Prog. Mater. Sci.* 2015, **69**, 183-212.
2 Zhu, M.; Diao, G. *Nanoscale* 2011, **3**, 2748-2767.
3 Iijima S. *Nature* 1991, **354**, 56-58.
4 Dresselhaus, M. S.; Dresselhaus, G.; Avouris, P. *Carbon Nanotubes: Synthesis, Structure, Properties, and Applications*; Springer-Verlag, New York, 2001.
5 Kwo, J. L.; Yokoyama, M.; Wang, W. C.; Chuang, F. Y.; Lin, I. N. *Diam. Rel. Mater.* 2000, **9**, 1270-1274.
6 Kreupl, F.; Graham, A. P.; Liebau, M.; Duesberg, G. S.; Seidel, R.; Unger, E.; Hönlein, W. *Microel. Eng.* 2002, **64**, 399-408.
7 Ryu, S.W.; Huang, X.-J.; Choi, Y.-K. *Appl. Phys. Lett.* 2007, **91**, 063110.
8 Balents, L.; Egger, R. *Phys. Rev. Lett.* 2000, **85**, 3464-3467.
9 Frackowiaka, E.; Béguin, F. *Carbon*, 2002, **40**, 1775-1787.
10 Pushparaj, V.L.; Shaijumon, M. M. ; Kumar, A.; Murugesan, S.; Ci, L.; Vajtai, R.; Linhardt, R. J.; Nalamasu, O.; Ajayan, P. M. *Proc. Natl. Acad. Sci.* 2007, **104**, 13574-13577.
11 Foldvari M, Bagonluri M. *Nanomed.: Nanotech. Biol. Med.* 2008, **4**, 173-182.
12 Foldvari M, Bagonluri M. *Nanomed.: Nanotech. Biol. Med.* 2008, **4**, 183-200.
13 Gupta, V. K.; Saleh, T. A. *Environ. Sci. Pollut. Res.* 2013, **20**, 2828-2843.
14 Sahoo, S.; Kontos, T.; Furer, J.; Hoffmann, C.; Gräber, M.; Cottet, A. *Nat. Phys*. 2005, **1**, 99-102.
15 Kneipp, K.; Kneipp, H.; Kneipp, J. *Acc. Chem. Res.* 2006, **39**, 443-450.
16 Obukhov. Y.; Pelekhov, D. V.; Kim, J.; Banerjee, P.; Martin, I.; Nazaretski, E.; Movshovich, R.; An, S.; Gramila, T. J.; Batra, S.; Hammel, P. C. *Phys. Rev. Lett.* 2008, **100**, 197601.
17 Yin, M.; Wang, M.; Miao, F.; Ji, Y.; Tian, Z.; Shen, H.; Jia, N. *Carbon* 2012, **50**, 2162-2170.
18 Hampel, S.; Kunze, D.; Haase, D.; Krämer, K.; Rauschenbach, M.; Ritschel, M.; Leonhardt, A.; Thomas, J.; Oswald, S.; Hoffmann, V.; Büchner, B. *Nanomed.* 2008, **3**, 175-82.
19 Svensson, K.; Olin, H.; Olsson, E. *Phys. Rev. Lett.* 2004, **93**, 145901.
20 Krupskaya, Y.; Mahn, C.; Parameswaran, A.; Taylor, A.; Krämer, K.; Hampel, S.; Leonhardt, A.; Ritschel, M.; Büchner, B.; Klingeler, R. *J. Magn. Magn. Mater.* 2009, **321**, 4067-4071.
21 Chaikittisilp, W.; Ariga, K.; Yamauchi, Y. *J. Mater. Chem. A* 2013, **1**, 14-19.
22 Hu, M.; Reboul, J.; Furukawa, S.; Radhakrishnan, L.; Zhang, Y.; Srinivasu, P.; Iwai, H.; Wang, H.; Nemoto, Y.; Suzuki, N.; Kitagawa, S.; Yamauchi, Y. *Chem. Commun.*, 2011, **47**, 8124-8126.
23 Hu, M.; Reboul, J.; Furukawa, S.; Torad, N. L.; Ji, Q.; Srinivasu, P.; Ariga, K.; Kitagawa, S.; Yamauchi, Y. *J. Am. Chem. Soc.* 2012, **134**, 2864-2867.
24 Hu, J.; Wang, H.; Gao, Q.; Guo, H. *Carbon* 2010, **48**, 3599-3606.
25 Yang, S. J.; Kim, T.; Im, J. H.; S. Kim, Y.; Lee, K.; Jung, H.; Park, C. R. *Chem. Mater.*2012, **24**, 464-470.
26 Chaikittisilp, W.; Hu, M.; Wang, H.; Huang, H.-S.; Fujita, T.; Wu, K. C.-W.; Chen, L.-C.; Yamauchi, Y.; Ariga, K. *Chem. Commun.* 2012, **48**, 7259-7261.
27 Torad, N. L.; Hu, M.; Ishihara, S.; Sukegawa, H.; Belik, A. A.; Imura, M.; Ariga, K.; Sakka, Y.; Yamauchi, Y. *Small* 2014, **10**, 2096-2107.
28 Zhang, L.; Wang, X.; Wang, R.;Hong, M. *Chem. Mater.* 2015, **27**, 7610-7618.
29 Chen, L.; Bai, J.; Wang, C.; Pan, Y.; Scheerc, M.; You, X. *Chem. Commun.* 2008, 1581-1583.
30 Madelung, W.; Kern, E. *Liebigs Ann. Chem.* 1922, **427**, 26-34.
31 Jürgens, B.; Milius, W.; Morys, P.; Schnick, W.Z. *Anorg. Allg. Chem.* 1998, **624**, 91-97.
32 Jürgens, B.; Irran,E.; Schneider,J.; Schnick, W. *Inorg. Chem.* 2000, **39**, 665-670.
33 Yancey, B.; Vyazovkin, S. *Phys. Chem. Chem. Phys.* 2014, **16**, 11409-11416.
34 Lotsch, B. V.; Schnick, W. *Chem. Mater.* 2006, **18**, 1891-1900.
35 Paraknowitsch, J. P.; Sukhbat, O.; Zhang, Y.; Thomas, A. *Eur. J. Inorg. Chem.*2012, 4105-4116.
36 Yuan, J. Y.; Giordano, C.; Antonietti, M. *Chem. Mater.* 2010, **22**, 5003-5012.
37 Paraknowitsch, J. P.; Zhang, J.; Su, D.; Thomas, A.; Antonietti, M. *Adv. Mater.* 2010, **22**, 87-92.

38 Jürgens, B.; Höppe, H. A.; Irran, E.; Schnick, W. *Inorg. Chem.* 2002, **41**, 4849-4851.
39 Lotsch, B. V.; Senker, J.; Kockelmann, W.; Schnick, W. *J. Solid State Chem.* 2003, **176**, 180-191.
40 Lotsch, B. V.; Senker, J.; Schnick, W. *Inorg. Chem.* 2004, **43**, 895-904.
41 Lotsch, B. V.; Schnick, W. *New J. Chem.* 2004, **28**, 1129-1136.
42 Lotsch, B. V.; Schnick, W. *Chem. Mater.* 2005, **17**, 3976-3982.
43 Zou, X.; Huang, X.; Goswami, A.; Silva, R.; Sathe, B. R.; Mikmeková, E.; Asefa, T. *Angew. Chem.* 2014, **126**, 4461-4465.
44 Schlueter, J. A; Manson, J. L.; Geiser, U. *Inorg. Chem.*2005, **44**, 3194-3202.
45 Bermúdez-García, J. M.; Sánchez-Andújar, M.; Yáñez-Vilar, S.; Castro-García, S.; Artiaga, R.; López-Beceiro, J.; Botana, L.; Alegría, A.; Señarís-Rodríguez, M. A. *Inorg. Chem.*, 2015, **54**, 11680-11687.
46 Bermúdez-García, J. M.; Sánchez-Andújar, M.; Yáñez-Vilar, S.; Castro-García, S.; Artiaga, R.; López-Beceiro, J.; Botana, L.; Alegría, A.; Señarís-Rodríguez, M. A. *J. Mater. Chem. C*, 2016, **4**, 4889-4898.
47 Mercury 3.5.1 (Build RC5) - Crystal Structure Visualisation (CCDC) www.ccdc.cam.ac.uk/mercury.
48 Larson, A. C.; Von Dreele, R.B. General Structure Analysis System (GSAS), Los Alamos National Laboratory Report LAUR 2000, 86-748.
49 Toby, B. H. EXPGUI, a graphical user interface for GSAS, *J. Appl. Cryst.* 2001, **34**, 210-213.
50 Manson, J. L.; Kmety, C. R.; Huang, Q.-Z.; Lynn, J. W.; Bendele, G. M.; Pagola, S.; Stephens, P. W.; Liable-Sands, L. M.; Rheingold, A. L.; Epstein, A. J.; Miller, J. S. *Chem. Mater.*1998, **10**, 2552-2560.
51 Neimark, A.V.; Lin, Y.; Ravikovitch, P.I.; Thommes, M. *Carbon*, 2009, **47**, 1617-1628.
52 El-Glendy, A. A.; Ibrahim, E. M. M.; Khaurus, V. O.; Krupskaya, Y.; Hampel, S.; Leonhardt, A.; Büchner, B.; Klingeler, R. *Carbon* 2009, **47**, 2821-2828.
53 Mahajan, A.; Kingon, Kukovecz, A.; Konya, Z., Vilarinho, P. M. *Materials Letters* 2013, **90**, 165-168.
54 Sadezky, A.; Muckenhuber, H.; Grothe, H.; Niessner, R.; Pöschl, U. *Carbon* 2005, **43**, 1731-1742.
55 Stoeckli, F. Porosity in Carbons: Characterization and Aplications. Ed. J. W. Patrick. Chapter 3, pages 67-92. Eduard Arnold. London 1995.
56 Pauthenet, R. *J. Appl. Phys.*1982, **53**, 8187-8192.
57 Ma, M.; Wu, Y.; Zhou, J.; Sun, Y.; Zhang, Y.; Gul, N. *J. Magn. Magn. Mater.* 2004, **268**, 33-39.
58 Zhu, Q.; Tao, F.; Pan, Q. *ACS Appl. Mater. Interfaces*, 2010, **2**, 3141-3146.

Chapter 6:

New properties in old systems: cooperative electric order in ferrocene and ammonia-borane

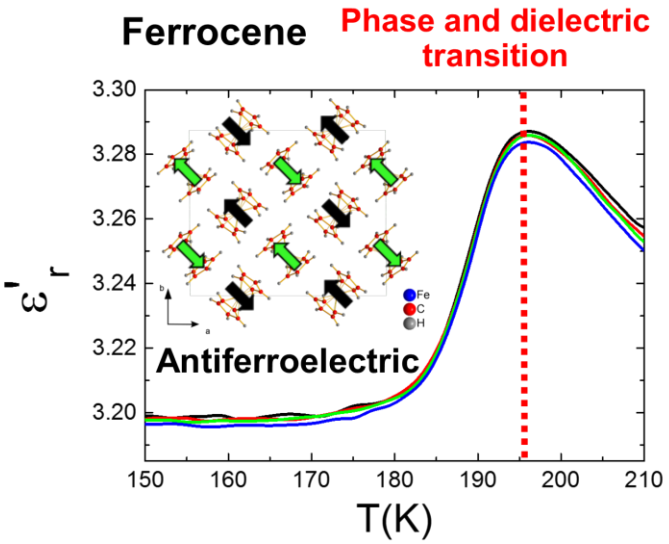

New properties in old systems: cooperative electric order in ferrocene and ammonia-borane

Abstract: In our search for novel functional properties associated with order-disorder or displacement phase transitions we revisit two "old" molecular compounds, namely ferrocene [$Fe(C_5H_5)_2$] and ammonia-borane ($H_3N{\cdot}BH_3$). After half a century of intensive and extensive studies on these "classical" compounds, it is very exciting to observe that they still hide interesting properties never described before. Despite it being well-known that they both experience phase transitions as a function of temperature, here, for the first time, we give experimental evidence for the dielectric transitions they experience associated to the former, results that we support with DFT calculations. In that context, we report that ferrocene displays a thermally-induced paraelectric to antiferroelectric transition associated to the monoclinic-triclinic transition, which implies order-disorder of the cyclopentadienyl (Cp) ligands and displacement of the Fe atoms within the ferrocene molecules. As for the ammonia-borane, we report a sharp dielectric transition at $T \approx 232$ K, associated to a structural transition that combines ordering and atomic displacement of the $H_3N{\cdot}BH_3$ molecules. In this case, we attribute such behaviour to the temperature dependent displacement of the $H_3N{\cdot}BH_3$ molecules out-of the crystal polar *c*-axis.

6.1. Introduction and objectives

Solids are known to undergo a variety of phase transitions accompanied by significant changes in some of the properties. Therefore, the study of structural transitions, as well as their implications, is of major interest to scientists working in very diverse areas, ranging from theoretical physics and chemistry to materials technology.

Typical examples of phase transitions that play a major role in driving a function to a material are those involving changes in magnetic, electrical and dielectric properties.[1] Within this latter, those leading to cooperative electric order (specially ferro- or ferri-electric dipole arrangements) attract great attention because of the significant applications of the resulting materials in electric and electronic devices, such as capacitors, temperature sensors, data storage memories, mechanical actuators, and so on.[2]

In that context, two main types of phase transitions are known to be the underlying cause for the appearance of cooperative electric ordering in some solids, namely displacive and order-disorder transitions[3] even if they often appear associated.[4]

Various approaches have been developed to prepare novel materials with phase transition-induced dielectric properties. Among them, the search for solid compounds in which freezing and reorientation of polar molecules and/or ionic groups can occur and easily lead to phase transitions and associated cooperative electric order. In this context, the organic–inorganic hybrid compounds also known as metal-organic frameworks (MOFs)[2] and molecular solids have been recently claimed to be excellent candidates to show phase transition behaviours,[5] even if their behaviours have been much less explored than that of other non-molecular solids. And very outstanding ferroelectric (and even multiferroic) materials have already been discovered among the former, such as (DMA)[$Mn(HCOO)_3$] (where DMA is the dimethylammonium cation).[6,7]

In this paper, we focus on the family of molecular solids to illustrate and emphasize the important role of phase transitions on the properties of "old" compounds, albeit with new properties, belonging to this category.

For this purpose, we revisit two very famous "classical" molecular compounds, such as ferrocene, bis(cyclopentadienyl)iron, [$Fe(C_5H_5)_2$] and ammonia-borane ($H_3N{\cdot}BH_3$). These compounds are known to experience phase transitions as a function of temperature, and their structural characteristics render them good candidates to display interesting dielectric behaviour even if such structure-property relationship has up to now remained unexplored.

As for the first of these compounds, since its discovery in 1951 the impact of such breakthrough and pioneering work has been enormous.[8] Ferrocene opened new areas of chemistry, deepened our understanding of structure, bonding, and reactivity, and paved the way for the burgeoning field of organometallic chemistry itself.[9]

It is well-known that ferrocene displays an order-disorder/displacive phase transition at $T_t \approx 164$K. From the structural point of view, this phase transition involves two different crystalline polymorphs:[10] the orange high temperature HT-phase (monoclinic) and the canary-yellow low-temperature LT-phase (triclinic). The first of them, that is also the room temperature polymorph, is monoclinic with space group $P2_1/a$, Z = 2. It contains only one type of centrosymmetric ferrocene molecules, that is the basis for the centrosymmetric staggered molecular structure[11] usually shown in textbooks (Figure 6-1a). Nevertheless, the apparent centrosymmetry of the ferrocene molecule is not a genuine molecular property, but the result of the statistical distribution of the cyclopentadienyl (Cp) ring orientations into the averaged structure (dynamically disordered). In fact, ferrocene is an artificial molecular rotor,[12] being perhaps the simplest type of molecular carousel, a compound consisting of two or more planar (or nearly planar) "decks" which rotate and remain parallel to each other.

Below $T_t \approx 164$ K, the rotation of the Cp rings gets frozen[13] and the ferrocene crystals become triclinic (space group $F\bar{1}$, Z = 16). The resulting LT-phase is closely related to the HT-phase one, but it presents two main differences respect to the HT-phase: (i) the ferrocene Cp rings adopt an almost eclipsed conformation ($\alpha \approx 9°$) (Figure 6-1b), and (ii) there are two slightly distinct types of non-centrosymmetric ferrocene molecules,[14] (we will come back to this point in the "Results and discussion" section).

In relation to the second compound, ammonia-borane is a white crystalline solid that was first prepared in 1955.[15] This compound is presented in almost all chemistry textbooks as an example of a Lewis acid/base adduct[16] and more recently it is attracting increased attention in view of its potential as a hydrogen storage material.[17]

The ammonia-borane displays an order-disorder/displacive phase transition at $T_t \approx 225$ K. From the structural point of view, ammonia-borane can adopt two different crystal structures at ambient pressure both of which are non-centrosymmetric: the tetragonal high temperature HT-phase with space group $I4mm$[18-20] and the orthorhombic low temperature LT-phase with space group $Pmn2_1$, see Figure 6-2. In the HT-phase, the $H_3N{\cdot}BH_3$ molecules are collinear to the *c*-axis and the H-atoms are disordered over different crystallographic sites.[21] On cooling below $T_t \approx 225$ K the ammonia-borane crystals become orthorhombic. In contrast with the HT-polymorph, in this LT-structure the $H_3N{\cdot}BH_3$ molecules are alternatively tilted along the *c*-axis and the H-atoms are ordered in a single crystallographic site, see Figure 6-2.

Despite extensive and intense studies on ferrocene and ammonia-borane in many different contexts, very little attention has been paid to their dipole moment structure and associated dielectric response.

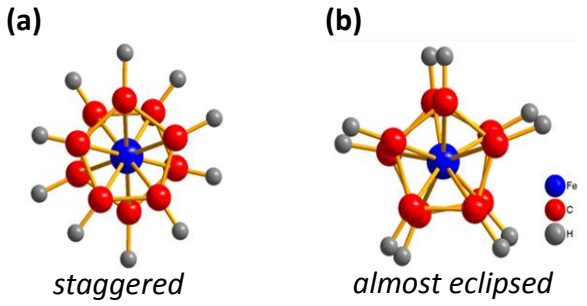

Figure 6-1. Representations of the two different molecular conformations of ferrocene presented in the two crystalline polymorphs of this compound: (a) staggered (monoclinic HT-phase) and (b) almost eclipsed (triclinic LT-phase).

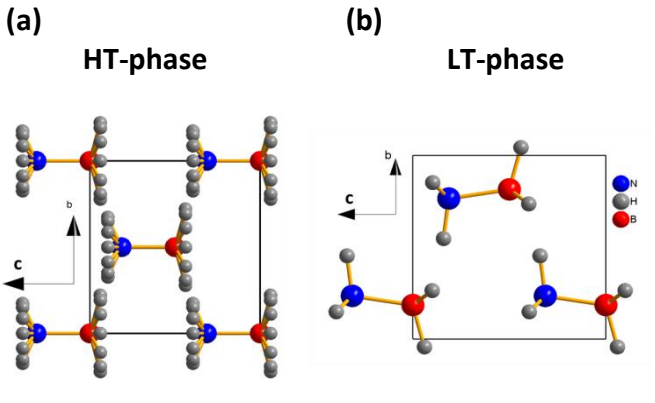

Figure 6-2. Crystal structure of the ammonia-borane polymorphs: (a) HT-phase with H-atoms disordered and the molecules collinear to the *c*-axis and (b) LT-phase with H-atoms ordered and the molecules tilted along the *c*-axis.

In that context, just Gaffar *et al.*[22] published a paper about the influence of γ-radiation on the electric and dielectric properties of ferrocene. However, this study had focused mainly on the former and just briefly makes reference to a weak dielectric anomaly associated to the order-disorder transition, without analysing its origin and implications. As for the ammonia-borane, to the best of our knowledge there are no previous studies that refer to its dielectric behaviour.

In the present work, we give experimental evidence of the dielectric response of both ferrocene and ammonia-borane and we use DFT calculations to justify their dipolar structures. Remarkably, we discover a dielectric transition associated to a phase transition in both inorganic compounds. We rationalize the obtained results on the basis of structure-properties relationships, which we establish taking into account their dipole moment distributions, and that we calculate using reported crystal data.

6.2. Experimental section

6.2.1. Materials

Ferrocene (98%, Aldrich) and ammonia-borane (97%, Aldrich) were commercially available and used as purchased without further purification.

6.2.2. Dielectric properties

The complex dielectric permittivity ($\varepsilon_r = \varepsilon'_r - i\,\varepsilon''_r$) of the cold-press pelletized samples was measured as a function of frequency and temperature with a parallel-plate capacitor coupled to a Solartron 1260A Impedance/Gain-Phase Analyzer, capable to measure in the frequency range from 10 μHz up to 32 MHz with an accuracy of 0.1% using an amplitude of 2 V. The capacitor was mounted in a Janis SVT200T cryostat refrigerated with liquid nitrogen, and with a Lakeshore 332 incorporated to control the temperature from 78 K up to 400 K. The data were collected on heating and cooling and before carrying out the measurements, the pellets were kept for two minutes at each temperature so as to reach the thermal equilibrium. The impedance analysis software SMART (Solartron Analytical) was used for data acquisition and processing. Impedance complex plane plots were analyzed using the LEVM program, a particular program for complex nonlinear least squares fitting.[23]

Pelletized samples made out of cold-press nonoriented single crystal with an area of approximately 530 mm^2 and a thickness of approximately 1 mm were prepared to fit into the capacitor, and silver paste was painted on their surfaces to ensure a good electrical contact with the electrodes.

All the dielectric measurements were carried out in a nitrogen atmosphere where several cycles of vacuum and nitrogen gas were performed to ensure that the sample environment is free of water.

Attempts to directly measure single crystals failed, as these break into powder at the phase transition.

6.2.3. Quantum calculations

All the values for the calculation of the electric dipole moments presented in this work were performed employing the Gaussian 09 package (Revision D.01).[24] Single point energy calculations were performed employing DFT within the hybrid-GGA (generalized gradient approximation) with the B3LYP exchange-correlation functional. Input geometries were generated from the crystallographic data of ferrocene[14] and of ammonia-borane[19,25] reported at the literature. The standard 6-31+G(d) basis set was used throughout this work for non-metallic atoms and TZVP (5d,7f)-valence triple-zeta plus polarization basis set was used for iron atoms.

6.3. Results and discussion

6.3.1. Ferrocene

Figure 6-3 shows the temperature dependence of the real part of the complex dielectric permittivity (the so-called dielectric constant) ε'_r of ferrocene measured upon heating and cooling the sample. Very interestingly, in both types of experiments, the ε'_r vs temperature curve displays a small and broad peak, that is seen to occur at $T_{heat.} \approx 195$ K on heating, and at $T_{cool.} \approx 175$ K on cooling.

Such features are fully reproducible and can not be attributed to the experimental error of the measurement. These anomalies in the dielectric constant occur close to the temperature reported for the phase transition, which according to differential scanning calorimetry (DSC) measurements take place on cooling at $T_{cool.} \approx 169$ K and ≈ 164 K.[26]

Also, the observed thermal hysteresis is characteristic of a first-order transition.[6]

In addition, for temperatures higher than T_t (region II in Figure 6-3), ε'_r is seen to decrease as temperature increases further following the typical trend of a paraelectric behaviour. Meanwhile the drop below T_t (region I) resembles a paraelectric-antiferroelectric transition.

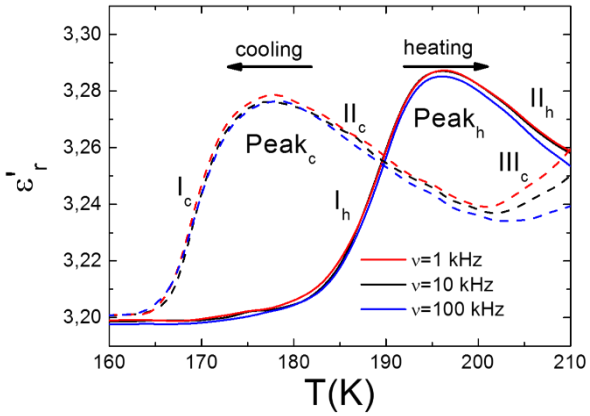

Figure 6-3. Temperature dependence of the dielectric constant of ferrocene, measured at different frequencies upon heating (solid lines) and cooling (dash lines). The presence of a broad maximum at the transition temperature, either $T_{cool.}$ or $T_{heat.}$, is highlighted and the roman numbers (with the corresponding subscript "h" for heating" and "c" for cooling) are labels for regions with different dielectric behaviours (see text).

It should be noted that in these two regions the dielectric response is purely intrinsic of the bulk of the material, as confirmed by impedance complex plane analysis of the obtained data (Figure 6-4).

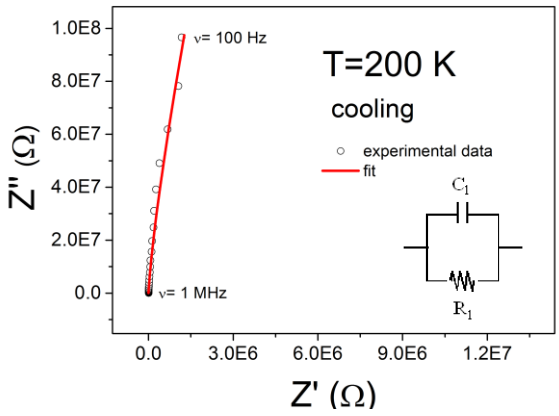

Figure 6-4. Typical impedance complex plane of ferrocene and its corresponding fit representative of the temperatures around the transition and below.

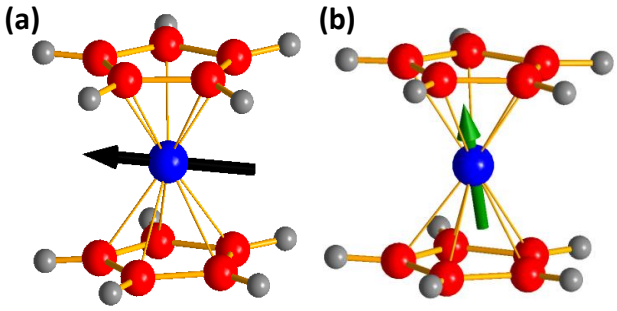

Type I-ferrocene molecule μ_I**=0.082 D**

Type II-ferrocene molecule μ_{II}**=0.043 D**

Figure 6-5. Representations of the two types of ferrocene molecules present in the LT-phase. The arrows represent the electrical dipole moments (not drawn to scale) of these molecules.

In addition to this intrinsic behaviour, an extrinsic one is observed for higher temperatures, region III (T > 200 K on cooling and T > 215 K on heating) that gives rise to a new rise in ε'_r as temperature increases.

With the aim of understanding the intrinsic dielectric response of the ferrocene, we have further explored the characteristics of the low and high temperature phases, paying special attention to the distribution of the associated dipole moments, as obtained from the DFT calculations. In the HT-phase, where the ferrocene molecules are centrosymmetric, the only possible origin for dipole moments are the cyclopentadienyl ligands, that carry a very weak dipole moment of μ = 0.006 D. Nevertheless, as in this HT-phase the Cp rings have a "free" rotation movement around the iron axle, their associated dipole moment gets averaged out. Meanwhile, in the LT-phase the situation is much more complex. As indicated before, in this polymorph there are two slightly different types of ferrocene molecules[14] (hereafter named as I and II). Their main differences rely in the rotation angle of the two Cp ligands and the position of the Fe atoms inside the Cp_2 sandwich.[14] In any case both types of ferrocene molecules are non-centrosymmetric as the Fe-atoms are off-center shifted from the inversion center of the sandwich. The calculated dipole moment associated to these ferrocene molecules is small, even if one order of magnitude higher than in the case of the Cp ligand; and its value in molecules type I is almost twice as high as that displayed by molecules type II: $\mu_{tricl\text{-}I}$ = 0.082 D versus $\mu_{tricl\text{-}II}$ = 0.043 D. Moreover, according to the calculations the orientation of their corresponding dipole moments also differs: in the case of the ferrocene molecules type I, the associated dipole is arranged parallel to the two cyclopentadienyl rings (see Figure 6-5a), while in the ferrocene molecules type II it is arranged towards one of the cyclopentadienyl rings (see Figure 6-5b).

The peculiar arrangement of both types of ferrocene molecules within the LT-crystal structure yields to a cooperative antiferroelectric arrangement of dipole moments, where all the dipoles get cancelled out in the unit cell, as sketched in Figure 6-6.

With all this information in mind, we can rationalize the dielectric response of ferrocene as follows:

The observed paraelectric behaviour for T > 190 K is due to the fact that at those temperatures the Cp ligands are not static but are rotating, as thermal energy is high enough to allow for such a process. As a consequence, the electrical dipoles associated to the ferrocene molecules will average in different directions upon rotation and account for the observed paraelectric behaviour. As temperature decreases, the speed of rotation of the cyclopentadienyl rings slows down and, as a consequence, ε'_r increases.

At around T_t ≈ 164 K, the order-disorder transition associated to the freezing of the molecular rotation of the Cp ligands takes place: below that temperature the Cp rings can no longer rotate and have their positions fixed within the ferrocene molecules. Simultaneously, the Fe atoms experience an off-center shift within the Cp_2 sandwiches, while the relative distribution of the ferrocene molecules is preserved, and a change in the symmetry of the crystal occurs.

Even more, the off-center shift of the Fe atoms within the molecules is cooperative, and results in a global compensation of their associated electric dipoles. This gives rise to a drop in the dielectric constant, which signals the occurrence of the corresponding paraelectric - antiferroelectric transition.

Nevertheless, as the values of the electric dipole moment of the ferrocene molecules are low, the observed dielectric anomaly is much smaller than in the case of other antiferroelectric materials.[3]

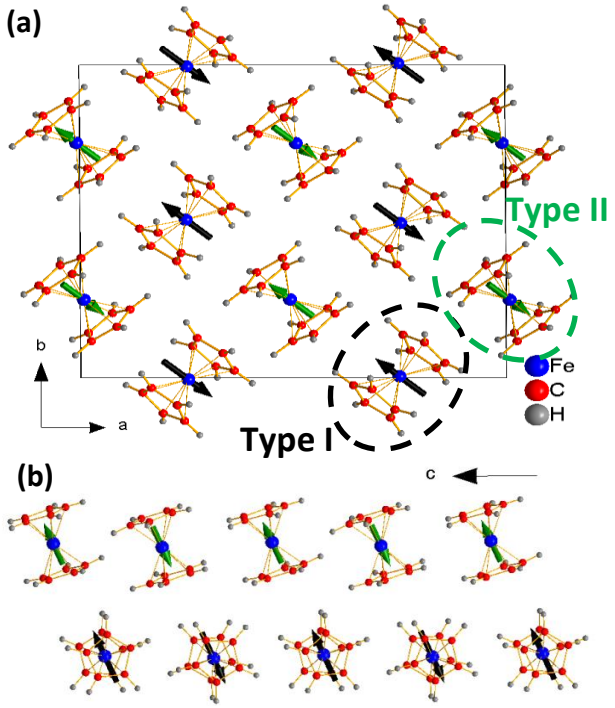

Figure 6-6. Dipole distribution in the triclinic LT-phase of ferrocene: (a) within the *ab*-plane and (b) along the *c*-axis. Arrows represent the electric dipole moment of the ferrocene molecules (black for molecules type I and green molecules type II).

Finally, we attribute the rise in ε'_r in region III to the presence of extrinsic effects, such as moisture molecules at the surface of the measured pellet, that the higher the temperature the more significantly contribute to the signal in that temperature interval.

A similar feature has been observed, for example, in the recently studied hybrid organic-inorganic compounds with perovskite-like structure of general formula (DMA)[M $(HCOO)_3$] (M^{2+} = Mg^{2+}, Mn^{2+}, Fe^{2+}, Co^{2+}, Ni^{2+} and Zn^{2+}) exhibiting dielectric transitions.[6,7]

6.3.2. Ammonia-borane

Figure 6-7 shows the temperature dependence of the real part of the complex dielectric permittivity ε'_r of ammonia-borane. Very interestingly, the ε'_r versus temperature curve displays a sharp kink around $T \approx 232$ K, close to the temperature reported for the structural transition as seen by DSC measurements.[27] As it can be observed ε'_r is frequency independent and increases with temperature in the whole studied temperature range. Another interesting remark is the almost linear behaviour of ε'_r(T) for $T > 232$ K.

To further deepen in the origin of the observed dielectric transition, we focus again our attention on the dipole moment associated to the molecules and their distribution within the crystal.

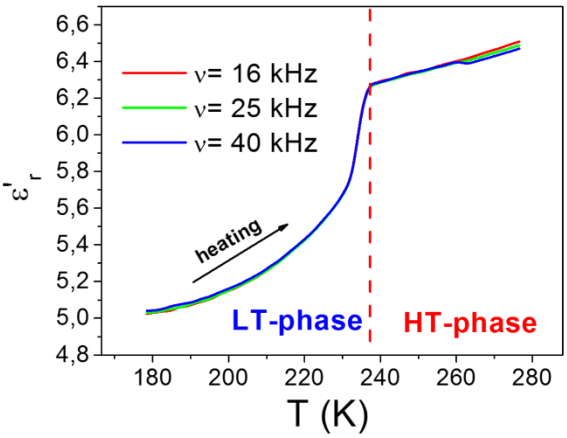

Figure 6-7. Dielectric constant of ammonia-borane as a function of temperature measured at different frequencies.

We have calculated an electric dipole moment of $\mu \approx 5.67$ D associated to the ammonia-borane molecules, which is collinear to the molecule axis. To estimate their distribution in the crystal, we have examined closely their contribution along the *c*-axis, taking into account that both polymorphs, LT-phase (orthorhombic) and HT-phase (tetragonal), display non-centrosymmetric space groups with an unique polar direction along the *c*-axis, (by symmetry the dipole is not cancelled uniquely along the *c*-axis). In the HT-phase, the $H_3N{\cdot}BH_3$ molecules are collinear with the *c*-axis, and so are the associated electric dipole moments (see Figure 6-8a). The parallel arrangement of the dipoles gives rise to a net polarization that accounts for the higher values of the dielectric constant for $T > 240$ K. Meanwhile, in the LT-phase (see Figure 6-8b), the molecule arrangement becomes buckled and the molecules are slightly inclined along the polar *c*-axis.

Since the material polarization comes exclusively from the component of the dipole moments along the *c*-axis, the effective net value gets reduced as a function of these dipole moments shift. Therefore, such contribution is related to the tilting of the $H_3N{\cdot}BH_3$ molecules out-of the polar *c*-axis, so that the larger is this tilting the smaller becomes the resulting dielectric constant, see Figure 6-9.

In that context, it is known that in this LT-phase the angle between the molecules and the polar *c*-axis increases upon cooling (from 18° at 200 K (ref. 19) to 26° at 90 K (ref 21)). That is the reason why the dielectric constant -that has already dropped as compared to the HT-phase- continues to decrease further as the temperature is reduced.

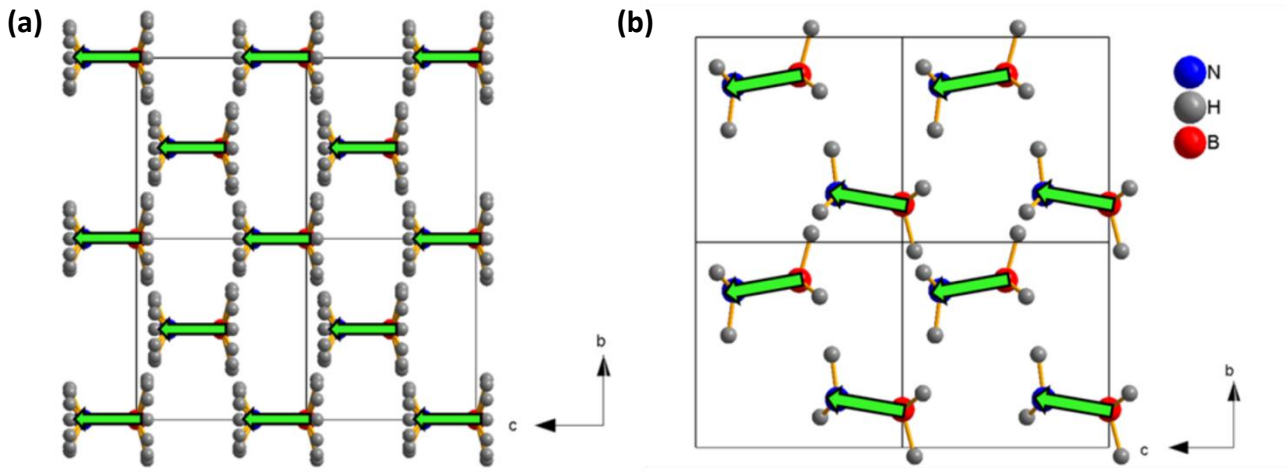

Figure 6-8. Dipole distribution in the two polymorphs of ammonia-borane viewed along [100] direction: (a) tetragonal HT-phase and (b) orthorhombic LT-phase, where the green arrows represent the electric dipole moment of the ammonia-borane molecules. We have expanded the number of unit cells to facilitate the visualization of the dipoles arrangement.

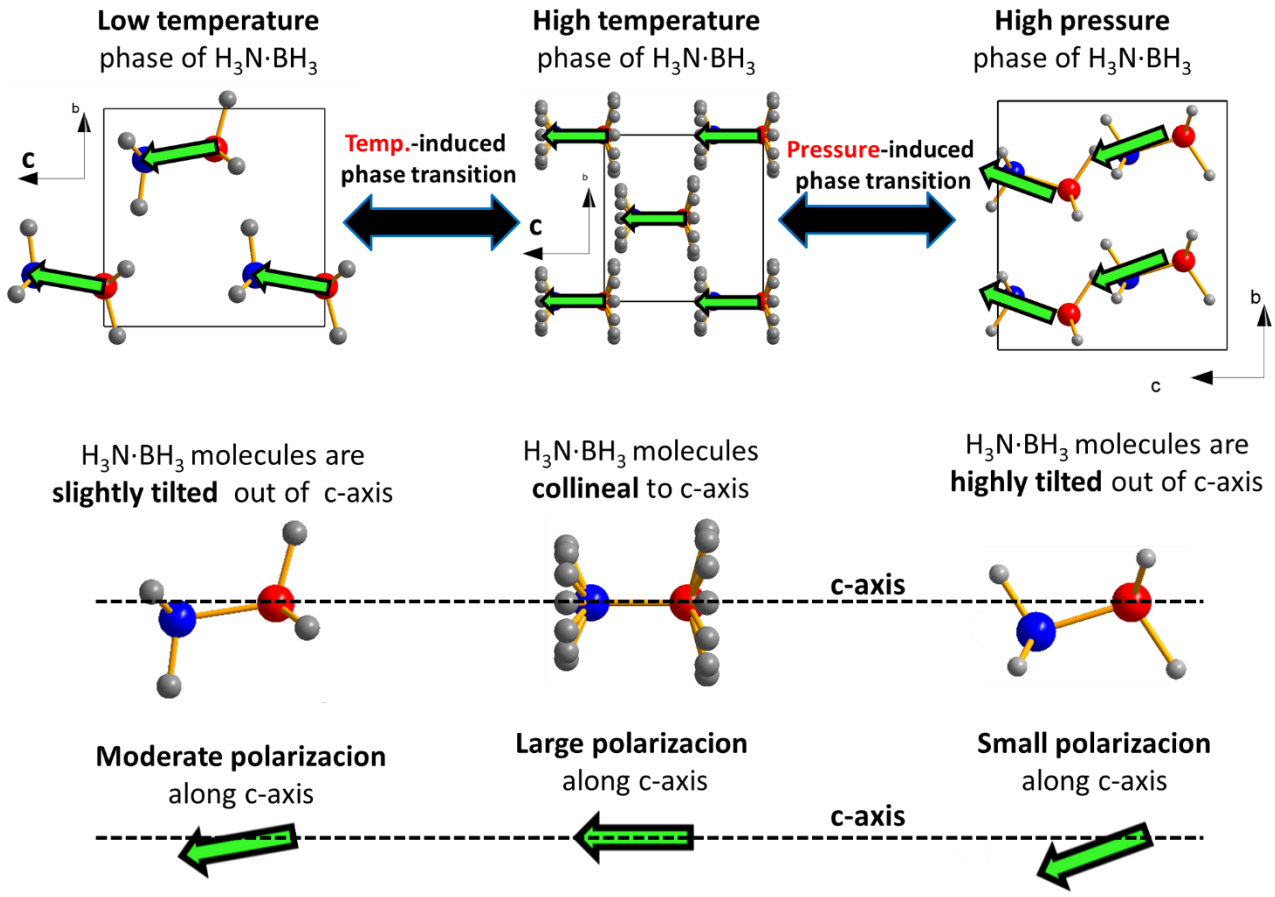

Figure 6-9. Scheme of phase transitions induced by temperature and pressure on ammonia-borane crystals. Also, we show the arrangement of ammonia-borane molecules and associated dipole moments along the *c*-axis.

In view of the obtained results, we attribute the observed rather sharp jump in the dielectric constant as a function of temperature to the transition between two ordered phases with the different ferroelectric arrangements described above. Hence, the order-disorder process of the H-atoms of the $H_3N{\cdot}BH_3$ molecules seem to be not significant for the reported dielectric anomaly.

Nevertheless, and despite such ferroelectric arrangements, ammonia-borane cannot be catalogued as a ferroelectric material. By definition this would mean that its polarization can be reversed by an applied external electric field. In this case, it is not possible because it would imply the rotation of all $H_3N{\cdot}BH_3$ molecules within the crystal by very large angles, up to 180º.

Finally, taking into account the here obtained findings, we propose that the ammonia-borane could display a huge dielectric transition induced by external pressure. In this context, Filinchuk *et al.*[28] have recently reported the structural evolution of this compound under external pressure using synchrotron powder diffraction. These authors have observed that this compound displays a reversibly phase transition, from the disordered HT-tetragonal phase to a new ordered phase (S.G.: $Cmc2_1$), phase transition that at room temperature takes place at around 1.2 GPa. In such high-pressure $Cmc2_1$ polymorph, the tilting of the $H_3N{\cdot}BH_3$ molecules with respect to the *c*-axis is very large (69º at 1.2 GPa and even up to 79° at 4.65 GPa), much larger than in the LT-orthorhombic phase.

Therefore, on the basis of the here presented results, we propose that external pressure will induce a transition from a ferroelectric arrangement of the electric dipoles to an almost antiferroelectric arrangement, so that the anomalies in the dielectric constant as a function of pressure should be much more pronounced than the here reported as a function of temperature.

Therefore, taking into account the characteristics of this compound, we propose that it would be used also as a sensitive pressure dielectric material.

6.4. Conclusions

In this work we show experimental studies of the solid state dielectric response of two very famous "classical" molecular inorganic compounds, namely ferrocene and ammonia-borane. Remarkably, both compounds display a dielectric transition associated to the structural phase transition as a function of temperature, which emphasizes the important role of order-disorder/displacive phase transitions on the dielectric properties.

We rationalize the obtained results on the basis of structure properties relationships, which we establish taking into account their dipole moment distributions, that we have calculated by means of quantum calculations using reported crystal data.

As shown, ferrocene displays a thermally-induced paraelectric to antiferroelectric transition associated to a phase transition that implies order-disorder of the Cp ligands and displacement of the Fe atoms within the ferrocene molecules. We rationalize the obtained results on the basis of a complex antiferroelectric arrangement of the electric dipole moments (induced by the displacement of the Fe atoms) in the LT-phase. Such arrangement gets destroyed as *T* increases above T_t: the ferrocene molecules become centrosymmetric and the dipole moments associated to the Cp rings become averaged as a result of their rotation.

On the other hand, we show that ammonia-borane displays a sharp dielectric transition at $T \approx 232$ K, associated to a structural transition that combines ordering and atomic displacement mechanisms of the $H_3N{\cdot}BH_3$ molecules. In this case, we attribute such behaviour to the temperature dependent displacement of the $H_3N{\cdot}BH_3$ molecules out-of the crystal polar *c*-axis. Above T_t, this compound exhibits a relative high polarization related to the collinear dipole moments, which lie parallel to *c*-axis. Meanwhile below T_t, the dipole moments display a shift out of *c*-axis, resulting in a polarization decrease. Additionally, we propose that external pressure will induce a transition from a ferroelectric to an almost antiferroelectric dipole arrangement.

These findings demonstrate that both ferrocene and ammonia-borane compounds are sensitive thermoresponsive dielectric materials, result that opens up new possibilities for their potential "novel" applications in a wide variety of fields, such as electronic materials.

6.5. Notes

The work presented in this chapter has been published in the following article:

Bermúdez-García, J. M.; Yáñez-Vilar, S.; Castro-García, S.; Señarís-Rodríguez, M. A.; Sánchez-Andújar, M. *RSC Adv.*, 2015, **5**, 83818-83824.

6.6. References

1 Rao, C. N. R.; Gopalakrishnan, J. *New Directions in Solid State Chemistry*, Cambridge University Press, 1997.
2 Zhang, W.; Xiong, R. G.; *Chem. Rev.*, 2012, **112**, 1163.
3 Lines, M. E.; Glass, A. M. *Principles applications of ferroelectric and related materials*, Oxford Unviersity Press, New York, 2001.
4 Bussmann-Holder, A.; Dalal, N. *Struct. Bonding*, 2007, **124**, 1-21.
5 Cairns, A. B.; Goodwin, A. L. *Chem. Soc. Rev.*, 2013, **42**, 4881-4893.
6 (a) Jain, P. ; Dalal, N. S.; Toby, B. H.; Kroto, H. W.; Cheetham, A. K. *J. Am. Chem. Soc.*, 2008, **130**, 10450-10451; (b) Jain, P.; Ramachandran, V.; Clark, R. J.; Zhou, H. D.; Toby, B. H.; Dalal, N. S.; Kroto, H. W.; Cheetham, A. K. *J. Am. Chem. Soc.*, 2009, **131**, 13625-13627.
7 Sánchez-Andújar, M.; Presedo, S.; Yáñez-Vilar, S.; Castro-García, S.; Shamir, J.; Señarís-Rodríguez, M. A. *Inorg. Chem.*, 2010, **49**, 1510-1516.

8 Kealy, T. J.; Pauson, P. L. *Nature*, 1951, **168**, 1039-1040.
9 Heinze, K.; Lang, H. *Organometallics*, 2013, **32**, 5623-5625.
10 Dunitz, J. D.; *Acta Crystallogr., Sect. B: Struct. Sci.*, 1995, **51**, 619-631.
11 Dunitz, J. D.; Orgel, L. E.; Rich, A. *Acta Crystallogr.*, 1956, **9**, 373-375.
12 Kottas, G. S.; Clarke, L. I.; Horinek, D.; Michl, J. *Chem. Rev.*, 2005, **105**, 1281-1376.
13 Edwards, J. W.; Kington, L.; Mason, R. *Trans. Faraday Soc.*, 1960, **56**, 660-667.
14 Seiler, P.; Dunitz, J. D. *Acta Crystallogr. Sect. B: Struct. Crystallogr. Cryst. Chem.*, 1979, **35**, 2020-2032.
15 Shore, S. G.; Parry, R. W. *J. Am. Chem. Soc.*, 1955, **77**, 6084-6085.
16 Li, H.; Yang, Q.; Chen, X.; Shore, S. G. *J. Organomet. Chem.*, 2014, **751**, 60.
17 Staubitz, A.; Robertson, A. P. M.; Manners, I. *Chem. Rev.*, 2010, **110**, 4079-4124.
18 Shore, S. G. *J. Am. Chem. Soc.*, 1965, **4**, 8-12.
19 Klooster, W. T.; Koetzle, T. F.; Siegbahn, P. E. M.; Richardson, T. B.; Crabtree, R. H. *J. Am. Chem. Soc.*, 1999, **121**, 6337-6343.
20 Hess, N. J.; Schenter, G. K.; Hartman, M. R.; Daemen, L. L.; Proffen, T.; Kathmann, S. M.; Mundy, C. J.; Hartl, M.; Heldebrant, D. J.; Stowe, A. C.; Autrey, T. *J. Phys. Chem. A*, 2009, **113**, 5723-5735.
21 Bowden, M. E.; Gainsford, G. J.; Robinson, W. T. *Aust. J. Chem.*, 2007, **60**, 149-153.
22 Gaffar, M. A.; Hussien, A. G. *J. Phys. Chem. Solids*, 2011, **62**, 2011.
23 Macdonald, J. R. *LEVM version 8.0 Comlex Nonlinear Squares Fitting Program*, 2003.
24 Gaussian 09, Revision D.01, Frisch, M. J.; Trucks, G. W.; Schlegel, H. B.; Scuseria, G. E.; Robb, M. A.; Cheeseman, J. R.; Scalmani, G.; Barone, V.; Mennucci, B.; Petersson, G. A.; Nakatsuji, H.; Caricato, M.; Li, X.; Hratchian, H. P.; Izmaylov, A. F.; Bloino, J.; Zheng, G.; Sonnenberg, J. L.; Hada, M.; Ehara, M.; Toyota, K.; Fukuda, R.; Hasegawa, J.; Ishida, M.; Nakajima, T.; Honda, Y.; Kitao, O.; Nakai, H.; Vreven, T.; Montgomery Jr., J. A.; Peralta, J. E.; Ogliaro, F.; Bearpark, M.; Heyd, J. J.; Brothers, E.; Kudin, K. N.; Staroverov, V. N.; Kobayashi, R.; Normand, J.; Raghavachari, K.; Rendell, A.; Burant, J. C.; Iyengar, S. S.; Tomasi, J.; Cossi, M.; Rega, N.; Millam, N. J.; Klene, M.; Knox, J. E.; Cross, J. B.; Bakken, V.; Adamo, C.; Jaramillo, J.; Gomperts, R.; Stratmann, R. E.; Yazyev, O.; Austin, A. J.; Cammi, R.; Pomelli, C.; Ochterski, J. W.; Martin, R. L.; Morokuma, K.; Zakrzewski, V. G.; Voth, G. A.; Salvador, P.; Dannenberg, J. J.; Dapprich, S.; Daniels, A. D.; Farkas, Ö.; Foresman, J. B.; Ortiz, J. V.; Cioslowski, J.; Fox, D. J. *Gaussian 09, Revision D.01, Gaussian, Inc.*, 2009.
25 Inorganic crystal structure database ICSD-164034.
26 Ogasahara, K.; Sorai, M.; Suga, H. *Mol. Cryst. Liq. Cryst.*, 1981, **71**, 189-211.
27 Palumbo, O.; Paolone, A.; Rspoli, P.; Cantelli, R.; Autrey, T.; Navarra, M. A. *J. Alloys Compd.*, 2011, **509**, S709.
28 Filinchuk, Y.; Nevidomskyy, A.; Chernyshov, D.; Dmitriev, V. *Phys. Rev. B*, 2009, **79**, 214111.

Chapter 7:

General conclusions

General conclusions

The here presented *Ph.D. Thesis* explores new functional properties of "emergent" organic-inorganic hybrid materials and very-well known "classic" molecular materials, with promising applications in the coming future technologies for alternative energy and environmental solutions.

This research memory enclose outstanding results in the areas of multifunctional and multistimuli responsive materials, as well as of nanostructured carbon materials. The systems that have been studied herein exhibit dielectric and multiferroic properties very sensitive towards temperature and/or pressure (external isostatic/uniaxial pressure and internal chemical pressure).

Ferroic phase and dielectric transitions of order-disorder and displacive nature are identified within the organic-inorganic hybrid perovskite family of molecular formula $[TPrA][M(dca)_3]$ (M = Mn^{2+}, Fe^{2+}, Co^{2+} and Ni^{2+}), and also in the "classic" ferrocene and ammonia-borane molecular materials. In the specific case of the $[TPrA][M(dca)_3]$ (M = Fe^{2+}, Co^{2+} and Ni^{2+}) compounds, where the Fe and Co members have been synthesized for the first time in this work, they exhibit multiple (up-to three) structural phase and dielectric transitions near room temperature. Very interestingly, these transitions in all of the compounds are found to be easily modulated by temperature and/or mechanical/chemical pressure, turning these materials into promising (multi)stimuli sensors.

Anomalous and very scarce properties of high technological interest have been revealed during these studies. This is the case of the $[TPrA][Mn(dca)_3]$ that exhibit large and anisotropic thermal expansion, especially along the *c*-axis where it reach *colossal* values of up to $\alpha > 100 \times 10^{-6}\ K^{-1}$ near the transition temperature. This is a very uncommon and exceptional behaviour even for the well-known and highly flexible organic-inorganic hybrids.

Even more, this singular $[TPrA][Mn(dca)_3]$ material has been revealed as a prominent caloric material for solid-state refrigeration. It represent the first example of organic-inorganic hybrid materials with pressure-driven caloric effect, the so-called barocaloric effect. In this material, an unprecedented giant response is obtained under very small pressures comparable to the working pressure of the current commercial refrigerant gases, P < 70 bar. Moreover, we anticipate that this hybrid will not be an isolated example for such an extraordinary behaviour as many other organic-inorganic hybrids exhibit the basic ingredients to also display large caloric effects.

In addition, the Ni and Co members of the $[TPrA][M(dca)_3]$ have been used to develop a novel, scalable and inexpensive synthetic method to obtain carbon nanotubes embedded with magnetic nanoparticles (M@CNTs) for environmental applications. Moreover, preliminary analysis revealed a promising oil adsorption capacity of the so-obtained M@CNTs.

All these findings broad new horizons in multistimuli sensing, solid-state refrigeration and pollutant removal materials based on "emergent" organic-inorganic hybrids and "classic" molecular compounds, offering alternative solutions for technological, energy and environmental applications.

Annexe I:

Crystallographic data

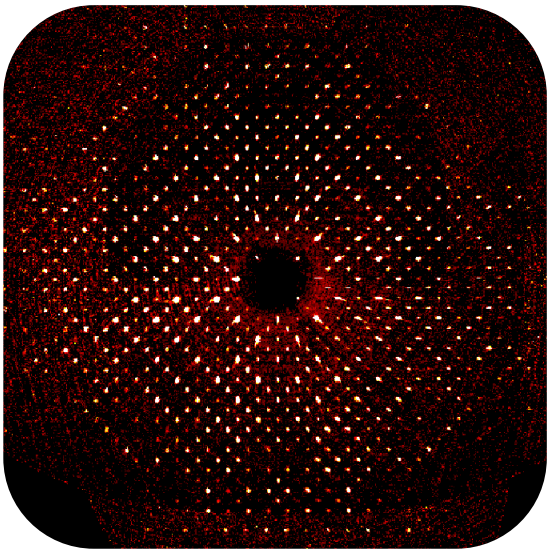

Crystallographic data

Table AI-1. Crystallographic data for *polymorphs I* and *II* of [TPrA][Mn(dca)$_3$].

	1 Mn	2 Mn
Formula	$C_{18}H_{28}N_{10}Mn$	$C_{18}H_{28}N_{10}Mn$
Formula weight	439.44	439.44
Temperature (K)	300(2)	368(2)
Crystal system	Tetragonal	Tetragonal
Space group	*P*-42$_1$*c*	*I*4/*mcm*
Superlattice	2a × 2a × 2a	~√2a × ~√2a × 2a
***a* (Å)**	16.2752(5)	11.5684(3)
***b* (Å)**	16.2752(5)	11.5684(3)
***c* (Å)**	17.4231(4)	17.6500(5)
Unit cell volume (Å^3)	4615.1(2)	2362.06(11)
Z	8	4
Nº. of reflections measured	127100	31347
Nº. of independent reflections	4725	677
R_{int}	0.0526	0.0740
Final R_1 values ($I > 2\sigma(I)$)	0.0401	0.0653
Final $wR(F^2)$ values ($I > 2\sigma(I)$)	0.0958	0.1585
Final R_1 values (all data)	0.0533	0.0740
Final $wR(F^2)$ values (all data)	0.1052	0.1774
Goodness of fit on F^2	1.024	1.097
Flack parameter	0.10 (3)	

Table AI-2. Summary of selected bond lengths and angles for the *polymorph I* of [TPrA][Mn(dca)$_3$] at 300 K.

Distance (Å)		Angle (°)	
Mn-N1	2.214(3)	**M-N1-C1**	172.4(2)
Mn-N2	2.235(3)	**M-N2-C2**	170.6(2)
Mn-N3	2.221(3)	**M-N3-C3**	161.0(2)
Mn-N4	2.230(3)	**M-N4-C4**	172.8(2)
Mn-N5	2.236(3)	**M-N5-C5**	159.0(2)
Mn-N6	2.203(3)	**M-N6-C6**	153.8(2)
Mn-Mn (*ab*)	8.217(7)-8.244(5)	**Tilting**	
Mn-Mn (*c*)	8.747(7)	***c*-axis**	3.2(7)-11.6(7)
		***ab*-plane**	26.6(8)-32.8(8)

Table AI-3. Summary of selected bond lengths and angles for the *polymorph II* of [TPrA][Mn(dca)$_3$] at 368 K.

Distances		Angles	
M-N1 (*c*)	2.224(6)	**M1-N1-C1**	155(5)
M-N2 (*ab*)	2.230(3)	**M1-N2-C2**	174(3)
Mn-Mn (*ab*)	8.180	**Tilting**	
Mn-Mn (*c*)	8.825	***c*-axis**	0
		***ab*-plane**	30.39

Table AI-4. Crystallographic data obtained from single crystal X-ray diffraction for the three polymorphs of the [TPrA][Fe(dca)$_3$] compound. The *polymorph Ia* data are not available because the refinement of this structure is excessively complicated due to the proximity of the transition temperatures *T1* and *T2*. We have to note that the Fe compound exhibit the same crystal structure at 100 K and 200 K, so we only will show the 200 K data.

	1Fe	**1bFe**	**2Fe**
Formula	$C_{18}H_{28}N_{10}Fe$	$C_{18}H_{28}N_{10}Fe$	$C_{18}H_{28}N_{10}Fe$
Formula weight	440.33	440.33	440.33
Temperature (K)	200(2)	323(2)	368(2)
Crystal system	Tetragonal	Orthorhombic	Tetragonal
Space group	*P*-42*(1)c*	*Ibam*	*I4/mcm*
Superlattice	2a × 2a × 2a	~√2a × ~√2a × 2a	~√2a × ~√2a × 2a
***a* (Å)**	16.1494(6)	11.5219(4)	11.4980(2)
***b* (Å)**		11.5355(4)	
***c* (Å)**	17.2252(5)	17.3841(5)	17.4980(3)
Unit cell volume (Å^3)	4492.4(3)	2310.54(13)	2313.31(7)
Z	8	4	4
V/Z (Å^3)	561.5(5)	577.63(5)	578.32(9)
N°. of reflections measured	39586	16957	17874
N°. of independent reflections	4558	1319	713
R_{int}	0.0605	0.0308	0.0269
Final R_1 values ($I > 2\sigma(I)$)	0.0480	0.0445	0.0423
Final $wR(F^2)$ values ($I > 2\sigma(I)$)	0.1315	0.1271	0.1310
Final R_1 values (all data)	0.0549	0.0605	0.0514
Final $wR(F^2)$ values (all data)	0.1370	0.1425	0.1436
Goodness of fit on F^2	1.142	1.036	1.122
Flack parameter	0.58(3)		
CSD-number	431141	431140	431139

Table AI-5. Crystallographic data obtained from single crystal X-ray diffraction for the four polymorphs of the [TPrA][Co(dca)$_3$] compound. We have to note that this compound exhibit the same crystal structure at 100 K and 200 K, so we only will show the 200 K data.

	1Co	1aCo	1bCo	2Co
Formula	$C_{18}H_{28}N_{10}Co$	$C_{18}H_{28}N_{10}Co$	$C_{18}H_{28}N_{10}Co$	$C_{18}H_{28}N_{10}Co$
Formula weight	443.41	443.41	443.41	443.41
Temperature (K)	200(2)	300(2)	323(2)	368(2)
Crystal system	Tetragonal	Orthorhombic	Orthorhombic	Tetragonal
Space group	*P-42(1)c*	*Pnna*	*Ibam*	*I4/mcm*
Superlattice	2a × 2a × 2a	2a × ~2√2a × ~2√2a	~√2a × ~√2a × 2a	~√2a × ~√2a × 2a
***a* (Å)**	16.1258(4)	17.2246(6)	11.4145(2)	11.4551(2)
***b* (Å)**		23.0205(9)	11.5693(2)	
***c* (Å)**	17.1229(4)	22.8310(8)	17.3062(3)	17.4294(3)
Unit cell volume (Å^3)	4452.66(19)	9052.9(6)	2285.42(7)	2287.07(7)
Z	8	16	4	4
V/Z (Å^3)	556.58(27)	565.8(1)	571.35(6)	571.76(9)
N°. of reflections measured	9646	90479	12962	790
N°. of independent reflections	4953	7731	1316	790
R_{int}	0.0134	0.1592	0.0211	0.0000
Final R_1 values ($I > 2\sigma(I)$)	0.0507	0.0747	0.0402	0.0493
Final $wR(F^2)$ values ($I > 2\sigma(I)$)	0.1389	0.2068	0.1145	0.1433
Final R_1 values (all data)	0.0529	0.1370	0.0491	0.0587
Final $wR(F^2)$ values (all data)	0.1409	0.2717	0.1251	0.1559
Goodness of fit on F^2	1.198	1.036	1.115	1.127
Flack parameter	0.53(3)			
CSD-number	431145	431144	431143	431142

Table AI-6. Crystallographic data obtained from single crystal X-ray diffraction for the four polymorphs of the [TPrA][Ni(dca)$_3$] compound. This material exhibit the same crystal structure at 100 K and 180 K, so we only will show the 180 K data.

	1Ni	1aNi	1bNi	2Ni
Formula	$C_{18}H_{28}N_{10}Ni$	$C_{18}H_{28}N_{10}Ni$	$C_{18}H_{28}N_{10}Ni$	$C_{18}H_{28}N_{10}Ni$
Formula weight	443.17	443.17	443.17	443.17
Temperature (K)	180(2)	300(2)	323(2)	368(2)
Crystal system	Tetragonal	Orthorhombic	Orthorhombic	Tetragonal
Space group	*P*-42(1)*c*	*Pnna*	*Ibam*	*I*4/*mcm*
Superlattice	2a × 2a × 2a	2a × ~2√2a × ~2√2a	~√2a × ~√2a × 2a	~√2a × ~√2a × 2a
***a* (Å)**	16.0830(4)	17.1299(5)	11.3524(3)	11.390(5)
***b* (Å)**		22.9364(6)	11.5038(3)	
***c* (Å)**	17.0185(4)	22.6975(6)	17.1916(4)	17.301(5)
Unit cell volume (Å^3)	4402.05(19)	8917.8(4)	2245.15(10)	2244.5(15)
Z	8	16	4	4
V/Z (Å^3)	550.25(64)	557.3(6)	561.28(77)	561.12(87)
Nº. of reflections measured	75393	84174	24633	27474
Nº. of independent reflections	4868	7354	1292	699
R_{int}	0.0412	0.1158	0.0491	0.0480
Final R_1 values (I> 2σ(I))	0.0720	0.0671	0.0382	0.0364
Final $wR(F^2)$ values (I> 2σ(I))	0.1724	0.1814	0.1019	0.1036
Final R_1 values (all data)	0.0740	0.1075	0.0470	0.0440
Final $wR(F^2)$ values (all data)	0.1757	0.2257	0.1140	0.1157
Goodness of fit on F^2	1.262	1.042	1.091	1.162
Flack parameter	0.45(4)			
CSD-number	431138	431137	431136	431135

Table AI-7. Summary of selected bond lengths and angles for the *polymorph I* of [TPrA][M(dca)$_3$] (M = Fe^{2+}, Co^{2+} and Ni^{2+}) compounds.

Distance (Å)	Fe 200 K	Co 200K	Ni 200 K	Angle (º)	Fe 200 K	Co 200K	Ni 200 K
M-N1	2.161(5)	2.119(4)	2.099(5)	**M-N1-C1**	175.4(5)	176.6(5)	175.1(7)
M-N2	2.188(3)	2.106(3)	2.051(5)	**M-N2-C2**	169.9(4)	160.5(4)	162.0(7)
M-N3	2.167(3)	2.153(3)	2.075(5)	**M-N3-C3**	173.1(3)	170.6(4)	165.0(5)
M-N4	2.185(3)	2.145(3)	2.096(5)	**M-N4-C4**	161.1(4)	163.3(4)	173.3(5)
M-N5	2.154(3)	2.130(3)	2.109(5)	**M-N5-C5**	162.7(3)	172.7(4)	171.8(6)
M-N6	2.138(4)	2.116(3)	2.092(5)	**M-N6-C6**	159.6(4)	164.6(3)	165.2(5)
M-M (*c*-axis)	8.640(3)	8.582(8)	8.525(1)	**Tilting**	**Fe 200 K**	**Co 200K**	**Ni 200 K**
M-M (*ab*-plane)	8.151(4)-8.183(5)	8.126(2)-8.156(1)	8.091(1)-8.118(1)	***c*-axis**	4.6(1)-12.6(1)	5.4(1)-13.0(1)	6.2(2)-12.8(2)
				***ab*-plane**	26.0(4)-32.3(1)	25.4(1)-31.2(7)	24.6(1)-30.2(1)

Table AI-8. Summary of selected bond lengths and angles for the *polymorph Ia* of [TPrA][M(dca)$_3$] (M = Fe^{2+}, Co^{2+} and Ni^{2+}) compounds.

Distance (Å)	Co 300K	Ni 300 K	Angle (º)	Co 300K	Ni 300 K
M1-N1	2.136 (5)	2.090(5)	**M1-N1-C***	171.6(8)	169.9(5)
M1-N2	2.098 (5)	2.086(5)	**M1-N2-C***	161.5(7)	174.6(6)
M1-N3	2.133 (7)	2.090(5)	**M1-N3-C***	166.9(6)	175.9(5)
M1-N4	2.122 (5)	2.081(5)	**M1-N4-C***	168.7(5)	173.3(5)
M1-N5	2.123 (5)	2.087(5)	**M1-N5-C***	175.8(5)	170.0(5)
M1-N6	2.121 (5)	2.082(5)	**M1-N6-C***	170.7(5)	172.7(4)
M2-N7	2.128 (7)	2.057(5)	**M2-N7-C***	168.0(8)	162.1(6)
M2-N8	2.110 (5)	2.104(5)	**M2-N8-C***	173.7(7)	170.9(7)
M2-N9	2.124 (5)	2.085(5)	**M2-N9-C***	171.3(5)	169.0(4)
M2-N10	2.126 (5)	2.094(5)	**M2-N10-C***	169.8(5)	176.0(5)
M2-N11	2.110 (5)	2.080(5)	**M2-N11-C***	173.1(5)	171.4(4)
M2-N12	2.133 (5)	2.095(5)	**M2-N12-C***	175.6(5)	167.5(5)
M1-M1 (*a*-axis)	8.529(1)-8.707(1)	8.478(4)-8.659(9)	**Tilting**	**Co 300K**	**Ni 300 K**
M2-M2 (*a*-axis)	8.619(1)-8.619(1)	8.570(1)-8.570(1)	***a*-axis**	2.5(1) - 10.5(2)	2.8(1)-10.5(1)
M1-M2 (*bc*-plane)	8.094(1)-8.154(1)	8.058(1)-8.112(1)	***bc*-plane**	26.1(1)-31.0(2)	25.2(1)-30.1(1)

C*: carbon bonded to the respective dicyanamide N-terminal atom.

Table AI-9. Summary of selected bond lengths and angles for the *polymorph Ib* of [TPrA][M(dca)$_3$] (M = Fe^{2+}, Co^{2+} and Ni^{2+}) compounds.

Distance (Å)	Fe 323 K	Co 323 K	Ni 323 K	Angle (°)	Fe 323 K	Co 323 K	Ni 323 K
M-N1	2.158(3)	2.127(2)	2.082(3)	**M-N1-C1**	172.2(3)	173.4(3)	174.2(3)
M-N2	2.158(3)	2.120(2)	2.078(2)	**M-N2-C2**	172.0(3)	172.5(3)	173.2(3)
M-N4	2.149(5)	2.125(3)	2.082(3)	**M-N4-C3i**	150(2)	150 (2)-157 (3)	151(2)-158(2)
M-M (*c*-axis)	8.692(1)	8.653(1)	8.595(8)	**Tilting**	**Fe 323 K**	**Co 323 K**	**Ni 323 K**
M-M (*ab*-*plane*)	8.152(0)	8.126(2)	8.081(1)	***c*-axis**	0.0(1)	0.00(9)	0.00(9)
				***ab*-plane**	28.86(9)-28.97(9)	27.93(8)-28.48(6)	27.13(8)-27.62(8)

C3i: carbon bonded to the respective dicyanamide N-terminal atom, where i = A, B.

Table AI-10. Summary of selected bond lengths and angles for the *polymorph II* of [TPrA][M(dca)$_3$] (M = Fe^{2+}, Co^{2+} and Ni^{2+}) compounds.

Distance (Å)	Fe 368 K	Co 368 K	Ni 368 K	Angle (°)	Fe 368 K	Co 368 K	Ni 368 K
M-N1	2.164(3)	2.131(3)	2.104(5)	**M-N1-C1i**	160.7(7)-174.9(7)	160.6(7)-174.7(6)	160.7(7)-175.4(6)
M-N2	2.170(5)	2.149(5)	2.083(4)	**M-N2-C2**	156(4)	156.1(8)	157(6)
M-M (*c*-axis)	8.749(0)	8.714(7)	8.650(2)	**Tilting**	**Fe 368 K**	**Co 368 K**	**Ni 368 K**
M-M (*ab*-plane)	8.130(3)	8.100(0)	8.054(3)	***c*-axis**	0.0(1)	0.0(1)	0.0(1)
				***ab*-plane**	29.56(9)	29.19(9)	28.42(9)

C1i: carbon bonded to the respective dicyanamide N-terminal atom, where i = A, B.

Annexe II:

Spanish summary

Spanish summary

Hoy en día, la comunidad científica se enfrenta a nuevos retos para dar respuesta a los problemas que presentan la sociedad actual, entre ellos, el consumo masivo de recursos energéticos y tecnológicos, el calentamiento global y la contaminación medioambiental. En este contexto, urge la necesidad de desarrollar nuevas formas de aprovechamiento energético, reduciendo al máximo el impacto medioambiental y evitando el uso de materiales costosos y/o escasos (tierras raras, litio, indio, etc.), así como de sustancias que puedan contribuir al efecto invernadero. Además, otra de las estrategias a seguir para favorecer el ahorro energético y reducir el consumo de recursos naturales, es mejorar la eficiencia de los dispositivos tecnológicos actuales, que a su vez se desea que cada vez sean más y más pequeños.

Tratando de buscar soluciones innovadoras, en las últimas décadas, investigadores del ámbito de la Ciencia de Materiales y del Estado Sólido han dedicado grandes esfuerzos para desarrollar de "*materiales (multi)funcionale*s y *(multi)sensitivos*", es decir, materiales donde a través de diferentes estímulos externos (temperatura, presión, etc.) inducen una determinada funcionalidad (una respuesta magnética o eléctrica, por ejemplo).

Tradicionalmente, la mayor parte de estos estudios se han centrado en materiales cerámicos y más concretamente en los óxidos de metales de transición con estructura tipo perovskita. Estos compuestos, con fórmula molecular ABX_3 (A = cationes alcalinos, alcalinotérreos o lantánidos, B = cationes de metales de trasición, X = O^{2-}), son sólidos cristalinos que presentan una estructura en forma de redes tridimensionales de octaedros $[BX_6]$ que comparten vértices y, a su vez, dan lugar a una cavidad pseudo-cubooctaedra donde se aloja el catión A. Estas perovskitas son muy conocidas por presentar una gran variedad de propiedades funcionales, como piezoelectricidad, ferroelectricidad, ferromagnetismo, magnetorresistencia, superconductividad, multiferroicidad, etc.

Más recientemente, ha surgido un creciente interés en la búsqueda de nuevas propiedades multifunctionales y respuestas multiestímulo (multisensitivas) en materiales híbridos organico-inorganicos, entre los que se incluyen los denominados "*metal-organic frameworks*" (MOFs) y los polímeros de coordinación. Este tipo de compuestos ofrece una mayor versatilidad, flexibilidad y riqueza estructural debido a la posibilidad de combinar una gran variedad de subunidades inorgánicas y orgánicas en su estructura. Dentro de esta familia de compuestos, se está prestando bastante a atención aquellos materiales híbridos que presentan una estructura tipo perovskita, donde las posiciones A y/o B pueden ser ocupadas por iones orgánicos, dando lugar a las denominadas perovskitas híbridas.

Algunos de estos materiales ya han presentado propiedades funcionales muy interesantes, como es el caso del compuesto $[MA]PbI_3$ (MA = catión metilamonio, $CH_3NH_3^+$), cuyas recientemente descubiertas propiedades fotovoltaicas han marcado un hito sin precedentes en el campo de la energía fotovoltaica. Otros ejemplos destacados son los materiales con fórmula molecular $[Amino][M(X)_3]$ (Amino = diferentes cationes amino, M = cationes de metales de

transición divalentes, X = distintos ligandos poliatómicos como $HCOO^-$, N_3^- o CN^-), que presentan orden magnético, eléctrico y/o elástico. Además, los compuestos con fórmula [DMA][$M(HCOO)_3$] (DMA: catión dimethilamonio, $(CH_3)_2NH_2^+$) han resultado tener un comportamiento multiferroico tipo-I; e incluso, más recientemente, se ha descubierto que el compuesto [MA][$Co(HCOO)_3$] (MA = catión metilamonio, $CH_3NH_3^+$) presenta un acoplamiento magnetoeléctrico, siendo el primer ejemplo de perovskita híbrida con comportamiento multiferroico tipo-II.

Por otro lado, la elección de las subunidades orgánicas e inorgánicas en la estructura de los híbridos permite controlar la porosidad y la composición química de dichos materiales, lo que les confiere un gran potencial en otra área emergente de la Ciencia de Materiales: el diseño estratégico de precursores de materiales nanoestructurados de carbono con aplicaciones energéticas y medioambientales (almacenamiento de energía, adsorción de gases, eliminación de contaminantes, etc.).

Teniendo en cuenta todo lo anterior, los objetivos principales de la presente ***Tesis Doctoral***, que ha sido elaborada en el ***Programa de Doctorado de Química Ambiental y Fundamental de la Universidade da Coruña***, engloban el desarrollo de nuevos materiales (multi)funcionales y (multi)sensitivos y la búsqueda de materiales híbridos orgánico-inorgánicos como precursores de materiales nanoestructurados de carbono.

A pesar de que los estudios aquí presentados se han centrado principalmente en materiales híbridos "emergentes", también se han revisitado materiales moleculares "clásicos", concretamente ferroceno y amino-borano, buscando nuevas propiedades funcionales. Al mismo tiempo, en el transcurso de la investigación, se ha descubierto que algunos de estos materiales presentan un gran efecto calórico inducido por la presión y que tienen potenciales aplicaciones en sistemas de refrigeración, lo que ha sido objeto de estudio en los últimos meses de este trabajo de doctorado. Por tanto, los estudios realizados abarcan desde la síntesis de los distintos compuestos, hasta su caracterización estructural y el estudio de sus propiedades físico-químicas: dieléctricas, multiferroicas, calóricas, de adsorción, etc.

De este manera, la presente *Tesis Doctoral*, titulada ***"Classic molecular compounds and emergent organic-inorganic hybrid perovskites with (multi)functional properties and (multi)stimuli responsiveness"*** (en castellano: *"Compuestos moleculares clásicos y perovskitas híbridas orgánico-inorgánicas emergentes, con propiedades (multi)funcionales y respuesta (multi)estímulo"*), expone los principales resultados alcanzados durante dicha investigación predoctoral. Esta memoria se encuentra estructura del siguiente modo:

El capítulo 1 consiste en una introducción general al campo de los materiales con propiedades dieléctricas, multiferroicas y de refrigeración en estado sólido, presentando los ejemplos más recientes y relevantes de estos comportamientos en el ámbito de los compuestos híbridos orgánico-inorgánicos. Además, se presenta los antecedentes de estos híbridos como precursores de materiales nanoestructurados de carbono.

En los capítulos 2 y 3 se estudian por primera vez las propiedades multifuncionales y multisensitivas de una novedosa familia de híbridos orgánico-inorgánicos con estructura tipo perovskita y fórmula molecular [TPrA][$M(dca)_3$] (TPrA = catión tetrapropilamonio, $(CH_3CH_2CH_2CH_2)_4N^+$; M = Mn^{2+}, Fe^{2+}, Co^{2+} y Ni^{2+}; dca = anión dicianamida).

A lo largo de estos dos capítulos se describe la síntesis de dichos compuestos, se profundiza en su caracterización estructural y se estudian por primera vez sus propiedades dieléctricas.

Desde el punto de vista estructural, el compuesto [TPrA][Mn(dca)$_3$] presenta una transición estructural cerca de temperatura ambiente (T_t ≈ 330 K) que no se conocía anteriormente. Así, por debajo de esta temperatura, este compuesto cristaliza dando lugar a un *polimorfo I* con grupo espacial no centrosimétrico ($P\bar{4}2_1c$); mientras que por encima de T_t, el material exhibe un *polimorfo II* con un grupo espacial centrosimétrico (*I4/mcm*). En esta transición estructural concurre una combinación singular de varios procesos: (i) el desplazamiento de los cationes apolares TPrA del centro de las cavidades pseudo-cubooctaédricas, (ii) fenómenos de orden-desorden de los ligandos polares dca y de los brazos propilo de los cationes TPrA, y (iii) modificaciones en la inclinación ("tilting") de los octaedros [MnN$_6$].

Complementariamente, se profundizó en la caracterización estructural de este compuesto mediante experimentos de difracción de radiación sincrotrón en función de la temperatura sobre muestras de polvo policristalino. Los resultados de estos experimentos muestran que el material presenta una gran expansión térmica anisotrópica asociada a la transición estructural, especialmente destacable a lo largo del eje c, alcanzando valores colosales de hasta $\alpha > 100 \times 10^{-6}$ K^{-1} a temperatura ambiente.

Por otro lado, también se han sintetizado los miembros con M = Fe^{2+}, Co^{2+} and Ni^{2+}, donde los compuestos de hierro y cobalto se han obtenido por primera vez en este trabajo. La caracterización estructural de dichos compuestos, [TPrA][M(dca)$_3$] (M = Fe^{2+}, Co^{2+} and Ni^{2+}), ha dado lugar a la identificación de múltiples transiciones estructurales que originan hasta cuatro polimorfos diferentes (*I*, *Ia*, *Ib* and *II*) en un rango de temperaturas cercano a temperatura ambiente (210-360 K). Además, el estudio de la estructura cristalina de los distintos polimorfos, realizado mediante difracción de rayos X de monocristal, muestra que el volumen de la celda unidad (normalizada por el valor de Z) decrece cuando el radio iónico de los cationes de metales de transición disminuye. Del mismo modo, la inclinación de los octaedros en el plano *ab* (o *bc* en el caso del *polimorfo Ia*) también decrece, minimizando la tensión estructural en estos planos. Como consecuencia, la estabilidad térmica de los polimorfos intermedios *Ia* y *Ib* se ve afectada y disminuye con el incremento del radio iónico, desde el compuesto de Ni que presenta el rango de temperaturas donde existen ambos polimorfos, hasta el compuesto de Mn, donde los polimorfos *Ia* y *Ib* no se han observado.

En cuanto a las propiedades dieléctricas, todos los compuestos de la serie [TPrA][M(dca)$_3$] (M = Mn^{2+}, Fe^{2+}, Co^{2+} and Ni^{2+}) presentan transiciones dieléctrica asociadas a cada una de las transiciones estructurales, cuyo origen se debe a procesos de orden-desorden y de desplazamiento de los iones. Concretamente, en los polimorfos *I* y *Ia*, se observa una distribución antiferroeléctrica (AFE) de los dipolos eléctricos asociada al desplazamiento de los cationes apolares TPrA con respecto al centro de las cavidades, y en combinación con procesos de orden-desorden de sus brazos propilo y de los ligados polares dca. Por el contrario, los polimorfos *Ib* y *II*, en los que los cationes TPrA se sitúan ya en el centro de las cavidades, muestran una respuesta paraeléctrica (PE) debido al desorden de los ligandos dca, que actúan como rotores.

En este sentido, resulta muy interesante destacar que el origen de la respuesta dieléctrica en estos materiales es diferente al encontrado en otras perovskitas híbridas, como los compuestos de fórmula [DMA][M(HCOO)$_3$] (DMA = catión dimetilamonio, $(CH_3)_2NH_2^+$; M = distintos cationes de metales de transición), ya que, en este caso, el catión TPrA es apolar y además no puede formar enlaces de hidrógeno. De este modo, se propone que el mecanismo que da lugar a la respuesta dieléctrica, como ya ha sido explicado en el párrafo anterior, deriva de un desplazamiento cooperativo de los cationes TPrA, en conjunción con un proceso de orden-desorden de dichos cationes y de los ligandos dca, que actúan como rotores al aumentar la temperatura.

En paralelo estos resultados, se ha descubierto además que estos compuestos son muy sensibles a la presión externa, tanto hidrostática como uniaxial, encontrándose una gran dependencia de las transiciones estructurales y dieléctricas con dicha presión. Así, se han encontrado valores de $\delta T_t/\delta P \approx 25$ K kbar^{-1}, valores que son mucho mayores que aquellos hallados en otras pervoskitas AFE ampliamente conocidas como, por ejemplo, el compuesto $PbZrO_3$ con una dependencia $\delta T_t/\delta P = 4.5$ K kbar^{-1}. Además, se ha observado un efecto similar al modificar la presión química interna mediante el incremento del radio iónico de los cationes de metales de transición, que afecta directamente al factor de tolerancia de la estructura. Por lo tanto, es posible modular la temperatura de las transiciones estructurales y dieléctricas en función de la presión, tanto externa como interna, y se puede reducir el rango de temperatura en el cual los polimorfos intermedios *Ia* y *Ib* son estables, incluso pudiéndose suprimir.

En el capítulo 4, se abre la puerta a un campo totalmente innovador en el área de los materiales híbridos orgánico-inorgánicos, mostrando por primera vez su gran potencial como materiales avanzados para refrigeración en estado sólido. En este capítulo, se presenta el primer ejemplo conocido de un material híbrido orgánico-inorgánico, el compuesto [TPrA][Mn(dca)$_3$], que muestra un enfriamiento inducido por la presión (efecto barocalórico).

Resulta muy significativo que este efecto se alcanza a presiones fácilmente accesibles para los equipos de refrigeración comerciales (P < 70 bar). Además, las propiedades refrigerantes encontradas hacen de este material una alternativa muy competente con respecto a los mejores refrigerantes sólidos conocidos hasta el momento, principalmente materiales magnetocalóricos, que incluso sobrepasan su capacidad calorífica y poder refrigerante. En concreto, el incremento adiabático de la temperatura en el material [TPrA][Mn(dca)$_3$] alcanza valores de hasta 5.1 K al aplicar presiones tan pequeñas como P < 70 bar. Además, su poder de enfriamiento relativo se calcula en torno a 9724 J kg^{-1} GPa^{-1}, siendo diez veces mayor que el encontrado en aleaciones magnetocalóricas tan conocidas y estudiadas como $Gd_5Si_2Ge_2$ o $Fe_{49}Rh_{51}$.

Asimismo, los resultados obtenidos permiten establecer la relación entre la estructura y las propiedades calóricas, pudiéndose anticipar que este compuesto no será un caso aislado; sino que se establece que otros muchos materiales híbridos, tanto MOFs como polímeros de coordinación, tienen los ingredientes necesarios para mostrar grandes efectos calóricos.

En conclusión, estos resultados abren nuevos horizontes en el área de los materiales híbridos orgánico-inorgánicos y en las posibilidades de refrigeración basadas en materiales sólidos económicamente más accesible que las aleaciones de tierras raras.

En el **capítulo 5**, se muestra otra aplicabilidad muy relevante de los materiales híbridos orgánico-inorgánicos con fórmula [TPrA][M(dca)$_3$]: su uso como precursores de materiales nanoestructurados de carbono. Utilizando el caso concreto de los compuestos de Ni y Co, se describe un nuevo método sencillo, económico y escalable, para sintetizar nanotubos de carbono con nanopartículas magnéticas de níquel y/o cobalto embebidas (M@CNT, M = Ni^{2+} o Co^{2+}, según corresponda). Este método se basa en una descomposición térmica, sencilla y en un solo paso, de los precursores a temperaturas de en torno a 900 °C. Además, estos M@CNTs ofrecen aplicaciones con gran potencial para la adsorción de aceites contaminantes y su posterior desorción por hipertermia, es decir, por aumento de la temperatura inducido mediante un campo magnético alterno.

Este estudio demuestra que la incorporación de ligandos dca como "building blocks" en materiales híbridos es una estrategia muy prometedora como método de síntesis sencillo para la obtención de nanotubos de carbono con nanopartículas magnéticas embebidas en su interior. En este trabajo, la descomposición térmica de los precursores ha sido monitorizada por difracción de rayos X, microscopía electrónica, termogravimetría y análisis espectroscópicos, lo que nos ha permitido proponer un mecanismo sintético, así como establecer las condiciones óptimas para la obtención de los materiales M@CNTs.

Los materiales así obtenidos, M@CNTs (M = Ni^{2+} and Co^{2+}), muestran una morfología regular y con un área específica de 250 m^2/g. El compuesto de Co@CNT presenta una distribución del tamaño de poro de hasta 6 nm, mientras que el compuesto Ni@CNTs muestra una distribución del tamaño de poro más estrecha centrada alrededor de 5 nm. Este trabajo muestra, por tanto, que estos materiales son capaces de adsorber selectivamente aceite en una matriz acuosa, con una capacidad de en torno a 2.2 g/g, que es comparable a la de otros materiales similares pero que tienen un coste de producción superior al aquí presentado.

Por su parte, el estudio de las propiedades magnéticas reveló un comportamiento ferromagnético con valores del campo coercitivo muy pequeños, que se deben al reducido tamaño de las nanopartículas.

Por último, el gran contenido de nitrógeno detectado en estos M@CNTs, junto a las propiedades físico-químicas aquí mostradas, hacen de estos materiales interesantes candidatos para otras aplicaciones características de nanotubos de carbono enriquecidos con nitrógeno, como sensores de gases o catalizadores, entre otras.

En el capítulo 6, en búsqueda de nuevas propiedades funcionales, se revisitan dos compuestos moleculares "clásicos", que han sido ampliamente estudiados durante más de medio siglo: ferroceno, [Fe(C_5H_5)$_2$], y amino-borano ($H_3N{\cdot}BH_3$).

En el caso del ferroceno se encuentra una transición antiferroeléctrica-paraeléctrica (AFE-PE) que ocurre a 195 K calentando y a 175 K enfriando, y que está asociada a una transición estructural entre los polimorfos de simetría monoclínica y triclínica. Dicha transición estructural está originada tanto por procesos de orden-desorden de los ligandos orgánicos ciclopentadienilo (Cp), como por procesos de desplazamiento del átomo de hierro (Fe) dentro de las moléculas de ferroceno. La fase de baja temperatura muestra un complejo orden antiferroelectrico (AFE) de los dipolos eléctricos, en el que los átomos de Fe experimentan un desplazamiento del centro de los

anillos Cp_2. Al aumentar la temperatura, este orden eléctrico cooperativo se suprime dando lugar a la fase de alta temperatura, en la que los ligandos Cp se encuentran rotando y los dipolos eléctricos asociados a las moléculas de ferroceno se compensan en todas las direcciones, dando lugar a un comportamiento paraelectrico (PE).

En el compuesto amino-borano se encuentra una transición dieléctrica alrededor de 232 K asociada a la transición estructural entre los polimorfos de alta temperatura (G.E.: *I4mm*) y de baja temperatura (G.E.: $Pmn2_1$), que combina tanto procesos de orden-desorden como de desplazamiento de las moléculas $H_3N{\cdot}BH_3$. En la fase de alta temperatura los momentos dipolares asociados a dichas moléculas se mantienen paralelos al eje c, orientados en el mismo sentido y dando lugar a una contante dieléctrica más alta en el material. Por su parte, en la fase de baja temperatura, estos dipolos están desplazados en un ángulo entre 0° y 180° con respecto al eje c, lo que supone un decrecimiento neto de la polarización. Por otro lado, teniendo en cuenta los resultados encontrados en este trabajo y el efecto de la presión en la estructura descrito en la bibliografía, se propone que para valores de presión P > 1.2 GPa se induciría una transición dieléctrica desde una fase ferroeléctrica (FE) a una fase quasi-antiferroeléctrica (quasi-AFE).

En el **capítulo 7**, se recogen las conclusiones generales de la presente *Tesis Doctoral*, englobando los resultados más destacables de los estudios llevados a cabo. Los resultados aquí mostrados abren nuevos horizontes en diversas áreas de investigación en el campo de Ciencia de Materiales y del Estado Sólido, describiéndose nuevos materiales multifuncionales y multisensitivos, y precursores híbridos de materiales nanoestructurados de carbono. Además, se destacan potenciales aplicaciones tecnológicas (sensores multiestímulo, memorias multiferroicas, etc.), energéticas (sistemas de refrigeración) y medioambientales (eliminación y recuperación de residuos).

Por último, la presente memoria cuenta con una serie de anexos incluidos al final del texto, que recogen información adicional y de interés para *Tesis Doctoral* aquí expuesta. Estos anexos son los siguientes:

El **anexo I** muestra una selección de datos cristalográficos de los compuestos de la serie $[TPrA][M(dca)_3]$ ($M = Mn^{2+}$, Fe^{2+}, Co^{2+} and Ni^{2+}) que, como se ha indicado anteriormente, han sido estudiados en los capítulos 2 y 3.

El **anexo II,** que usted está leyendo en este momento, es un resumen global en lengua castellana del trabajo realizado y mostrado en la presente *Tesis Doctoral*.

El **anexo III** recoge las publicaciones en revistas científicas y las comunicaciones a congresos realizadas por Juan Manuel Bermúdez García durante su periodo de investigación predoctoral.

Annexe III:

Publications and communications

Publications in scientific journals

Coexistence of magnetic and electrical order in the new perovskite-like $(C_3N_2H_5)[Mn(HCOO)_3]$ formate

Breogan Pato-Doldán,[a] L. Claudia Gómez-Aguirre,[a] Juan M. Bermúdez-García,[a] Manuel Sánchez-Andújar,[a] Alfonso Fondado,[b] Jorge Mira,[b] S. Castro-García[a] and M. A. Señarís-Rodríguez*[a]

a. Department of Fundamental Chemistry, Faculty of Science, University of A Coruña, Campus A Coruña, 15071 A Coruña, Spain. E-mail: msanchez@udc.es
b. Department of Applied Physics, University of Santiago de Compostela, 15782 Santiago de Compostela, Spain.

RSC Adv., 2013, **3**, 22404-22411

New properties in old systems: cooperative electric order in ferrocene and ammonia-borane

Juan M. Bermúdez-García,[a] Susana Yáñez-Vilar,[a,b] Socorro Castro-García,[a] María A. Señarís-Rodríguez,[a] Manuel Sánchez-Andújar*[a]

a. QuiMolMat Group, Department of Fundamental Chemistry, Faculty of Science and CICA, University of A Coruña, Campus A Coruña, 15071 A Coruña, Spain. E-mail: msanchez@udc.es
b. Department of Applied Physics, University of Santiago de Compostela, 15782 Santiago de Compostela, Spain.

RSC Adv., 2015, **5**, 83818-83824

Role of temperature and pressure on the multisensitive multiferroic dicyanamide framework $[TPrA][Mn(dca)_3]$ with perovskite-like structure

Juan M. Bermúdez-García,*[a] Manuel Sánchez-Andújar,[a] Susana Yáñez-Vilar,[a,b] Socorro Castro-García,[a] Ramón Artiaga,[c] Jorge López-Beceiro,[c] Luis Botana,[d] Ángel Alegría[d,e] and María A. Señarís-Rodríguez*[a]

a. QuiMolMat Group, Department of Fundamental Chemistry, Faculty of Science and CICA, University of A Coruña, Campus A Coruña, 15071 A Coruña, Spain.
b. Department of Applied Physics, University of Santiago de Compostela, 15782 Santiago de Compostela, Spain.
c. Department of Industrial Engineering II, University of A Coruña. Campus Ferrol, 15403 Ferrol, Spain.
d. Material Physical Center, CSIC-UPV/EHU, P. Manuel de Lardizabal 5, 20018 Donostia-San Sebastian, Spain.
e. Material Physical Department, University of the Basque Country, PO Box 1072, 20008 Donostia-San Sebastian, Spain.

Inorg. Chem., 2016, **54**, 11680-11687

Multiple phase and dielectric transitions on a novel multi-sensitive $[TPrA][M(dca)_3]$ (M: Fe^{2+}, Co^{2+} and Ni^{2+}) hybrid inorganic-organic perovskite family

Juan M. Bermúdez-García,*[a] Manuel Sánchez-Andújar,[a] Susana Yáñez-Vilar,[a,b] Socorro Castro-García,[a] Ramón Artiaga,[c] Jorge López-Beceiro,[c] Luis Botana,[d] Ángel Alegría[d,e] and María A. Señarís-Rodríguez*[a]

a. QuiMolMat Group, Department of Fundamental Chemistry, Faculty of Science and CICA, University of A Coruña, Campus A Coruña, 15071 A Coruña, Spain.
b. Department of Applied Physics, University of Santiago de Compostela, 15782 Santiago de Compostela, Spain.
c. Department of Industrial Engineering II, University of A Coruña. Campus Ferrol, 15403 Ferrol, Spain.
d. Material Physical Center, CSIC-UPV/EHU, P. Manuel de Lardizabal 5, 20018 Donostia-San Sebastian, Spain.
e. Material Physical Department, University of the Basque Country, PO Box 1072, 20008 Donostia-San Sebastian, Spain.

J. Mater. Chem. C, 2016, **4**, 4889-4898

Dielectric properties induced by the framework in the hybrid organic-inorganic compounds $M(dca)_2pyz$ M = Fe, Co and Zn

Alberto García-Fernández,[a] Juan M. Bermúdez-García,[a] Socorro Castro-García,[a] Ramón Artiaga,[b] Jorge López-Beceiro,[b] María A. Señarís-Rodríguez[a] and Manuel Sánchez-Andújar*[a]

a. QuiMolMat Group, Department of Fundamental Chemistry, Faculty of Science and CICA, University of A Coruña, Campus A Coruña, 15071 A Coruña, Spain.
b. Department of Industrial Engineering II, University of A Coruña. Campus Ferrol, 15403 Ferrol, Spain.

Polyhedron, 2016, **114**, 249-255

Liquid self-diffusion of H_2O and DMF molecules in Co-MOF-74: molecular dynamics simulations and dielectric spectroscopy studies

Juan M. Bermúdez-García,[a] José M. Vicent-Luna,[b] Susana Yáñez-Vilar,[a] Said Hamad,[b] Manuel Sánchez-Andújar,[a] Socorro Castro-García,[a] Sofía Calero*[b] and María A. Señarís-Rodríguez*[a]

a. QuiMolMat Group, Department of Fundamental Chemistry, Faculty of Science and CICA, University of A Coruña, Campus A Coruña, 15071 A Coruña, Spain.
b. Department of Physical, Chemical, and Natural Systems, Universidad Pablo de Olavide, Ctra. Utrera km. 1, ES-41013 Seville, Spain.

Phys.Chem.Chem.Phys., 2016, **18**, 19605-19612

A facile synthesis of Co_3O_4 hollow microtubes by decomposition of a cobalt metal-organic framework

L. Claudia Gómez-Aguirre,*[a] Socorro Castro-García,*[a] Manuel Sánchez-Andújar,[a] Susana Yáñez-Vilar,[a] Jorge Mira,[b] Juan M. Bermúdez-García,[a] Teresa A. Centeno[c] and María A. Señarís-Rodríguez[a]

a. QuiMolMat Group, Department of Fundamental Chemistry, Faculty of Science and CICA, University of A Coruña, Campus A Coruña, 15071 A Coruña, Spain.
b. Department of Applied Physics, University of Santiago de Compostela, 15782 Santiago de Compostela, Spain.
c. Instituto Nacional del Carbón (INCAR-CSIC), P. O. Box 73, 33080 Oviedo, Spain.

Eur. J. Inorg. Chem., 2016, DOI: **10.1002/ejic.201600192**

Giant barocaloric effect in the ferroic organic-inorganic hybrid [TPrA][Mn(dca)$_3$] perovskite under easily accessible pressures

Juan M. Bermúdez-García,*[a] Manuel Sánchez-Andújar,[a] Socorro Castro-García,[a] Jorge López-Beceiro,[b] Ramón Artiaga[b] and María A. Señarís-Rodríguez*[a]

a. QuiMolMat Group, Department of Fundamental Chemistry, Faculty of Science and CICA, University of A Coruña, Campus A Coruña, 15071 A Coruña, Spain.
b. Department of Industrial Engineering II, University of A Coruña. Campus Ferrol, 15403 Ferrol, Spain.

Submitted

A simple method to synthesize carbon nanotubes embedded with magnetic nanoparticles by using the organic-inorganic hybrid perovskite [TPrA][M(dca)$_3$] (M = Ni^{2+} and Co^{2+}) as precursor

Juan M. Bermúdez-García,[a]* Susana Yáñez-Vilar,[b] Alberto García-Fernández,[a] Manuel Sánchez-Andújar,[a] Socorro Castro-García,[a] Jorge Mira,[b] J. Agostinho Moreira,[c] Teresa A. Centeno[d] and M. A. Señarís-Rodríguez*[a]

a. QuiMolMat Group, Department of Fundamental Chemistry, Faculty of Science and CICA, University of A Coruña, Campus A Coruña, 15071 A Coruña, Spain.
b. Department of Applied Physics, University of Santiago de Compostela, 15782 Santiago de Compostela, Spain.
c. IFIMUP-IN, Faculdade de Ciencias, Universidade do Porto, 4169-007 Porto, Portugal
d. Instituto Nacional del Carbón (INCAR-CSIC), P. O. Box 73, 33080 Oviedo, Spain.

Submitted

Phase transition, dielectric properties and ionic transport in the $[(CH_3)_2NH_2]PbI_3$ organic-inorganic hybrid with 2H-hexagonal perovskite structure

Alberto García-Fernández,[a] Juan M. Bermúdez-García,[a] Socorro Castro-García,[a] Antonio L. Llamas-Saiz,[b] Ramón Artiaga,[c] Jorge López-Beceiro,[c] Shunbo Hu,[d,e] Wei Ren,[d,e] Alessandro Stroppa,[d,f] Manuel Sánchez-Andújar[a] and María A. Señarís-Rodríguez[a]

a. QuiMolMat Group, Department of Fundamental Chemistry, Faculty of Science and CICA, University of A Coruña, Campus A Coruña, 15071 A Coruña, Spain.
b. RIAIDT X-Ray Unit, University of Santiago de Compostela, 15782 Santiago de Compostela, Spain.
c. Department of Industrial Engineering II, University of A Coruña. Campus Ferrol, 15403 Ferrol, Spain.
d. International Center for Quantum and Molecular Structures, Physics Department, Shanghai University, Shanghai 200444, China.
e. Materials Genome Institute and Shanghai Key Laboratory of High Temperature Superconductors, Shanghai University, Shanghai 200444, China.
f. CNR-SPIN, L'Aquila, Italy.

Submitted

Communications in scientific congresses

Oral Communication: "Multiple phase transition and dielectric transition of dicyanamide (TPrA)[M(dca)$_3$] compounds with perovskite-like structure"

Juan M. Bermúdez-García,*[a] Manuel Sánchez-Andújar,[a] Susana Yáñez-Vilar,[b] Jorge Mira,[b] Alfonso Fondado,[b] Jorge López-Beceiro,[c] R. Artiaga,[c] Socorro Castro García[a] and María A. Señarís-Rodríguez*[a]

a. QuiMolMat Group, Department of Fundamental Chemistry, Faculty of Science and CICA, University of A Coruña, Campus A Coruña, 15071 A Coruña, Spain.
b. Department of Applied Physics, University of Santiago de Compostela, 15782 Santiago de Compostela, Spain.
c. Department of Industrial Engineering II, University of A Coruña. Campus Ferrol, 15403 Ferrol, Spain.

VIII Encuentro Franco-Español: Química y Física del Estado Sólido
2-4 April 2014, Vila-Real (Spain)

Oral Communication: "A simple method to synthesize carbon nanotubes with magnetic nanoparticles, using dicyanamidometallate coordination polymers as precursors"

Juan M. Bermúdez-García,*[a] Manuel Sánchez-Andújar,[a] Susana Yáñez-Vilar,[b] Jorge Mira,[b] Alfonso Fondado,[b] Socorro Castro García[a] and María A. Señarís-Rodríguez*[a]

a. QuiMolMat Group, Department of Fundamental Chemistry, Faculty of Science and CICA, University of A Coruña, Campus A Coruña, 15071 A Coruña, Spain.

16ª Reunión Científica Plenaria de Química Inorgánica y
10ª Reunión Plenaria de Química del Estado Sólido, QIES 2014
15-18 June 2014, Almería (Spain)

Oral Communication: "Temperature and pressure dependence on functional properties in a novel multisensitive [TPrA][Mn(dca)$_3$] perovskite"

Juan M. Bermúdez-García,*[a] Alberto García-Fernández,[a] Manuel Sánchez-Andújar,[a] Susana Yáñez-Vilar,[a] Socorro Castro-García,[a] Ramón Artiaga,[b] Jorge López-Beceiro,[b] Ángel Alegría[c] and María A. Señarís-Rodríguez*[a]

a. QuiMolMat Group, Department of Fundamental Chemistry, Faculty of Science and CICA, University of A Coruña, Campus A Coruña, 15071 A Coruña, Spain.
b. Department of Industrial Engineering II, University of A Coruña. Campus Ferrol, 15403 Ferrol, Spain.
c. Material Physical Center, CSIC-UPV/EHU, P. Manuel de Lardizabal 5, 20018 Donostia-San Sebastian, Spain.

XXXV Reunión Bienal de la Real Sociedad Española de Química
19-23 July 2015, A Coruña (Spain)

Poster Communication: "A new perovskite-like MOF $[C_3N_2H_5][Mn(HCOO)_3]$ with coexistence of magnetic and polar order"

Breogan Pato-Doldán,[a] L.Claudia Gómez-Aguirre,[a] Juan M. Bermúdez-García,[a] Manuel Sánchez-Andújar,[a] Alfonso Fondado,[b] Jorge Mira,[b] Socorro Castro-García[a] and María A. Señarís-Rodríguez*[a]

a. Department of Fundamental Chemistry, Faculty of Science, University of A Coruña, Campus A Coruña, 15071 A Coruña, Spain.
b. Department of Applied Physics, University of Santiago de Compostela, 15782 Santiago de Compostela, Spain.

European Congress and Exhibition on Advanced Materials and Processes, FEMS EUROMAT2013
8-13 September 2013, Sevilla (Spain)

Poster Communication: "Synthesis, characterization and dielectric properties of a novel series of $[G][Cd(HCOO)_3]$ compounds templated by different alkylammonium"

Breogan Pato-Doldán,[a] L. Claudia Gómez-Aguirre,[a] Juan M. Bermúdez-García,[a] Susana Yáñez-Vilar,[a] Manuel Sánchez-Andújar,[a] Socorro Castro-García[a] and María A. Señarís-Rodríguez*[a]

a. Department of Fundamental Chemistry, Faculty of Science, University of A Coruña, Campus A Coruña, 15071 A Coruña, Spain.

European Congress and Exhibition on Advanced Materials and Processes, FEMS EUROMAT2013
8-13 September 2013 Vila-Real, Sevilla (Spain)

Poster Communication: "A microporous luminiscent metal organic framework $[Zn_2(NH_2\text{-}bdc)_2(dabco)][G]$ as chemical sensor"

L. Claudia Gómez-Aguirre,[a] Manuel Sánchez-Andújar,[a] Breogan Pato-Doldán,[a] Juan M. Bermúdez-García,[a] Susana Yáñez-Vilar,[a] Socorro Castro-García[a] and María A. Señarís-Rodríguez*[a]

a. Department of Fundamental Chemistry, Faculty of Science, University of A Coruña, Campus A Coruña, 15071 A Coruña, Spain.

European Congress and Exhibition on Advanced Materials and Processes, FEMS EUROMAT2013
8-13 September 2013, Sevilla (Spain)

Poster Communication: "$[Co_2(NH_2\text{-}bdc)_2(dabco)]$ metal-organic framework as precursor to prepare Co_3O_4 as hollow micro/nanotubes"

L. Claudia Gómez-Aguirre,[a] Breogan Pato-Doldán,[a] Susana Yáñez-Vilar,[a] Juan M. Bermúdez-García,[a] Alfonso Fondado,[b] Jorge Mira,[b] Manuel Sánchez-Andújar,[a] Socorro Castro-García[a] and María A. Señarís-Rodríguez*[a]

a. Department of Fundamental Chemistry, Faculty of Science, University of A Coruña, Campus A Coruña, 15071 A Coruña, Spain.
b. Department of Applied Physics, University of Santiago de Compostela, 15782 Santiago de Compostela, Spain.

European Congress and Exhibition on Advanced Materials and Processes, FEMS EUROMAT2013
8-13 September 2013, Sevilla (Spain)

Poster Communication: "On the first-order structural transition in the multiferroic perovskite-like formate $[(CH_3)_2NH_2][Mn(HCOO)_3]$"

Manuel Sánchez-Andújar,[a] L. Claudia Gómez-Aguirre,[a] Breogan Pato-Doldán,[a] Juan M. Bermúdez-García,[a] Susana Yáñez-Vilar,[a] Ramón Artiaga,[b] Rudra S. Manna,[c] Frank Schnelle,[c] Michael Lang,[c] Frank Ritter,[c] Amir. A. Haghighirad,[c,d] María A. Señarís-Rodríguez*[a]

a. Department of Fundamental Chemistry, Faculty of Science, University of A Coruña, Campus A Coruña, 15071 A Coruña, Spain.
b. Department of Industrial Engineering II, University of A Coruña. Campus Ferrol, 15403 Ferrol, Spain.
c. Institute of Physics, Goethe University, 60438 Frankfurt am Main, Germany.
d. Clarendon Laboratory, University of Oxford, Parks Road, Oxford OX1 3PU, U.K.

VIII Encuentro Franco-Español: Química y Física del Estado Sólido
2-4 April 2014, Castelló (Spain)

Poster Communication: "Comparative study of chlorinated and non-chlorinated additives on $MAPbI_3$ perovskite solar cells with flat and inverted architecture"

Juan M. Bermúdez-García,*[a] Jacob Tse-Wei Wang,[b] Manuel Sánchez-Andújar,[a] Socorro Castro-García[a], María A. Señarís-Rodríguez[a] and Henry J. Snaith*[b]

a. QuiMolMat Group, Department of Fundamental Chemistry, Faculty of Science and CICA, University of A Coruña, Campus A Coruña, 15071 A Coruña, Spain.
b. Clarendon Laboratory, University of Oxford, Parks Road, Oxford OX1 3PU, U.K.

Hybrid and Organic Photovoltaic Conference, HOPV15
10-13 May 2015, Rome (Italy)

Poster Communication: "Híbridos orgánico-inorgánicos [M(dca)$_2$pyz] (M: Fe^{2+}, Co^{2+}, Ni^{2+}, Zn^{2+}) con transiciones dieléctricas"

Alberto García-Fernández,[a] Juan M. Bermúdez-García,*[a] Socorro Castro-García[a], Manuel Sánchez-Andújar[a] and María A. Señarís-Rodríguez*[a]

a. QuiMolMat Group, Department of Fundamental Chemistry, Faculty of Science and CICA, University of A Coruña, Campus A Coruña, 15071 A Coruña, Spain.

XXXV Reunión Bienal de la Real Sociedad Española de Química

19-23 July 2015, A Coruña (Spain)

Poster Communication: "Role of transition metal cations (Fe^{3+}, Co^{2+}, Ni^{2+}) doping on photovoltaic properties of MAPbI$_{(3-x)}$Cl$_x$ thin-films"

Juan M. Bermúdez-García,*[a] Jacob Tse-Wei Wang,[b] Manuel Sánchez-Andújar,[a] Socorro Castro-García[a], María A. Señarís-Rodríguez[a] and Henry J. Snaith*[b]

a. QuiMolMat Group, Department of Fundamental Chemistry, Faculty of Science and CICA, University of A Coruña, Campus A Coruña, 15071 A Coruña, Spain.
b. Clarendon Laboratory, University of Oxford, Parks Road, Oxford OX1 3PU, U.K.

Solution Processed Innovative Solar Cells, SPINS15

9-11 September 2015, Santiago de Compostela (Spain)

Poster Communication: "The role of mixed-additives MACl:NH$_4$Cl on MAPbI$_3$ perovskite solar cells performance"

Juan M. Bermúdez-García,*[a] Jacob Tse-Wei Wang,[b] Manuel Sánchez-Andújar,[a] Socorro Castro-García[a], María A. Señarís-Rodríguez[a] and Henry J. Snaith*[b]

a. QuiMolMat Group, Department of Fundamental Chemistry, Faculty of Science and CICA, University of A Coruña, Campus A Coruña, 15071 A Coruña, Spain.
b. Clarendon Laboratory, University of Oxford, Parks Road, Oxford OX1 3PU, U.K.

Solution Processed Innovative Solar Cells, SPINS15

9-11 September 2015, Santiago de Compostela (Spain)

Poster Communication: "Looking for new hybrid inorganic-organic materials suitable as absorbent for solar cell devices"

Alberto García-Fernández,[a] Juan M. Bermúdez-García,[a] Manuel Sánchez-Andújar,[a] Socorro Castro-García[a], and María A. Señarís-Rodríguez*[a]

a. QuiMolMat Group, Department of Fundamental Chemistry, Faculty of Science and CICA, University of A Coruña, Campus A Coruña, 15071 A Coruña, Spain.

Solution Processed Innovative Solar Cells, SPINS15

9-11 September 2015, Santiago de Compostela (Spain)

Poster Communication: "Searching new visible light absorbing and Pb-free inorganic-organic hybrid materials for photovoltaic applications"

Alberto García-Fernández,[a] L. Claudia Gómez-Aguirre,[a] Juan M. Bermúdez-García,[a] Socorro Castro-García[a], Manuel Sánchez-Andújar[a] and María A. Señarís-Rodríguez*[a]

a. QuiMolMat Group, Department of Fundamental Chemistry, Faculty of Science and CICA, University of A Coruña, Campus A Coruña, 15071 A Coruña, Spain.

17ª Reunión Científica Plenaria de Química Inorgánica y
11ª Reunión Plenaria de Química del Estado Sólido, QIES 2016
19-22 June 2016, Málaga (Spain)

Poster Communication: "Cooperative electric order in ferrocene and ammonia-borane: new functional properties in two "classic" molecular compounds"

Juan M. Bermúdez-García,[a] Susana Yáñez-Vilar,[a,b] Socorro Castro-García[a], Manuel Sánchez-Andújar[a] and María A. Señarís-Rodríguez[a]

a. QuiMolMat Group, Department of Fundamental Chemistry, Faculty of Science and CICA, University of A Coruña, Campus A Coruña, 15071 A Coruña, Spain.
b. Department of Applied Physics, University of Santiago de Compostela, 15782 Santiago de Compostela, Spain.

17ª Reunión Científica Plenaria de Química Inorgánica y
11ª Reunión Plenaria de Química del Estado Sólido, QIES 2016
19-22 June 2016, Málaga (Spain)

Poster Communication: "Dicyanamide-bridge ligands as building blocks for multifunctional and multistimuli responsive organic-inorganic hybrid perovskites"

Juan M. Bermúdez-García,*[a] Susana Yáñez-Vilar,[a,b] Manuel Sánchez-Andújar,[a] Jorge López-Beceiro,[c] Socorro Castro-García,[a] Ramón Artiaga,[c] and María A. Señarís-Rodríguez*[a]

a. QuiMolMat Group, Department of Fundamental Chemistry, Faculty of Science and CICA, University of A Coruña, Campus A Coruña, 15071 A Coruña, Spain.
b. Department of Applied Physics, University of Santiago de Compostela, 15782 Santiago de Compostela, Spain.
c. Department of Industrial Engineering II, University of A Coruña. Campus Ferrol, 15403 Ferrol, Spain.

Challenges and Prospects for Solid State Chemistry, CPSSC16
9-10 September 2016, Sevilla (Spain)

Poster Communication: "Synthesis and phase transition of the $[(CH_3)_2NH_2]PbI_3$ organic-inorganic hybrid with 2H-hexagonal perovskite structure"

Alberto García-Fernández,[a] Juan M. Bermúdez-García,[a] Socorro Castro-García,[a] Antonio L. Llamas-Saiz,[b] Ramón Artiaga,[c] Jorge López-Beceiro,[c] Manuel Sánchez-Andújar[a] and María A. Señarís-Rodríguez*[a]

a. QuiMolMat Group, Department of Fundamental Chemistry, Faculty of Science and CICA, University of A Coruña, Campus A Coruña, 15071 A Coruña, Spain.
b. RIAIDT X-Ray Unit, University of Santiago de Compostela, 15782 Santiago de Compostela, Spain.
c. Department of Industrial Engineering II, University of A Coruña. Campus Ferrol, 15403 Ferrol, Spain.

Semiconductor Ferroelectrics and Photoferroelectrics, SEFERR16

12-13 September 2016, Berlin (Germany)

Poster Communication: "Dielectric properties and ionic transport in the $[(CH_3)_2NH_2]PbI_3$ organic-inorganic hybrid material"

Alberto García-Fernández,[a] Juan M. Bermúdez-García,[a] Manuel Sánchez-Andújar,*[a] Shunbo Hu,[b,c] Wie Ren,[b,c] Alessandro Stroppa,[b,d] Socorro Castro-García,[a] and María A. Señarís-Rodríguez*[a]

a. QuiMolMat Group, Department of Fundamental Chemistry, Faculty of Science and CICA, University of A Coruña, Campus A Coruña, 15071 A Coruña, Spain.
b. International Center for Quantum and Molecular Structures, Physics Department, Shanghai University, Shanghai 200444, China.
c. Materials Genome Institute and Shanghai Key Laboratory of High Temperature Superconductors, Shanghai University, Shanghai 200444, China.
d. CNR-SPIN, L'Aquila, Italy.

Semiconductor Ferroelectrics and Photoferroelectrics, SEFERR16

12-13 September 2016, Berlin (Germany)